

**Characterization of Fuel Spray Injected by Hole-Type
Nozzle into Cross-Flow Ambient**

(横風気流中にホールノズルから噴射した燃料噴霧の特性)

by

Min Guo

Dissertation

Submitted to the Graduate School of Engineering

Hiroshima University

in Partial Fulfillment of the Requirements

For the Degree of

Doctor of Engineering

Hiroshima University

March, 2015

ABSTRACT

A Direct Injection (DI) technique has promoted the overall performances of a gasoline engine, since the technique offers opportunities to run the engine in the stratified charge combustion mode and the homogeneous charge combustion mode. The fuel injection usually occurs during the intake stroke in the homogeneous charge combustion mode, therefore the pressure in combustion chamber is close to the atmospheric pressure; while in the stratified charge combustion mode the fuel injection occurs during the compression stroke, and the pressure in combustion chamber is higher than the atmospheric pressure. To fundamentally understand the effects of the air flow on the fuel spray in the combustion chamber of the DI gasoline engine, the characteristics of the fuel spray in a uniform cross-flow field were experimentally investigated in this study. The experiments are divided into two parts, in which the measurement of the spray characteristics under the atmospheric and high pressure ambient conditions are taken coinciding to the two modes.

An atmospheric wind tunnel and a high pressure wind tunnel are utilized to provide the uniform cross-flow field in the atmospheric pressure and high pressure ambient. Ethanol is employed as test fuel in this study. The structure, velocity distribution and droplet size are measured by high speed video photography, particle image velocimetry and laser diffraction size analyzer. The spray was injected perpendicularly into the cross-flow field by the valve covered orifice nozzle. The trigger for the fuel injection was controlled by an automatic control system, which can emit a trigger signal when the pressure and velocity satisfying the experimental conditions in the experiments using the high pressure wind tunnel.

The structures of the spray are bended obviously by the cross-flow, especially in the lower part of the spray. The most droplets of the spray concentrate near the edge of the spray in the upstream of the cross-flow while some tiny droplets are entrained into the cross-flow in the upper part of the spray. The penetrations of the spray tip are measured and the empirical correlations are deduced. The structural fluctuations appears in the distribution of the velocity components in the horizontal, and the value exceed even the velocity of cross-flow. The vortex phenomenon in the leeward of the spray is verified by analyzing the velocity distributions and the structures of the spray in the horizontal planes. This phenomenon is similar to the Karman vortex street, which happen when a fluid flows passes a circular cylinder. Droplets are concentrated in the spray center without cross-

flow, while the large amount of droplets are blown downstream of the spray with cross-flow. The larger droplets distribute in the high concentration area and the diameter of droplets is decreased along the direction of the cross-flow.

The numerical simulations were conducted under a few representative conditions. The real size simulating model with same boundary conditions are selected in the simulation. The spray profiles, penetrations, velocity distributions, and droplet size distributions of the simulation have been represented and compared with the experimental results.

ACKNOWLEDGMENTS

I would like to express my sincere gratitude and appreciation to my academic advisor, Professor Keiya Nishida, for his support, encouragement, patience, and guidance of my research activities throughout the three years when I was at the Fluid Engineering and Spray Technology Laboratory, University of Hiroshima. I would not finish my PhD without this expert guidance and generous support, Professor Keiya Nishida has given me so much help and advice in my subject research, writing papers, Japanese learning, even daily life in Japan during all my doctoral course. I extremely proud and honored to have the opportunity to associate my name with him.

I can also never thank Professor Youichi Ogata enough. It is a great privilege and joy to work with Professor Youichi Ogata. I admire him for his rigorous working amplitude, preciseness and patience in teaching. He has given me great help in the theoretical learning of liquid knowledge. I would like to thank Professor Baolu Shi for his patiently help in experiments and paper writing during my learning period. I have learned much from his experience and knowledge about the experiment implements and paper writing. I would like to thank our team members Mr. Ryosuke Kishi, Mr. Ryohei Sugawa, and Mr. Nagisa Shimasaki. Without their cooperation, I cannot finish the experiments in three years. Mr. Ryosuke Kishi has given me so much help not only in researches but also in daily life, especially in learning Japanese. I would like to thank Dr. Kuichun Li, Dr. Run Chen and Mr. Pengbo Dong for the kind and patiently help in Japan. I would like to thank our Fluid Engineering and Spray Technology Laboratory members for their support. They are a group of young men with good abilities, enthusiasm, outgoing personality and optimism. They helped me to learn Japanese language and understand culture in the daily life and laboratory activities.

I would like to express my sincere gratitude to my parents, sisters and other families. Without their love, support and encouragement, I would not finish the learning in Japan. I would like to thank my sweet lover Ms. Qingrong Fan for her selfless dedication. She has given a great help in application of entering the University of Hiroshima when I was still in China. She has provided comfortable condition during my busy study periods. I also want to thank my dear friends in Japan, their concerns make my life colorful in Japan.

Last and not least, I would like to thank the staff in Hiroshima University and all the Japanese around us. They provided nice, peaceful environment and help for us to research and living in Japan.

TABLE OF CONTENTS

Abstract	I
Acknowledgments	III
Table of Contents	V
Nomenclatures	IX
Chapter 1 Introduction	1
1.1 Background and Motivation	1
<i>1.1.1 Energy trends and climate change</i>	<i>1</i>
<i>1.1.2 DISI engine</i>	<i>5</i>
<i>1.1.3 Injector and spray</i>	<i>9</i>
1.2 Objective and Approaches	12
1.3 Outlines	13
1.4 Literature Review	14
<i>1.4.1 Spray mixture formation and DISI engine</i>	<i>14</i>
<i>1.4.2 Spray diagnosing methods</i>	<i>22</i>
<i>1.4.3 Air-flow in cylinder of DISI engine</i>	<i>24</i>
<i>1.4.4 Spray/jet in cross-flow</i>	<i>27</i>
1.5 Summary	32
Chapter 2 Experimental Apparatus and Procedures	33
2.1 Experimental Methods	33
<i>2.1.1 Spray visualization</i>	<i>33</i>
<i>2.1.2 Velocity distribution measurement</i>	<i>34</i>
<i>2.1.3 Droplet size measurement</i>	<i>39</i>
2.2 Experimental Setup	43
<i>2.2.1 Experiment setup Units</i>	<i>43</i>
<i>2.2.2 Structure of wind tunnel</i>	<i>46</i>
<i>2.2.3 Performance evaluation</i>	<i>48</i>
2.3 Summary	50

Chapter 3 Experimental Apparatus for High Pressure Cross-Flow Condition	51
3.1 Theoretical Calculation.....	51
3.2 Structure of High Pressure Wind Tunnel.....	56
3.3 Control System	60
3.4 Performance Evaluation	62
3.5 Summary	69
Chapter 4 Global Structure of Spray in Cross-Flow.....	71
4.1 Structure of Spray Injected by VCO Nozzle.....	71
4.2 Temporal Profiles in Atmospheric Ambient.....	73
4.3 Spray Penetration and Empirical Correlations.....	76
4.4 Tomographic Profiles of Spray.....	81
4.5 Summary	84
Chapter 5 Cross-Sectional Structure of Spray	85
5.1 Three Dimensional Spray Structure.....	85
5.2 Spray Details in Cross-sectional Planes.....	88
5.3 Projected Spray Angle.....	92
5.4 Vortex Phenomenon and Frequency Analysis.....	94
5.4.1 <i>Vortex phenomenon of droplets in cross-flow</i>	94
5.4.2 <i>Vortex in cross-flow field</i>	95
5.5 Summary	99
Chapter 6 Spray Droplets Flow Field	101
6.1 Velocity Distribution in Vertical Planes.....	101
6.2 Velocity Distribution in Horizontal Planes.....	112
6.3 Vorticity Distribution	117
6.4 Summary	120
Chapter 7 Spatial Distributions of Droplets and Their Sizes	121
7.1 Spatial Distributions	121
7.2 Droplet Size Distribution	126

7.3 Cross-flow Effects on Atomization.....	128
7.4 Summary	130
Chapter 8 Effects of Ambient Pressure on Spray Characteristics	131
8.1 Temporal Profiles in Various Pressure Ambient.....	131
8.2 Penetrations of Spray in Various Pressure Ambient.....	137
8.3 Velocity Distribution in Vertical Planes.....	141
8.4 Droplet Distribution	146
8.5 Summary	151
Chapter 9 Numerical Simulation	153
9.1 Basic Equations and Modeling.....	153
<i>9.1.1 Basic Equations.....</i>	<i>153</i>
<i>9.1.2 Simulation mesh and injection.....</i>	<i>156</i>
9.2 Spray Profile Variations.....	157
9.3 Spray Penetrations	161
9.4 Velocity Distributions	164
9.5 Droplet Size Distributions.....	167
9.6 Summary and Future Simulation Work	169
Chapter 10 Conclusions.....	171
10.1 Experimental Methods and Implementation.....	171
10.2 Global Structure of Spray in Cross-Flow.....	172
10.3 Cross-Sectional Structure of Spray	172
10.4 Spray Droplets Flow Field.....	173
10.5 Spatial Distribution of Droplets and Their Sizes.....	173
10.6 Effect of Ambient Pressure on Spray Characteristics.....	174
10.7 Numerical Simulation	174
10.8 Recommendations for Future Works	175
Reference.....	177
Appendix	188

NOMENCLATURES

A	Section area (m ²)
A_{drop}	Sum of all droplet surface areas (m ²)
d	Nozzle hole diameter (m)
d_p	Particle diameter (m)
d_s	Sac hole diameter (m)
D	Diameter of the spray beam (m)
D_{fr}	Flexural rigidity
e	Internal energy (J)
f	Vortex shedding frequency (Hz)
F	Force (N)
f_i	Secondary vortex shedding frequency (Hz)
f_j	Body force (N)
h	Distance from the edge of spray to x axis for constant horizontal x position (mm)
h_p	Thickness of plate (m)
h_w	Thickness of window (m)
i	The i th sample
I	Laser intensity (W/cm ²)
L	Length of nozzle hole (m)
L_C	Liquid cone length (m)
L_{con}	Length of contraction section curve (m)
N	Total number of sample

m	Mass (kg)
P_1	Pressure in tank (Pa)
P_2	Pressure in observation section (Pa)
P_{inj}	Injection pressure (Pa)
P_a	Ambient pressure/Atmospheric pressure (Pa)
q	Liquid-to-air momentum flux ratio ($\rho_l U_l / \rho_g U_x$)
Q	Air flowrate (m ³ /s)
\dot{Q}_s	Heat flux (J)
r	Radius of inlet edge of nozzle hole (m)
Re	Reynolds number
S	Vertical penetration without cross-flow (m)
St	Strouhal number
S_s	Vertical penetration with cross-flow (m)
t	Time (after the start of injection, s)
t_{break}	Time when liquid jet begins to disintegrate (s)
t_d	Injection duration (s)
T	Temperature (K)
T_a	Ambient temperature (K)
We	Weber number
X_l	A constant horizontal distance (mm)
u	Velocity component in x axis (m/s)
v	Velocity component in y axis (m/s)
$u_x(i)$	Actual velocity for the i th sample (m/s)

u'_x/U_x	Turbulence intensity
U	Velocity (m/s)
U_I	Initial injection velocity (m/s)
U_x	Mean velocity of cross-flow (m/s)
V_1	Volume of tank (m ³)
V_2	Volume of observation section (m ³)
V_{drop}	Sum of all droplet volumes (m ³)
α	Projected spray half angle (°)
λ	Horizontal distance between two adjacent peaks at the edge of the spray (mm)
λ_h	Heat transfer coefficient (w/(m·K))
λ_L	Wave length of laser (m)
μ_p	Poisson ratio
μ	Dynamic viscosity (Pa·S)
ν	Air kinematic viscosity (m ² /s)
ρ_1	Air densities in tank (kg/m ³)
ρ_2	Air densities in observation section (kg/m ³)
ρ_a	Atmospheric air densities (kg/m ³)
ρ_g	Gas density (kg/m ³)
ρ_l	Liquid densities (kg/m ³)
σ	Stress (Pa)
τ_{ij}	Stress tensor (N)
φ	Dissipation function

Φ	Spray cone Angle ($^{\circ}$)
ω	Deflection (m)
ΔP	$\Delta P = P_{inj} - P_a$, pressure drop across the nozzle (Pa)
ΔS_0	Displacement of the spray in the same period (1 ms) in the line of $x = 0$ mm (mm)
ΔS_{C1}	Displacement of the leeward edge of the spray in horizontal direction in the upper part of the spray ($y < 75$ mm) (mm)
ΔS_{C2}	Distance between two points that are the farthest horizontal points at the leeward edge of the lower part of the spray ($y > 75$ mm) (mm)
ΔX	Particle displacement in x axis in image plane
Δy	Particle displacement in y axis in object plane
ΔY	Particle displacement in y axis in image plane
ASOI	After Start Of Injection
BTDC	Before Top Dead Center
CFD	Computational Fluid Dynamics
DISI	Direct Injection Spark Ignition
EGR	Exhaust Gas Recirculation
GDI	Gasoline Direct Injection
HCCI	Homogenous Charge Compression Ignition
HSV	High Speed Video
ILIDS	Interferometric Laser Imaging for Droplet Sizing
LDA	Laser Doppler Anemometry
LDSA	Laser Diffraction Size Analyzer

LDV	Laser Doppler Velocimetry
LEA	Laser Extinction and Absorption
LIEF	Laser Induced Exciplex Fluorescence
PDA	Phase Doppler Analyzer
PFI	Port Fuel Injection
PLIF	Planar Laser Inducted Fluorescence
PIV	Particle Image Velocimetry
PTV	Particle Tracking Velocimetry
SCSI	Stratified Combustion Spark Ignition
SF	Safety factor
SMD	Sauter Mean Diameter
VCO	Valve Covered Orifice

Chapter 1 Introduction

1.1 Background and Motivation

1.1.1 Energy trends and climate change

Energy is considered as one of the most important survival and development element, which is concerned by human beings all the time. Environmental issues, which accompany with the population growth and economic development, are induced by the heavy energy use, especially the fossil fuel use. Fossil fuel is a kind of buried combustible organic materials, which are formed from decayed plants and animals by exposure to heat and pressure in the crust of the earth over thousands and millions of years. The specific forms of the fossil fuel are crude oil, coal, natural gas, and heavy oils. Fossil fuel is non-renewable source, which will be used up in many years. The downstream industries will be affected when the fossil fuel is depleted. In addition, the consumption of the fossil fuel contributes the pollutions of the natural environment which the mankind depends on living. Climate warming is an indisputable fact, which has been presented by many researchers (Lacis et al, 2013; Dillon et al, 2010; Schneider, 1989). Greenhouse gas emission is considered as the immediate reason of the climate warming. The greenhouse gases and harmful gases pollute the environments, which threaten eco-system and the health of human beings. Improving energy efficiency and reducing the greenhouse gas emission are very significant as well as developing clean energies.

The world energy demand is increasing with the booming of the population. A research from ExxonMobil (Colton, 2014), in 2040, the population of world will reach approximate 9 billion, the GDP will exceed 150 trillion, and simultaneously the energy demand will rise to 1300 quadrillion BTUs (British thermal unit) following the tendency of the last two decades (see Fig. 1.1). If the energy conservation and efficient energy use implement well, the energy demand in 2040 will reduce to less than 700 quadrillion BTUs. It is interchangeable between the energy conservation and the energy efficiency, the former encourages people to use less energy like turning your lights off, while the latter is using energy more effectively by technological changes (Energy conservation vs. energy efficiency, 2014). The energy consumption will bring a series of problems. The fossil fuel will be exploited excessively, because the mainly energy is acquired from coal and oil. Although the renewable energy and clear energy will be developed, the main energy is still

fossil fuel. The emissions of the fossil fuel consumption are still a large percentage, especially, the greenhouse gases emission will increase significantly. There are many ways to save energy, except developing the new energies, energy efficiency improvement is still a meaningful research orientation. The technology improvement like optimizing the methods of combustion (Shi et al, 2013) and the restraining the emission like CO₂ capture and storage technology enhance the energy efficiency and reduce the harmful gases emission substantially.

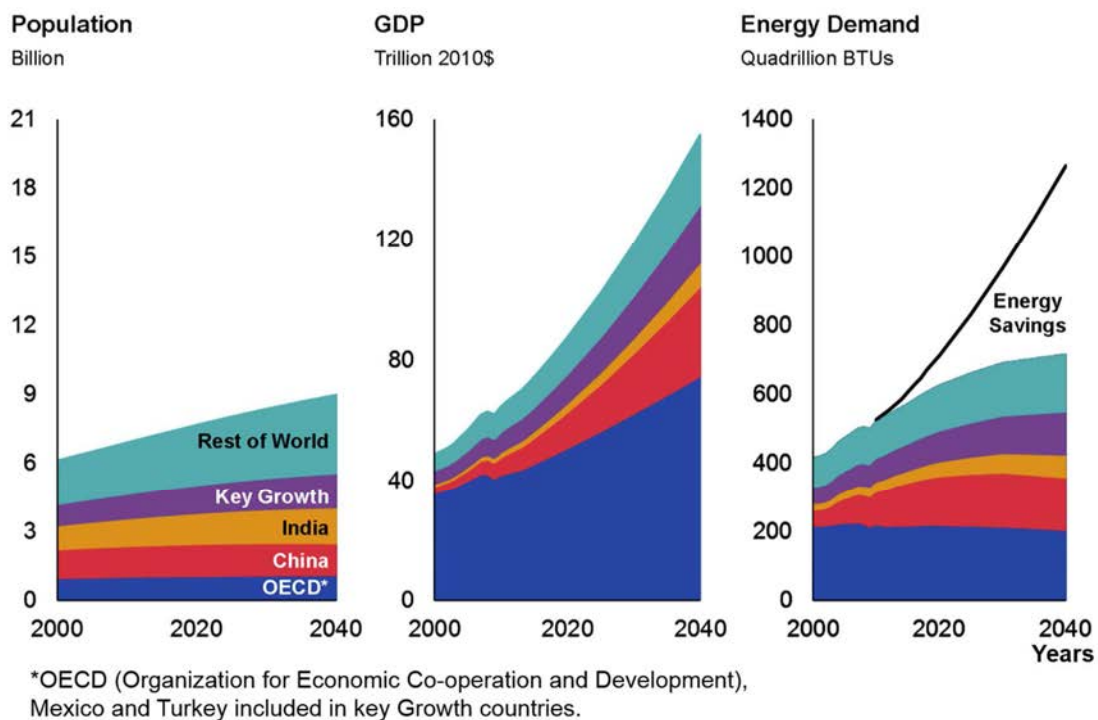


Figure 1.1 Global progress demand.

The environment problems are closely related with the energy consumption. The pollutions and climate warming are concerned no longer only the researchers, the most ordinary beings are conscious of the environment damage recently, for example the heavy haze appears in some area. The climate warming is contributed to the greenhouse gases emissions. The CO₂, which is produced by consuming fossil fuel, is main part of the greenhouse gases. The global annual CO₂ emission is 31 billion ton (Gt), recently. According to the investigation of IEA (2014), the CO₂ emission will increase to 55 Gt by 2050 following the tendency of the last two decades, and the average global temperature will rise at least 6°C, as shown in Fig. 1.2. It is called 6°C Scenario (6DS), which is largely an extension of current trends. 4°C Scenario (4DS) and 2°C Scenario

(2DS) are predicted. The 4DS takes into account recent pledges made by countries to limit emissions and step up efforts to improve energy efficiency, this scenario requires significant changes in policy and technologies. The significant additional cuts in emission is the main goal of 4DS. According to the recent climate science research, the emission should be decreased at least a half of recent value, which can meet the limiting of the average global temperature increase to 2°C. The 2DS sets the stricter targets of cutting energy and greenhouse gases emissions. Realizing the goals needs supports of various field, especially governments and technology sectors. The 2DS is a sustainable development plan, energy conservation and energy efficiency are also significant.

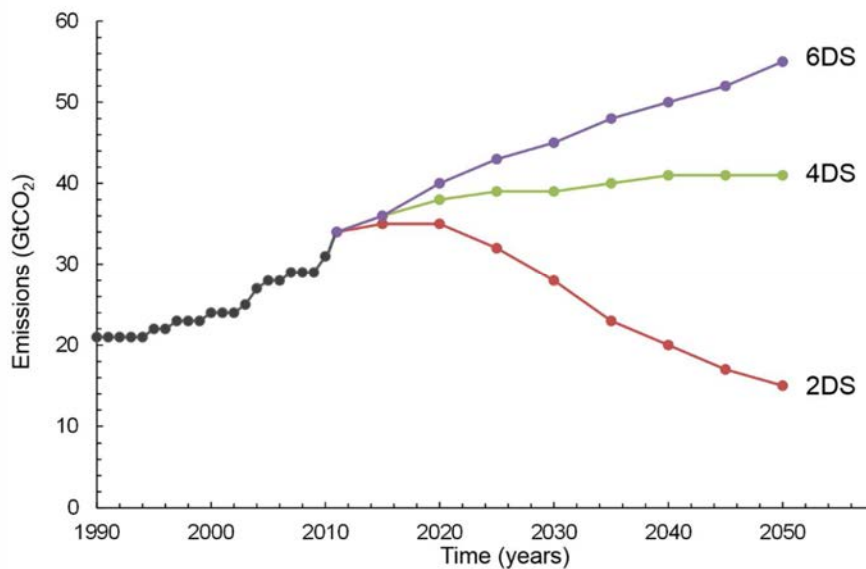


Figure 1.2 Global CO₂ emissions.

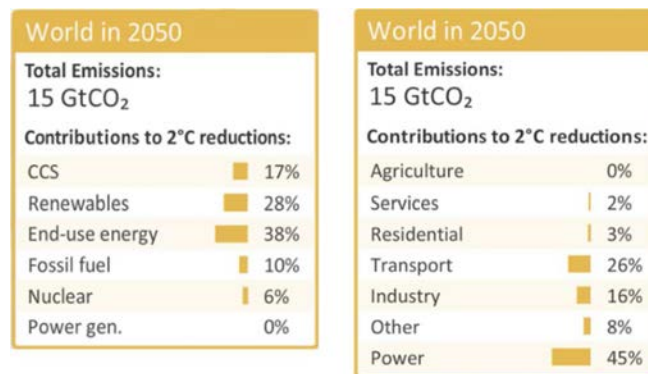


Figure 1.3 CO₂ emissions and contributions of technology and sector.

In the CO₂ emission cutting (see Fig. 1.3), the technologies, which include CO₂ capture and storage, renewable in power generation and end-use sectors, end-use fuel and electricity efficiency, end-use fuel switching from fossil fuel, nuclear, and power generation efficiency, will be developed. Energy efficiency improvement will widely implement in the future. The transport sector have large contributions in controlling the emission, it indicates that the fuel efficiency and renewable fuel should be enhanced in the transport sector. Because the greenhouse gases emission by transport sector is very large, only less than the power sector. With booming of the vehicles, the fossil consumption will increase inevitably. The quality of fuel and the vehicle fuel economy will be still hot topics and should be improved by technologies.

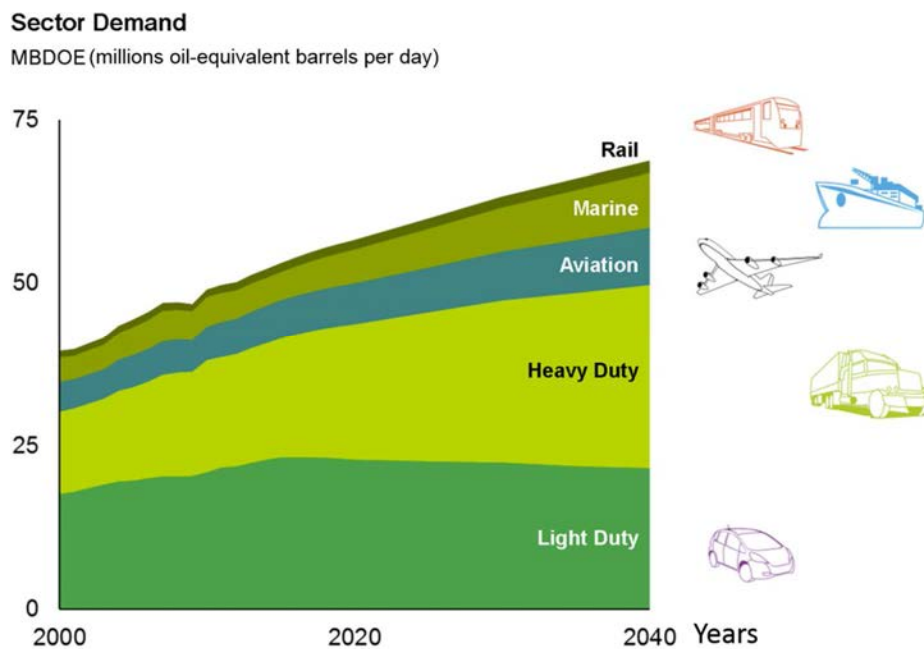


Figure 1.4 Transportation demand.

The energy supply in transportation include rail, marine, aviation, heavy duty, and light duty. The heavy duty and light duty are the main energy consuming sectors now and in the future, as shown in Fig. 1.4. The main energy consumption in transportation is fossil fuel. Now, the researchers are investigating the useful techniques to reduce the consuming the fossil fuel and decrease the emission with great efforts. The diesel and gasoline are widely used in the transportation, and they are still main fuel in normal lives. The diesel is main used in the heavy duty, except in the area of Europe. The gasoline is usually used in the fleet vehicles like passenger cars and motorcycles.

Figure 1.5 shows the energy demand and constitutions of the light duty in the next two decades. The energy consumption increases over time. And the constitutions also changes over time. The Full hybrid is considered as a significant in advancing the energy efficiency and reducing emissions. The achievements of hybrid are perceived even now, it is well known that the car with the hybrid technology needs much less fuel than the traditional car does in running the same mileages. Gasoline and diesel consumptions are supposed to be cut due to the fossil fuel conservation and harmful gases emissions (Myung, 2012). However, in a long period, the gasoline will still be the main fuel of the fleet vehicles.

The investigations like improving the fuel economy, reducing the emissions, and increasing the output should be continued and enhanced. In the researches of engines, many technologies, which are used to improve the engine performance, are investigating recently.

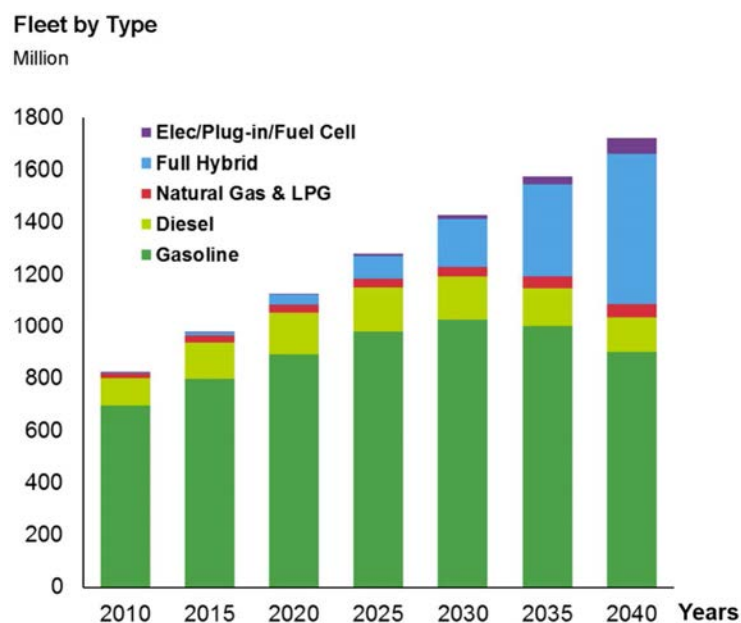


Figure 1.5 Fuel use in light duty vehicles.

1.1.2 DISI engine

The purpose of internal combustion engines is the production of mechanical power from the chemical energy contained in the fuel. The first spark-ignition engine was developed by Otto in 1876, and the first compression-ignition engine was invented by Diesel in 1892 (Heywood, 1998). In internal combustion engines, the energy is released by burning the fuel inside the engine, which is the difference with the external combustion engines. The fuel-air mixture before combustion

and the burned products after combustion are the actual working fluids. The energy are transferred from the working fluid to the mechanical components of the engine (Taylor, 2008).

To overcome the atmospheric engine's shortcoming of low thermal efficiency and excessive weight, Otto proposed an engine cycle with four piston strokes, an intake stroke, a compression stroke, a power stroke, and an exhaust stroke. The thermal efficiency was increased to 14 percent. By 1890, almost 50,000 of these engines were sold in Europe and the United States. Further developments had been taken by several engineers (such as Dugald Clerk, James Robson, and Karl Benz), the two-stroke internal combustion engines was successfully developed. The exhaust and intake processes occur during the end of the power stroke and the beginning of the compression stroke. By 1892, a new form of internal combustion engine was outlined in the patent of the German engineer Rudolf Diesel. The ignition of fuel is heated solely by compression, which would double the efficiency of other internal combustion engines. After five years efforts, a practical engine was developed by Diesel and the resources of M.A.N. in Ausburg combined. The appearing of rotary internal combustion engine has been considered as a major development in internal combustion engine field. The first rotary engine was successfully test in 1957, the engine was based on the designs of the German inventor Felix Wankel, and it took many years to develop the relative researches.

Fuels had impacted on engine development significantly. The earliest fuel used in engines were gas. Gasoline is the lighter fractions of crude oil, and was utilized in the late 1800s. To mix fuel with air in engines, the technologies, which were used to vaporize the gasoline, were developed after the availability of gasoline. After the quality of gasoline was markedly improved in the late 1930, the compression ratios steadily increased, which improved power and efficiency. The air pollutions and improvement in automotive consumption affected the engine design and operation. With the increasing internal combustion engine use, the large fossil fuel was consumed, and the huge harmful gases exhausted into atmosphere. The climate warming became a severe problem, the reducing of engine emission became a compulsory legislation, which was first introduced in California. In that case, the fuel economy and emission reduction became the goal of the researchers and manufacturers.

The mixture formation was implemented with the help of a carburetor in early gasoline engines. The disadvantages of this method were the high engine-out emission and fuel consumption. Thereafter, the multi-port fuel injection (PFI) system was applied in the gasoline engines due to

development of electrical controlling. The PFI engines are still used in passenger car recently. In PFI engine, the fuel is injected into the intake manifold and most of the mixture formation process is already completed when the charge has entered the combustion chamber. There are some disadvantages in PFI engines. The fuel film on the port wall and the intake valves could be formed when the injection pressure is relative low, which could cause the bad effects during cold start. The acute interactions between the spray and the air flow in manifold will lead to an intense turbulence in cylinder. To prevent the in-cylinder knocking, the PFI compression ratio is limited to 10:1. Additionally, although the emissions can be controlled in an acceptable level, it contribute to the work of the three-way exhaust after-treatment system (Alkidas, 2007).

To overcome the limitations of the PFI engines, the two combustion technologies were developed, the direct injection (DI) stratified combustion spark ignition (SCSI) technique (Moon et al., 2005), and the homogenous charge compression ignition (HCCI) technique (Harada et al, 1997; Imberdis et al., 2007). The lower fuel consumption and NO emission can come true in the DI SCSI engine comparing to the PFI engine (Tagaki et al, 1998). Although the HC emissions increase, the NO emissions are greatly reduced by the HCCI technique comparing to the PFI engine (Drack et al, 2003). The disadvantages of the two technologies are their limited/load range, it means the engine should possess the two combustion modes simultaneously.

The operational modes of a DISI engine is shown in Fig. 1.6. In the low load/speed operation, the mixed-mode DISI engine works with a stratified charge and lean mixture (Drake, 2005; Zhao et al, 1999). In the condition of higher load/speed, the engine runs with a homogeneous charge. The homogenous charge operation includes two parts, the medium load regions and higher load regions (Chigire, 1983). In the former, the charge is overall lean (or highly diluted stoichiometric). While, the charge is stoichiometric or even rich in the latter. Exhaust gas recirculation (EGR) is employed to control nitrogen oxides emissions in the high load. The optimal fuel economy determines the level of excess-air and EGR dilution use, and it maintains emission and combustion stability at acceptable regions.

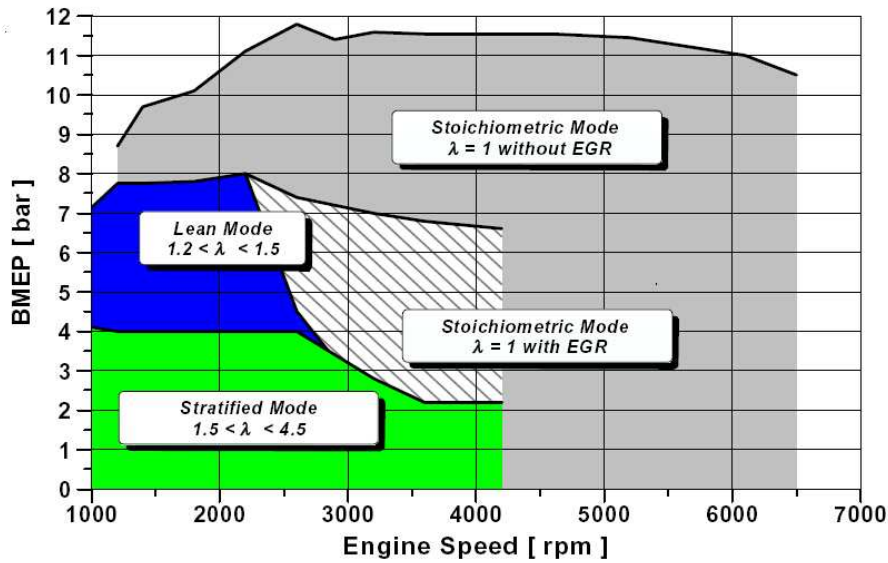


Figure 1.6 Operational modes of a DISI engine.

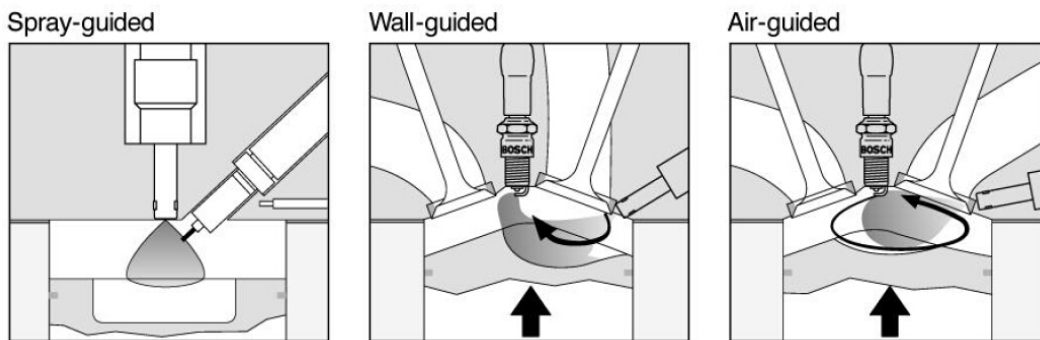


Figure 1.7 Classification of the GDI combustion systems.

There are three broad categories of the combustion system in the direct injection spark ignition engines, air-guided, wall-guided, and spray-guided, as shown in Fig. 1.7. In the spray-guided combustion system, the spark plug is close to the injector (Katashiba et al, 2006; Schwarz et al, 2006; Szekely et al, 2005). In the wall-guided and air-guided system, the spark plug is placed a long distance from the injector. In the wall-guided system, the spray is guided towards the spark plug by the air flow, which is caused by the interaction of spray and the piston combustion cavity. And in the air-guided system the spray is blown by the defined air motion in cylinder (Koch et al, 2002; Schanzlin et al, 2001). The wall-guided combustion system was widely used in the first generation of DISI engine. However, the spray guided combustion system may be employed in the second generation (VanDerWege et al, 2003).

1.1.3 Injector and spray

To meet the spray quality in the DISI engine, many injectors are designed for the various conditions (Fansler, 2005). Four types of gasoline direct injection injectors are widely employed in DISI engines, swirl injector, slit injector, outward-opening injector, and multi-hole injector. Characteristics of the sprays injector by various injectors are quite different.



Figure 1.8 Swirl injector and swirl spray (Kang et al, 2004).

A free cone-shaped spray, in which the droplets own rotational moment, is injected by a swirl injector. The structure of swirl injector and swirl spray are shown in Fig. 1.8. The fuel traverses tangentially arranged swirl ports in the high pressure swirl injector, the fuel gets a rotation motion after injecting (Kobayashi et al, 2008; Gavaises et al, 2002; Lee et al, 2001). The rotational momentum promote the spray atomization and reduces the spray penetration. In that case, the wall impingement can be prevented in some extent. Therefore, this spray is suit for the wall guided DISI engines. The disadvantages of the swirl spray is that the strong swirling or tumbling decreases the volumetric efficiency.

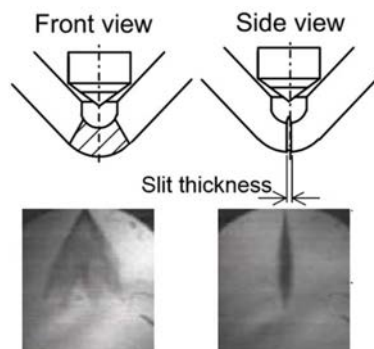


Figure 1.9 Slit injector and slit spray (Tanaka, 2003).

To overcome those disadvantages of the swirl nozzle, the slit injector was developed. The slit injector structure and the spray profiles are shown in Fig. 1.9. The slit injector is able to guide the

spray to the near area of the spark plug without the help of air motion, and the more wide fan-shaped spray structure was obtained as well as the fine atomization was ensured. The characteristics of the spray were enhanced, such as break-up, dispersion, droplet sizes, and penetration (Kawamura et al, 2003; Hayakawa, 2002). However, the ambient pressure affects the structures of swirl spray and slit spray (DeCorso and Kemeny, 1957; Saito et al, 1985).

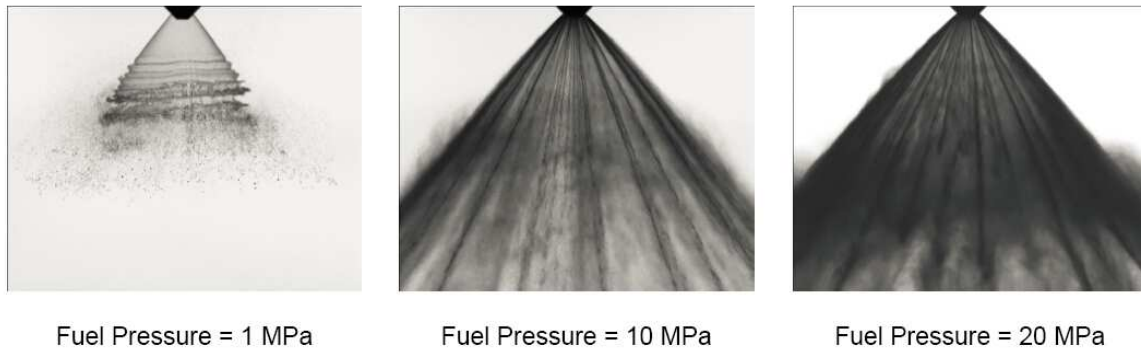


Figure 1.10 Sprays injected by electric outward-opening pintle injector (Befrui et al, 2008).

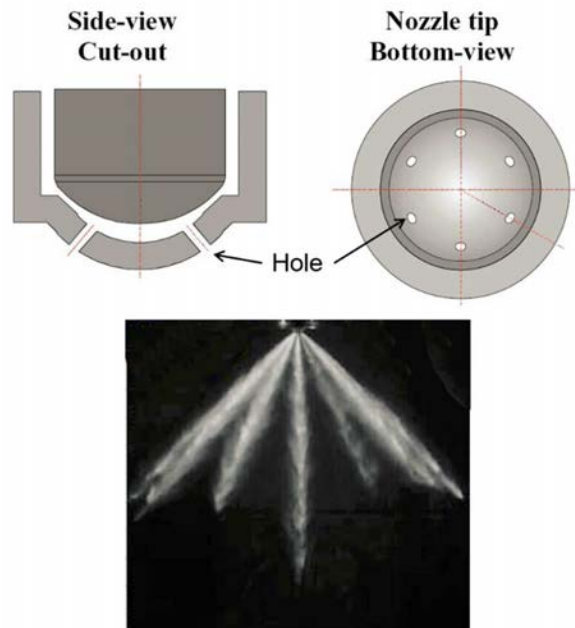


Figure 1.11 Multi-hole injector and spray (Mitroglou, 2007).

Although the slit injectors are widely used in the first generation DISI engines, the disadvantages are limited the engine performance. The electric outward-opening pintle injectors and solenoid-actuated multi-hole injectors were developed by the second generation DISI engines. In the electric outward-opening pintle injector, fuel is introduced form the high pressure rail into the

nozzle gallery, through three or four flow passages guide the spray towards the nozzle exit. There are many advantages in outward-opening pintle injectors, such as the short penetration, uniform droplet concentration, the stable spray angle (Skogsberg et al, 2007; Marchi et al, 2010). The spray injected by electric outward-opening pintle injector is shown in Fig 1.10. A fan shaped spray with a big spray angle can be obtained by the outward-opening pintle injector. The spray owns the good performance of air-fuel mixture. However, the complex structure of this injector and cost limit the application. The multi-hole injectors are predominantly used in the second generation DISI engines.

The spray injected by the multi-hole injector owns good shape, which have a big spray cone angle. The structure of the individual spray is similar to the high pressure diesel nozzle spray. The spray cone angle can keep constant during the pressure fluctuation in cylinder, because of the arrangement of the nozzle holes (Ortmann et al, 2001; Mitroglou et al, 2006). This is beneficial to realize the spray-guided method in DISI engines. The geometric flexibility of multi-hole injector is another reason why the multi-hole injectors are widely used in the second generation DISI engines (Zhang et al, 2013). The desirable spray plumes can be obtained by arranging the nozzle holes, in that case, the designing and manufacturing cost can become much lower than that of the outward opening pintle injector.

1.2 Objective and Approaches

The work was aimed at investigating the characteristics of the spray injected by a hole-nozzle under the cross-flow ambient, and the interactions of the spray and the cross-flow field. This investigation was a fundamental study for clarifying effects of the air flow in cylinder of DISI engine on the spray. For different combustion modes, the experiments were taken under different ambient pressure. The objectives are concentrated as follows:

- (1) The free spray of VCO nozzle was tested under various injection pressure and ambient pressure, the profiles, the velocity distributions, and droplet size distribution are measured in this study.
- (2) The structure of the spray in the cross-flow were analyzed using the whole images and many sectional plane images in the conditions of atmospheric ambient and pressure ambient. Those images were taken by the high speed video camera and illuminations, which included light illuminator and sheet laser.
- (3) The velocity distributions were measure in various sectional plane of field under the conditions of atmospheric ambient and pressure ambient. The velocity distributions included the spray droplet velocity distributions and cross-flow field velocity distributions.
- (4) The droplet sizes of the spray under quiescent ambient and under the cross-flow were measured in various points. The distribution of droplet sizes was assembled by SMDs in those points.
- (5) The interactions between the spray and the cross-flow were discussed, those discussions were based on the variations of the sectional planes and velocity distributions.
- (6) The numerical simulation was implemented to further understand the characteristics of the spray in the cross-flow field.

An atmospheric wind tunnel and a pressure ambient wind tunnel were used to obtain the spray surroundings, which simulated the surroundings of the cylinder under homogenous charge combustion mode and stratified charge combustion mode. The high speed video photography with Mie scattering method was employed to capture the structures and variations of the sprays in this study. The PIV system was utilized to measure the velocity distributions of the planes in the cross-flow field. The droplet sizes were measured by a laser diffraction size analyzer (LDSA) in various point.

1.3 Outlines

The outlines of this dissertation are shown as following.

Firstly, the background of this study was systematically represented from the energy and environment to the detailed DISI engine, a review of the previous studies of the spray, cross-flow, optical diagnostics of spray was expounded in Chapter 1.

Secondly, the experimental setups of this study were introduced in Chapters 2 and 3. The experiments included high speed video photography, PIV measurements, and Droplet size measurements. The structures of the atmospheric wind tunnel and high pressure wind tunnel were specified. The principle, theoretical calculations, designs, strength check, and evaluation of the high pressure wind tunnel were illuminated at detail.

Thirdly, the global structure of the spray under the cross-flow, the cross-sectional structure of spray, spray droplets flow field, and droplet/droplet size distribution under atmospheric condition were discussed in the Chapter 4~7. The profiles of the spray with/without the cross-flow under atmospheric ambient and high pressure ambient were presented, and the penetrations were discussed experimentally and theoretically in the Chapter 4. The cross-sectional structure of spray, and the vortex phenomenon in the cross-flow were discussed in Chapter 5. In Chapter 6, the velocity distributions and vorticity distribution in the cross-sectional planes were analyzed by PIV technique. The droplet size distribution of the spray were presented, and the reasons for the distributions were explained in Chapter 7. The characteristics of the spray in the cross-flow field under various pressure ambient were discussed in Chapter 8. The numerical simulations of the spray and the cross-flow were implemented in Chapter 9.

Finally, characteristics of the spray in the cross-flow and the interactions between the spray and the cross-flow were summarized in Chapter 10. The future prospect was attached in the end of this dissertation.

1.4 Literature Review

1.4.1 Spray mixture formation and DISI engine

1.4.1.1 Spray mixture formation

The fuel is ejected from the nozzle by the injection pressure, a fuel jet is formed at the very beginning. The fuel jet immediately breaks up and becomes to a conical spray. The primary break-up, which first happens near the nozzle, results in large ligaments and droplets that form the dense spray. When the injection pressure is high, cavitation and turbulence generated inside the injection holes can enhance the break-up. The subsequent break-up processes of the droplets, which are obtained by the primary break-up, are called secondary break-up. The smaller droplets can be got by the aerodynamic force, which is caused by the relative velocity between droplets and ambient gas. The droplets are decelerated by the resistance of the ambient gas. The strong drag force effect on the spray tip droplets, which results in the droplets lose their momentum more quickly than the droplets near the nozzle. The droplets are continuously replaced by new droplets at the spray tip with the increasing of the penetration. The droplets which are pushed aside by the air motion develop the cone shape of the spray (see Fig. 1.12).

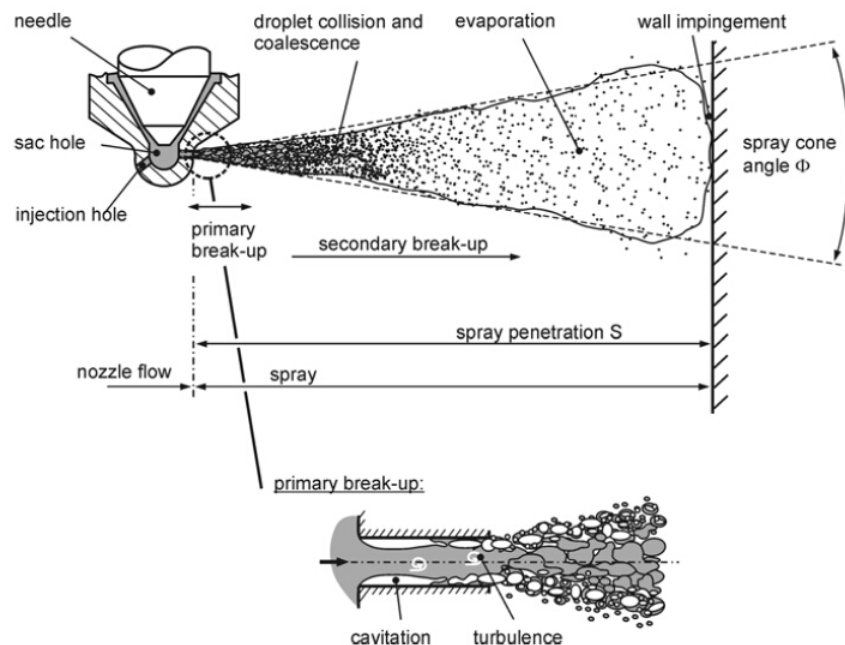


Figure 1.12 Spray break-up process from hole-injector.

The dense droplets are concentrated near the nozzle, and droplets are diluted downstream the nozzle by the entrainment air. Although some droplets and vapor exits in the outer spray regions,

the most of the dense droplets are concentrated near the axis of spray. This droplet distributions are caused by the interaction between the spray and entrained gas. In the dense droplet area, the collisions may happen. And this is the reason why the droplet size and velocity in that area are instable. The coalescence is induced by the collisions, and the broken up small droplets can combine into large droplets by the coalescence.

The boundary conditions, which include gas temperature, gas density, and gas flow in the in-cylinder, are influence the dilute spray downstream of the nozzle. The droplets are sensitive to those conditions in further spray disintegration and evaporation. The maximum penetration of the spray is the distance from the nozzle to the piston bowl. The impingement may occur on the wall, when the injection pressure is high, the injection duration is long, or the cylinder gas density is low. The liquid wall film forms after impingement. Because the wall film is hard to evaporate, and the mixture of air and fuel becomes bad, therefore the partially burning may happen. The final result is that the fuel economy decreases and the emissions increase.

Many fundamental experiments and semi-empirical relation about the behavior of the relevant spray parameters of sprays have been performed and published by many different researchers. The parameters of the spray were concentrated on spray cone angle, spray penetration, break-up length, and average droplet diameter with different boundary conditions. Because it is difficult to investigate the spray behaviors in the real engine, these experiments have usually been taken with quasi-stationary sprays, the main injection phase of full cone sprays can be referred by the results. In the following. The most detailed semi-empirical relations were investigated by Hiroyasu and Arai (1990).

There are two phases in the penetration development of the spray over time. The first phases refers to the procedure form the beginning of injection ($t = 0$ ms ASOI, needle begins to open) to the moment when the liquid jet begins to disintegrate ($t = t_{break}$, Eq. 1.1), in which S linearly grows with time (Eq. 1.2). During the second stage ($t > t_{break}$), the spray tip consists of droplets, and the penetration S becomes a function of $t^{\frac{1}{2}}$, as shown in Eq. 1.3. The penetration should be continuous during the whole procedure, hence the coefficients in Eqs. 1.1~1.3 can be obtained because Eq. 1.2 is equivalent to Eq. 1.3 at the moment of breakup.

$$t_{break} = \frac{28.65 \rho_l d}{(\rho_g \Delta p)^{\frac{1}{2}}} \quad (1.1)$$

$$t < t_{break}: \quad S = 0.39 \left(\frac{2\Delta p}{\rho_l} \right)^{\frac{1}{2}} t \quad (1.2)$$

$$t > t_{break}: \quad S = 2.95 \left(\frac{\Delta p}{\rho_g} \right)^{\frac{1}{4}} d^{\frac{1}{2}} t^{\frac{1}{2}}, \quad (1.3)$$

where, S is the vertical penetration, $\Delta P = P_{inj} - P_a$ is the pressure drop across the nozzle, ρ_g and ρ_l are the gas and liquid densities, d is the nozzle diameter and t is the time ASOI. The penetration increases with increasing injection pressure, while it will be reduced when the gas density increases. The fuel jet momentum is enhanced when the nozzle diameter increases, and the penetration enlarge due to the increased momentum. When the ambient temperatures exceeds 590K, the effect of the gas temperature on spray penetration is hardly observed. Based on this, the further empirical equations are deduced by Dent (1971) and Fujimoto et al. (1981). The effect of gas temperature T_g on the spray penetrations was added in the empirical equation, as shown in Eq. 1.4. That is important for the practical engine when the combustion temperature is high.

$$S = 3.07 \left(\frac{\Delta p}{\rho_g} \right)^{0.25} \cdot (t \cdot d)^{0.5} \cdot \left(\frac{294}{T_g} \right)^{0.25}. \quad (1.4)$$

The spray cone angle is also an important parameter of a spray. Many researches experimental and empirically illuminated the relations with the conditions. For sac hole nozzles, the authors give the following relation for the stationary spray cone angle (Hiroyasu and Arai, 1990):

$$\Phi = 83.5 \left(\frac{L}{d} \right)^{-0.22} \left(\frac{d}{d_s} \right)^{-0.22} \left(\frac{\rho_g}{\rho_l} \right)^{-0.22}. \quad (1.5)$$

where, Φ is the spray cone angle, d_s is the sac hole diameter, and L is the length of the nozzle hole. If the L/d ratios is small, the cavitation structure keep in the injection hole, and can enter the combustion chamber with fuel. The collapsing happens outside the nozzle, which enlarges the spray cone angle. A small value of d/d_s promotes the increasing of effective cross-sectional area at the entrance of the nozzle hole, enhances the static pressure at this point and restrains the inception of cavitation. The density ratio ρ_g/ρ_l plays an important role on the spray cone angle comparing with other parameters. The spray cone angle decreases when the ambient gas density increases. It

indicates that the spray diffusions are restrained by the increased ambient gas density. Another relation of the spray cone angle was given by Heywood (1988),

$$\tan\left(\frac{\Phi}{2}\right) = \frac{4\pi}{A} \left(\frac{\rho_g}{\rho_l}\right)^{0.5} f(Y) \quad (1.6)$$

where, A is a constant, which depends on the nozzle design and it may be obtained from experiments or approximately calculated as $A = 3.0 + 0.28(L/d)$. The $f(Y)$ is a weak function about the physical properties of the liquid and the injection velocity (Dan et al, 1997), as shown in Eq. 1.7. If the injection pressure is very high, the Y increases, then the $f(Y)$ tends to $\sqrt{3}/6$ (Reitz and Bracco, 1986).

$$f(Y) = \frac{\sqrt{3}}{6} (1 - \exp(-10Y)), Y = \left(\frac{Re_l}{We_l}\right)^2 \frac{\rho_l}{\rho_g} \quad (1.7)$$

The Sauter mean diameter (SMD) is usually used in quantity characterizing the average droplet in a spray, it can describe the extent of the spray break-up. The SMD is the diameter of a model droplet, the diameter is defined as the volume-to-surface-area ratio, which is equal to the ratio of the sum of all droplet volumes (V_{drop}) in the spray to the sum of all droplet surface areas (A_{drop}):

$$\left(\frac{V_{drop}}{A_{drop}}\right)_m = \frac{\left(\frac{\pi}{6}\right)SMD^3}{\pi SMD^2} = \frac{SMD}{6}, \quad (1.8)$$

$$\left(\frac{V_{drop}}{A_{drop}}\right)_{spray} = \left(\sum_{i=1}^n d_i^3\right) / \left(6 \sum_{i=1}^n d_i^2\right). \quad (1.9)$$

$$SMD = \frac{\sum_{i=1}^n d_i^3}{\sum_{i=1}^n d_i^2}. \quad (1.10)$$

When the SMD is small, it means the surface per unit volume is large. The enlarged surface provides more effective evaporation and mixture formation. It is well-known that the SMD is quantity in characterizing the spray formation process, however it can be used to describe the droplet size distribution of the spray. It is possible that two sprays with same SMD value can own quite different droplet size distributions. The empirical relation of the SMD based on experimental result was given by Hiroyasu et al (1989, 1990):

$$\frac{SMD}{d} = 0.38 Re^{0.25} We_l^{-0.32} \left(\frac{\mu_l}{\mu_g}\right)^{0.37} \left(\frac{\rho_l}{\rho_g}\right)^{-0.47}, \quad (1.11)$$

where, μ is the dynamic viscosity. The Sauter mean diameter (SMD) increases with the gas density increasing, because the coalescence of droplets intensifies with increased initial droplet diameter, which is caused by the enlarged nozzle hole diameter. The higher injection pressure enhances the atomization, and thus decreases the value of SMD. It is important to remember that the measurement of droplet sizes should be taken place in the lean spray area or at the long distance from the nozzle. The results of a complete spray always include a high uncertainty, however, it is meaningful to estimate the spray in a qualitative way.

To understand the detail of the spray break-up process, the fuel is an intact liquid core or large ligaments and droplets should be made sure. Because this two kinds breaking ways are different. The fuel may form an intact liquid core than divide into the separation of droplets downstream the nozzle, or the fuel already forms large ligaments after leaving the nozzle. Some researchers investigated this using electrical conductivity measurements (Hiroyasu et al, 1991; Chehroudi et al, 1985), which was used to explore the inner structure of the spray. The electrical resistance between the nozzle and a fine wire detector, which located in the spray jet, was measured. The core lengths results measured by different researchers presented different value, but it is agreed by most researchers that the core length is dependent on the ratio of liquid and gas density, and that is proportional to the nozzle diameter d , as the Eq. 1.12 shows.

$$L_c = C \cdot d \cdot \sqrt{\frac{\rho_l}{\rho_g}} \quad (1.12)$$

where, C is a the empirical constant, which are obtained experimentally, and it usually in the range of 3.3~11. The radial extent of the core region increases along the spray axis from the nozzle, and in the core region the construction is not pure liquid (Youle and Saltes, 1994). It is considered by the researchers this region consists of a very dense cluster of ligaments and droplets. With the laser optical technology use in the experiments (He and Ruiz, 1994; Gülder et al., 1992), the inner spray structure have been observed, the results showed the break-up zone includes high liquid content areas, which are separated from each other. By the help of the real size transparent nozzle introducing, the whole process have been cleared. In the high pressure injector, the spray begins already inside the nozzle holes, because the turbulence and cavitation disintegrate the spray before leaving the nozzle (Soteriou et al, 2001). Another more detailed relation is presented by Hiroyasu and Arai (1990),

$$L_b = 7 \cdot d \left(1 + 0.4 \frac{r}{d}\right) \cdot \left(\frac{p_g}{\rho_l u^2}\right)^{0.05} \cdot \left(\frac{L}{d}\right)^{0.13} \left(\frac{\rho_l}{\rho_g}\right)^{0.5} \quad (1.12)$$

where, u is the initial velocity of spray, and r is the radius of the inlet edge of the hole. The effect of the inlet edge rounding is added to the relation in Eq. 1.12. The L_b increases with a rounded inlet edge, which weakens the cavitation in the nozzle hole. $p_g/\rho_l u^2$ is the expression of the influence of cavitation and turbulence.

Primary break-up is the first disintegration of the coherent liquid into ligaments and large droplets. The break-up mechanisms are summarized in Fig. 1.13. The aerodynamic shear forces at the interface of gas and liquid are formed by the high relative velocities, this shear forces result in the disintegration of droplets. The strong turbulence which is form inside the nozzle and entrained in the liquid increases the primary break-up. The instable growth of waves influences the break-up only in the edge of the spray, the main reasons, which are proven, are the effects of turbulence and cavitation formed in the nozzle hole.

The turbulence induced disintegration is considered as one of possible break-up mechanism in the primary break-up. When the strong radial turbulence happens inside the nozzle, the turbulent eddies can form in the liquid, the thus the liquid can be collapsed by the strong eddies Wu et al. (1995). Turbulence induced primary break-up is regarded as one of the most important break-up mechanisms of high-pressure sprays.

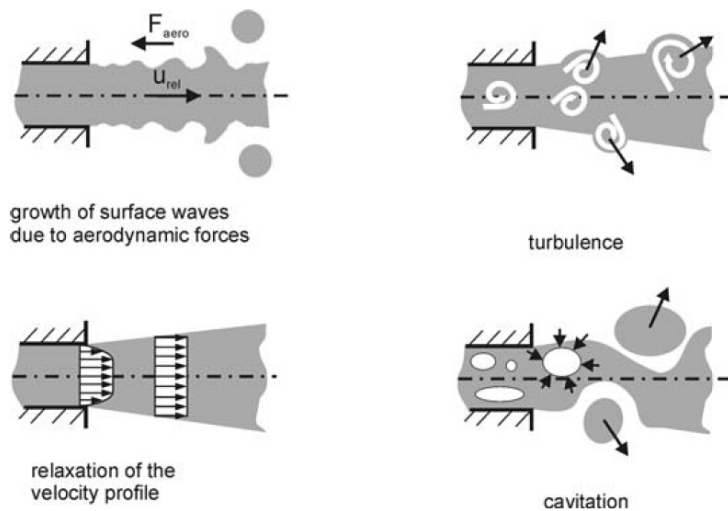


Figure 1.13 Mechanisms of primary break-up.

The relaxation of the velocity profile is considered as a potential primary break-up mechanism. Assuming L/d ratios are large and the liquid with cavitation in the nozzle hole, the velocity profile

may change at the moment the liquid leaving the nozzle. Because the wall boundary condition disappears, an acceleration of the liquid edge region accelerated by the viscous forces, and the velocity profile turns into a uniform profile, as shown in Fig 1.13. This process may lead to the break-up in the outer edge region. However, the assumption in the case of high-pressure injection is almost invalid, because the cavitation occurs, and L/d ratios are small.

The cavitation-induced disintegration is another important mechanism for primary break-up. In the high pressure nozzle, the cavitation structures form inside the nozzle holes. The strong acceleration of the liquid by the difference of the injection pressure and ambient pressure is one of the factors of the cavitation formation. The other factor is the strong curvature of the streamlines at the inlet edge. Therefore, the liquid and gaseous phase exist inside the nozzle holes simultaneously. The pressure difference (between injection pressure and ambient pressure) and the nozzle geometry decide the intensity and structure of the cavitation zones. The pressure difference between the bubbles and ambient pressure makes the cavitation bubbles imploding. It is very difficult to clarify the main reason, which caused the primary break-up, between the turbulence affect and the cavitation bubble collapses. Sometimes, the turbulence can transfer to cavitation (Arai et al., 2002; Hiroyasu et al., 1991; Soteriou et al., 1995; Tamaki et al., 2000). Hence, the two main primary break-up mechanisms are turbulence induced disintegration and cavitation induced disintegration, and the two mechanisms exist simultaneously in the high pressure spray.

The secondary break-up is mainly caused by aerodynamic forces, which consist of friction and pressure. The aerodynamic forces forms by the relative velocity between droplet and ambient gas. An instable growth waves are induced by the aerodynamic forces, this waves distribute on the interface of gas-liquid or the whole spray. Therefore, the droplets disintegrate by the strong waves. And this disintegration happens again and again, which results in the droplets break into smaller droplets. There are many break-up mechanisms for this disintegration, vibrational break-up, bag break-up, bag/streamer break-up, stripping break-up, and catastrophic break-up. Usually, all the break-up mechanisms can happen in the pressure spray.

1.4.1.2 DISI engine

The direct injection spark ignition (DISI) engine owns excellent performances comparing with the port fuel injection engine, such as the fuel consumption improvement and the CO₂ emission reduction. Since the first gasoline direct injection (GDI) engine was produced by Mitsubishi in

1995, the DISI engine entered a rapid development period. Fulfilling the future demands regarding CO₂ emission is dependent on the reducing the consumption of the fuel, which is the main reason why the DISI engine is developed so quickly. The fuel efficiency is significantly enhanced comparing with the diesel engine. The shortcoming of DISI engine is high soot and NO_x-emissions, but it can be resolved by three-way catalyst system for exhaust gas after treatment. In theory, the DISI engine can reduce 15-25% fuel consumption comparing to the similar PFI engine (Heil et al, 2001; Spicher et al, 1999; Zhao et al, 1997). There are many advantages of DISI engine on operation comparing to the PFI engine. Firstly, the average temperature of the in-cylinder charge is decreased by the evaporation of fuel. When the injection happens during the intake stroke, the volumetric efficiency will increase to 10% (Eichlseder et al, 2000). It is well-know the low temperature of the in-cylinder charge is benefit for preventing the knock, and the compression ratio also can be increased (Heil et al, 2001). The high compression ratio decides the thermal efficiency. The emission of unburned hydrocarbons during cold start is a serious problem in PFI engine, however, this problem is improved obviously by reducing the film formation and the precise control of the air-fuel mixtures (Zhao et al, 1997). Under the full load, the reduction of fuel consumption in DISI engine is slightly exceeded over PFI engine in the same condition. The adjustability fuel quantity of injection is the main advantage of the DISI engine, because the reduction of load is fulfilled by reducing the injected fuel mass, not throttling the air flow.

The most important difference between the diesel engine and the DISI gasoline engine is that the diesel fuel is ignited automatically by compression while the gasoline fuel is ignited by a spark. The fuel air mixture should be guided to the ignitable area at the time of ignition. In the DISI engine, the different operating modes are chosen coinciding the load and engine speed. A homogeneous stoichiometric mixture is necessary in the full load condition. Early injection during the intake stroke provides enough time to achieve the fuel quantity and the homogeneous fuel-air mixture, as shown in Fig. 1.14. The stratified-charge mode is applied to reduce pumping losses at medium and low part load. The fuel injected into combustion chamber during the compression stroke in the case of stratified operation. Three guided combustion concepts can be used in DISI engine for controlling the stratified-charge combustion, the spray guided, wall guided, and air guided approaches, which have been mentioned in section 1.4.11.

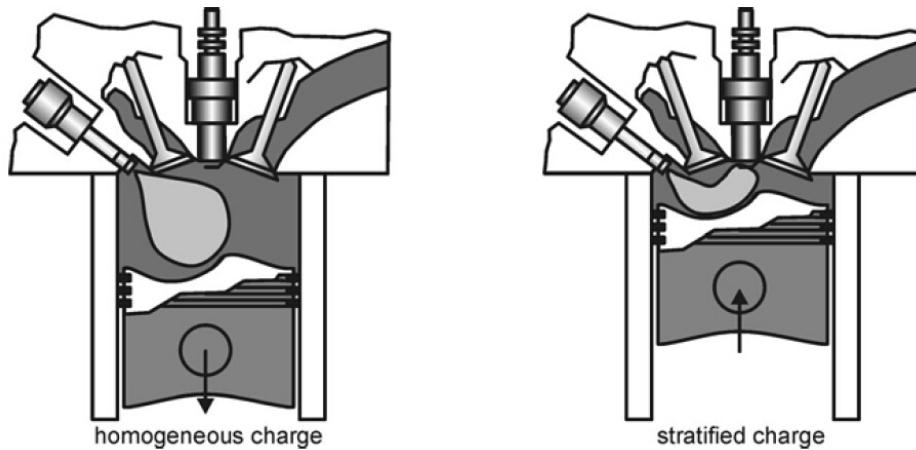


Figure 1.14 Homogeneous (early injection) and stratified-charge (later injection) mode.

1.4.2 Spray diagnosing methods

Spray usually occurs from a nozzle at a very short period of milliseconds, the droplets of the spray move rapidly, and the fuels are transparent in general, hence, the direct observation and analysis of spray are very difficult or impossible. To observe the profiles and evolution of spray, the high speed video photography is widely used in the experiments. Some velocity measuring methods, such as laser Doppler anemometry (LDA) and particle image velocimetry (PIV), are applied to detect the droplet velocities in spray. The droplet sizing are taken based on laser technology, such as laser diffraction method and phase Doppler analyzer.

The macroscopic spray evolution are detected by the optical techniques in spray diagnosing. Mie scattering, Schlieren and Shadowgraph techniques are employed to analyse the liquid/vapor phase development of spray (Padala et al, 2014; Settles, 2006). The scattering, which comes from molecules or very tiny particles (the diameter smaller than the wavelength of light or approximately equals the 1/10 wavelength), is predominantly Rayleigh scattering. When the particle (or droplet) size equals or bigger than the wavelength of light, the scattering changes to Mie scattering. In the spray visualization experiments without evaporating, the scattering is predominantly Mie scattering. Because the light wavelength is much smaller than the droplet size. Shadowgraph (schlieren) is an optical method that reveals non-uniformities in transparent media like air, water. It is a type of flow visualization, which is widely used to detect the boundary between vaporized fuel and background ambient gas, because of a different refractive index at the interface between the ambient gas and fuel and the dramatic density gradient forming as the

evaporating fuel cools down the ambient gas in evaporating fuel spray experiments (Naber and Siebers, 1996). The details have been discussed in section 2.1.1.

The velocity measurement in the single point of the cylinder can be taken by hot-wire anemometry or laser Doppler anemometry/velocimetry (LDA/LDV), which are used to measure the flow velocity and turbulence with high spatial resolution (Auriemma et al, 1996). The LDV was applied to analyze the air entrainment in a transient non-evaporating diesel spray by Cossali et al (1991). The hot-wire anemometry can be used to measure the pressure fluctuations in cylinder of manifold (Perssons et al, 2006).

To quantify the velocities in the complex unsteady in-cylinder flows, particle tracking velocimetry (PTV) and particle image velocimetry (PIV) have been developed (Zhao and Ladommatos, 2001). Two dimensional maps of velocity of the testing plane in cylinder can be acquired. In PTV and PIV measurements, small particles, which can be illuminate and recorded by camera, are fed into the flow field. TV has been used for the characterization of induction-like flows in water analog engine (Khalighi and Huebler, 1988). A variation on PTV is streak photography, which can record the movement of the particle during the exposure period. PIV provides a means of achieving high spatial resolution two-dimensional velocity measurement.

The principle of the PIV technique is that the velocity vector is calculated from the displacement of an element of fluid in a known time interval. The PIV technique requires a thin slice of the flow field to be illuminated by a laser light sheet in the simplest form. Particles in the flow within the light sheet scatter the light. The scattered light is detected by a camera which is placed at a right angle to the light sheet (Fig. 2.3). The laser light sheet is double-pulsed (switched on and off very quickly twice) at a known time interval, Δt . The first frozen images of the initial positions of particles by the first pulse of the laser is taken by the camera. The second frame of the camera is exposed to the light scattered by the particles from the second laser pulse. Two images are obtained, the first showing the initial position of the particles and the second their final positions due to the movement of the flow field. Alternatively, the double exposed particle images can be recorded on the same photographic film.

It is important to know the droplet size distributions in the spray, because the fuel atomization and vaporization processes are effected by the droplet size distribution. Two of typical optical techniques for droplet sizing are usually utilized in the measurements, the direct imaging techniques and light-scattering techniques. In the former, the simplest optical droplet sizing

technique is the direct imaging of fuel droplets by photography. The structure of the fuel spray and droplet size distribution can be provided from those images. From the recorded images, the droplet size distribution is determined by counting and sizing the diameter of the droplets. The light source for the direct imaging can be a pulsed laser or modulated continuous wave laser. The high-resolution images are needed in the photography, because the camera should have the ability of capturing the image of minimum droplets. The holographic recordings extend the photographic techniques into three-dimensional measurements. Holograms provide three-dimensional pictures of an object, which can be examined in much the same way as a photograph (Trolinger, 1991).

Integral methods and particle counting are the two approaches to light scattering measurements. The integral methods, which performed by the Fraunhofer diffraction, measure a number of droplets simultaneously. The intensity and a spatial average can be obtained from integration over space. This technique is moderate in the condition of high droplet concentrations. On the other hand, the particle counting techniques, such as a laser phase Doppler analyzer (PDA), the droplets are measured at a time. The moderate concentrations and a small sample volume are needed during the experiments. The higher the concentration, the smaller the volume needs to be. The PDA measures the size distribution over time, and a temporal average can be gained.

It is know that both liquid droplets and fuel vapor may be present at the same time in a fuel spray, simultaneously clarifying their characteristics is important. It can be realized by laser induced exciplex fluorescence (LIEF) method. Though elastic (Mie) scattering or fluorescence signal can be captured simultaneously from both the liquid and vaporized fuel, the signal from the liquid phase is many orders of magnitude stronger than that from the fuel vapor, which limits the elastic scattering or LIF techniques to the detection of liquid only. Laser Extinction/Absorption (LEA) is the other technique, which can detect simultaneously of fuel vapor and liquid droplets.

1.4.3 Air-flow in cylinder of DISI engine

The air-flow within the cylinders of internal combustion engines affects the spray structures and air-fuel mixture profoundly (Reeves, 1995). In DISI engine, in order to reduce emission and fuel consumption, the air flow is used as an important method to ensure the mixture in different modes. The air flow is controlled by the design of the inlet ports, the cylinder head, and piston crown geometry primarily. With the optimizing the combustion and emissions, the large-scale fluid motion and small-scale turbulent flow are introduced in cylinder. With the help of computational

fluid dynamics (CFD), the three dimensional air flow field of cylinder is investigated, which is very useful to clarify the details of the air motions. The CFD with validating of in-cylinder flow field measurements can describe the flow field clearly.

The turbulent nature of in-cylinder flow was observed by the introduction of smoke in a low speed optical engine in the early stage (Clerk, 1921). Then, tracers like feathers was used in the intake air system to record the motion, and the air flow was investigated by analyzing the motions (Lee, 1939). The hollow mircoballoons, which are light enough to follow the flow, were fed into cylinder to observe the movements of flow (Marko et al, 1986). With the development of the particle tracking technology in velocity measuring, the particle tracking velocimetry (PTV) was employed to detect the velocities in engine cylinder after the unremitting efforts of many researchers (Khalighi and Huebler, 1988; Shack and Reynolds, 1991; Church and Farrell, 1998). For the more accurate measurement, the advent of PIV provides a way to get the high spatial resolution two-dimensional velocity measurements. The thin laser sheets with high energy are used in the PIV measurement, and the vectors can be obtained after processing. The principle of PIV have been discussed in section 2.1.2.

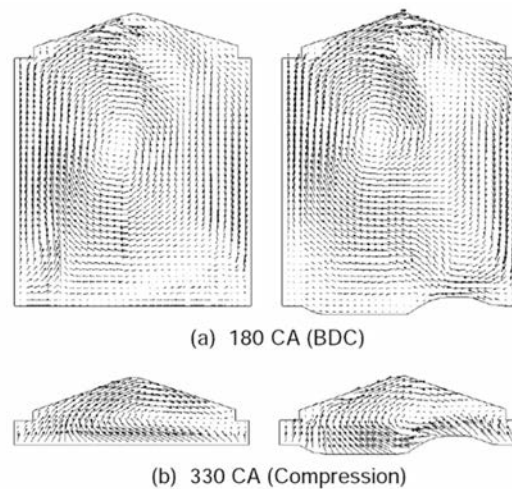


Figure 1.15 Computed velocity fields in combustion chamber (flat piston and bowled piston).

The directly observing of the air flow in the combustion chamber of DISI engine is difficult, because it needs complex optical devices and the chamber structure is limited to arrange the devices. The CFD can simulate the process in the same structure model with the real combustion chamber. The velocity distributions are shown in Fig. 1.15, a comparison of flow structures between the flat piston and the bowled piston is shown, the in-cylinder air motions are strong in both flow piston and bowled piston conditions (Kim et al, 1999). The air motion should influence

the spray structure and air-fuel mixture, hence the investigation about the effects and interactions are important for improving the performance of engine.

Figure 1.16 shows the velocity distributions in various time, which was used to analyze the rare misfire and partial burn cycles in a spray-guided spark ignited direct injection optical engine using PIV and planar laser induced fluorescence (PLIF) technology (Peterson et al, 2011; Peterson and Sick, 2009). The air flows in the combustion chamber are complex in both combustion modes (homogeneous charge and stratified charge), and they affect the spray structure and air-fuel mixture very much.

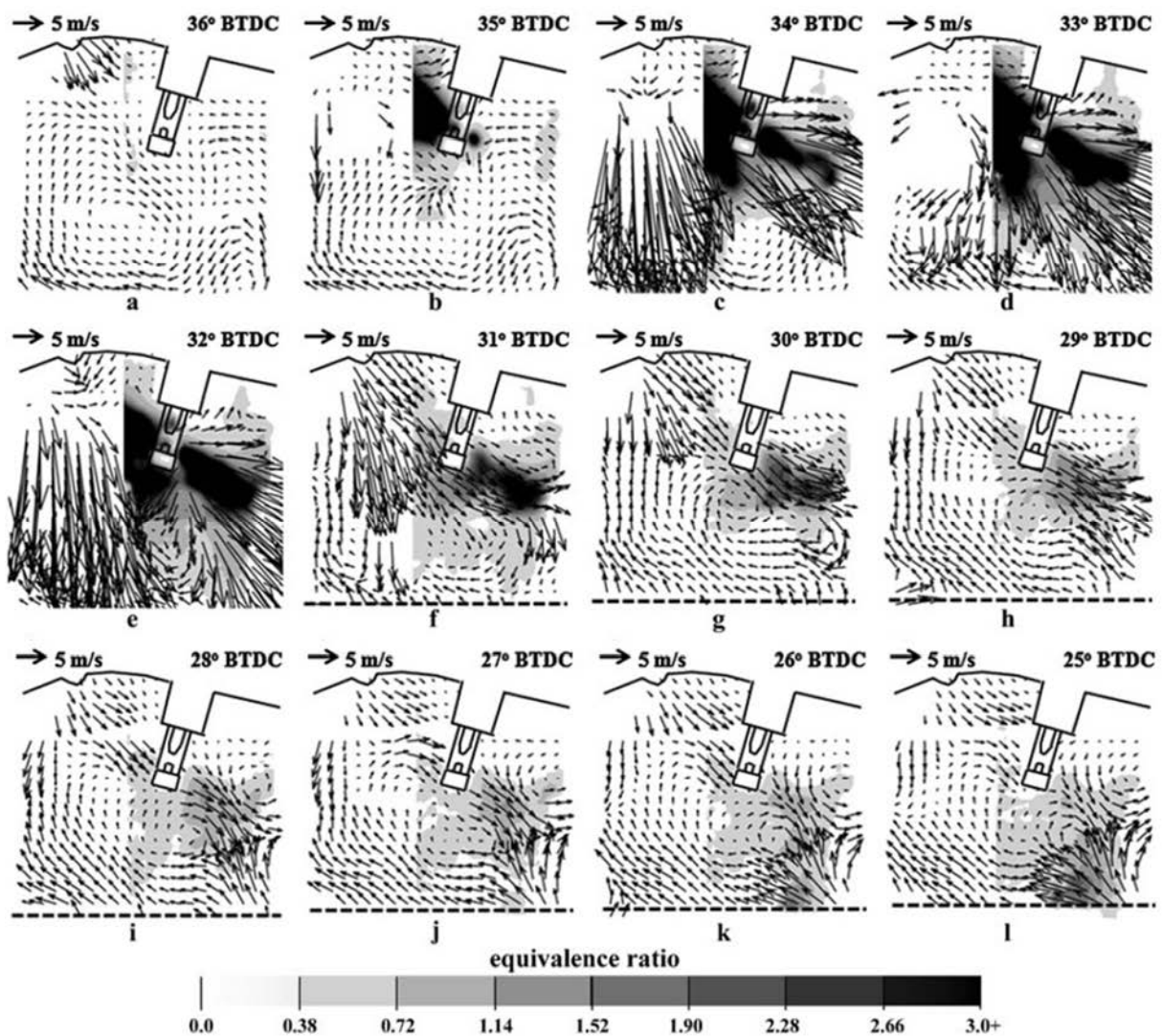


Figure 1.16 Velocity measurement in of air-fuel mixing inside a DISI engine.

Although the air motion and spray characteristics in combustion chamber have been investigated by many researches, it is hard to directly analyze the mechanism clearly. Because the conditions, such as pressure, velocity of flow, temperature in the combustion chamber, always changes. Some characteristics, from which the mechanism can be judged, are hidden by the overlap of different phenomena. In that case, to further understand the processing, some fundamental investigations should be taken in the single conditions.

1.4.4 Spray/jet in cross-flow

The injection of liquid jet/spray into the flow stream are investigated profoundly in modern propulsion and power applications, such as gas turbine, ramjet, and scramjet engine (Im et al, 2011). The liquid atomization, spray penetration, and the mixing process decide the combustion performance in practical applications. The effects of cross-flow on spray in DISI engine are attended recently (Moon et al, 2007; Nouri and Whitehelaw, 2007). In agricultural field, the interactions between the crossflow and spray are investigated in chemicals spray (Ghosh and Hunt, 1998).

A liquid jet injected into a cross-flow of air experience a series of processes, which include break-up and vaporizing (Sedarsky et al, 2010). The primary break-up is that the liquid initially breaks in to drops, and the secondary break-up is that the drops break into the smaller droplets. Thereafter, the smaller droplets evaporate into a cloud of vapor. The researchers were focus on the jet, which doesn't experience cavitation within the liquid. In other words, the atomization of jet is mainly contributed to the cross-flow. The jet keep a vertical, cylindrical column of liquid without cross-flow. The cross-flow bend the liquid column by the difference of the pressure between leeward and windward. A low pressure wake forms in the leeside. The entrained air with momentum can cause the break-up of the liquid or drops. The penetration height is a curve of spray profile in the windward, it is considered as an important parameter. The penetration height of the liquid jet into the gas have a greatly relation with q , the ratio of jet momentum flux to gas momentum flux,

$$q = \rho_l U_l^2 / \rho_g U_x^2, \quad (1.13)$$

where, ρ_l is the density of fuel, U_l is the initial velocity of jet, ρ_g is the ambient gas density, and U_x is the cross-flow velocity. From Eq. 1.13, the long penetration height will be obtain when the

jet owns more relative momentum than the air flow, while the short penetration height appear or bended more seriously, when the jet owns low relative momentum.

The primary breakup of jets in cross-flow through mixed mode breakup, which includes many processes. The waves are formed by the interaction of the gas flow and the liquid column, the wave length is larger than the liquid column, and the waves grows in the leeward of jet. Then the jet column breaks into large drop by a wave pinch-off (Reitz and Rutland 1995), which is called column breakup. The drops are disintegrated in a bag breakup way.

It is known that when the surface forces exceed the surface tension, the disintegration happens. The bag structures form downstream of the column, and disintegrate by the longitudinal wave. When the cross-flow velocity increases, the bag structures become smaller, the smaller droplets can be obtained. As the cross flow velocity increases further, the more membranes form and they disintegrate until the membranes themselves cannot be sustained. The liquid falls off from the column surface and entrain into the longitudinal. The longitudinal waves are observed as the surface stripping in the leeward. This bag breakup and surface stripping are caused by the shear breakup.

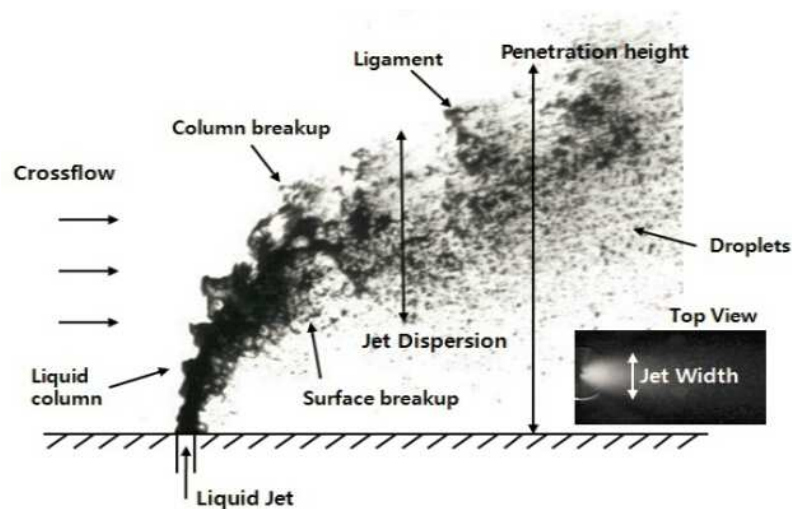


Figure 1.17 Typical parameters of liquid jet in cross flow.

The spray penetration is one of important parameters in the investigation of macroscopic spray characteristics. Therefore, effects of the cross-flow on the spray of diesel are investigated by many researchers (No, 2007; 2008). To understand the mechanism of the interaction of cross-flow and spray/jet, several parameters such as column and surface breakup, penetration height, jet width, droplet size, droplet velocity for the liquid jet in crossflow are measured, as shown in Fig. 1.17.

The analysis of trajectory and breakup processes is considered as important method, which is widely used in the ramjet and scram jet combustors (Lefebvre, 1989). There are many correlations for penetration height of jet in cross-flow.

Table 1.1 Basic power-law form: $y/d = Aq^B(x/d)^C$

Investigators	A	B	C	Remarks
Wotel et al.(1991)	1.19	0.45	0.45	$x/d < 10$
Wu et al.(1997a)	1.37	0.5	0.5	
Wu et al.(1997b)	4.30	0.33	0.33	$x/d > 10$
Lin et al.(2002)	3.17	0.33	0.40	
Ahn et al.(2006)	1.297	0.491	0.509	
Masuda and McDonel (2006)	0.92	0.50	0.33	$2 < q < 30$
Iyogun et al.(2006)	1.997	0.444	0.444	

Some detailed investigations of the correlations about the jet trajectory and penetration height in various conditions have been represented by Wotel et al. (1991), Wu et al. (1997a; 1007b), Lin et al. (2002), Ahn et al. (2006), Masuda and McDonell (2006), Iyogun et al.,(2006), as shown in Table 1.1. Some of them had mixed up the theoretical model or numerical model in the empirical correlations, however, it is difficult to cover all the parameter with available physical significance in the empirical correlations.

Moriyoshi et al. (2009) examined the spray formation process in cross-flow by using ILIDS (Interferometric Laser Imaging for Droplet Sizing) technique with a fan-shaped injector of the D.I. gasoline engine. It was concluded that the effect of the cross-flow on the atomization was determined by the relative mean velocity between the droplet and the ambient flow, and that small droplets were guided to the downstream by the cross-flow obviously. Moon et al. (2007) investigated the influences of the airflow on the fuel spray with using a slit injector. It was found that with increasing the airflow velocity the spray presented a significant change in the bottom part of the spray while a slight change was observed close to the nozzle exit. Panão et al. (2013) considered that the cross-flow could promote secondary atomization and affect the transport of secondary droplets. Breakup and spray formation of swirl liquid jets introduced into a low-speed cross-flow were experimentally investigated by Lee et al. (2010), who manifested that the cross-flow promoted the jet breakup and rendered a finer spray in an entire range of injection velocities, and this deduction was also demonstrated by Padala et al. (2013). Bai et al. (2009) considered that the addition of droplets into the gas cross-flow enhanced the turbulence intensity of the gas cross-flow. While Nouri and Whithelaw (2007) investigated that the cross-flow decreased the

penetration on the incident side of the cone spray and caused a small increase on the lee side. However, the spray tip penetrations at quiescent and cross-flow conditions are almost similar during the fuel injection period according to the research by Padala et al. (2014).

In summary, with different injectors, the cross-flow has large effects on atomization, breakup, penetration and so on of spray. While in the current study the characteristics of fuel spray injected by a VCO nozzle, including the variations of spray profile, penetration and velocity distribution are discussed in detail. Usually the penetration is defined as the distance from the nozzle hole to spray tip (Stegemann et al., 2002; Roisman et al., 2007). In this study, owing to the influences of the cross-flow, the spray moves not only along the original direction of spray but also along the direction of cross-flow, therefore the spray penetration consists of horizontal penetration (along the direction of cross-flow) and vertical penetration (initial injection direction).

It is well known that the penetration height (corresponding to the profile of spray in upstream side in this study) of a liquid jet in the cross-flow is a function of the liquid to air momentum flux ratio and the normalized distance from the injector along the direction of cross-flow (Wu et al., 1997; Stenzler et al., 2006). Several researcher incorporated the Weber number, liquid-to-water or air viscosity ratio and pressure ratio or Reynolds number in the empirical correlations (No, 2011). While in this study, through penetration heights measured from images taken by a high speed video camera, the empirical correlations are deduced and analyzed in detail.

The structure of the spray is distinctly changed by the cross-flow. However, the changes are different in various parts of the spray. A significant change exists at the bottom part of the spray, while a slight change is observed close to the nozzle exit with increasing airflow velocity (Moon et al., 2007). In addition, small droplets are obviously guided downstream by the cross-flow, which was found by Moriyoshi et al. (2009). In respect to the droplets breaking, the cross-flow could promote secondary atomization and affect the transport of secondary droplets (Panão et al., 2013); by investigating the breakup and spray formation of swirl liquid jets introduced into a low-speed cross-flow, it was shown that the cross-flow promotes the jet breakup and renders a finer spray in an entire range of injection velocities (Lee et al., 2010). Furthermore, these conclusions were verified by Padala et al. (2013), and it was suggested that the ambient airflow has a significant impact on the ethanol droplet breakup (Padala et al., 2014). The effects of the cross-flow on the atomization were determined using the relative mean velocity between the droplets and the ambient flow (Moriyoshi et al., 2009). The droplet sizes in a cross-flow are different from those

under a no-cross-flow condition. The droplet diameters with the cross-flow were larger than those of the free spray at smaller radii within the normal cone spray (Nouri and Whitelaw, 2007). Thus, not only the effects of the cross-flow on the spray but also the effects of the spray on the cross-flow field must be considered. The addition of droplets into the gas cross-flow enhanced its turbulence intensity (Bai et al., 2009). A counter-rotating vortex pair behind a jet in a cross-flow has been observed in some investigations (Fric and Roshko, 1994; Ghosh and Hunt, 1998; Getsinger et al., 2014).

1.5 Summary

The background and motivation of this study are represented from the global energy consumption to the performance improvements of DISI engine. The objectives are listed and analyzed in this part. The investigation of characterization of fuel spray into cross-flow ambient is benefit for the fundamental researches of the DISI engine. The spray characteristics of DISI gasoline engine have been investigated by many researches, however, the effects of the air flow in combustion are represented in multiply conditions, the mechanisms are not yet clarified. To further understand the characteristics of the process in combustion, the fundamental single condition experimental studies are necessary.

The energy and environmental issues are always concerned all over the world. As the tendency of energy consumption, the conventional energy like fossil fuel will use up in several decades, the accompanying environmental issues (like climate warming) will deteriorate. The transportation sector is a large part of energy consumption and harmful gases emission. The energy efficiency improvements are greatly significant. In gasoline engine, the fuel efficiency have been observably developed with the application of the DISI technique. However, to meet the goal of controlling energy consumption and emissions, the stricter improvements should be taken in DISI engine. The spray characteristics are very important to investigate the fuel combustion.

The spray mixture formation of DISI engine have been represented by reviewing the pervious researches. Thereafter, the diagnosing methods, which are usually used in the engine spray, are listed in this part. The air flow of DISI combustion chamber are introduced during various period, the air flow is complex in the combustion chamber. The investigations of the effects of cross-flow (air flow) on spray in internal combustion engine are insufficient recently. Those studies are focus on the interactions between cross-flow and jet in the modern propulsion and power applications, such as gas turbine, ramjet, and scramjet engine. Those studies are also significant in the study of the interactions in the DISI gasoline engine.

Chapter 2 Experimental Apparatus and Procedures

2.1 Experimental Methods

2.1.1 *Spray visualization*

The fuel is directly injected into the combustion chamber in a gasoline direct injection (GDI) engine. The spray is injected in a very short period of time. The liquid and fuel vapor exist in the combustion chamber at the same time. The characteristics of liquid fuel atomization and vaporization are critical important, because those factors directly influence the engine's performance and emissions.

The direct imaging of sprays is considered as the simplest and most utilized optical technique for fuel spray characterization. Recently, photographic and digital imaging using a solid state camera have been employed to characterize automotive fuel sprays. Optical imaging, which include direct imaging, high-speed cinematography, and holography, has been reviewed by Chigier (1991). Direct imaging of fuel sprays with back-illumination is used widely to measure spray profiles, penetration, wall impingement, and subsequent combustion in engines (Zhao and Ladommatos, 2001) Shadowgraph (schlieren) is an optical method that reveals non-uniformities in transparent media like air, water. It is a type of flow visualization, which is widely used to detect the boundary between vaporized fuel and background ambient gas, because of a different refractive index at the interface between the ambient gas and fuel and the dramatic density gradient forming as the evaporating fuel cools down the ambient gas in evaporating fuel spray experiments (Naber and Siebers, 1996).

The scattering photography is widely used in the engine diagnosis visualization. The scattering, which comes from molecules or very tiny particles (the diameter smaller than the wavelength of light or approximately equals the 1/10 wavelength), is predominantly Rayleigh scattering. When the particle (or droplet) size equals or bigger than the wavelength of light, the scattering changes to Mie scattering. In the spray visualization experiments without evaporating, the scattering is predominantly Mie scattering. Because the light wavelength is much smaller than the droplet size. The direct imaging of Mie scattering method schematic is shown in Fig. 2.1 using a high intensity light source. In this case, the characteristics, such as profiles, droplet movement of whole spray, can be observed directly. The laser sheet photography is employed to observe the sectional plane

of the spray, as shown in Fig. 2.2.

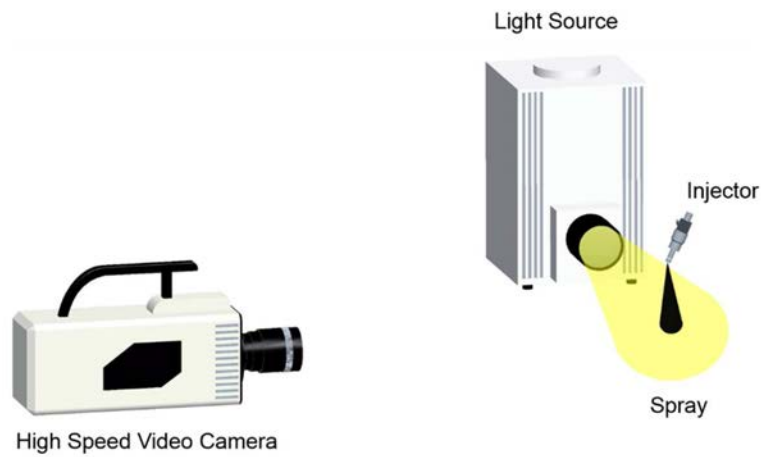


Figure 2.1 A simplest schematic of direct scattering photography

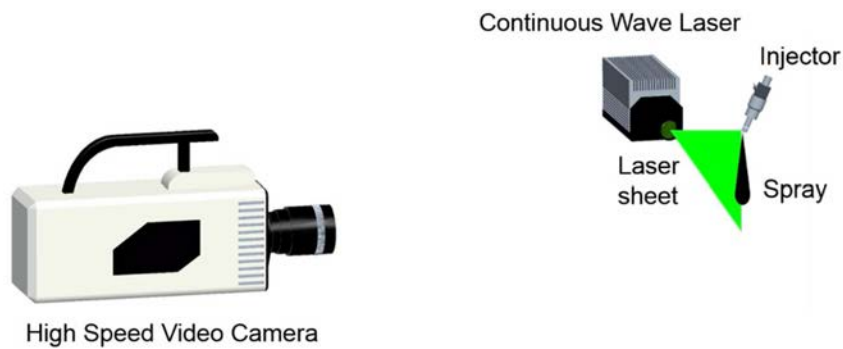


Figure 2.2 Laser sheet photography

2.1.2 Velocity distribution measurement

The velocity measurement in the single point of the cylinder can be taken by hot-wire anemometry or laser Doppler anemometry/velocimety (LAD/LDV), which are used to measure the flow velocity and turbulence with high spatial resolution. The hot-wire anemometry can output a continuous recordings of velocity over time, however, the velocity direction cannot be obtained and the accurate calibration should be done before measuring. The wires which are used in hot-wire anemometry are very thin, and easy to break, the hot-wire anemometry are not suit to use in the combustion condition. LDA is non-intrusive method, which is better than hot-wire in avoiding the effects on the flow. Therefore, LDA is widely used in recent researches. Although the continuous data of velocity in the testing point can be get by LDA, the testing points are limited in

the actual experiments, especially in the engine cylinders due to the complex structure and the piston moving. Otherwise, the whole field velocity distribution cannot be obtained simultaneously by LDA. To understand the whole field velocity distribution, in the early stage, the flow was visualized by the introduction of smoke, and the turbulent nature of in-cylinder flow is used to confirm the qualitative observation (Clerk, 1921).

To quantify the velocities in the complex unsteady in-cylinder flows, particle tracking velocimetry (PTV) and particle image velocimetry (PIV) have been developed. Two dimensional maps of velocity of the testing plane in cylinder can be acquired. In PTV and PIV measurements, small particles, which can be illuminate and recorded by camera, are fed into the flow field. TV has been used for the characterization of induction-like flows in water analog engine (Khalighi and Huebler, 1988). A variation on PTV is streak photography, which can record the movement of the particle during the exposure period. PIV provides a means of achieving high spatial resolution two-dimensional velocity measurement. In PIV measurement, the particle displacement in a short period is calculated by two frozen images illuminated by the sheet laser, which can emit two high-energy laser pulses. The recorded image is divided into many small areas, in which the mean velocity is determined by performing a spatial correlation of the region. Because the spatial correlation process of PIV is not based on the single particle movement, a sufficiently high density of particles can be used in the measurement, hence the more complete and detailed velocity maps can be obtained than that in PTV. The micron-sized particles are allowed to use and the measurement can suit high-frequency flows due to the application of high-energy, short pulse duration laser illumination.

Particle image velocimetry (PIV) is originate from laser speckle photography (LSP), which has been used for measuring surface displacement fields. The principle of the PIV technique is that the velocity vector is calculated from the displacement of an element of fluid in a known time interval. The PIV technique requires a thin slice of the flow field to be illuminated by a laser light sheet in the simplest form. Particles in the flow within the light sheet scatter the light. The scattered light is detected by a camera which is placed at a right angle to the light sheet (Fig. 2.3). The laser light sheet is double-pulsed (switched on and off very quickly twice) at a known time interval, Δt . The first frozen images of the initial positions of particles by the first pulse of the laser is taken by the camera. The second frame of the camera is exposed to the light scattered by the particles from the second laser pulse. Two images are obtained, the first showing the initial position of the particles

and the second their final positions due to the movement of the flow field. Alternatively, the double exposed particle images can be recorded on the same photographic film.

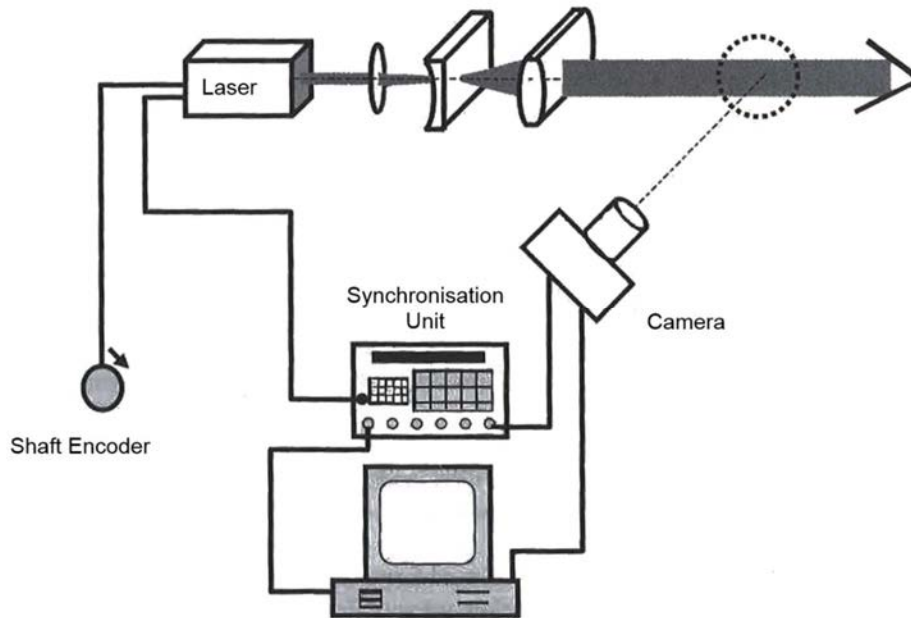


Figure 2.3 Typical PIV experimental setup

The intersection volume between the region illuminated by the laser light sheet and the field of view of the imaging optics determines the region of the flow to be measured (see Fig. 2.4). The interrogation area (IA) is defined as the smallest resolvable area of the film or detector. The interrogation volume (IV), which is projected back onto the measure region of IA, constitutes a single velocity vector. The displacement of the particle in the object plane (Δx and Δy) and the displacement in the image plane (ΔX and ΔY) have a correlation as,

$$\Delta x = \frac{1}{M} \Delta X, \text{ and } \Delta y = \frac{1}{M} \Delta Y \quad (2.1)$$

$$u = \frac{\Delta x}{\Delta t}, \text{ and } v = \frac{\Delta y}{\Delta t} \quad (2.2)$$

where, M is the magnification factor of the imaging optics, Δt is the time separation between the two laser pulses, u and v are the velocity projections on the object plane.

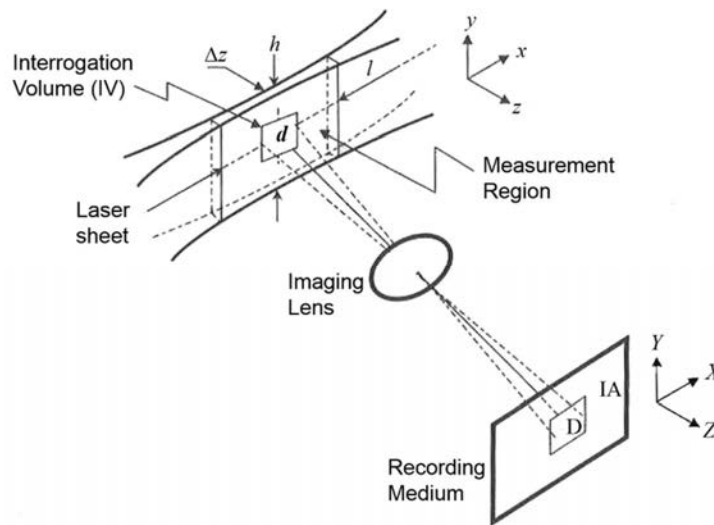


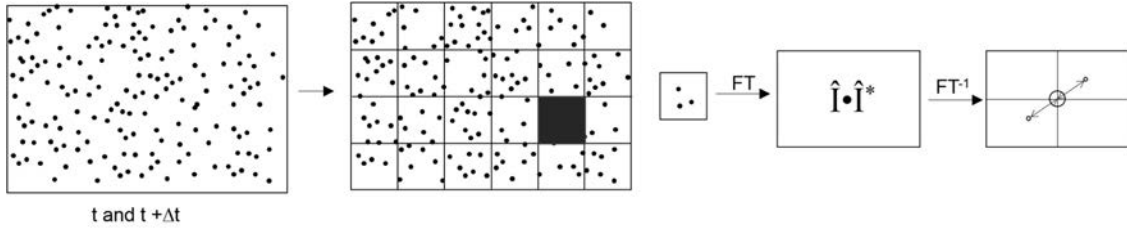
Figure 2.4 Definition of measurement region and measurement volume.

Illumination source and light sheet is preeminent important part in PIV system. Lasers are ideally suited as the light source for PIV measurements due to the conveniently collimated and intense form light. The average intensity of a particle image can be increased by shorter wavelengths compared to longer wavelengths. The blue-green wavelength light performs better in photographic emulsions than red light. The frequency doubled Nd: YAG pulsed laser is the most commonly employed in the PIV measurement. Two types of Nd: YAG lasers have been used in PIV system, the single-cavity Nd: YAG laser with the double pulse option, and the twin-oscillator, twin-amplifier frequency doubled Nd: YAG laser. In the former, the first laser pulse is triggered externally, and the timing of the second pulse is adjusted by a potentiometer on the double pulse option, the pulse separation are limited to typically 20 μs to 200 μs , however, the energy of each pulse is weakened. In the latter, each of the pulse is triggered separately, there is no reduce of the pulse energy, however, the accurate co-alignment of the two separate outputs should be utilized in the system.

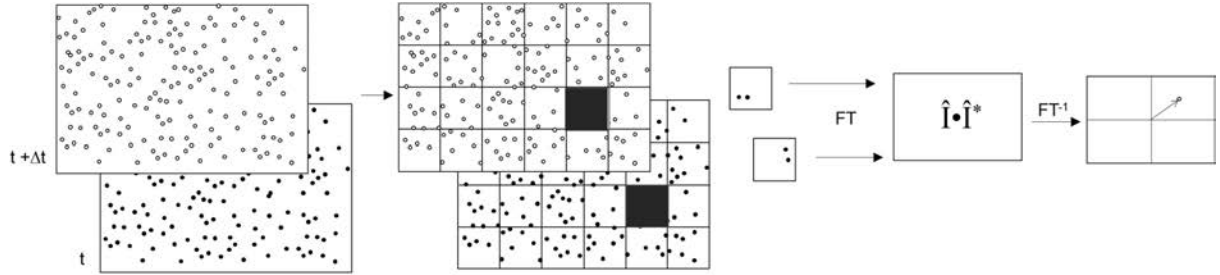
The supply of seeding particles is often significant for the quality and feasibility of PIV measurements. The requirements of particle seeding for PIV measurements are summarized by (Zhao and Ladommatos, 2001), including particle flow-following ability, particle light scattering characteristics, particle number density in the flow, tendency of particles to foul optical windows, tendency of particles to abrade cylinder surfaces, and ability of particles to withstand high-temperature environment in a fired engine.

There are two main categories of the PIV recoding modes: methods that capture the illuminated

flow onto a single frame (single-frame/double-exposure PIV) and methods that provide a single illuminated particle image for each illumination pulse (double-frame/single-exposure PIV). It is normal that the single-frame/double-exposure approach is used in photographic PIV recordings while the double-frame/single exposure is adopted in digital recording.



(a) Analysis of single frame/double exposure recordings: the fully digital auto-correlation method.



(b) Analysis of double frame/single exposure recordings: the digital cross-correlation method.

Figure 2.5 Two methods of recording analysis.

The cross-correlation algorithm owns the advantages of reducing the in-plane loss of correlation and increasing the correlation peak strength. The comparison of the flow chart of the auto-correlation and cross-correlation by FFT analysis are shown in Fig. 2.5.

The two frames are sub-divided into a number of interrogation windows, the cross-correlation function $R_{II}(S, \Gamma, D)$ is calculated in each interrogation window. The displacement peak is determined, they correspond to the vectors of the particle image displacement. There are three terms including in the cross-correlation function,

$$R_{II}(S, \Gamma, D) = R_C(S, \Gamma, D) + R_F(S, \Gamma, D) + R_D(S, \Gamma, D) \quad (2.3)$$

where the R_C and R_F are the contribution of the background noise in the correlation plane. R_D represents the component of the cross-correlation function, which corresponds to the correlation of image of particles. Those image particles are obtained from two exposures.

$$R_D(S, \Gamma, D) = R_T(s - d) \sum_{i=1}^N V_0(X_i) V_0(X_i + D) \quad (2.4)$$

where d is the particle displacement in the image plane, s is the separation vector in the correlation plane. Therefore, the displacement correlation peak reaches a maximum when $s=d$ for a given distribution of particles in the flow. The composition of peaks in the cross-correlation function is shown in Fig. 2.6.

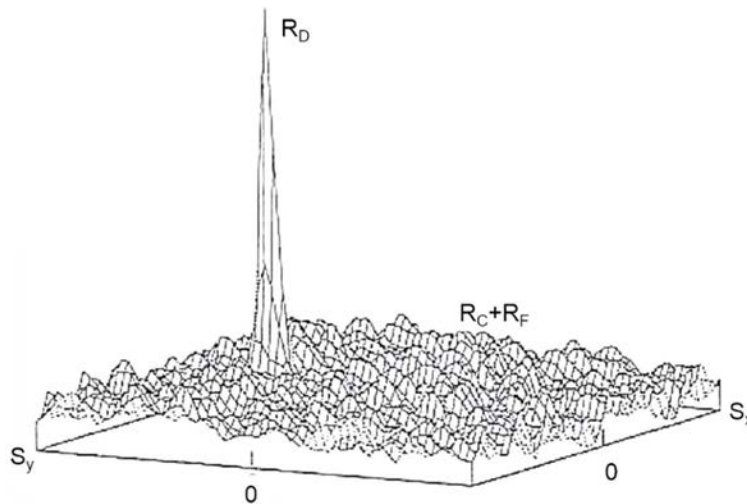


Figure 2.6 Composition of peaks in cross-correlation function.

The integral formulation of the cross-correlation function,

$$R_{II}(x, y) = \sum_{i=-K}^K \sum_{j=-L}^L I(i, j) I'(i + x, j + y) \quad (2.5)$$

The plain of the image is sub-divided into a number of interrogation windows with I rows and j columns. The I and I' are the variable intensity value coinciding to the samples of two images. The product of all overlapping pixel intensities generates one cross-correlation value for each sample shift (x, y) . The composition of correlation plain is formed using this operation in a range of shifts. It should have a peak in the correlation plain, in which shift value aligns the particles of the samples with each other. In that case, the particle displacement in image plane can be calculated in the sample window according to the peak correlation value.

2.1.3 Droplet size measurement

It is important to know the droplet size distributions in the spray, because the fuel atomization and vaporization processes are effected by the droplet size distribution. Two of typical optical techniques for droplet sizing are usually utilized in the measurements, the direct imaging techniques and light-scattering techniques. In the former, the simplest optical droplet sizing technique is the direct imaging of fuel droplets by photography. The structure of the fuel spray and

droplet size distribution can be provided from those images. From the recorded images, the droplet size distribution is determined by counting and sizing the diameter of the droplets. The light source for the direct imaging can be a pulsed laser or modulated continuous wave laser. The high-resolution images are needed in the photography, because the camera should have the ability of capturing the image of minimum droplets. The holographic recordings extend the photographic techniques into three-dimensional measurements. Holograms provide three-dimensional pictures of an object, which can be examined in much the same way as a photograph (Trolinger, 1991).

Integral methods and particle counting are the two approaches to light scattering measurements. The integral methods, which performed by the Fraunhofer diffraction, measure a number of droplets simultaneously. The intensity and a spatial average can be obtained from integration over space. This technique is moderate in the condition of high droplet concentrations. On the other hand, the particle counting techniques, such as a laser phase Doppler analyzer (PDA), the droplets are measured at a time. The moderate concentrations and a small sample volume are needed during the experiments. The higher the concentration, the smaller the volume needs to be. The PDA measures the size distribution over time, and a temporal average can be gained.

It is know that both liquid droplets and fuel vapor may be present at the same time in a fuel spray, simultaneously clarifying their characteristics is important. It can be realized by laser induced exciplex fluorescence (LIEF) method. Though elastic (Mie) scattering or fluorescence signal can be captured simultaneously from both the liquid and vaporized fuel, the signal from the liquid phase is many orders of magnitude stronger than that from the fuel vapor, which limits the elastic scattering or LIF techniques to the detection of liquid only. Laser Extinction/Absorption (LEA) is the other technique, which can detect simultaneously of fuel vapor and liquid droplets.

In this study, the droplet size distributions are measure by light scattering method. The principle will be introduced in the following content.

The light scattering methods base on the theory of Fraunhofer diffraction. The droplet size information from the angular distribution of the elastically scattered radiation is obtained by the Fraunhofer diffraction method. When a relatively large opaque particle ($d_p \gg \lambda_L$) is illuminated by a beam of parallel monochromatic light, the Fraunhofer diffraction pattern can be projected on a screen at a great distance from the particle. This pattern is characterized by a series of alternating dark and bright rings that relate to the location of zero and peak intensities, as shown in Fig. 2.7. The Fraunhofer diffraction pattern is observed at the focal plane using a lens in the practical

measurement.

The Fraunhofer diffraction pattern can be described mathematically as,

$$I = I_0 \left(\frac{2J_1(X)}{X} \right)^2 \quad (2.3)$$

$$X = \frac{\pi dR}{\lambda f} \quad (2.4)$$

where I_0 is the intensity at the center of the diffraction pattern, $J_1(X)$ is the first order spherical Bessel function, X is a dimensionless size parameter, f is the length of the collection lens, and R is the radial distance in the detection plane. From the Eq. (2.3), the diffraction pattern, which is irrelevant to refractive index or shape, is unique for a particle or a collection of particle of different sizes. Hence, the size distribution of a collection of particles can be deduced from their diffraction patterns.

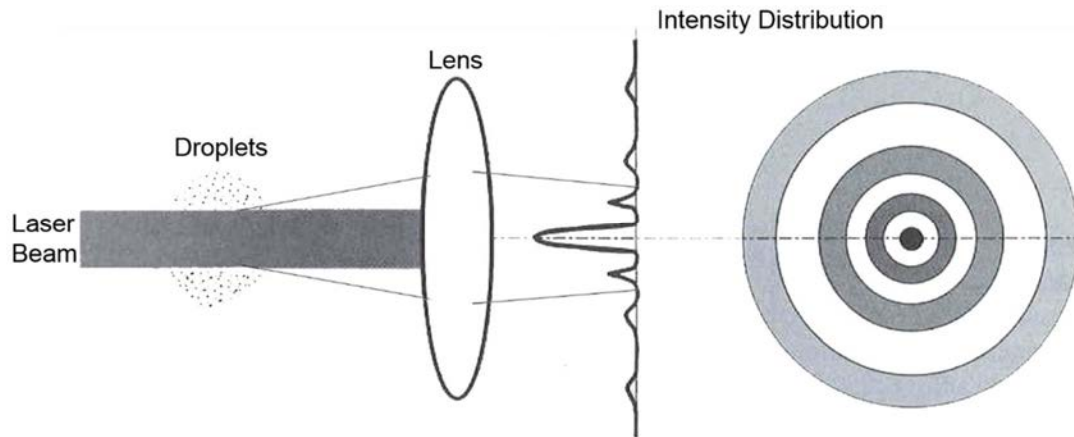


Figure 2.7 Radial intensity distribution of the Fraunhofer diffraction pattern.

A monochromatic parallel light beam, which usually be emitted from a laser (a low-power He-Ne laser), traverses a cloud of droplets or particles, as shown in Fig. 2.8. The intensity distribution of the transmitted and scattered light is observed in the focal plane by the collection of a lens. This distribution can be measured by traversing a photo-detector (usually an array of detectors) across the focal plane.

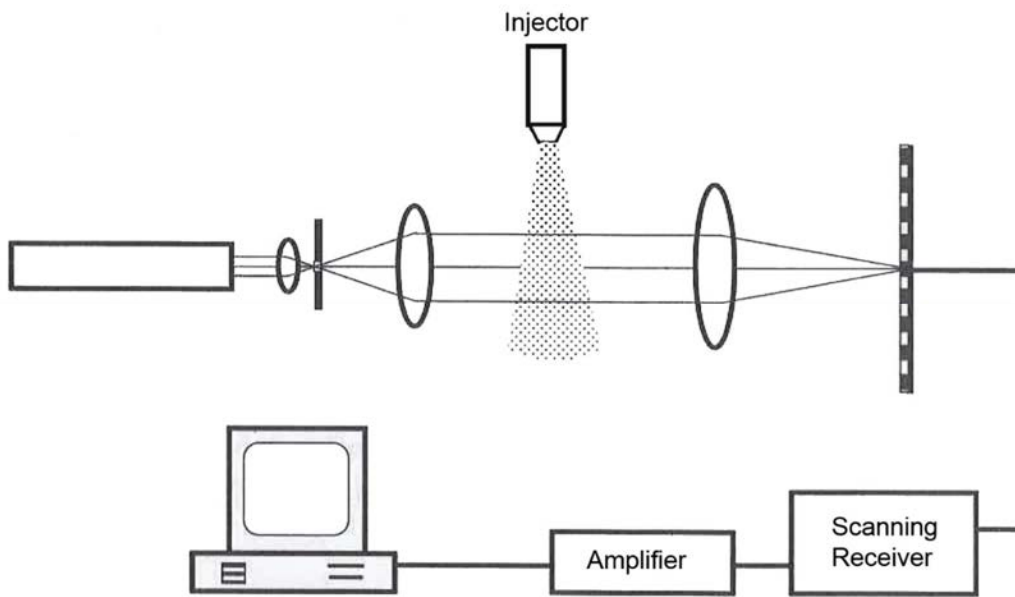


Figure 2.8 Experimental setup for the Fraunhofer diffraction technique.

The droplet size measuring range can cover 0.2~2000 μ m using different focal lengths for the receiving lens. The instrument can be calibrated using the standard particles whose sizes are known. The results rely on the scattering pattern shape, not the actual intensities. Therefore, it is independent of variations in incident intensity. The noises, which are caused by the scattering from dust on lenses or windows, can affect the measuring results, especially in the low level of droplet concentration. Keeping the collection lens and windows clean is important during experiments. In the high concentration condition, the multiple scattering occurs, it can change the diffraction pattern. Some special procedures can extend the applicable range of the diffraction method (Zhao and Ladommatos, 2001). In a high-temperature environment condition, the central spot moves due to the deflection which is caused by the density changes. The increasing the spot size as well as reducing the maximum measurable droplet size will happen over a finite time.

2.2 Experimental Setup

2.2.1 Experiment setup Units

To investigate the characteristics of the spray in the cross-flow, many experiments have been taken, such as Mie scattering photography (whole spray and sectional plane of spray), PIV measurements in various planes, and droplet size distributions. First of all, the spray perpendicularly injected into the air-flow, which is called cross-flow in this study. The spray structure changes under the cross-flow, the experimental devices should be adjusted to suit the situations.

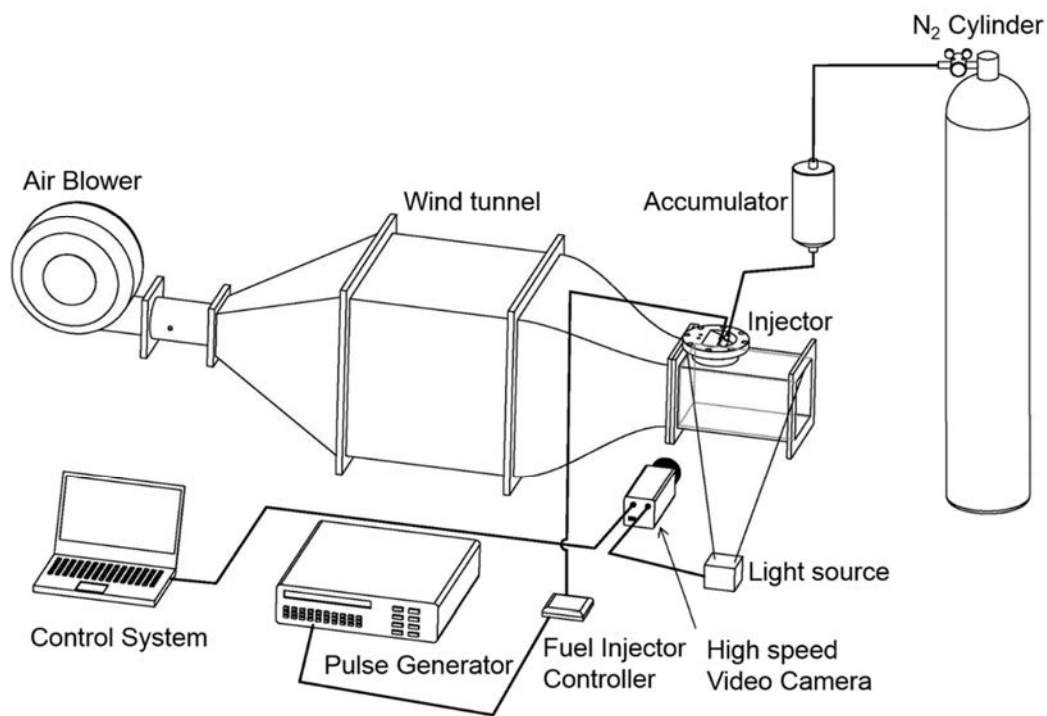


Figure 2.9 Schematic of experimental setup for high speed photography.

Direct photography of the spray using high speed video camera is shown in Fig. 2.10. To investigate the effects of cross-flow on spray, a wind tunnel was made to provide a uniform cross-flow field during spray injections. The wind tunnel is composed of a diffusion chamber, a rectification chamber and a contraction chamber. There are five pieces of meshes with different size in the rectification chamber, the details will be introduced in Part 2.2.2. Downstream the wind tunnel, an observation chamber was connected, which was made of transparent acryl with size of 300mm in length and 150mm×150mm for inner section. An adaptor for the VCO-type injector

was fixed in the upper surface of the observation chamber, and through the adaptor the nozzle tip was set to reach the inner wall of the upper surface in the observation chamber. The VCO-type injector with 25° spray angle and 0.15mm hole diameter was adjusted to keep the direction of spray perpendicular to the direction of the cross-flow. High pressure nitrogen was used to promote the process of spray. The injection duration was controlled through a pulse generator while injection time was operated by the fuel spray controller.

Two types of high speed video camera (Photron Co., FASTCAM-APX RS, and NAC Image Technology Inc., HX-3) of 10000 frame/s were employed to obtain the continuous spray images, according to which the profiles of spray and motion tendency have been analyzed. The HSV camera was triggered by hand. In whole spray structure photography experiments, the light source was a xenon lamp (USHIO corp., SX-UID501XAMQ) which can emit the continuous and high intensity light. The xenon lamp was not always placed in the bottom of the observation section. For the clear images, the xenon lamp was also adjusted to be in the same height of camera, and kept the horizontal light an angle with the camera (avoiding the light perpendicular irradiates into the camera). In the sectional plane photography, the xenon lamp was replaced by a continuous-wave laser (DPGL-2W, JAPAN LASER Corp., wavelength 532 nm), which can emit a 1 mm thickness laser sheet. The laser sheet is also placed in various horizontal and vertical planes for taking different parts of the spray.

To measure the velocity of the spray and the cross-flow velocity, a PIV system (Seika Corp., 2DPIV system) was utilized, which consisted of a PIV camera (PCO Inc, PCO1600), a double-pulsed Nd: YAG laser (NEW WAVE RESEARCH Corp., DPIV-N50, a sheet with a wavelength of 532nm and thickness of 1mm was provided), a host computer, and a synchronizer, as shown in Fig. 2.10. Double-pulsed laser sheets were directed to the observation chamber, parallel to the direction of the cross-flow. The laser sheets were adjusted to illuminate various vertical and horizontal planes, in which the velocity distributions of the spray droplets and the cross-flow field were measured. The observations were made in a plane where the nozzle tip located. To measure the velocity of the cross-flow, magnesium oxide (MgO) particles with a few microns in diameter were seeded into the wind tunnel through the tracer particle inlet while the velocity distribution of the spray could be obtained without additional tracer.

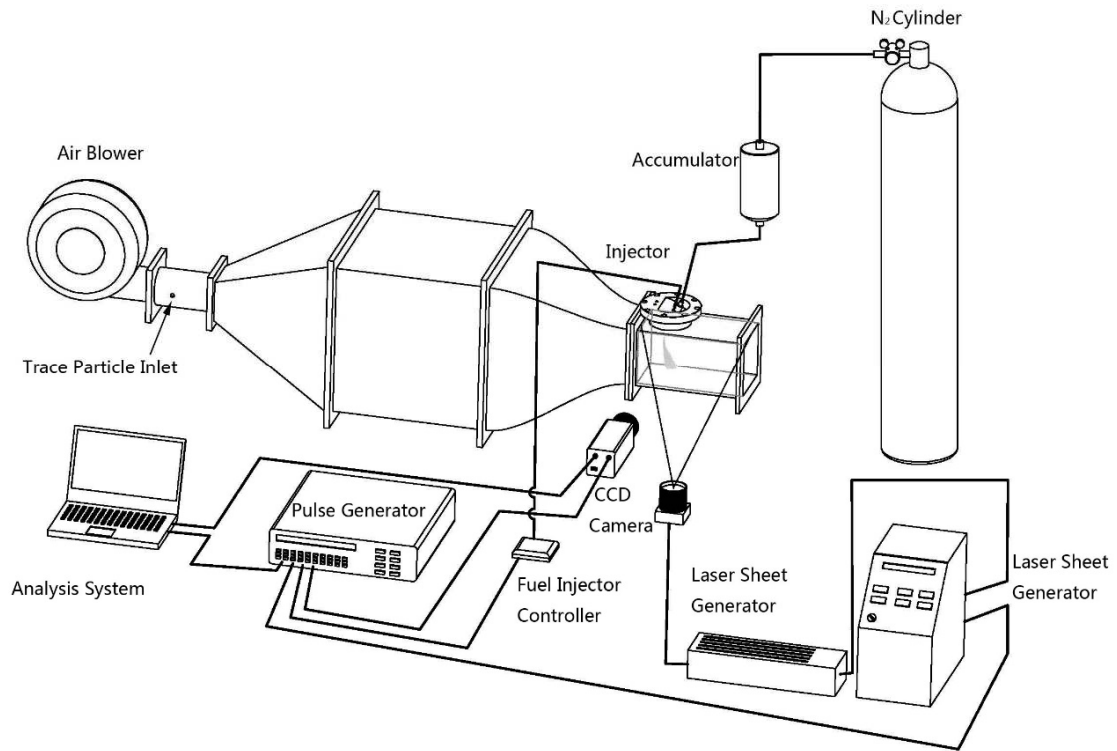


Figure 2.10 Schematic of experimental setup for PIV measurement.

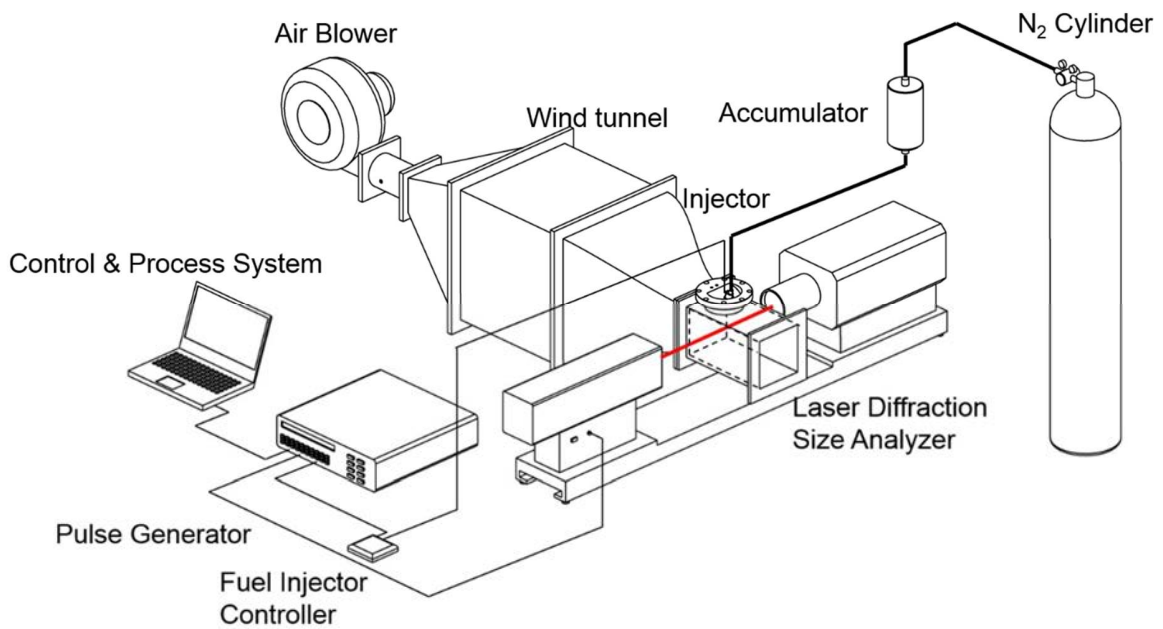


Figure 2.12 Schematic of experimental setup for droplet size measurement.

To determine the effect of the cross-flow on the droplet size distribution, a droplet size analyzer (NIKKISO Corp., LDSA-1400A) was utilized to measure the diameter of the spray droplets, as shown in Fig. 2.12. Laser diffraction size analysis is based on the principle that particles of a given size diffract light through a given angle, which increases with decreasing size. The analyzer provided a measurable area within a cylinder with a diameter of 8 mm. The testing range for the droplet size was 1.4~1000 μm . In the measurement, the analyzer was triggered by a pulse generator, which controlled the injection time as well as the sampling time. Otherwise, the trigger time for the LDSA would have been 0.3 ms in advance, because the sampling duration of the LDSA-1400A is 0.6 ms (the minimum sampling duration of this equipment was used in this investigation). The droplet size results were time-averaged for 0.6 ms. For example, the test time was 7 ms ASOI, and the trigger time was 6.7 ms ASOI. Thus, the sampling time was from 6.7 to 7.3 ms in this study. The laser beam of the analyzer was set perpendicular to the cross-flow direction and spray direction (the laser beam of the analyzer was perpendicular to the XOY plane). The droplet size and corresponding percentages, as well as the mean diameter such as the Sauter mean diameter (SMD), were obtained.

2.2.2 Structure of wind tunnel

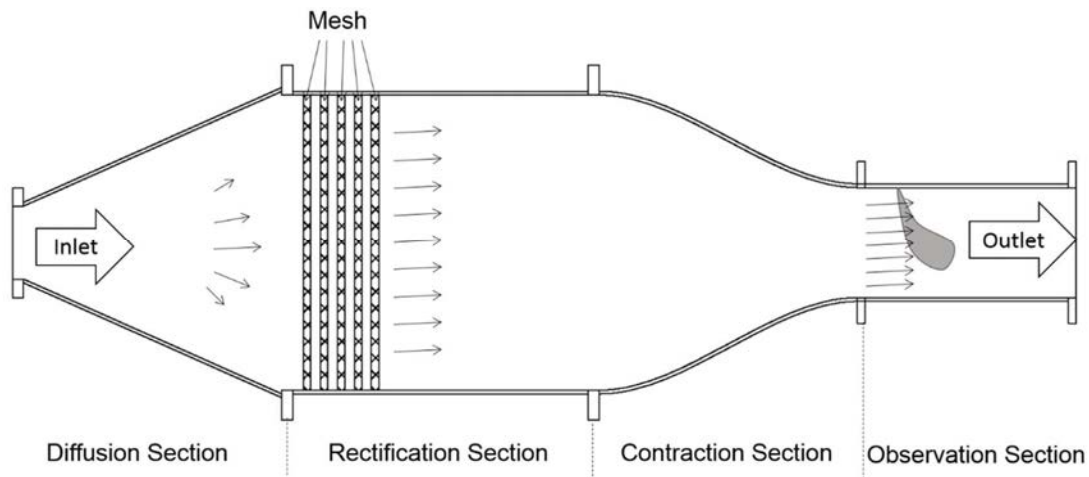


Figure 2.13 Structure of atmospheric wind tunnel.

There are four parts in the atmospheric wind tunnel, diffusion section, rectification section, contraction section, and observation section. The air is blown by an air blower into the diffusion section whose profile is like a horizontal placed frustum of a Square Pyramid, the section area

increases along the direction of the air flow. Five mesh screens with different mesh size are arranged in the rectification section. The mesh screen has positive effects in unifying the velocity distribution in observation section, because the suitable mesh can control the span-wise variations of surface shear stress in a rational range (Bradshaw, 1965) and the turbulence can be reduced by those mesh screens (Groth and Johansson, 1988). The shape curves of the contraction section walls are important in unifying the velocity distribution in the observation section. The transition of curve should be smooth enough to reduce the turbulence. The curve will be introduced in the next part. The observation chamber was made of transparent acryl with size of 300mm in length and 150mm×150mm for inner section. In the upper surface of the observation section, a groove with an oblique hole (at 25° to vertical) was made, this structure is used to assemble the adaptor of the injector, and the injector can inset to the observation through the oblique hole. The observation can be taken from three sides of the observation section only except the upper surface. The joints of all the sections of the wind tunnel are gastight. The tracer particles are fed before the diffusion section during the PIV experiments, in that case, keeping the mesh screens clean is necessary.

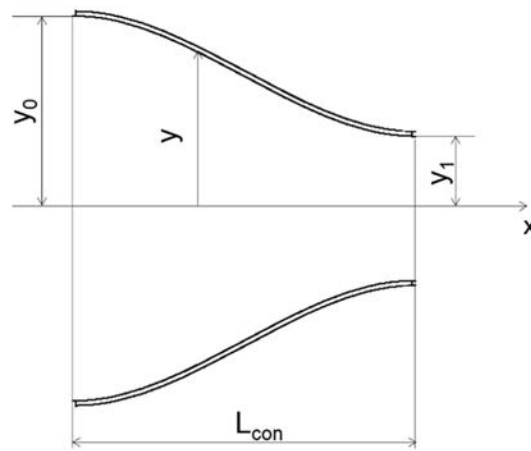


Figure 2.14 Curve of contraction section wall.

To obtain the uniform velocities in observation chamber, the structure of the contraction section wall has been optimized, a cubic curve shape of the wall was used (see the Eq. 2.5).

$$y = \frac{2(y_0 - y_1)}{L_{con}^3} x^3 + \frac{3(y_1 - y_0)}{L_{con}^2} x^2 + y_0 \quad (2.5)$$

2.2.3 Performance evaluation

Before experiments, the velocity distribution in the observation section should be checked. The uniformity of the field can be tested by measuring velocity variations of a number of points in the air flow by hot-wire anemometer, or measuring velocity distributions in some planes. The results of the hot-wire anemometer are based on time, hence the turbulence can also be measured.

The experimental coordinate was defined in Fig. 2.15. The original point O was set at the position of the nozzle hole, and OX and OY were the cross-flow and the injection directions, respectively. XOY plane is the middle plane of the observation section.

The cross-flow velocity was examined with using a hot-wire anemometer as well as the PIV system. The hot-wire anemometer was employed to measure the velocities and turbulence. Figure 2.16 (a) and (b) shows the velocity of cross-flow and its turbulence, respectively; they are measured just below the nozzle tip and 50 mm away from the nozzle tip along the direction of the cross-flow, indicating by $x=0\text{mm}$ and $x=50\text{mm}$. In this study, the turbulence u'_x/U_x is defined as:

$$u'_x/U_x = \frac{\frac{1}{N} \sum_{i=0}^N \sqrt{(u_x(i) - U_x)^2}}{U_x}, \quad (2.6)$$

where i is the measuring number of each point, N is the total number of sampling, $u_x(i)$ is the actual velocity for the i th sampling, U_x is the mean velocity during the sampling time calculated through the following relation,

$$U_x = \frac{1}{N} \sum_{i=0}^N u_x(i). \quad (2.7)$$

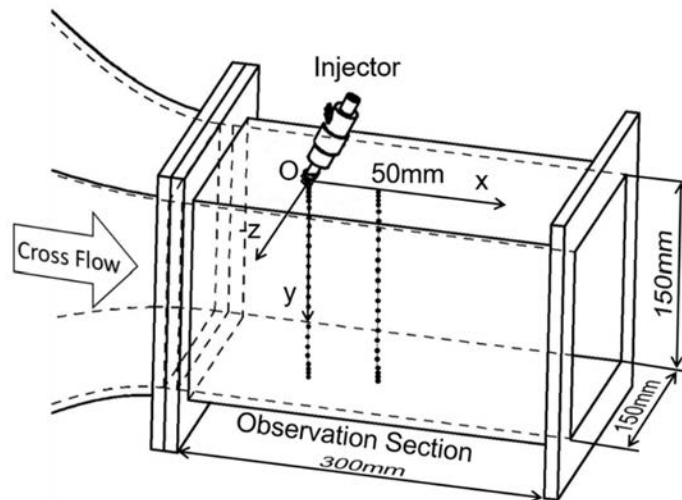


Figure 2.15 Experimental coordinate and testing location
(Black dots are the locations of the testing points).

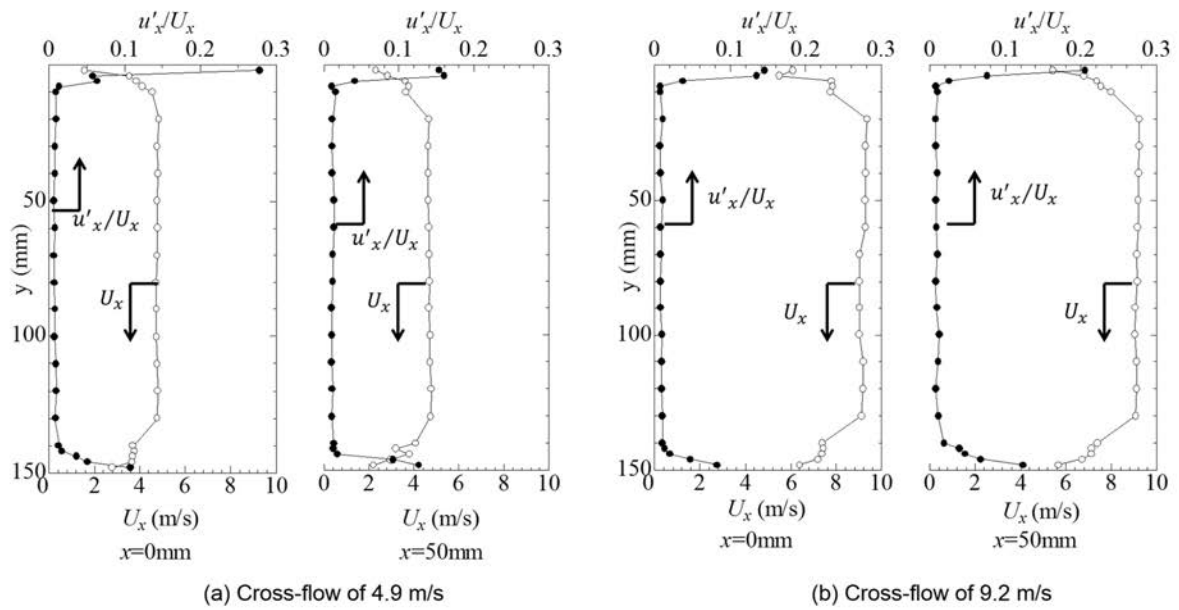


Figure 2.16 Velocity profiles (open circles) and turbulence intensity (solid circle) of the cross flow.

Hence based on Eq. 2.6, the turbulence value can indicate the actual velocity fluctuations. Two typical conditions are shown in Fig. 2.16, in which the velocities are 4.9 and 9.2 m/s, respectively. It is seen that the velocity increases from the wall until 20 mm away from the wall, where the turbulence is large especially within the boundary layer. Within the domain from $y=20\text{mm}$ to $y=130\text{mm}$, the velocity of the cross-flow is almost uniform, which provides a stable condition for the development of the spray.

2.3 Summary

The experimental methods, which were used in this study, were illuminated with the backgrounds and principles. There are two main kinds of experiments in this study, the experiments based on the atmospheric wind tunnel and the experimental based on the pressure wind tunnel. In this chapter, the experimental methods and apparatus were introduced. It is used to simulate the condition of the surrounding of the homogenous charge combustion model,

The high speed video photography was employed using Mie scattering method, the profiles, penetration, and droplet concentration could be analyzed from those images, which were taken in various planes in horizontal and vertical. The continuous illuminators, which include the Xenon lamp and the continuous wave laser (sheet), were used in experiments. The PIV system was used to measure the velocity distributions of the spray and air field. The principle of the PIV was briefly introduced. Laser diffraction size analyzer was employed to measure the droplet sizes in various points, hence the droplet size distribution could be obtained by assembling those points.

The experimental setup of the atmospheric ambient (based on atmospheric wind tunnel) was presented, the details of the components were listed, such as the functions, types, and arrangements. The wind tunnel is composed of a diffusion chamber, a rectification chamber and a contraction chamber. There are five pieces of meshes with different size in the rectification chamber, and the observation section was made of transparent acryl. The cross-flow performance was checking by measuring the velocity distributions and turbulence in various points.

Chapter 3 Experimental Apparatus for High Pressure Cross-Flow Condition

3.1 Theoretical Calculation

The circuit wind tunnel was used to provide the air flow under high pressure by Tajima et al. (2011). However, the complex structure and cost are the significant problems for air flow experiments. In this part, another method is introduced to obtain the air flow under high pressure ambient using pressure tank. The principle schematic is shown in Fig. 3.1. Compressed air is stored in the pressure tank, the valve 3 keeps partly opening, when the valve 2 is opened, the pressure in observation chamber can increase rapidly, and the velocity in observation chamber can also be obtained. Because the throttling of valve 3 and the supplement from pressure tank, the pressure in observation chamber will not change to atmosphere rapidly. In that case, the velocity and pressure conditions can be kept in observation chamber, the matching of them can be control by valves. When the velocity and pressure meet the experimental conditions, the measurement can be triggered by a quick-response control system. Some theoretical exploration will be taken in the following.

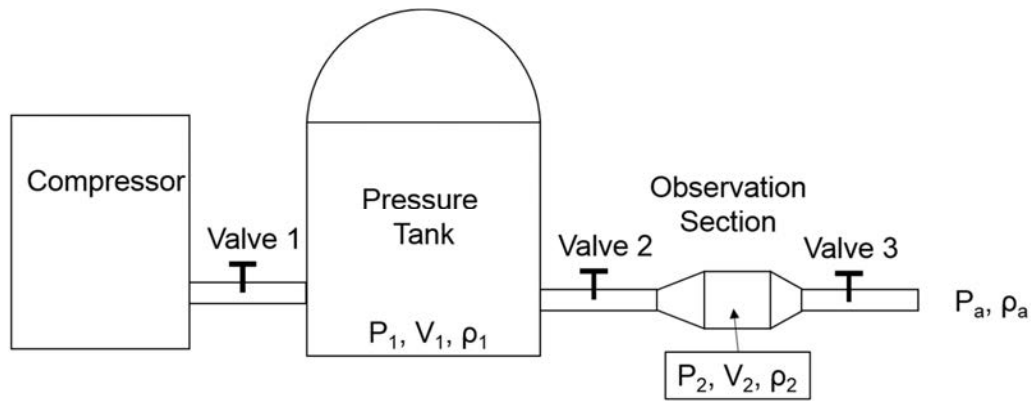


Figure 3.1 Principle schematic of high pressure wind tunnel.

As Fig. 3.1 shows, a compressor, a tank, and an observation chamber/section are connected in series. P_1 is the pressure of tank, V_1 is the tank's volume, ρ_1 is the air density in tank. A_1 is the section area of valve 2, A_2 is the section area of observation chamber, A_a is the section area of valve 3, P_2 is the pressure of chamber, V_2 is the volume of chamber, ρ_2 is the air density of chamber, P_a is atmospheric pressure, ρ_a is the atmospheric density, U_2 is the air's velocity in chamber.

Firstly, the valve 2 close, the valve 1 open, when the tank's pressure reach the experimental pressure, close the valve 1, and open the valve 2, open valve 3 in K% (partly open), as shows in Fig. 3.2. In this way the tank pressure will decrease and the observation chamber pressure will increase first and then decrease, the velocity in chamber will be constant in a period and then decrease, as shows in Fig. 3.3 and Fig. 3.4.

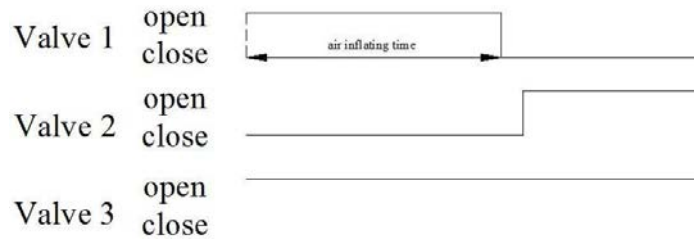


Figure 3.2 Statuses of valves (Operating sequence).

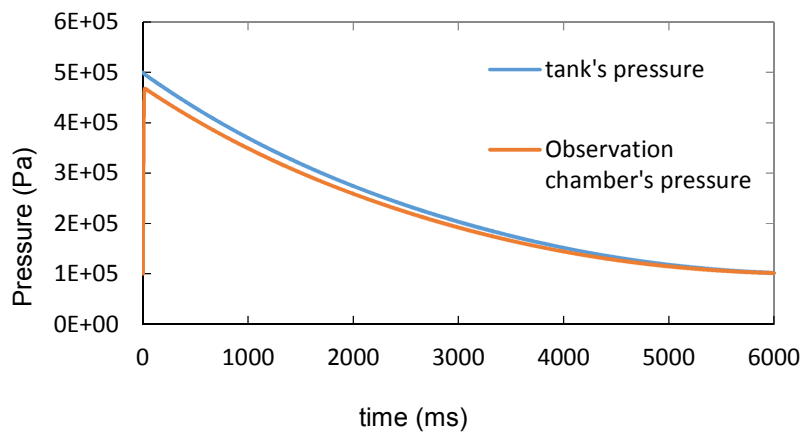


Figure 3.3 Pressure variations of tank and observation chamber.

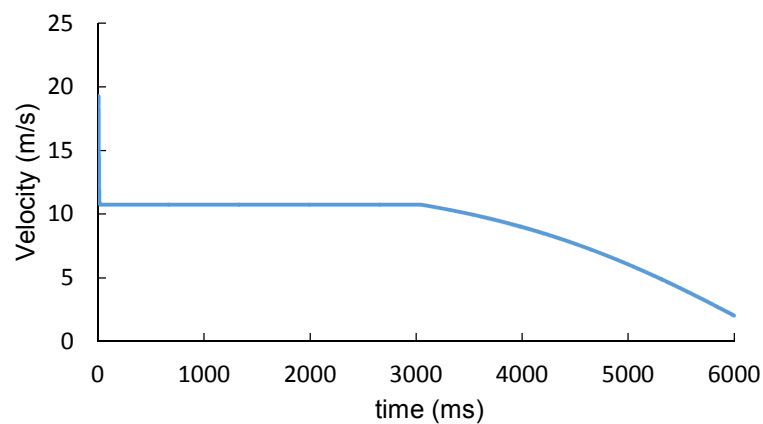


Figure 3.4 Velocity in observation chamber.

It is assume that the temperature is constant, the air density changes by the pressure, and the air flow conform to flow conservation, the correlations between pressure, mass, density, flow-rate, velocity are expressed by the Eqs. 3.1~3.12.

$$\rho_1 = \frac{P_1}{R_g T} \quad (3.1)$$

$$m_1 = \rho_1 V_1 \quad (3.2)$$

$$\rho_2 = \frac{P_2}{R_g T} \quad (3.3)$$

$$m_2 = \rho_2 V_2 \quad (3.4)$$

$$Q_1 = \begin{cases} A_1 \sqrt{\frac{2\gamma}{\gamma-1} P_1 \rho_1 \left[\left(\frac{P_a}{P_1} \right)^{\frac{2}{\gamma}} - \left(\frac{P_a}{P_1} \right)^{\frac{\gamma+1}{\gamma}} \right]} & \frac{P_2}{P_1} > \frac{P_*}{P_1} = 0.528 \quad (3.5) \\ \left(\frac{2}{\gamma+1} \right)^{\frac{\gamma+1}{2(\gamma-1)}} A_1 \sqrt{\gamma \rho_1 P_1} & \frac{P_2}{P_1} \leq \frac{P_*}{P_1} = 0.528 \quad (3.6) \end{cases}$$

$$U_1 = \begin{cases} \sqrt{\frac{2\gamma}{\gamma-1} \frac{P_1}{\rho_1} \left[1 - \left(\frac{P_2}{P_1} \right)^{\frac{\gamma-1}{\gamma}} \right]} & \frac{P_2}{P_1} > \frac{P_*}{P_1} \quad (3.7) \\ \sqrt{\frac{2\gamma}{\gamma+1} \frac{P_1}{\rho_1}} & \frac{P_2}{P_1} \leq \frac{P_*}{P_1} \quad (3.8) \end{cases}$$

$$Q_2 = \begin{cases} A_a \sqrt{\frac{2\gamma}{\gamma-1} P_2 \rho_2 \left[\left(\frac{P_a}{P_2} \right)^{\frac{2}{\gamma}} - \left(\frac{P_a}{P_2} \right)^{\frac{\gamma+1}{\gamma}} \right]} & \frac{P_a}{P_2} > \frac{P'_*}{P_2} = 0.528 \quad (3.9) \\ \left(\frac{2}{\gamma+1} \right)^{\frac{\gamma+1}{2(\gamma-1)}} A_1 \sqrt{\gamma \rho_2 P_2} & \frac{P_a}{P_2} \leq \frac{P'_*}{P_2} = 0.528 \quad (3.10) \end{cases}$$

$$U_2 = \begin{cases} \sqrt{\frac{2\gamma}{\gamma-1} \frac{P_2}{\rho_2} \left[1 - \left(\frac{P_a}{P_2} \right)^{\frac{\gamma-1}{\gamma}} \right]} & \frac{P_a}{P_2} > \frac{P'_*}{P_2} \quad (3.11) \\ \sqrt{\frac{2\gamma}{\gamma+1} \frac{P_2}{\rho_2}} & \frac{P_a}{P_2} \leq \frac{P'_*}{P_2} \quad (3.12) \end{cases}$$

where, Q_1 is the air flowrate valve 2, U_1 is the valve 1's air velocity, Q_2 is the valve 2's air

flowrate, U_a is the valve 3's air velocity. γ is isentropic exponent. According to the continuity of the flow, the flow-rates in the two sections should be same, as shown in Eqs. 3.13 and 3.14,

$$A_1 U_1 = A_2 U_2, \text{ or } U_2 = \frac{A_1 U_1}{A_2}, \quad (3.13)$$

$$A_2 U_2 = A_a U_a, \text{ or } U_a = \frac{A_2 U_2}{A_a}. \quad (3.14)$$

In theory, these two kinds of calculation can get same result, but in actually, there is some tiny difference, so average them in Eq. 3.15,

$$U_2 = \left(\frac{A_2 v_2}{A_a} + \frac{A_1 v_1}{A_a} \right) / 2, \quad (3.15)$$

In a short enough time Δt , the weight of air flow from tank to chamber is Δm_1 (Eq. 3.16),

$$\Delta m_1 = Q_1 \Delta t. \quad (3.16)$$

So after Δt , the air's weight in tank becomes m_{11} , the density becomes ρ_{11} and pressure in tank becomes P_{11} , the correlations are shown in Eq. 3.17~3.19. Because the temperature's influence is insignificant, the influence of the change of temperature is ignored.

$$m_{11} = m_1 - \Delta m_1 \quad (3.17)$$

$$\rho_{11} = \frac{m_{11}}{V_1} \quad (3.18)$$

$$P_{11} = \frac{m_{11}}{m_1} P_1 \quad (3.19)$$

During Δt period, air flow into chamber, the weight and pressure in chamber increase, air became into ambience though the valve 3. The air's weight in chamber is m_{21} , the density of air in observation chamber is ρ_{21} , the air weight lost from valve 3 is Δm_{21} (Eqs.3.20~3.23),

$$m_{21} = m_2 + \Delta m_1 - \Delta m_{21} \quad (3.20)$$

$$\Delta m_{21} = Q_2 \Delta t \quad (3.21)$$

$$\rho_{21} = \frac{m_{21}}{V_2} \quad (3.22)$$

$$P_{21} = \frac{m_{21}}{m_2} P_2 \quad (3.23)$$

The calculations are taken by iterating, the following is an example.

The initial $P_1=1.0\text{MPa}$, $V_1=0.4\text{m}^3$, valve 2 and valve 3 are DN40 ball valves, the $P_a=P_2=0.1\text{MPa}$, the all opening area of valve's sectional $A_1=0.001257\text{m}^2$, the chamber's sectional area $A_2=0.015\text{m}^2$, $V_2=0.00225\text{m}^3$, $R_g=287\text{J}/(\text{kg} \cdot \text{K})$, $T=300\text{K}$, R_g is gas constant. If $\Delta t = 0.001\text{s}$, $A_2 = 0.46A_1$ (valve 2 46% open), using these equations to do iteration, we can get the curves as shows

in Fig. 3.5 and Fig. 3.6.

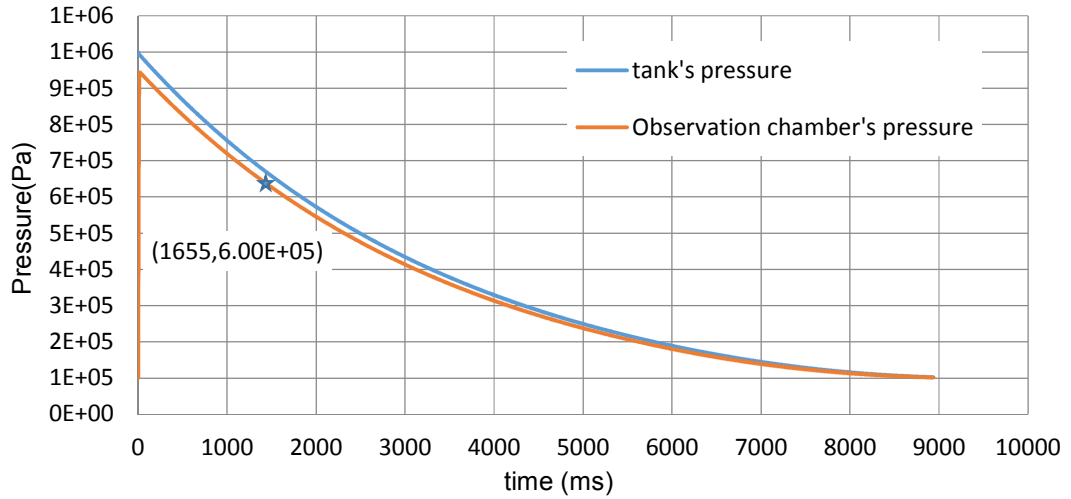


Figure 3.5 Pressure of tank and observation chamber.

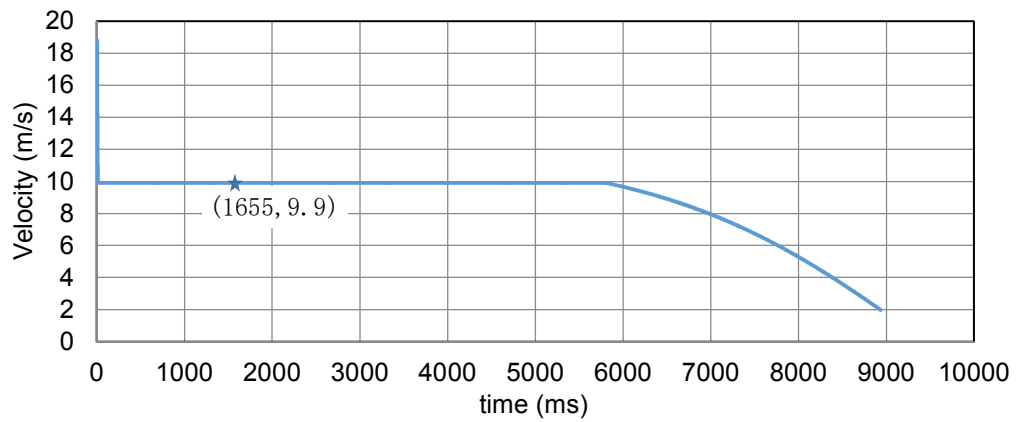


Figure 3.6 Air velocity in observation chamber.

The five-pointed star in Fig. 3.5 and Fig. 3.6 is the experiment point for gasoline spray experiment. In this case, the time point is 1.655s, so the valve 2 should be opened rapidly.

3.2 Structure of High Pressure Wind Tunnel

First of all, the high pressure wind tunnel is a pressure vessel, the components should own the ability of enduring the high pressure, and the sealing property should be guaranteed. Hence, the material choice and their strength calculation are important during the design.

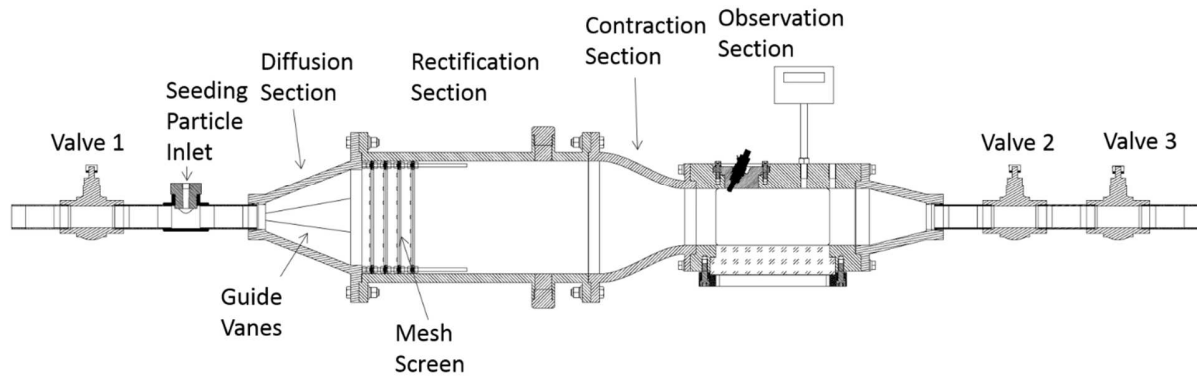


Figure 3.7 Pressure wind tunnel structure.

The inner structures of the pressure wind tunnel are almost similar to the atmospheric wind tunnel, the main parts include the valves, diffusion section, rectification section, contraction section, and observation section, as shown in Fig. 3.7. DN 40 ball valves were chosen in the pressure wind tunnel, because the ball valve can be opened quickly and the opening section was decided by the flow-rate, which have been discussed in the last section. The seeding particle inlet was reserved by a T-joint connecting the valve 1 and diffusion section. The four guide vanes were set in the diffusion section, the air could be guided to the bigger area before arriving the mesh screens. The five pieces mesh screens were fixed by screws attaching in the end of the diffusion section. The rectification section sizes were 400mm in length and 200mm × 200mm for inner section. The maximum section of the contraction section was 200mm × 200mm, which equals the area of the inner diffusion section, while the minimum section was 100mm × 100mm, which equals the area of the inner section of the observation section. This design is for purpose of controlling the turbulence caused by the rough wall in a minimum value. The curve of the contraction section wall is similar to that in the atmospheric wind tunnel, it is also based on Eq. 2.5. The observation section will be introduce in the following section. There were two ball valves (DN40) in the end of the tunnel. Two ball valves in series could provide flexible control methods during the experiments. The thinnest plate which is used for making the window tunnel was 16mm, the stress analysis will be implemented in section 3.1.4.

There were three windows in the observation section, they were in the both sides and bottom with some sizes, as shown in Fig. 3.8. The window was designed to embossment, which can keep the inner face in same plane of the inner section of observation section and is convenient to be assembled. The windows are made by Pyrex, which can endure high pressure or temperature. An adaptor which can provide 25° with vertical for injector was fixed in the upper wall of the observation section. The bottom surface of the adaptor was evened up with the inner upper surface of the observation section. The pressure sensor was linked with the observation section by the hole in the upper surface, and the hot-wire probe was inset into the section using the sealing grand joint.

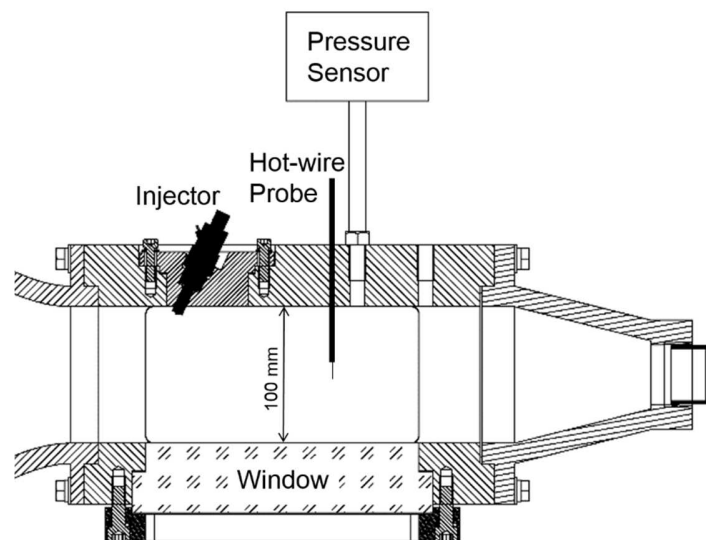


Figure 3.8 Observation section structure.

The high speed photography and PIV measurement have been taken in the pressure wind tunnel. The devices and methods were almost same to that in the atmospheric experiments, as shown in Figs. 3.9 and 3.10. In the pressure wind tunnel experiments, the one of method difference from the atmospheric experiment was the control system. In the atmospheric experiments, the status of the cross-flow velocity and the ambient pressure could keep in a constant value, in that case, it was available to trigger the injection and experimental system during in the constant status. However, in the pressure wind tunnel experiments, the experiment was triggered at a time, which was long and stable enough for injection. This time should meets two conditions, velocity and ambient pressure. The control system will be introduced in section 3.1.3. The tracer particle (seeding particle) feeding was a difficult problem in the pressure wind tunnel. Many tentative experiments

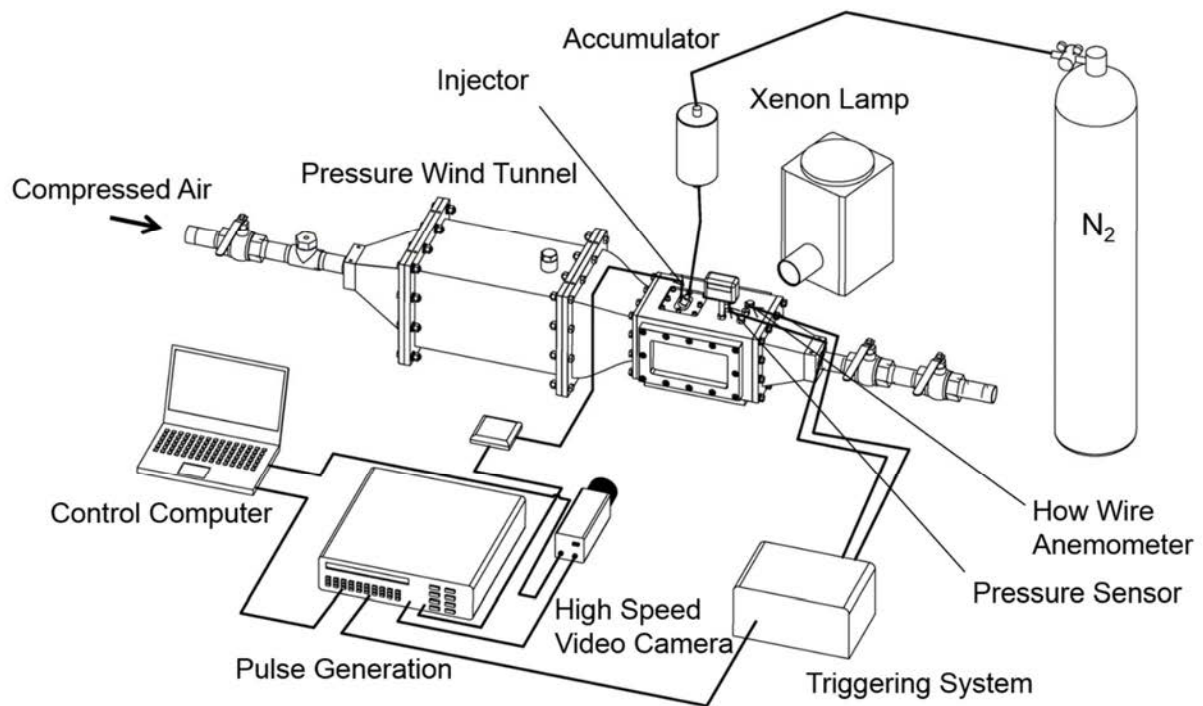


Figure 3.9 Experimental setup for high speed photography.

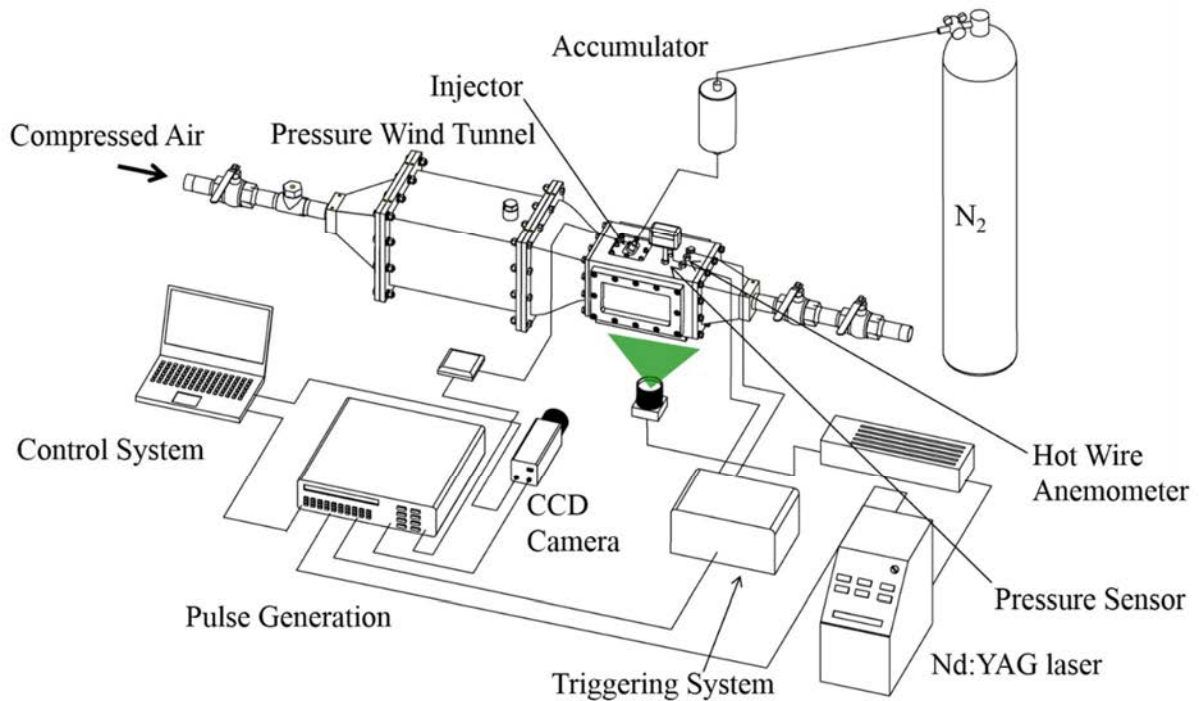


Figure 3.10 Experimental setup for PIV measurement.

have been taken, such as using liquid droplets, solid particles as the tracer particle, using mechanical device to feed particles, and using high pressure device to feed particles. So far, MgO was the most suitable particles in the pressure wind tunnel experiments. The disadvantage of the using MgO was the cleaning problem in the window tunnel, because the particles could attach in the wall and mesh screens after using.

3.3 Control System

The triggering in the pressure wind tunnel experiments was decided by meeting two conditions, pressure and velocity in observation section. The pressure and velocity were always changing in this section, the experimental conditions should meet them simultaneously.

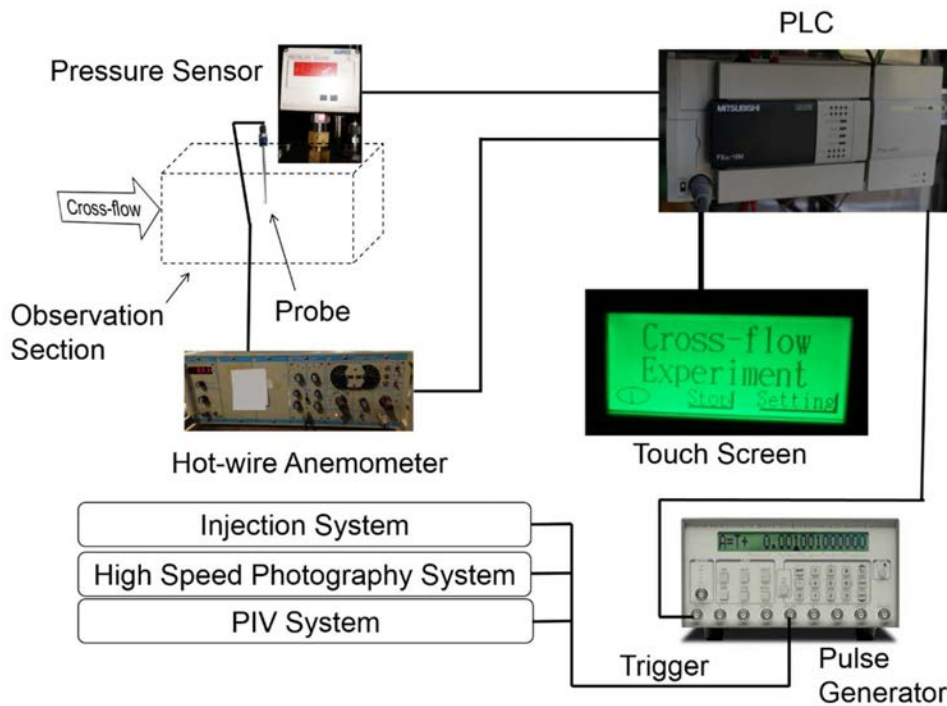


Figure 3.11 Control system for pressure wind tunnel.

A pressure sensor (NSK, GC75243) and hot-wire anemometer (KANOMAX 0251R-T5) were employed to detect the pressure and velocity signals simultaneously, as shown in Fig. 3.11. The response times of them are short than 1 ms. Those signals of the pressure sensor and anemometer were converted from analog signals to digital signals by an analog-digital conversion (Mitsubishi, FX3U-4AD). The converted signals were transferred into a Programmable Logic Controller (PLC, Mitsubishi, FX3U-16MR/ES), which could compare with the two signals by wrote program. The interface of the system was a touch screen (Mitsubishi, GT1020-LWD), by which the pressure and velocity value could be displayed and operations could be taken. An experimental system for this experiments was written into the touch screen. When the pressure and velocity signals met the experimental conditions, a pulse would be outputted by PLC. This pulse was received by the pulse generator, which can control the injection system, high speed video camera, and PIV system. In this experiment, the velocity measurement was intrusive way, because the difficulty of the velocity

measurement in a sealed space with changing pressure.

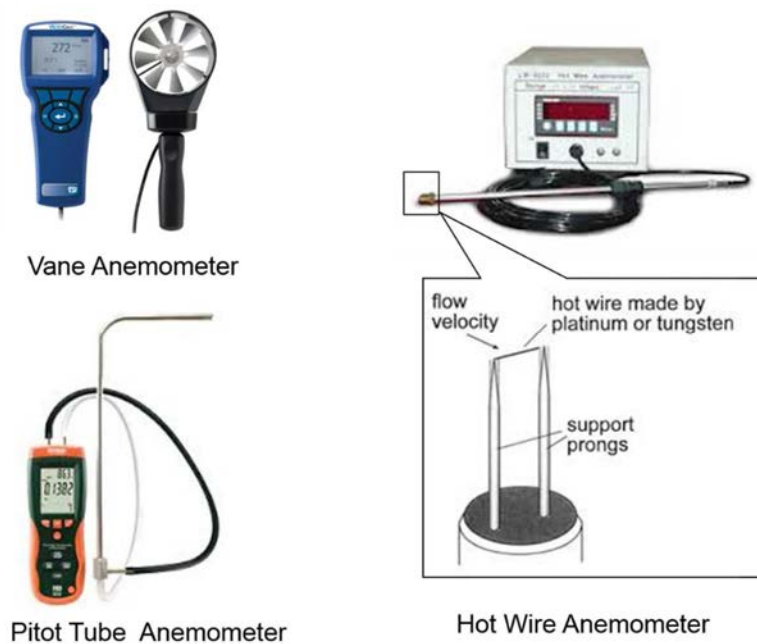


Figure 3.12 Typical Anemometers.

The mechanical anemometer, such as cup anemometer, vane anemometer, is widely used in the natural wind measurement. The principle of them is that the velocity is converted into electric signals using a set of cup or vane. The field of the air flow would be influenced very much after measuring. The Pitot tube anemometer is a very useful anemometer, which is popular in aviation. The Pitot tube anemometer is a pressure-based velocity measuring device (Klopfenstein, 1998). Hot-wire anemometer is a thermal anemometer, which can measure the velocity and turbulence. The hot-wire anemometer measures the rate at which heat is transferred from a heated filament to the flow in which it is immersed (Motallebi, 1993; Bhatia et al., 1982; Andrews et al., 1972). The structure of the probe is shown in Fig. 3.12, the hotwire is made by platinum or tungsten.

In this investigation, the vane anemometer was excluded due to the effects on the air flow and the structure of the probe part. The Pitot tube anemometer could be used in the measurement, however, the transferring process was very complex due to the unsteady pressure, and the response time was also a problem. Hot-wire anemometer was used in this study, the response time of the anemometer is smaller than 1 ms, and the results were not influenced by the pressure changing. The testing point for the hot-wire probe was set on the middle of the observation chamber, because in that area the velocity is more stable and the turbulence is the smallest.

3.4 Performance Evaluation

The safety of the pressure vessel is one of most important specifications. The stress calculation and checking should be taken before and after design. In this section, the safety checking is discussed by strength checking, analyzing the stress distribution, and confirming critical stress.

The whole plate area of the rectification section of the pressure wind tunnel was the biggest in the all part of the components. If the maximum stress was in the safe range of the material which was chosen, there is no risk for other part using the same thickness.

The strength checking includes bending stress checking, shearing stress checking, and tensile stress checking.

First is bending stress checking. The chamber is a rectangular container with square cross section. The inner pressure (P_2) is higher than external pressure (P_a), as shown in Fig. 3.13 (a). The stress analysis belongs to the plate model. Plates A or B (see Fig. 3.13 (b) can be simplified as rectangular plate with all edges built in, and its stress can also be simplified uniformly loaded plates with small deflection(Timoshenko and Woinowsky-Krieger, 1959).

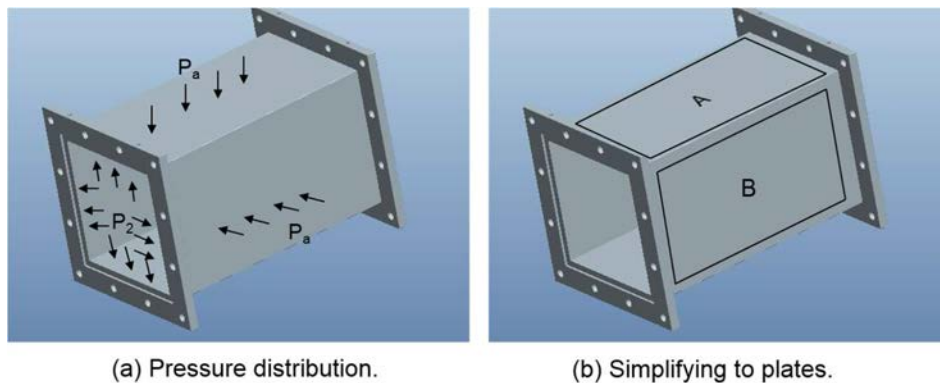


Figure 3.13 Pressure distribution and simplifying of rectification section.

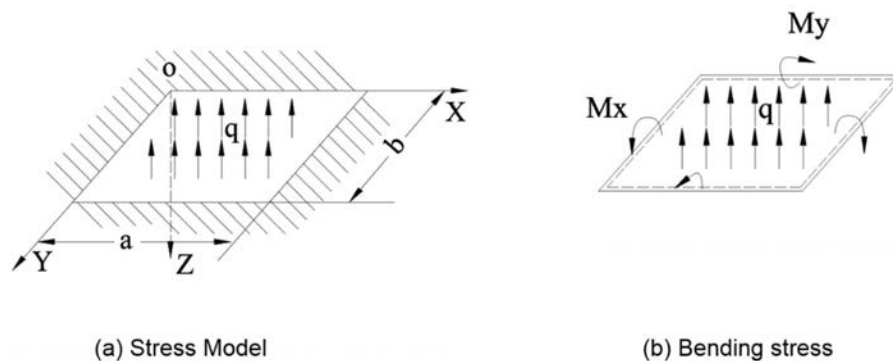


Figure 3.14 Bending stress producing and distribution.

The differential equation of the deflection surface is

$$\frac{\partial^4 \omega}{\partial x^4} + 2 \frac{\partial^4 \omega}{\partial x^2 \partial y^2} + \frac{\partial^4 \omega}{\partial y^4} = \frac{q}{D_{fr}}, \quad (3.24)$$

in which, ω is the deflection, D_{fr} is flexural rigidity ($D_{fr} = \frac{Eh^3}{12(1-\mu_p^2)}$), h_p —thickness of plate, q is the difference between P_2 and P_a .

$$M_x = -D_{fr} \left(\frac{\partial^2 \omega}{\partial x^2} + \mu_p \frac{\partial^2 \omega}{\partial y^2} \right), \quad (3.25)$$

$$M_y = -D_{fr} \left(\frac{\partial^2 \omega}{\partial y^2} + \mu_p \frac{\partial^2 \omega}{\partial x^2} \right), \quad (3.26)$$

where, μ_p is Poisson ratio.

The stress of X and Y ,

$$\sigma_x = \frac{12M_x z}{h_p^3}, \quad (3.27)$$

$$\sigma_y = \frac{12M_y z}{h_p^3}, \quad (3.28)$$

The maximum stress,

$$(\sigma_x)_{max} = \frac{6M_x}{h_p^2}, \quad (3.29)$$

$$(\sigma_y)_{max} = \frac{6M_y}{h_p^2}, \quad (3.30)$$

Deflections and bending moments in a uniformly loaded rectangular plate with built-in:

$$\omega_{(x=\frac{a}{2}, y=\frac{b}{2})} = \alpha \frac{qa^4}{D_{fr}}, \quad (3.31)$$

$$(M_x)_{(x=0, y=\frac{b}{2})} = \beta qa^2, \quad (3.32)$$

$$(M_y)_{(x=\frac{a}{2}, y=0)} = \beta_1 qa^2, \quad (3.33)$$

$$(M_x)_{(x=\frac{a}{2}, y=\frac{b}{2})} = \gamma qa^2, \quad (3.34)$$

$$(M_y)_{(x=\frac{a}{2}, y=\frac{b}{2})} = \gamma_1 qa^2, \quad (3.35)$$

In this study, $\mu_p = 0.3, b=0.4\text{m}, a= 0.17\text{m}, \frac{b}{a} = 2.35, q = 0.7\text{MPa}, h = 15\text{mm} = 0.015\text{m} D = 6.0 \times 10^4$. And $\alpha = -0.00254, \beta = 0.0829, \beta_1 = 0.0571, \gamma = -0.0412, \gamma_1 = -0.0158$ (The parameters were provided by Timoshenko and Woinowsky-Krieger (1959)). The results are,

$$\omega_{(x=\frac{a}{2}, y=\frac{b}{2})} = -0.047\text{mm},$$

$$(M_x)_{(x=0, y=\frac{b}{2})} = \beta qa^2 = 2.3 \times 10^3 \text{N} \cdot \text{m},$$

$$(M_y)_{(x=\frac{a}{2},y=0)} = \beta_1 qa^2 = 1.6 \times 10^3 \text{ N} \cdot \text{m},$$

$$(M_x)_{(x=\frac{a}{2},y=\frac{b}{2})} = \gamma qa^2 = -1.15 \times 10^2 \text{ N} \cdot \text{m},$$

$$(M_y)_{(x=\frac{a}{2},y=\frac{b}{2})} = \gamma_1 qa^2 = -4.42 \times 10^2 \text{ N} \cdot \text{m},$$

If the thickness of the rectification wall is assumed as $h_p = 10\text{mm}$, corresponding stress could be calculated as follows,

$$(\sigma_x)_{(x=0,y=\frac{b}{2})_{\max}} = 62.0\text{MPa} < [\sigma] = 82\sim 143\text{MPa},$$

$$(\sigma_y)_{(x=\frac{a}{2},y=0)_{\max}} = 42.6\text{MPa} < [\sigma],$$

$$(\sigma_x)_{(x=\frac{a}{2},y=\frac{b}{2})_{\max}} = 31\text{MPa} < [\sigma],$$

$$(\sigma_y)_{(x=\frac{a}{2},y=\frac{b}{2})_{\max}} = 12\text{MPa} < [\sigma],$$

The minimum thickness (The allowable stress uses SPV355)

$$(\sigma_x)_{(x=0,y=\frac{b}{2})_{\max}} = [\sigma] = 355\text{MPa},$$

$$h_{p\min} = \sqrt{\frac{6M_x}{[\sigma]}} = 6.3\text{mm},$$

$$\text{SF} = \frac{15}{6.3} = 2.4,$$

If material is SUS304,

$$\sigma_s = 205\text{MPa},$$

$$h_{p\min} = \sqrt{\frac{6M_x}{[\sigma]}} = 8.2\text{mm},$$

$$\text{SF} = \frac{15}{8.2} = 1.8,$$

The shearing stress often happen in the shearing section in the edge of the plate, as S_A shown in Fig. 3.15.

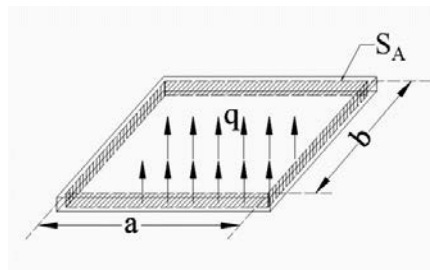


Figure 3.15 Shearing stress section in plate.

In a uniformly loaded rectangular plate with built-in, The loaded equilibrium is the shearing stress, as the Fig. 3.15 shows, the shearing section area is S_A , the loaded area is S ($S = a \times b$),

$$F = q \times S, \quad (3.36)$$

$$\tau = \frac{F}{S_A}, \quad (3.37)$$

where, $S_A = 1.14 \times 10^{-2} \text{m}^2$; $q = 0.7 \text{MPa}$; $S = 0.068 \text{m}^2$.

The shearing stress is, $\tau = \frac{F}{S_A} = 4.175 \times 10^6 \text{Pa} = 4.175 \text{MPa} < [\tau] = 70 \text{MPa}$, $[\tau]$ is allowable shearing stress of SPV355.

Tensile stress analysis should be checking in long-edge direction and short-edge direction, because the stress sections are different in this two conditions.

The tensile stress along the long-edge direction is caused by the force of F , as shown in Fig 3.16. The tensile stress section is shown in Fig. 3.16(b).

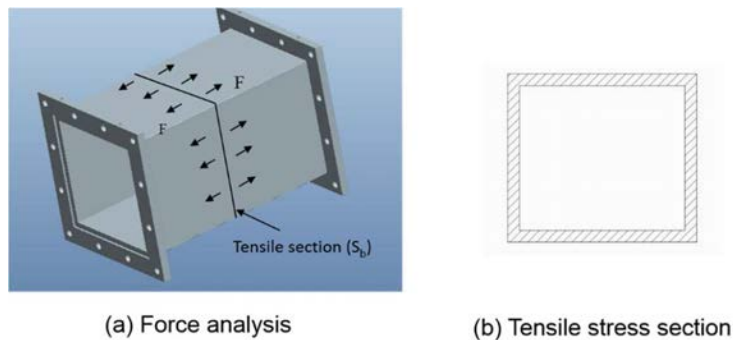


Figure 3.16 Tensile analysis in length direction.

The tensile stress can be obtained by Eqs. 3.38 and 3.39,

$$F = q \times S, \quad (3.38)$$

$$\sigma = \frac{F}{S_B}, \quad (3.39)$$

where, S is the inner section area of the rectification section. $S_B = 4(a + h) \times h = 8.2 \times 10^{-3} \text{m}^2$, $q = 0.7 \text{MPa}$, $S = 0.17 \times 0.17 = 0.0289 \text{m}^2$, the tensile stress in long-edge direction is,

$$\sigma = \frac{F}{S_b} = 2.47 \times 10^6 \text{Pa} = 2.47 \text{MPa} < [\sigma] = 176 \text{MPa}.$$

The tensile stress along short-edge direction is calculated in the following, as the Fig. 3.17 and Eqs. 3.40 and 3.41.

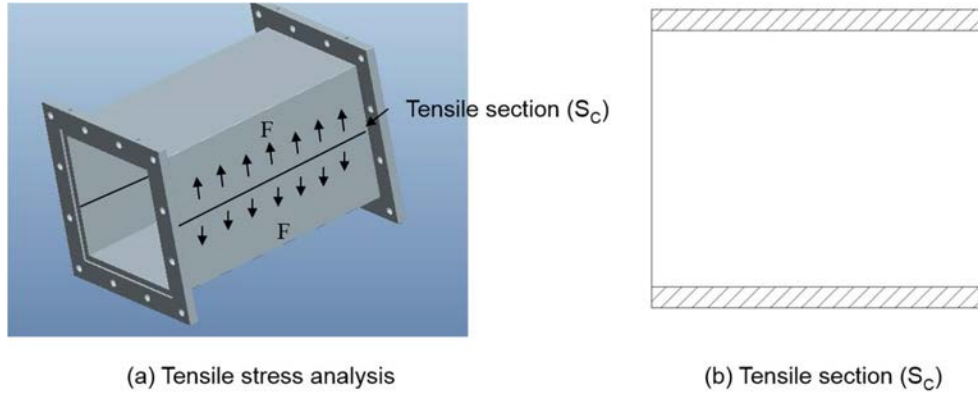


Figure 3.17 Tensile analysis in width direction.

$$F = q \times S, \tag{3.40}$$

$$\sigma = \frac{F}{S_c}, \tag{3.41}$$

The results are shown, $S_c = 2b \times h = 8 \times 10^{-3} \text{m}^2$, $q = 0.7 \text{MPa}$, $S = 0.17 \times 0.4 = 0.068 \text{m}^2$, $\sigma = \frac{F}{S_b} = 5.94 \times 10^6 \text{Pa} = 5.94 \text{MPa} < [\sigma] = 176 \text{MPa}$.

The strengths with different material in rectification section are different, the table 3.1 shows the results of the calculation. The SM490 was chosen as the wind-tunnel material, because of its outstanding welding property. For the safety, the minimum thickness of the wind tunnel was chosen as 16 mm.

Table 3.1 Minimum thickness of plates in different material ($h=h_p$).

	C	Si	Mn	P	S	Yield Stress (N/mm ²)	Allowable Stress (N/mm ²) T=300K	Minimum thickness of plate (mm)
SPV355	≤0.2%	≤0.55%	≤1.6%	≤0.03%	≤0.03%	520	130	9.26
SM490A	$h < 50 \text{mm}$, ≤0.20 $> 50 \sim 200 \text{mm}$, ≤0.22	≤0.55%	≤1.6%	≤0.035%	≤0.035%	490	122	9.56
SM490B	$h < 50 \text{mm}$, ≤0.18 $> 50 \sim 200 \text{mm}$, ≤0.20	≤0.55%	≤1.6%	≤0.035%	≤0.035%	490	122	9.56
SM490C	$h < 100 \text{mm}$, ≤0.18	≤0.55%	≤1.6%	≤0.035%	≤0.035%	490	122	9.56
SS400						400	100	10.6
JIS G3115, JIS G3106, JIS G3101						Pressure Vessel Design Manual		

The window thickness was confirmed by Oken Corp (2013)., the window was fixed as shown in Fig. 3.18.

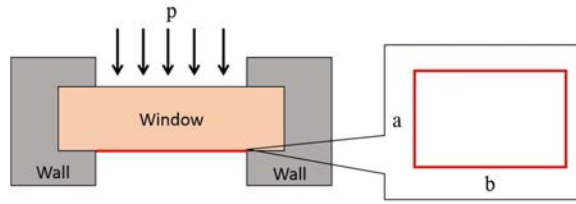


Figure 3.18 Force analysis of window.

The thickness can be obtained by Eqs. 3.42,

$$h_w = 1.23b \left(\frac{p}{F_a(1+c^2)} \right)^{\frac{1}{2}}, \quad (3.42)$$

where, h_w is the window thickness, b is the long-edge of the force area, $c=b/a$. Pyrex was chosen as the window material, and the minimum thickness is 13 mm. In the real design, 15mm was chosen as the fixing thickness, the total thickness is 30 mm.

The calculations of the stress analysis were taken using the simplified models, for the further checking, the simulation was implement by the analysis software. From the Figs. 3.19 and 3.20, the maximum stresses are below the allowable stress. It is indicated that the pressure wind tunnel is safe.

The real tests have been taken by feeding liquid (ethenol) in to the sealed tunnel (close valve 1 and 2). There is no leakage or breaking in all components under the pressure of 1 MPa.

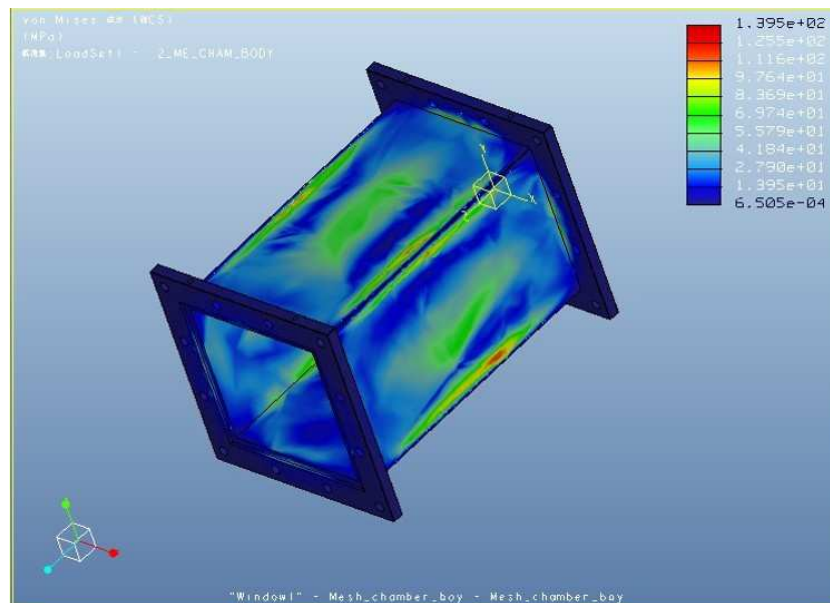


Figure 3.19 Stress analysis of rectification section.

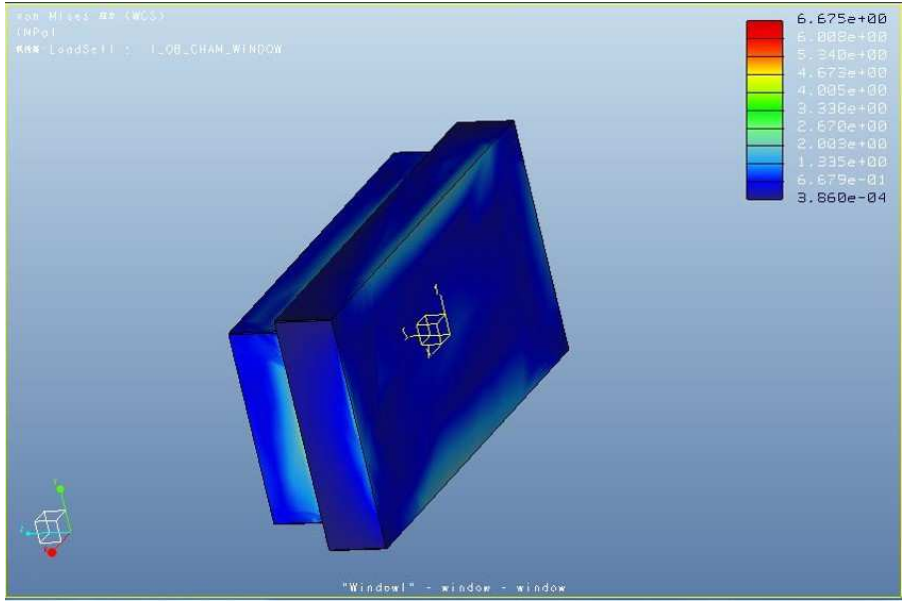


Figure 3.20 Stress analysis of window in observation section.

The velocity distribution has been measured in the vertical plane under ambient pressure of 0.4 MPa by PIV, the results are shown in Fig. 3.21. It is difficult to test the velocities using the hot-wire anemometer, because the probe positions should be set in various points in the sealed pressure field. The PIV measurement is a non-intrusive method and the whole plane velocity distribution can be obtained. The velocities near the wall are small, and the velocities become uniform from approximately $y=15$ mm to $y=85$ mm. The velocity distributions are uniform from the observations.

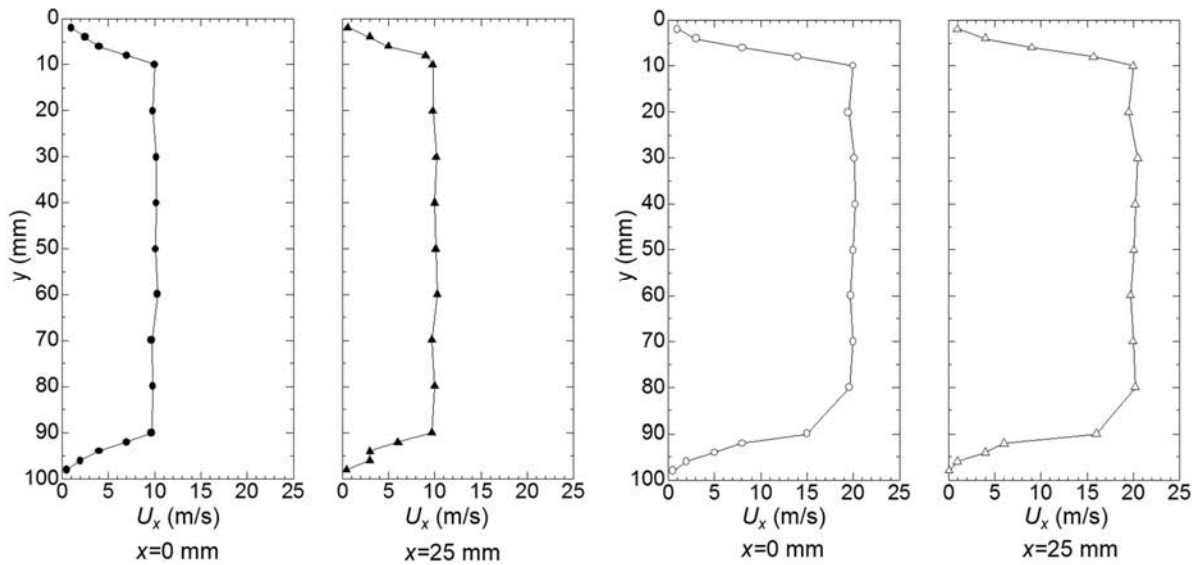


Figure 3.21 Velocity distributions in observation section ($P_2 = 0.4$ MPa).

3.5 Summary

The experimental methods, which were used in this study, were illuminated with the backgrounds and principles. There are two main kinds of experiments in this study, the experiments based on the atmospheric wind tunnel and the experimental based on the pressure wind tunnel. The high pressure ambient experiments are used to simulate the condition of the surrounding of the stratified charge combustion model.

The high speed video photography, the PIV technique, and laser diffraction sizing method were used in the high pressure ambient experiments as the atmospheric ambient experiments.

The high pressure wind tunnel was designed for the high pressure ambient cross-flow experiments. This wind tunnel was different from the circuit wind tunnel. The pressure wind tunnel was implemented using the velocity and back pressure, which were provided by the pressure gas and throttling of pressure wind tunnel. Before the design, the confirmatory calculations were made. The parts of the pressure wind tunnel were presented, such as sizes, material, and assembly. The pressure wind tunnel was a pressure vessel in some sense. The design and strength checking were followed the standards of the pressure vessel design manual. Before the experiments, the safety checking was implemented by filling liquid into pressure wind tunnel and pressurizing the liquid. The control system was designed for triggering the experiments. A pressure sensor and a hot-wire anemometer with high sensitivity were used for acquiring the pressure and velocity signals, a PLC was employed as the control unit, and a touch screen was used as a man-machine interface.

Chapter 4 Global Structure of Spray in Cross-Flow

From Chapter 4 to Chapter 7, the experimental measurements and discussions under atmospheric condition will be taken. The discussions include spray profiles, penetrations, velocity distributions, and droplet size distributions.

4.1 Structure of Spray Injected by VCO Nozzle

In the direct injection engines, the sac hole nozzle and VCO nozzle are used as that in diesel engine. The sac hole nozzle has an additional volume below the needle seat while the holes are sealed by needle blocking in the VCO nozzle as shown in Fig. 4.1. A very symmetric overall spray is produced by the sac hole nozzle, because the increased distance between needle seat and injection hole, an eccentricity or radial motion of the needle tip does not influence the mass flow through the different holes. Whereas, the large liquid volume between needle seat and combustion chamber causes problems in terms of increased hydrocarbon emissions. The VCO nozzle is superior to the sac hole nozzle in avoiding the fuel entering the cylinder after the end of injection. That fuel is usually not well dispersed and increases soot emissions (Baumgarten, 2006). However, the structure of spray injected by the VCO nozzle is usually asymmetric, especially in a low pressure ambient.

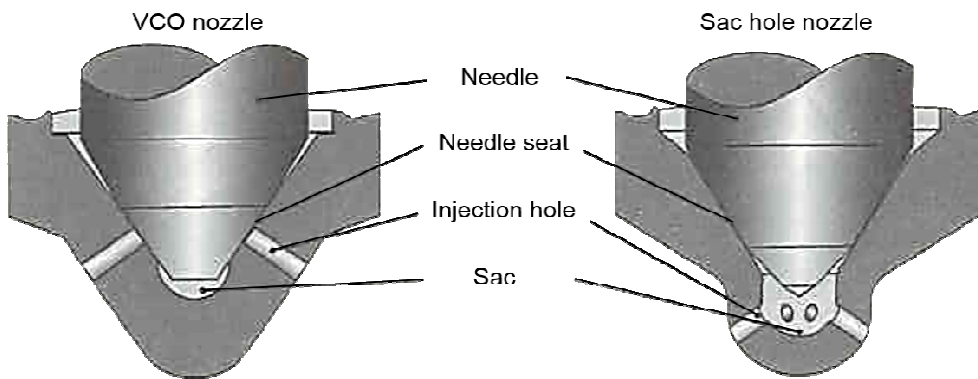


Figure 4.1 Nozzle structures of VCO and sac hole nozzles

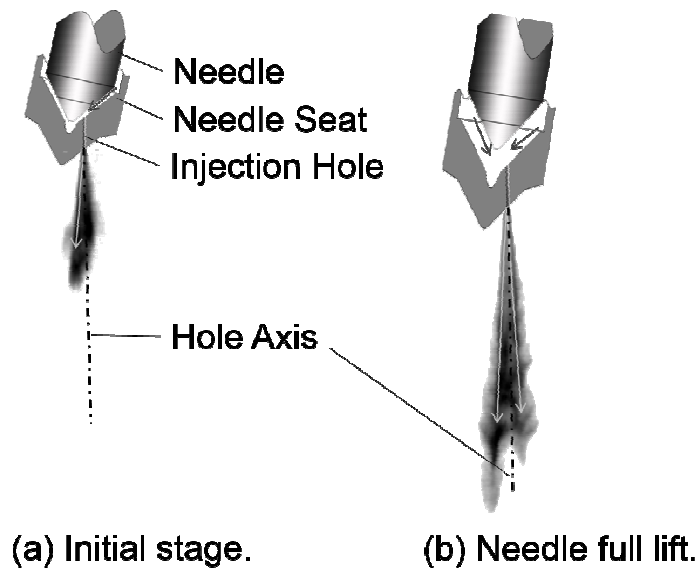


Figure 4.2 Formation of spray by VCO nozzle

At the beginning (0 to 1.5 ms ASOI) of injection, there were two asymmetric spray tips due to the structure of the VCO type nozzle (Kong et al, 2012). The pressure from the right upstream of the nozzle hole is stronger than that in left part in the initial stage, then the spray tip direction would be tilted to the left side, and the direction of the main spray is not vertical, see Fig. 4.2(a). With the needle lifting, the left side pressure increases, which causes the second tip in the right part of spray. When the needle is fully lifted, the flow in the upstream of the nozzle hole becomes symmetric, and the spray tip direction coincides with the nozzle hole axis, as shown in Fig. 4.2(b). In the measurements of penetration, the longest tip is used as the tip in the left part of spray.

4.2 Temporal Profiles in Atmospheric Ambient

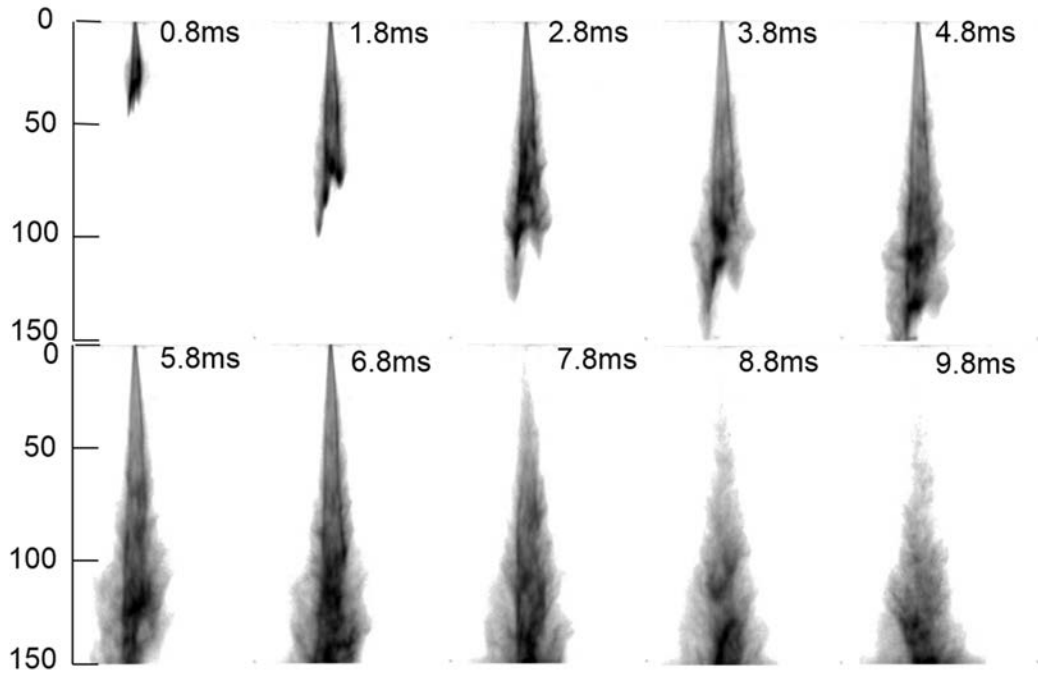


Figure 4.3 Temporal variations of spray profile ($P_{inj} = 10$ MPa, $U_x = 0$ m/s, and time is ASOI)

Without cross-flow, the profiles of spray varying with time are shown in Fig. 4.3, in which the injection pressure is 10 MPa. The spray injected by a VCO type nozzle owns two tips with different velocities, and hence the spray is not symmetrical (Rottenkolber et al, 2002; Nouri and Whitelaw, 2001; Hiroyasu and Arai, 1990). Since the start of injection did not coincide with that of the photographing, the firstly recorded spray in each team is different while the shoot interval is 1ms. At the beginning of the spray the droplets do not break, and the penetration distance is a linear function of time. The starting time of spray can be estimated from the first and the second penetration coordinates based on the linear relation. It is seen that the spray develops along the injection direction till impinged on the bottom of the observation chamber around 3.8 ms; while the fuel injection is finished at 7 ms (between two photographs of 6.8 ms and 7.8 ms).

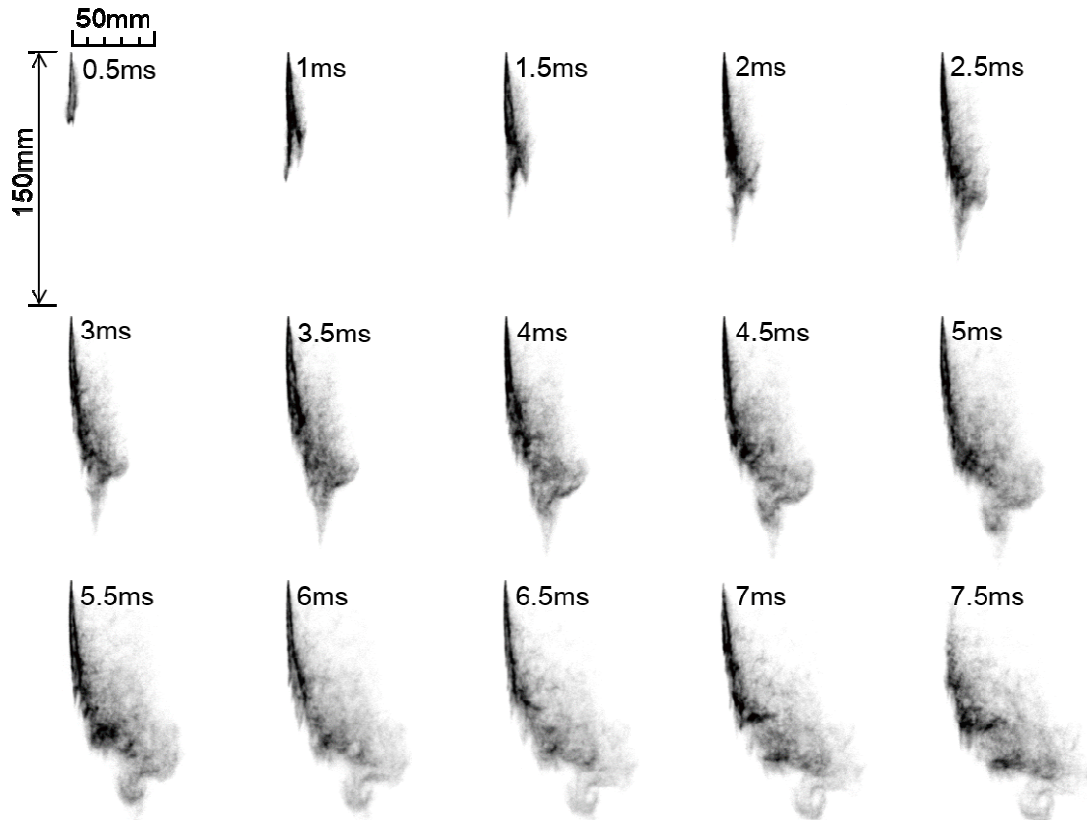


Figure 4.4 Temporal variations of spray profile in the cross-flow ($P_{inj} = 10$ MPa, $U_x = 9.2$ m/s and time is ASOI)

The variations of spray including profiles and penetration distances in vertical directions were investigated through photographs recorded by a high speed video camera; the velocity of the cross-flow varied from 0 to 9.2 m/s.

Figure 4.4 shows the profiles of the spray in the cross-flow of 9.2 m/s and the injection pressure of 10 MPa. At the beginning (0 to 1.5 ms ASOI), there were two asymmetric spray tips due to the structure of the VCO type nozzle (Baumgarten, 2006; Kong and Bae, 2012). The pressure from the right upstream of the nozzle hole is stronger in the initial stage, then the spray tip direction would be tilted to the left side. The spray was almost perpendicular to the direction of the cross-flow during this period, owing to the high vertical momentum. Thereafter, the spray was bended gradually especially the lower part of the spray, however, the dense droplets remained around the upstream of the cross-flow. In the vicinity of the nozzle, though the spray retained its initial shape due to the large momentum flux and the low velocity of the cross-flow (close to or within the boundary layer), tiny droplets with low momentum were observed to be blown away downstream.

Around the spray tip, the droplets were significantly affected by the cross-flow, as indicated by the large bending along the cross-flow and expansion in volume of the spray.

4.3 Spray Penetration and Empirical Correlations

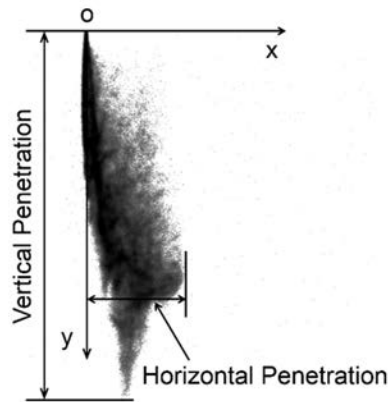


Figure 4.5 Definitions of vertical penetration and horizontal penetration.

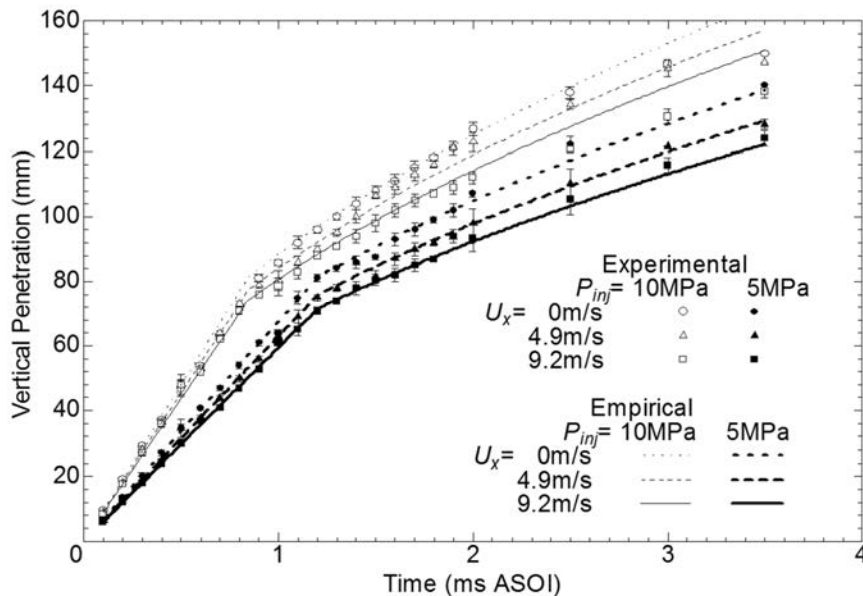


Figure 4.6 Vertical penetration under various injection pressure and cross-flow velocities.

On the basis of the spray profiles, the vertical and horizontal penetration distances, as defined in Fig. 4.5, were examined. The horizontal distance between the nozzle hole axis and the farthest place that the droplets reached along the cross-flow direction was defined as the horizontal penetration. The measured vertical penetration was plotted against time in Fig. 4.6. At the injection pressure of 5 MPa, without cross-flow, the vertical penetration linearly increased until approximate 1.2 ms ASOI, which was around the breakup time. Thereafter the penetration followed a linear variation with the square root of injection time, however, the slope decreased. In

cross-flow condition, the vertical penetration varies with time linearly before the breakup time and the slope decreased slightly with the increase of velocity of cross-flow. Then the vertical penetration became almost proportional to the square root of the injection time. In addition, the penetration decreased with an increase of the cross-flow velocity. At the injection pressure of 10 MPa, the same variations of penetration tendencies were obtained though there were some deviations after 2.5 ms ASOI. Owing to higher injection pressure, i.e., higher momentum of spray in vertical direction, the penetration increased and the time for breakup decreased to around 0.9 ms ASOI, resulting in a higher slope than that of the 5 MPa before breakup. However, after breakup, the variation of vertical penetration became slower with time. This phenomenon may be attributed to the formation of plenty of tiny droplets that were easier to be blown away by the cross-flow.

To obtain a more fundamental understanding, the empirical correlations were discussed, as the lines shown in Fig. 4.6; the vertical penetration curves of 5 MPa were plotted by fine lines while the curves of 10 MPa were plotted by thick lines, furthermore the curves on velocities of 0, 4.9 and 9.2 m/s were plotted by solid lines, dashed lines and dotted lines respectively. The vertical penetration without cross-flow was firstly examined, which followed the similar equation as Hiroyasu and Arai (1990), as shown in Eqs. 4.1-4.3,

$$t_{break} = \frac{24.85 \rho_l d}{(\rho_g \Delta p)^{\frac{1}{2}}} \quad (4.1)$$

$$t < t_{break}: \quad S = 0.41 \left(\frac{2\Delta p}{\rho_l} \right)^{\frac{1}{2}} t \quad (4.2)$$

$$t > t_{break}: \quad S = 4.3 \left(\frac{\Delta p}{\rho_g} \right)^{\frac{1}{4}} d^{\frac{1}{2}} t^{\frac{1}{2}}, \quad (4.3)$$

where S is the vertical penetration, $\Delta P = P_{inj} - P_a$ is the pressure drop across the nozzle, ρ_g and ρ_l are the gas and liquid densities, d is the nozzle diameter and t is the time ASOI. Owing to different experimental conditions as well as fuel type, the modified coefficients were deduced through the following. As is known, the penetration S can be divided into two stages. The first stage refers to the procedure from the beginning of injection ($t = 0$ ms ASOI, needle begins to open) to the moment when the liquid jet begins to disintegrate ($t = t_{break}$, Eq. 4.1), in which S linearly grows with time (Eq. 4.2). During the second stage ($t > t_{break}$), the spray tip consists of droplets, and

the penetration S becomes a function of $t^{\frac{1}{2}}$, as shown in Eq. 4.3. The penetration should be continuous during the whole procedure, hence the coefficients in Eqs. 4.1-4.3 can be obtained because Eq. 4.2 is equivalent to Eq. 4.3 at the moment of breakup. The correlations for the vertical penetrations without cross-flow were depicted using solid lines in Fig. 4.6; they are in good agreement with the experimental measurements.

Next, the empirical correlation under the cross-flow condition was analyzed. Hiroyasu and Nishida (1989) investigated the penetration of multi-hole spray in a swirling combustion chamber, while in the following investigation, Yoshizaki et al. (1996) addressed the important role of the ratio of cross-flow velocity to initial injection velocity and introduced an empirical equation. In the current study, effects of cross-flow on single spray is similar to those mentioned above, and the correlations can be given by Eq. 4.4,

$$\frac{S_s}{S} = \left(1 + \frac{U_x}{U_I}\right)^{-1}, \quad (4.4)$$

where S_s is vertical penetration with cross-flow, U_x and U_I are the cross-flow velocity and the initial injection velocity, respectively. It is seen that the vertical penetration in the cross-flow will decrease with increasing the velocity of the cross-flow while increase with an increase of the injection pressure (an increase of injection velocity). In addition, the results based on Eq. 4.4 are shown in Fig. 4.6 (dashed and dotted lines), which agree well with the experimental data.

Next, the horizontal penetrations in Fig. 4.7 are discussed. Without cross-flow, the horizontal penetration is mainly influenced by the diffusion of the spray and correlated to the spray angle. The penetration increases when the injection pressure is increased from 5 (solid circle) to 10 MPa (open circle). With cross-flow, at low injection pressure of 5 MPa, the horizontal penetration (solid triangle) almost linearly increases with time, and the slope increases with increasing the velocity of cross-flow. Since a cross-flow with higher velocity can provide the droplets more kinetic energy to increase the horizontal momentum, resulting in longer displacement. The similar phenomenon is observed in 10 MPa, however, the slopes are larger than those in 5 MPa injection pressure. Owing to the enhancement of the atomization under the increased injection pressure, more tiny droplets which are easy to be transported by the cross-flow are formed. The velocities of cross-

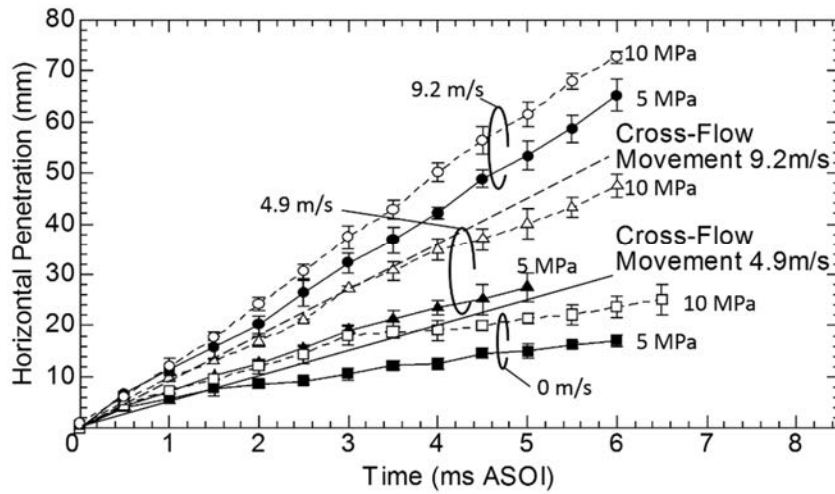


Figure 4.7 Horizontal penetration under various injection pressure and cross-flow velocities.

flow 4.9 and 9.2 m/s are also plotted in Fig. 4.7. In the same cross-flow velocity, the slopes of both conditions are larger than the value of the cross-flow, namely the droplet velocity is higher than cross-flow in horizontal direction. It is easy to understand this phenomenon near the nozzle, because of the spray angle which can cause the high component of the droplet velocity in horizontal direction. Some complex movement may have happened in the downstream, and lead to the droplets moving faster than cross-flow. This movement will be investigated in the future work.

Next, profiles of spray in upstream side defined in Fig. 4.8 (b) are investigated, in order to describe the extent of bending of the spray in the cross-flow. The profile is similar to the penetration height which defined by No (2011). To clearly distinguish the spray and background, a threshold of 20 out of 255 (8%) was adopted in the HSV images. The measured profiles against the horizontal distance (OX) were plotted in Fig. 4.8 (a). With low velocity of 4.9 m/s, the profiles are almost the same for the two cases of 5 and 10 MPa injection pressure; the profiles are weakly bended at the lower part of the spray (around the tip of the spray). In the cross-flow velocity of 9.2 m/s, the spray starts to be effectively imposed from the middle region, and the spray around the bottom of the observation chamber is blown far downstream. There are small differences between 5 and 10 MPa, illustrating that the effect of cross-flow is more significant than the injection pressure.

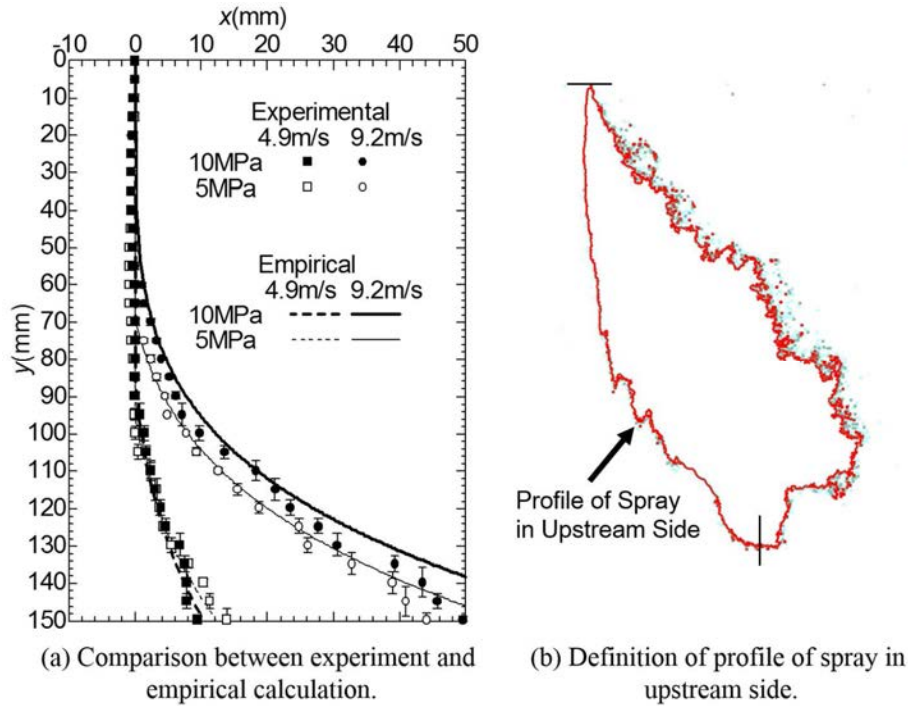


Figure 4.8 Profile of spray in upstream side ($P_{inj}= 10 \text{ MPa}$, $U_x= 9.2 \text{ m/s}$ and $t= 7 \text{ ms ASOI}$)

In the investigation of No (2011), it is concluded that the penetration height of a liquid jet in a cross-flow is a function of the liquid to air momentum flux ratio and normalized downstream distance from the injector. In this study, to intuitively express the profile of the spray, an empirical correlation was derived, as shown in Eq. 4.5,

$$\frac{y}{d} = 1.9q^{0.45} \left(\frac{x}{d}\right)^{0.23}, \quad (4.5)$$

where q is liquid to air momentum flux ratio ($\rho_l U_l^2 / \rho_g U_x^2$). By using the least square method, one equation is obtained in each experimental result of one condition, and the final coefficients are mean values of the coefficients of all equations of different conditions. On the basis of Eq. 4.5, curves of profiles of spray in upstream side were obtained, as the solid and broken curves shown in Fig. 4.8. It is found that both curves obtained by Eq. 4.5 are in good agreement with the present experimental data.

4.4 Tomographic Profiles of Spray

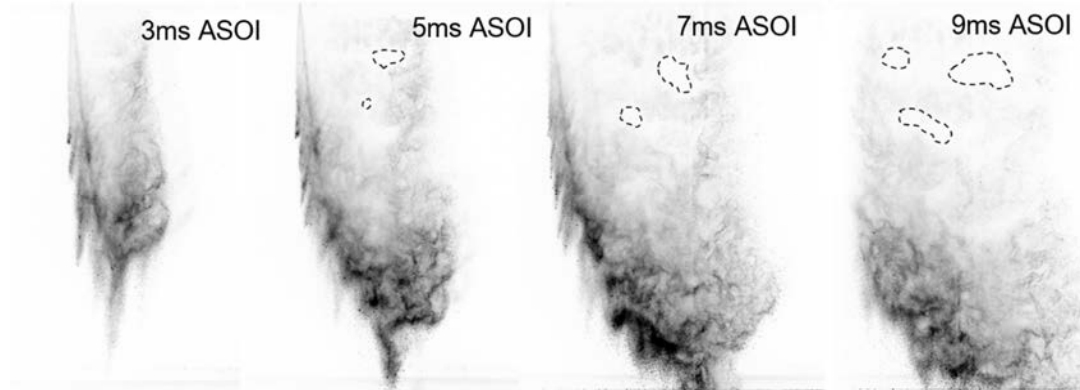


Figure 4.9 Tomographic images of the spray ($P_{inj} = 10$ MPa, $U_x = 9.2$ m/s), indicated by dashed lines are the areas where few droplets are found.

Figure 4.9 shows the tomographic images of the spray under cross-flow of 9.2 m/s and the injection pressure of 10 MPa. They were taken by a CCD camera (laser sheet as the light source) in the plane of XOY at different times after injection. In the upper region of the spray, some tiny droplets were distributed along the direction of cross-flow, while they were not observed in HSV observation owing to insufficient intensity of the illuminator. Moreover, the droplets distribution presented inhomogeneous, which can be observed from some blank areas shown by dashed line circles in Fig. 4.9. This phenomenon indicates that the motion of droplets in this region is not limited in the plane of XOY (a three-dimensional model). In Fig. 4.9, there were several tips in the upstream profile of the spray due to the special structure of the spray injected by the VCO nozzle, and tiny droplets with low vertical momentum lost their vertical momentum and were entrained into the cross-flow, while those with large diameter (higher vertical momentum) remained in the tips.

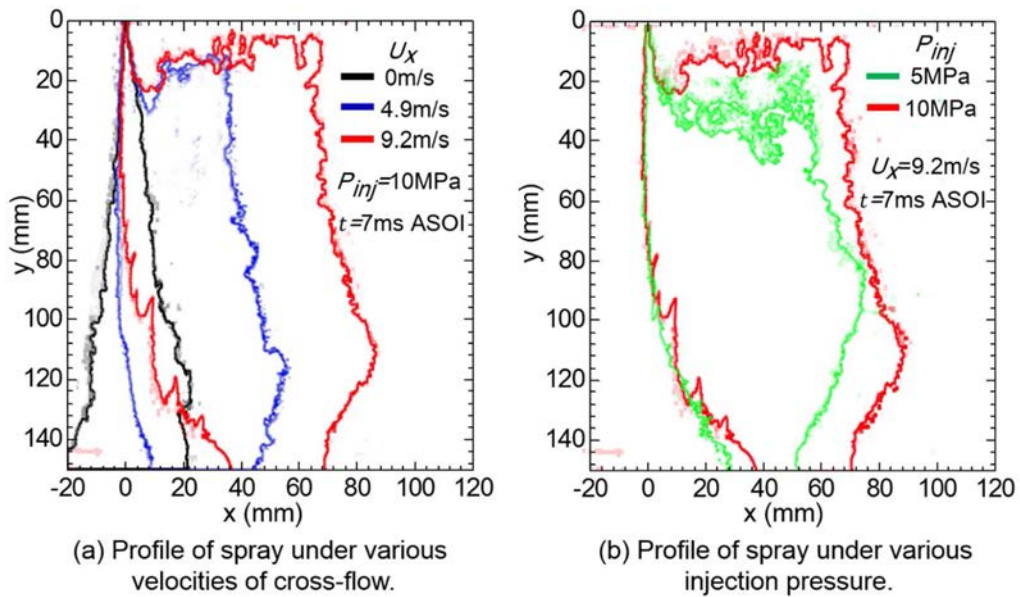


Figure 4.10 Profiles of spray ($t = 7$ ms ASOI).

To get a direct image of the effects of cross-flow and the injection pressure, outlines of the tomographic images of the spray in XOY plane are discussed in Fig. 4.10. To obtain the appropriate outline, a threshold of 13 out of 255 (5%) is adopted for image process. The left figure shows the outlines of the spray under various cross-flow velocities, in which the injection pressure is 10 MPa and the injection time is 7 ms ASOI. It is seen that without cross-flow, the profile of the spray is distributed almost symmetric, however, with cross-flow of 4.9 m/s, the spray shifts along the direction of cross-flow especially the downstream outline which expands even close to the vicinity of the nozzle. By increasing the velocity, the spray is further shifted downstream and expanded. While with the same velocity of cross-flow (9.2 m/s), the upstream outlines are almost the same for 5 and 10 MPa injection pressures, however, owing to the enhancement of atomization at higher pressure, the downstream outline of 10 MPa expands further, as the right image in Fig. 4.10 shown. The results again show the more important role of the cross-flow than the injection pressure on the spray.

The profiles of spray in various times plotted by colored curves are listed in Figs. 4.11. It is observed that the profiles of spray in no cross-flow condition own two tips and the velocities of droplets in the bottom edge of the spray decrease gradually according to the distance of edge points, as the ΔS_0 shows in the Fig. 4.11(a). The profiles of spray present asymmetrical structures below

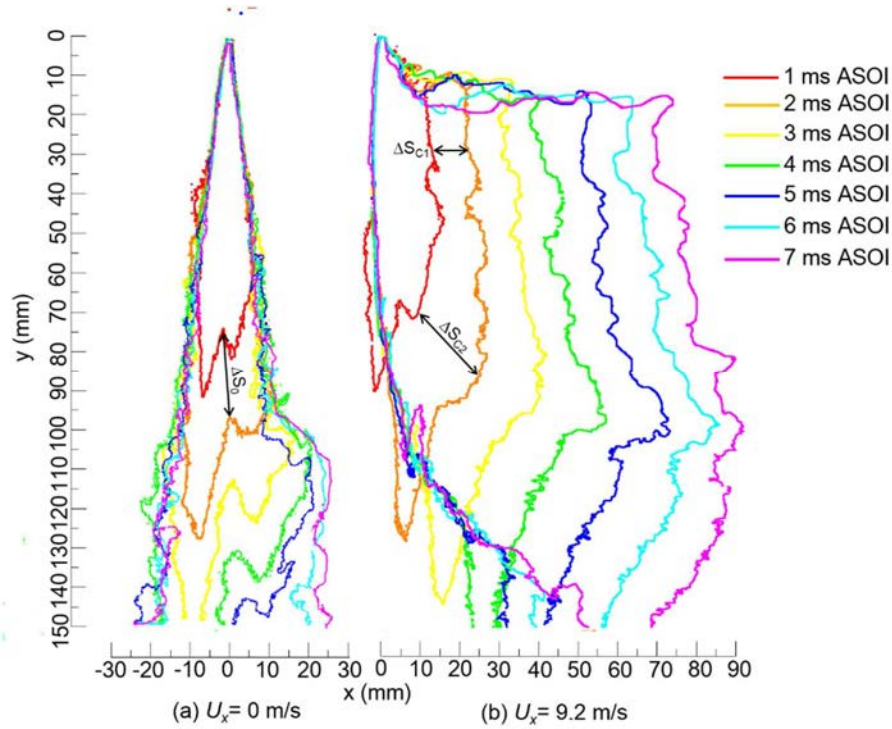


Figure 4.11 Temporal variations of spray profile in horizontal plane ($P_{inj} = 10$ MPa, $U_x = 0, 9.2$ m/s).

$y = 100$ mm due to the two tips structure of spray injected by VCO nozzle (Baumgarten, 2006; Kong and Bae, 2012). The different points in the edge of spray in cross-flow field move different distances in 1 ms, as the ΔS_{C1} and ΔS_{C2} shows in the Fig. 4.11(b). The distances (ΔS_{C1}) of the droplets in the upper part of the spray seem to be uniform, however, those (ΔS_{C2}) in the lower part of the spray decrease against time. In the upper part of the spray, the droplets are in the breaking stage, in which the atomization is inadequate and the most droplets own strong vertical momentum, hence only the tiny droplets, which lose their vertical momentum easily, are entrained into the cross-flow. The profiles of spray in the upper part are not simply offset curves, it means those tiny droplets entrained by the cross-flow moves not only along the direction of the cross-flow. In the lower part of the spray, the atomization enhances, the droplets vertical momentum decreases gradually against time and the horizontal momentum can be provided from the cross-flow. Hence the movement of droplets is the composition of the horizontal and vertical. This reason can result in the two tips structure of spray becomes inconspicuous, and the movements in the leeward (ΔS_{C2}) decrease.

4.5 Summary

The spray injected by the VCO nozzle is asymmetrical in the low ambient pressure due to the special structure of the nozzle.

At constant injection pressure, the vertical penetration decreases with an increase of the cross-flow velocity, however, such tendency becomes weak when the injection pressure is increased. With increasing the velocity of the cross-flow and the injection pressure, the horizontal penetration increases. The droplets distribution presents inhomogeneous in the upper region of spray; the horizontal component of spray velocity shows large fluctuations, especially in the downstream region of the spray where the value even exceeds the cross-flow velocity.

Chapter 5 Cross-Sectional Structure of Spray

In this part, the characteristics of the cross-sectional structures of spray in the cross-flow field will be discussed. It is not enough to understand the information such as the images, intensity of the spray in vertical is employed to analyze the features of the spray. The droplets in the spray under the cross-flow present complex movements, to further understand the structures and movements of the spray, the horizontal plane images were taken by the high speed video camera and a continuous wave laser (sheet).

5.1 Three Dimensional Spray Structure

The spray was perpendicularly injected into the uniform cross-flow field, the characteristics of the spray in the vertical plane have been discussed in previous study, such as the penetrations, profiles and droplets velocity distributions. Some phenomena like the non-uniform distributions of droplets in the upper area of spray (from approximate $y=0$ to $y=75$ mm) are very difficult to be explained by the observations of vertical planes. To clarify the features of interactions between cross-flow and spray, the horizontal plane pictures were taken by a HSV camera and a continuous wave laser sheet. Figure 5.1 shows the images of spray in horizontal planes, in the upper area of spray the images were taken in 10 mm intervals while in the lower part of spray (from approximate $y=75$ to $y=150$ mm) the images were taken in 25 mm intervals, and the red dot shows the location of nozzle hole. The images were cut out from the row pictures and deleted the background by using a threshold of 8 out of 255 (3%). The tiny droplets whose intensity is closed to the background were ignored in Fig. 5.1. In that way the main structures of the spray are clearly represented in these images. Because the spray movement in upper area changed more seriously than that in lower area, the detailed images in the complex area are needed. The droplets in the upper area of spray present asymmetrical distributions, as shown in the planes of $y= 25$ and 50 mm, and the change happened between $y= 30$ and 40 mm planes. The reasons of the movements in the upper of spray will be discussed in the part of 5.4. This phenomenon becomes faint in the lower part of spray like the planes of $y= 75$, 100 and 125 mm, in which the droplets distribute symmetrically. Like the vertical plane images, the strong movements are also observed in the horizontal plane images, the droplets in the spray move not only vertically and horizontally, but vertically with the cross-flow.

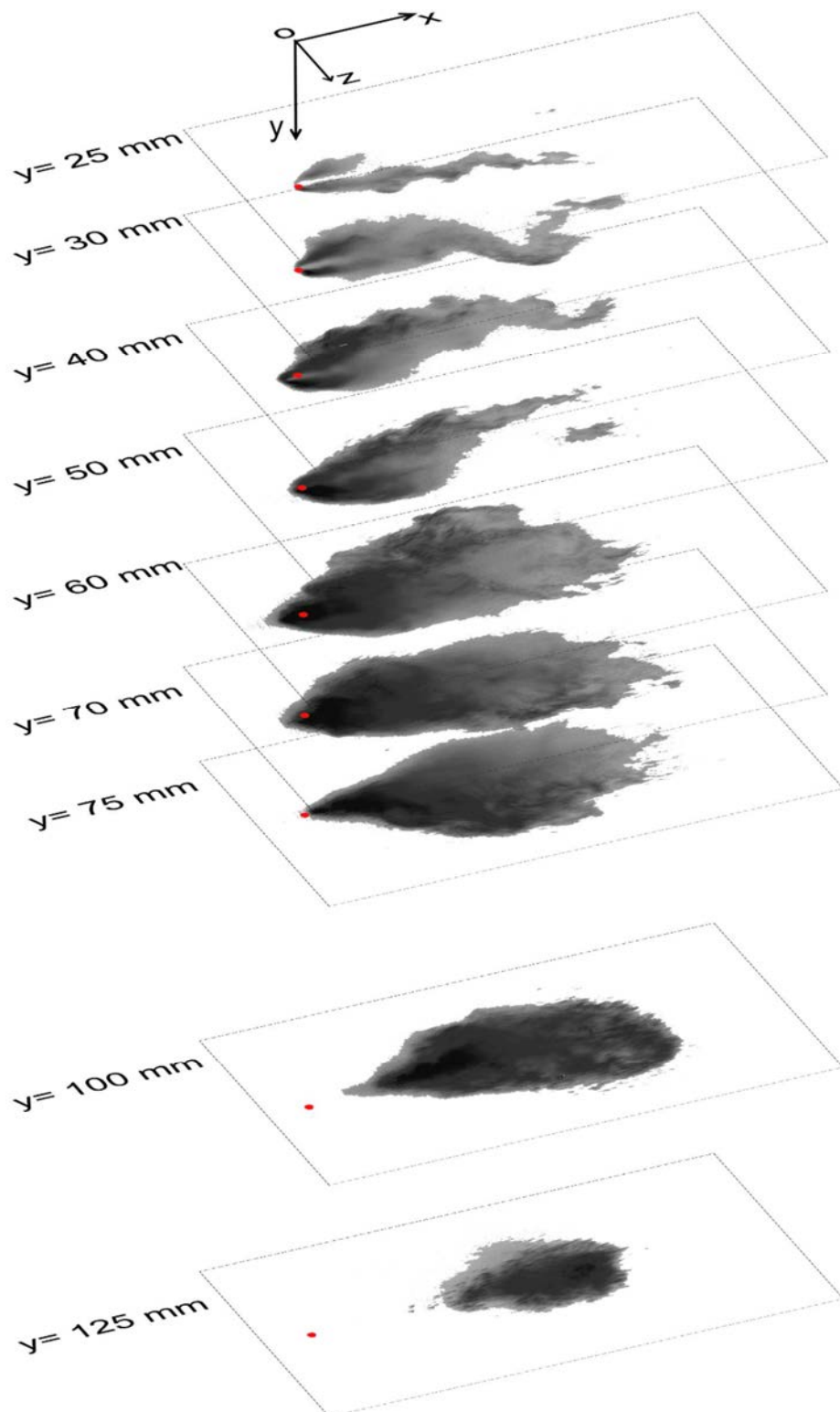


Figure 5.1 Three dimensional expression of spray structure
 (Red dot is the location of nozzle hole, $P_{inj} = 10\text{MPa}$, $U_x = 9.2\text{m/s}$, 5 ms ASOI).

The spray profiles in the upper were diffused in the upstream of the cross-flow according to the change of the nozzle hole position, then the profiles in the lower part of the spray were out and away from the nozzle hole position. It indicate that the profile of the spray in the upper part did not change, because the momentum of the droplets was very large, the droplets were in the stage of breaking, the cross-flow effect on that part was very limited. With the increase in the vertical direction, the droplets were breakup into more small droplets, moreover the droplets were decelerated by the ambient air friction, the cross-flow effect on the lower part of spray began to work. It cause the more obviously bended profile in the lower part of the spray.

5.2 Spray Details in Cross-sectional Planes

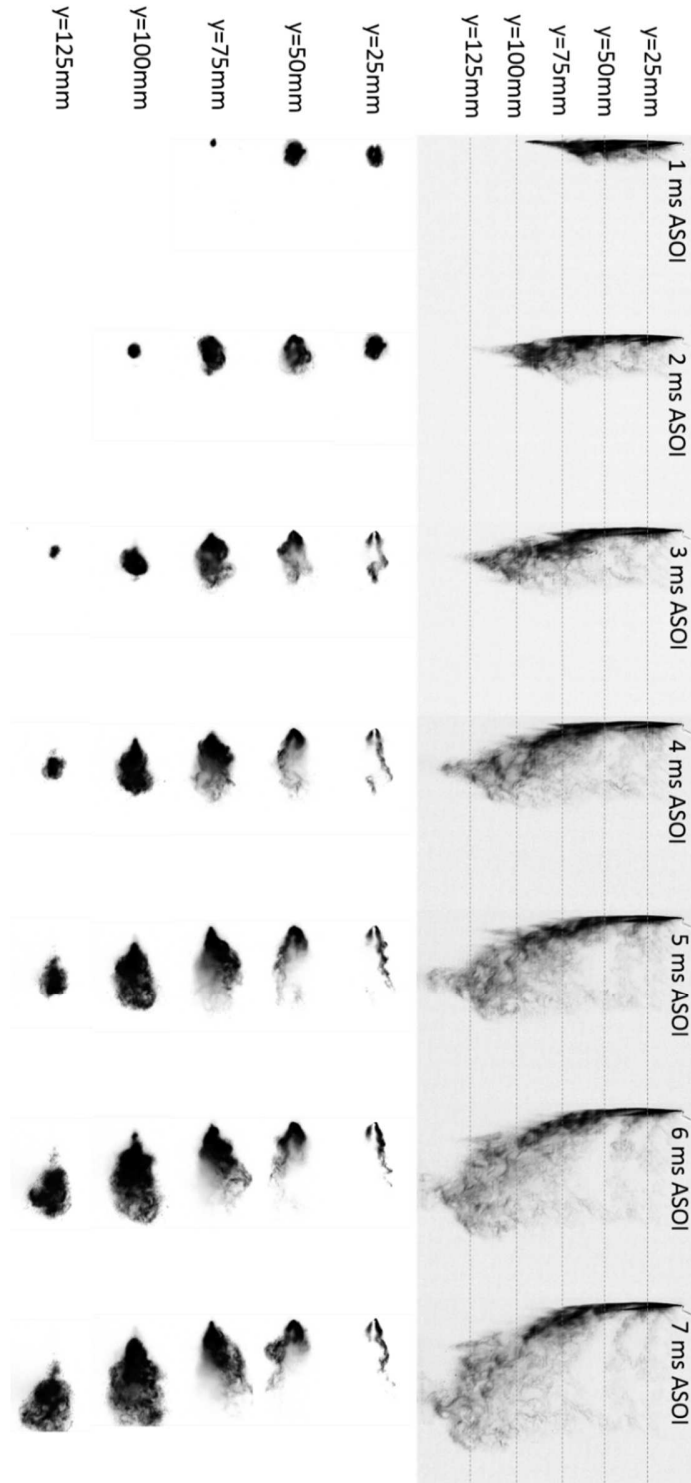


Figure 5.2 Temporal variations of the spray in vertical and horizontal plane ($P_{inj} = 10\text{MPa}$, $U_x = 9.2\text{m/s}$).

The vertical images ($z=0$ plane) and the horizontal images ($y=25, 50, 75, 100$ and 125 mm planes) are listed from 1ms ASOI to 7 ms ASOI (the end of the injection) in Fig. 5.2. From these vertical images, the profiles of the spray in the windward side presented a straight line structure, however it did not bended. The effect of the cross-flow on spray in the upper part is restraining the diffusion in the windward side as well as promoting the diffusion in the leeward side. The tiny non-uniformly droplets were observed in the leeward side in the upper part of the spray. In the 1ms ASOI, the two tips structure of the spray disappeared in the cross-flow condition, however the tip of spray became more sharp than that in the no cross-flow condition in the vertical planes. From 3ms ASOI, some small tips appeared in the lower part of the spray in the windward side, this phenomenon could be caused by the special structure of the VCO nozzle and the cross-flow effects. Some complex movements were observed in the lower part in the spray.

The profiles of the spray in the horizontal planes ($y=25, 50, 75, 100$ and 125 mm planes) represented a tendency of diffusing, namely the area of the spray profile in the each horizontal planes increased with the time going. At the beginning of 1 ASOI, the profiles of the spray in the horizontal planes liked ellipses the droplets concentrated in this area according to the intensity of the images. From 3ms ASOI, the profiles of the spray in $y=25$ and 50 mm planes changed very much, the shapes no longer keep in ellipses but became asymmetrical; the most part of the spray in the $y=25$ mm plane cannot be observed and some wave structure appeared in the profiles, and the same phenomena happened in the plane of $y=50$ mm with the opposite structures. There are lots of reasons can lead to these phenomena, the most possible reason is the vortices happened, which will be introduced in the part of 5.4.

The profiles in the lower part of the spray changed from ellipses to triangles and the area of them increased obviously with the time going. The droplets concentration in the upper part of the spray decreased along the direction of the cross-flow while this phenomenon became blurred in the $y=100$ and 125 mm planes. Additionally, the areas of spray in $y=125$ mm plane were smaller than that in other plane. It is illuminated that the cross-flow blown away the most droplets around $y=125$ mm plane, and only very few droplets impinged the button wall in the cross-flow of 9.2 m/s.

Some fluctuations in the spray are observed and the area of spray increase obviously with time in planes of $y=25$ and 50 mm (as shown in Fig. 5.3). Some wave like structures can be found along the profile of spray in the images (5 and 7ms ASOI), moreover many tiny eddies fill the spray. The fluctuation seems like the movement of vortex, but the wave shapes were not very

similar to those of the normal Karman vortex street (Zdravkovich, 1997). This phenomenon can be easily distinguished after the end of injection by the images of 9 ms ASOI. In the lower part of spray, the large fluctuation was replaced by many small swirling movements. The asymmetrical structure of spray in horizontal plane can be observed clearly in Fig. 5.3.

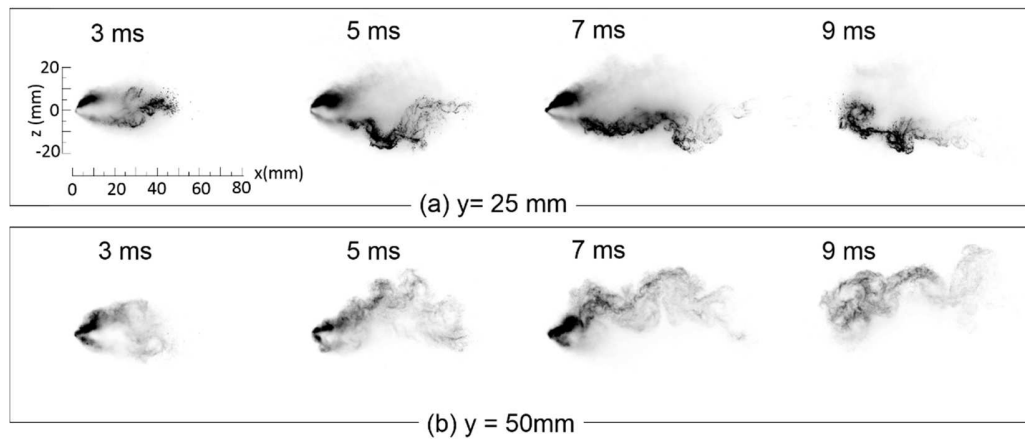


Figure 5.3 Temporal variations of the spray in the horizontal planes of $y=25$ and 50 mm. ($P_{inj}=10$ MPa, $U_x=9.2$ m/s).

The profiles in the upper part of the spray represent asymmetrical structures, but the inclinations of spray are opposite between the plane $y=25$ mm and $y=50$ mm, as shown in Fig. 5.4. In the plane of $y=25$ mm, the droplets had a tendency of inclining to positive Z axis, while the tendency was changed to negative Z axis in the plane of $y=50$ mm. It is not difficult to find the critical plane (approximate $y=30$ mm plane) of the tendency changing in Fig. 5.4. In the lower part of spray the original point of the spray (nozzle exit position) was out of the profiles and the profiles become almost symmetrical.

The windward profiles of the spray in the upper part present a round and blunt structure, the leeward profile of spray in the upper part are crumpled and the tail parts presents unstable. In the lower part of the spray, the windward profiles become a cusp structure and the leeward profiles no longer change so seriously. The area of the profiles of the spray in the each plane increased with the time. Otherwise, the profiles moved along the direction of cross-flow in the lower part of spray.

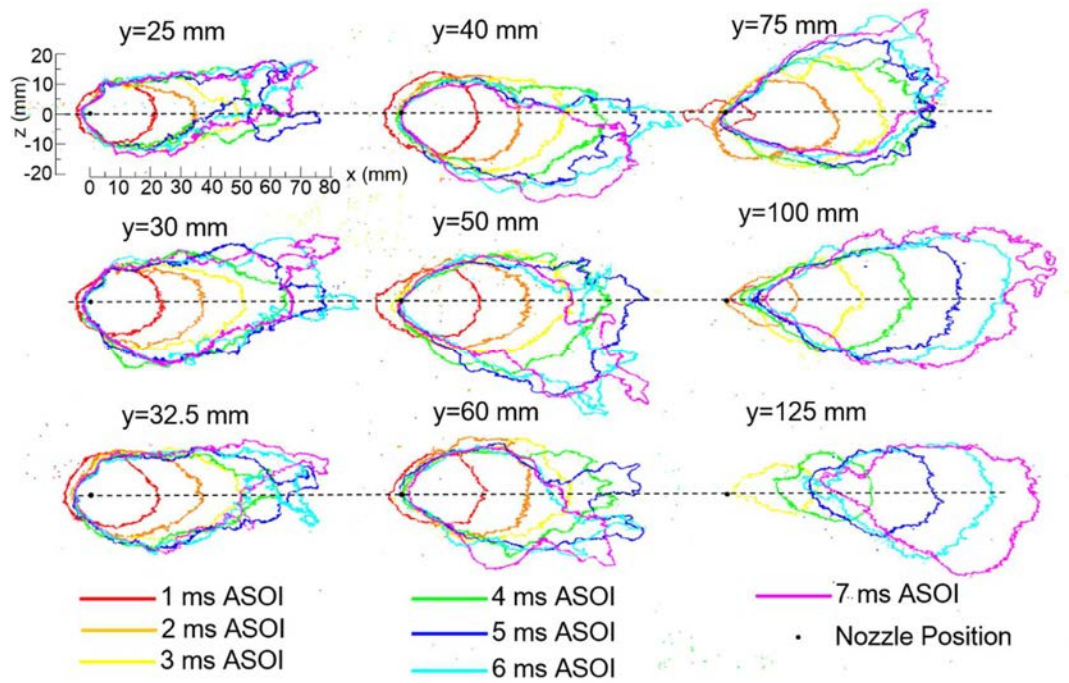
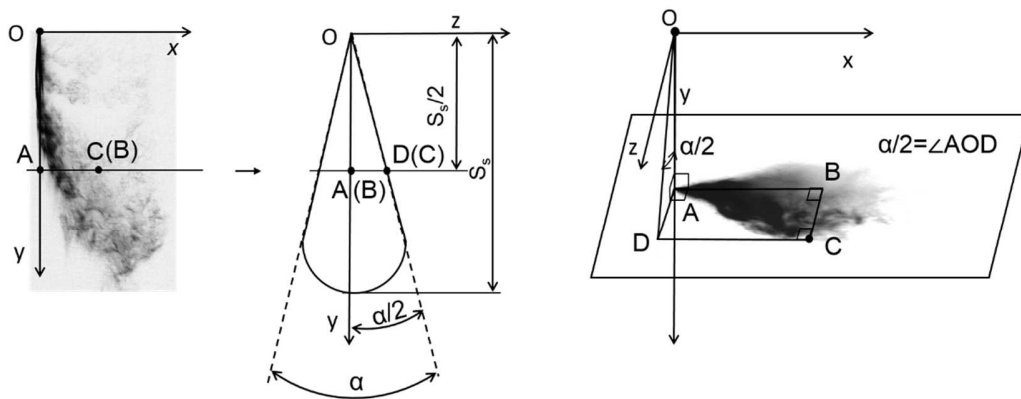


Figure 5.4 Profile variations of the spray in the horizontal planes from $y= 25$ to 125 mm. ($P_{inj} = 10$ MPa, $U_x = 9.2$ m/s).

5.3 Projected Spray Angle

Spray cone angle is a very important parameter in analysis the characteristics of the spray. In this experiments, the direct way to measure the spray angle is very difficult, because the experimental condition limit. The camera should take the pictures in the direction of the cross-flow, it means the camera should be set in the end of the wind tunnel or using the mirrors to reflect the spray image from the end of wind tunnel. However these experiments cannot be taken when the cross-flow existing. In order to understand the expansion of spray in Z axis and investigate that characteristic, a projected spray angle was defined in this study.

Because there is no way to take the pictures along the Z axis, the measurement of the spray cone angle, which have been defined by some researchers, cannot be carried out directly. Figure 5.5 shows the projected spray angle (α) definition, which is just used to compare the expansion with the situation of no cross-flow. S_s is the vertical penetration of the spray in cross-flow, the measure plane is the section of the half S_s position from the nozzle hole. In this study, the interpolation was utilized when the test planes did not coincide to the planes in which the images were taken; after the spray impinged the bottom wall the test sections were fixed in $y=75$ mm plane (half height of spray). The plane of ABC is the picture taking plane like $y=25$ mm; OA is perpendicular to the plane ABC ; CB is also perpendicular to the plane AOB ; C is the maximum edge point to line AB ; D is the projected point of C in section of YOZ along the X direction. So the projected spray half angle ($\alpha/2$) equals $\angle AOD$.



(a) Definition of projected spray angle.

(b) Calculation of projected spray half angle.

Figure 5.5 Definition of projected spray angle α .

In the no cross-flow conditions, the projected spray half angles present two flat lines in both sides

(as the open circles and open triangles show in Fig. 5.6 (a)); the values of them in positive and negative are almost symmetrical about $\alpha = 0^\circ$; the positive values are around 9° as well as the negative values are around -9° ; before 2ms ASOI the projected spray angle, which equals the absolute values of the two projected spray half angles, are slight smaller than that in following time. The breakup of droplets was happening before 2ms ASOI, the droplets owned large downward momentum. In the cross-flow of 9.2 m/s, the projected spray half angles distribute unsteadily; the symmetry about $\alpha = 0^\circ$ does not exist; the positive projective angles fluctuate around 11° while the absolute value of negative values represent an increasing tendency from 12° to 22° (as the closed circles and closed triangles shows in Fig. 5.6 (a)). The projected spray angle in both sides (z and $-z$ axis) in a same time can illustrate that the projected spray angles are larger with cross-flow obviously than that without cross-flow (as shown in Fig. 5.6 (b)), namely the dispersion of the spray increases in both directions of z axis in cross-flow condition.

The spray in the cross-flow field is not simply bended, and the droplets in the spray move not like a parabolic motion. In the z axis direction, the droplets displacement also happened, and the droplets diffused in some extent. The tendencies of the projected spray half angle in both sides are different, in the positive z axis the projected spray half angles present flat while the increasing tendency happened in the negative z axis side. The projected spray angles which own some fluctuations are larger than that in the no cross-flow field. It is indicated that the cross-flow enhances the spray diffusing in z axis direction, this phenomenon can be leaded by the vortex which will be introduce in the part of 5.4.

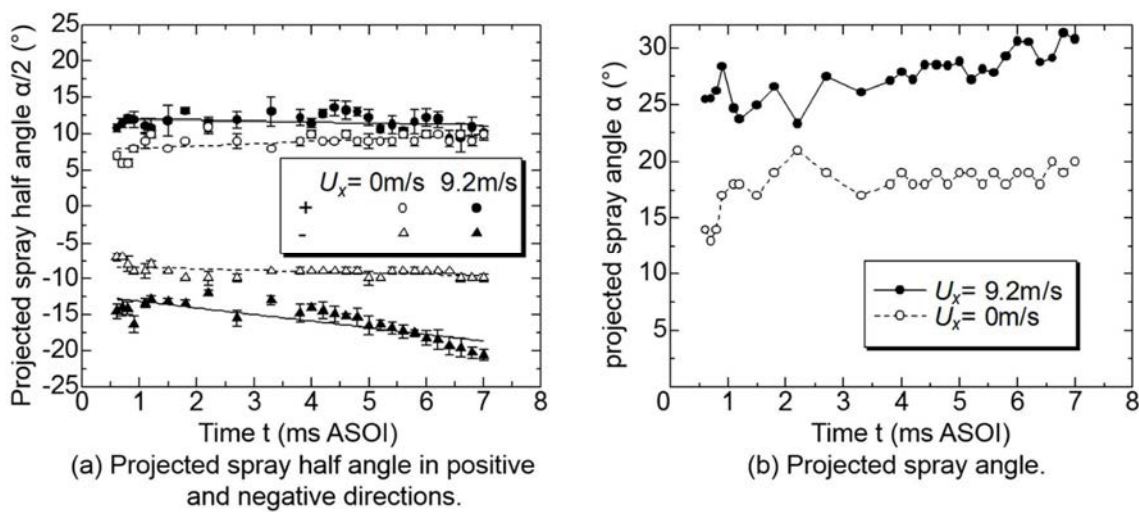


Figure 5.6 Temporal variation of projected spray half angle and projected spray angle.

5.4 Vortex Phenomenon and Frequency Analysis

5.4.1 Vortex phenomenon of droplets in cross-flow

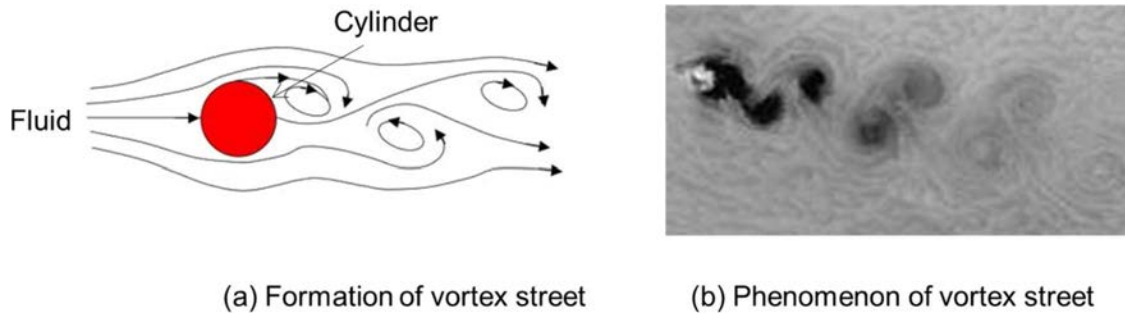


Figure 5.7 Phenomenon of the vortex street.

The vortex phenomenon was raised by Theodore Von Karman in 1911. When a fluid flows past a stationary body or, equivalently, when a body moves in a fluid at rest, a region of disturbed flow is always formed around the body. The extent of the disturbed flow is largely dependent on the shape, orientation, and size of the body, the velocity and viscosity of the fluid, and may be influenced by a wide variety of small disturbances. When the fluid flows past a cylinder in an appropriate Reynolds number the vortex phenomenon will happen, as shown in the Fig. 5.7(a). Figure 5.7 (b) shows the practical image of the vortex phenomenon.

In the upper part of spray, the droplets concentrate in the center line of spray and the most of droplets owns high vertical momentum. When the cross-flow flows past this part, which likes a solid cylinder, the vortex street phenomenon could happens if the Reynolds number meet the condition of the vortex happening, as shown in Fig. 5.8.

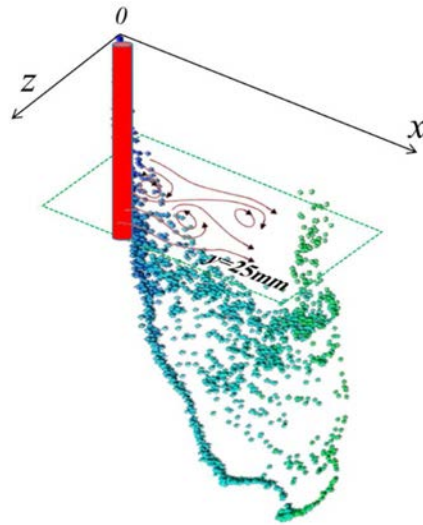


Figure 5.8 Movements in the upper part of spray in the leeside of cross-flow

5.4.2 Vortex in cross-flow field

In the upper part of the spray with cross-flow, the droplets distribute non-uniformly and some wave shape fluctuations are observed in the horizontal images. The structure and the movements of the spray are very similar to that of Karman vortex. To confirm this conjecture, some measurements and calculations are carried out in the following discussion.

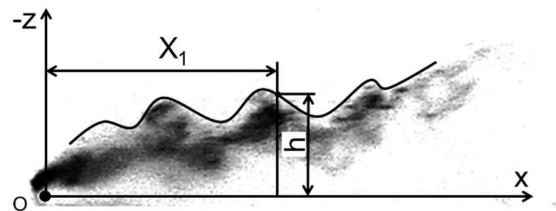


Figure 5.9 h : the distance from the edge of spray to axis of x in a constant x position in horizontal plane.

Firstly, it is assumed that the vortices happen when the cross-flow passes the spray beam, the main spray keep the vertical movement but the tiny droplets which are easy to lose their momentum are entrained into cross-flow. So the droplets can be seen as the tracer particle in this field, the characteristics of the field in the lee area can be observed by the droplets movements. The vortex shedding frequency is an important parameter in analyzing the vortex (Zdravkovich, 1997). To measure the frequency, the fluctuation of an edge point in a constant position in x axis and distance between the two adjacent peaks in the edge of the spray have been measured in this study. The

distance from the edge of spray to axis of x in a constant $X_l=50$ mm position in horizontal plane was defined as h , as shown in Fig.5.9. The value of h have been measured in 5 samples (Fig. 5.10(a)), the curves are based on various times, however they are not regular and different from each other. The frequencies are exacted by Fast Fourier Transform (FFT), the main frequencies focus on 344 Hz, as shown in Fig. 5.10(b). The vortex shedding frequency f can be obtained in the Eq. 5.1.

$$f = \frac{1}{\tau} = \frac{U_x}{\lambda} , \quad (5.1)$$

where, τ is the period of vortex shedding, U_x is the velocity of the cross-flow. The results are shown in Fig. 5.10, the measure plane is $y=25$ mm. These results approximate the results by measuring the fluctuations h .

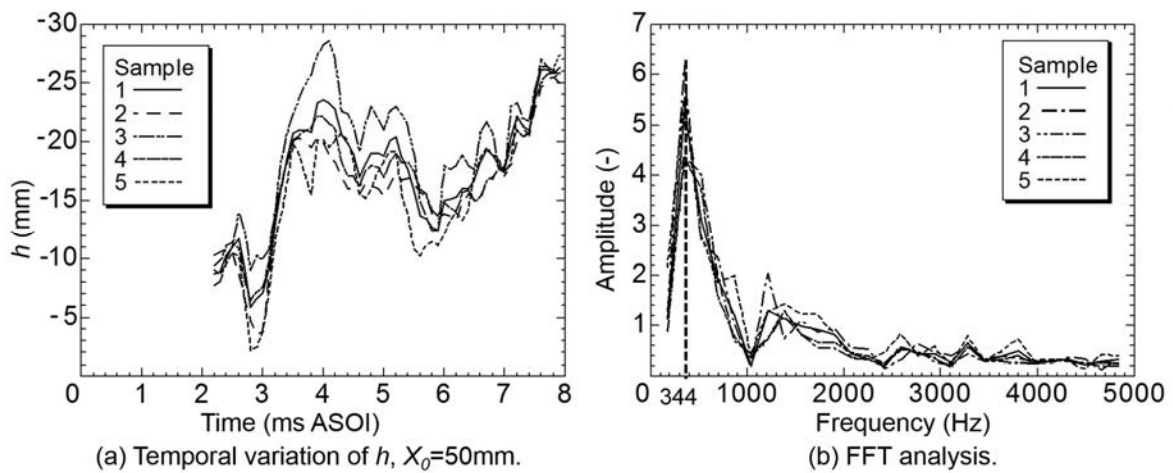


Figure 5.10 Characteristic length h and frequency distribution, $y= 25$ mm.

The other calculation method was taken by measuring the distance of two adjective peaks (λ), as shown in Fig. 5.11(b). The velocity of droplets equals that of the cross-flow approximately, due to the preceding supposition. The value of λ are from 26 to 26.6 mm, its results in the frequencies are around 350 Hz, as shown in Fig. 5.12.

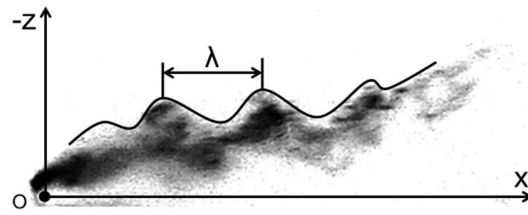


Figure 5.11 λ (wavelength): distance between two adjacent peaks in the edge of the spray in horizontal plane.

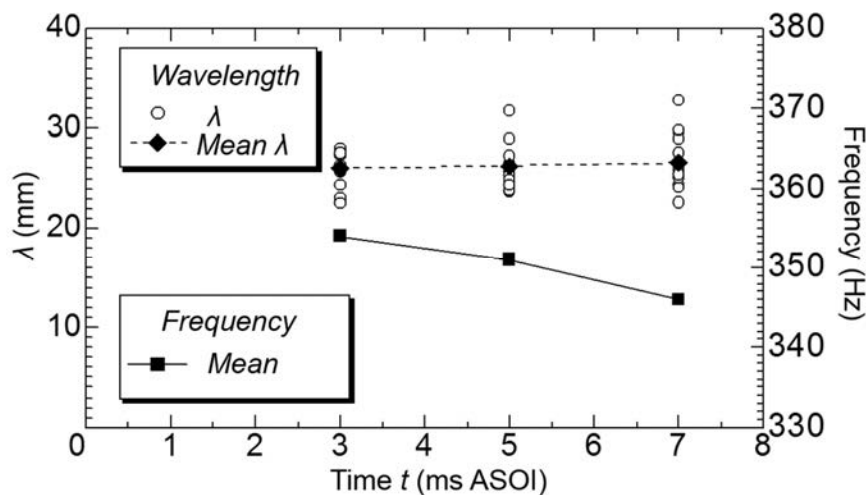


Figure 5.12 Wavelength λ and coinciding frequencies.

Next, if the vortices happened it is very likely to be produced by the interaction of the cross-flow and the main beam of the spray in the upper area. A theoretical calculation which simulates the field of the same flow passing a cylinder is to be taken for comparing the frequencies with the measured results, the cylinder diameter refers to the diameter of the beam of spray in the no cross-flow condition, and the flow velocity is similar to that of cross-flow. 5 mm is chosen as the diameter of the circular cylinder, the size equals the diameter of spray in the $y = 25$ mm plane without cross-flow. According to the experimental conditions, the spray is injected in room temperature and pressure, so the Reynolds number is 3070. In $250 \sim 400 < Re < 10^5 \sim 2 \times 10^5$, the flow is in the state of Transition-in-shear-layers (Zdravkovich, 1997), in which the secondary transition takes place along the free shear layers while the boundary layers remain full laminar. In $1000 \sim 2000 < Re < 2 \times 10^4 \sim 4 \times 10^4$, the flow is in the intermediate regime of this state, and the transition eddies form in this condition. It means the boundary of the vortices distribution can be observed clearly, however, the swirling phenomenon became weak in the vortex and movement in

the vortex become complex due to the secondary vortices (Bloor, 1964). The reason why the droplets distribution are not regular is the effect of the secondary vortices. The Strouhal number, St , is found experimentally to be approximately equal to 0.2 for all Reynolds number above 180 (Zdravkovich, 1997). So from Eq. 5.2, the vortices shedding frequency can be obtained.

$$St = \frac{fD}{U_x}, \quad (5.2)$$

where, D is the spray beam diameter, 5 mm. when the Reynolds number is 3070, the coinciding frequency is 388Hz. The secondary vortex shedding frequency f_i depends on the strouhal vortex shedding frequency f and the Reynolds number Re (Wei and Smith, 1986), as shown in Eq. 5.3,

$$\frac{f_i}{f} = \left(\frac{Re}{470}\right)^{0.87}. \quad (5.3)$$

So the value of the secondary vortex shedding frequency f_i is 1988 Hz. Because the secondary vortex can interfere the frequencies f measured by horizontal images, perhaps the profile of the spray in horizontal plane can be affected. To acquire a range of the frequency f , the difference and sum between the strouhal period τ ($1/f$) and secondary vertex shedding period τ_i ($1/f_i$) are employed as the minimum and maximum value of range, respectively. Hence, the vortex shedding frequency should be in 325 ~ 483 Hz.

Finally, Comparing with the experimental results and calculative results, the frequencies of vortices are very close, moreover all the vortex shedding frequencies which measured from images are in the range of 325 ~ 483 Hz . It can be speculated that the vortices happen in the upper part when the cross-flow passes the spray. The measured results are slightly smaller than that of the simulation due to the errors. There are several reasons which can result in the errors. The measurements in processing experimental data contain errors. Then, the model in the calculation is simplified, in the real field the shape of the spray beam is not a strict circular cylinder structure. Furthermore, the secondary vortices could affect the frequency which is calculated.

5.5 Summary

The structures in horizontal plane in the upper part of the spray present asymmetrical, and the droplet distributions are different in various horizontal planes. In the lower part of the spray the structure becomes symmetrical, however the strong movements can be observed.

The projected spray half angles present two flat lines in both sides, and the values of them in positive and negative are almost symmetrical about $\alpha = 0$ without the cross-flow. The projected spray half angles distribute unsteadily with increasing of the cross-flow velocity, otherwise the absolute value of the projected spray angles with cross-flow are much bigger than that without cross-flow.

The Karman vortices happen in the upper part of the spray in leeward when the cross-flow flow past the spray. The frequencies of the vortices are measured in two ways, the results are in the frequency range of the theoretical calculation. Additionally, the secondary vortices could happen in the upper part of the spray in the leeward, which leads to the distinct interlaced Strouhal vortices cannot be observed clearly.

Chapter 6 Spray Droplets Flow Field

The movement of the droplets in the spray can be utilized to analyze the formation of the structure of the spray and droplet distributions, and it is the important proof for discussing the effects of the cross-flow on the spray. In this chapter the velocity distribution of the droplets of the spray will be discussed in the vertical and horizontal planes by the results of the PIV experiments.

6.1 Velocity Distribution in Vertical Planes

The characteristics of the free spray and the spray in the various cross-flow will be discussed in this part. The injection pressure was set in 10 MPa and the spray injection duration is 7 ms. The experiments were taken in the normal pressure and temperature wind tunnel with the cross-flow 0, 9.2 m/s.

Figure 6.1 shows the images of the spray and the droplets velocity distributions of the spray in the quiescent surroundings in the vertical plane of $z=0$ mm. In the 3 ms ASOI pictures (before impingement), the phenomenon of the two tips structure is very distinct and the main directions of the velocity vectors are ahead along the two tips; in the period of $y=50$ to 100mm, the spray presents a swelling tendency and the droplets velocities become unsteady. After impingement, the two tips structure and its velocity distribution phenomena present no longer distinctly and the velocity distributions of the droplets become normal, the high velocity parts concentrate in the center line of the spray, and the low velocity vectors distribute in the both sides of the main spray. The rolling-up phenomenon happens after impingement in the 9 ms ASOI images, otherwise the vector directions meet this movement.

It is well known that the high velocity part of spray is the near nozzle hole part, the spray initial velocity was obtained by the pressure difference between injection pressure and ambient pressure. After the breaking-up, the liquid beam is divided into lots of droplets, because of the resistance of the ambient gas the droplets are decelerated rapidly. In this result, the highest velocity distributions are not in the tip of the spray or some strange vector appears in that area. The main reasons for this problem is caused by the PIV measurement. The tracer particles, which should be entrained in the whole test field, are the necessary when using the PIV system. In this study, the tracer particles are the droplets in the spray, in the near nozzle hole part of the spray the droplet is not yet formed, results in the system cannot observe the velocity distribution in that area. Another reason

is the PIV system range cannot reach so big velocity distributing range. As the theoretical calculation, the initial velocity of the spray can reach approximate 70 m/s or higher in the injection pressure of 10 MPa, however the lowest velocity in the spray is close to 0 m/s. That is very difficult to measure all the true velocities in the spray by using the same Δt which is the interval time between two laser sheets. So in the experiments, the velocity rang which can illuminate the whole spray characteristics is chosen as the test rang by controlling the value of the Δt and the grid size, which can be set during the processing.

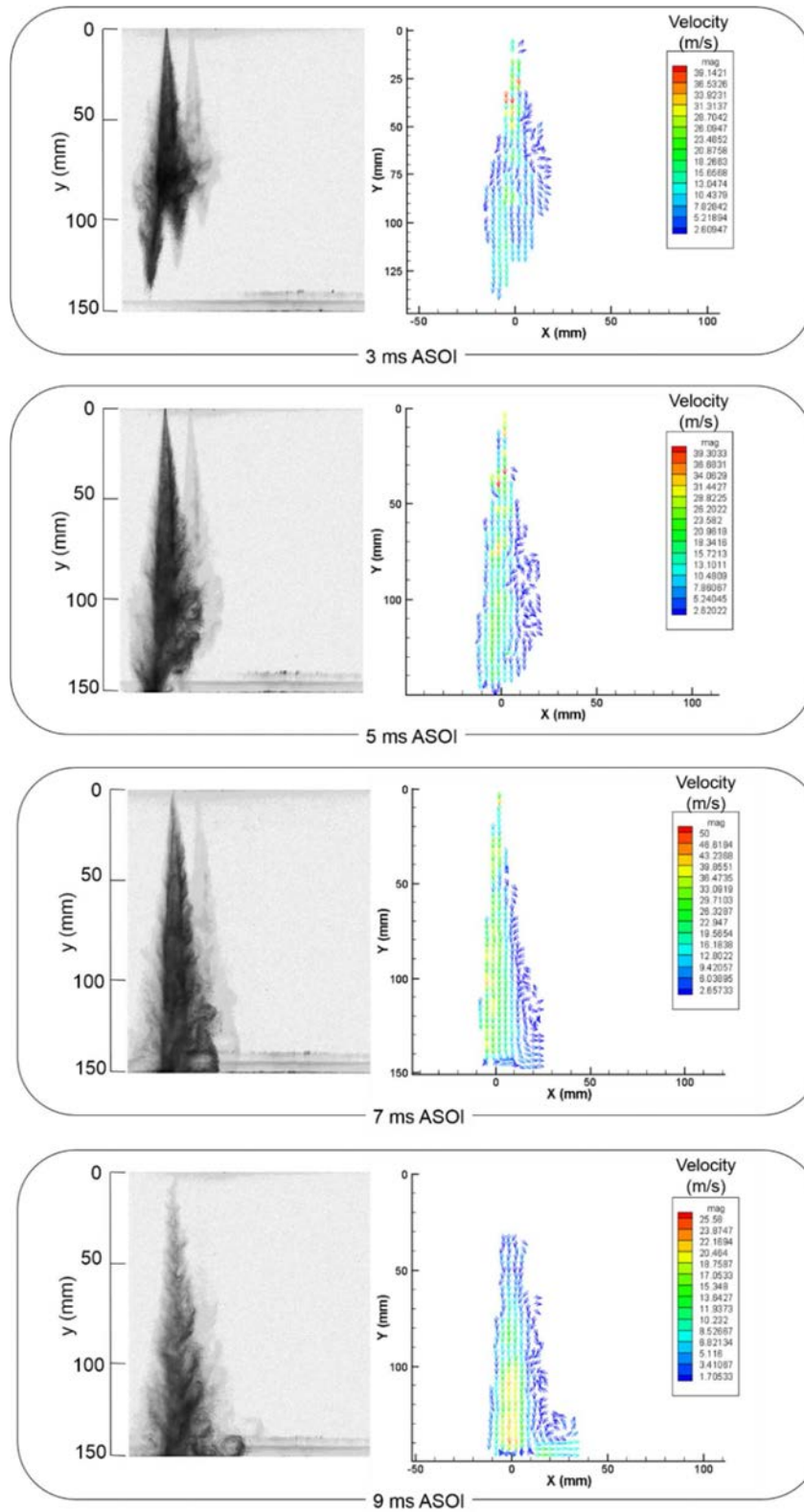


Figure 6.1 Velocity distribution of spray without cross-flow in various time ($P_{inj} = 10\text{MPa}$, $T_d = 7\text{ms}$).

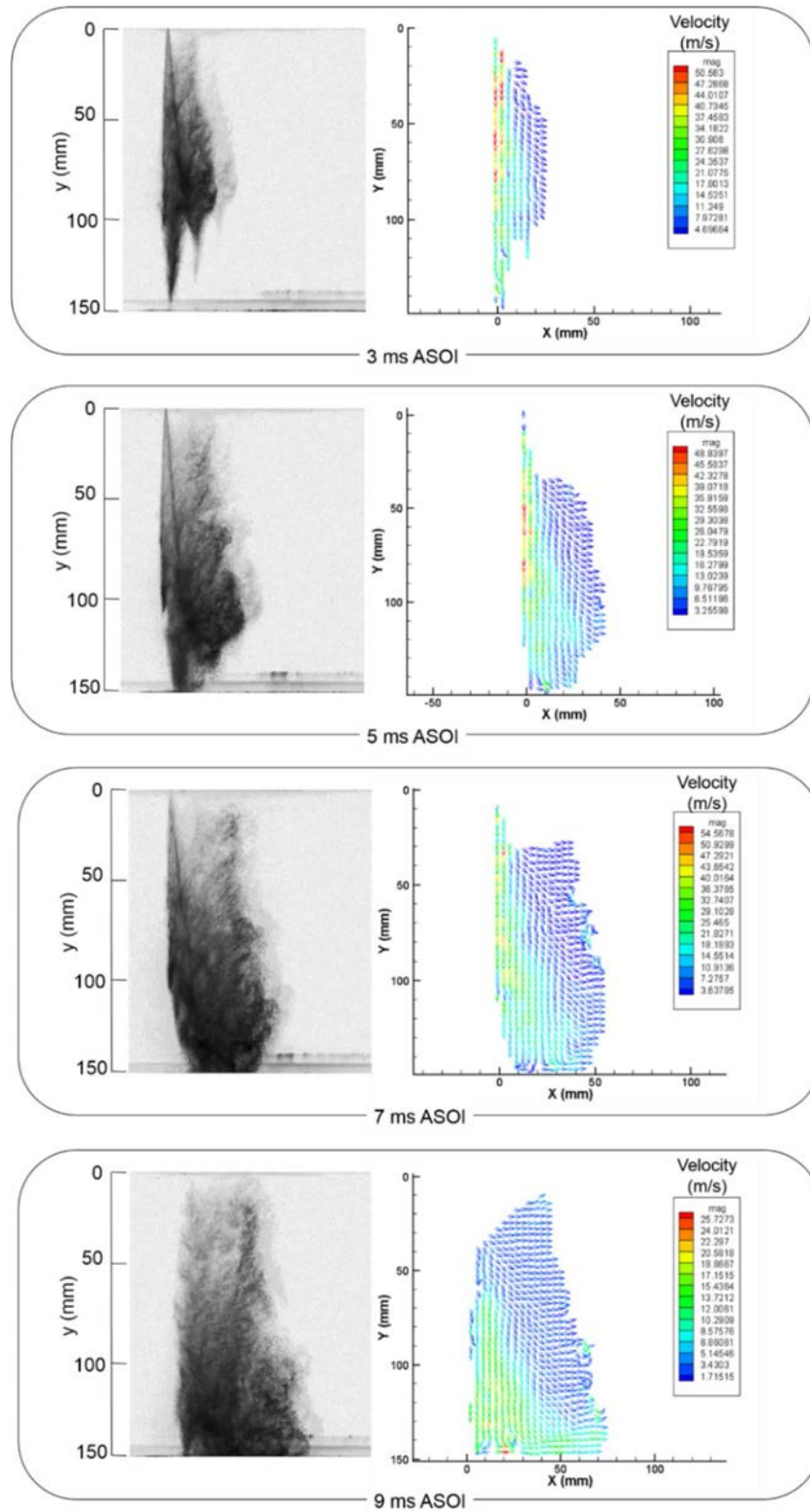


Figure 6.2 Velocity distribution of spray in cross-flow of 4.9 m/s in various time ($P_{inj} = 10\text{MPa}$, $T_d = 7\text{ ms}$).

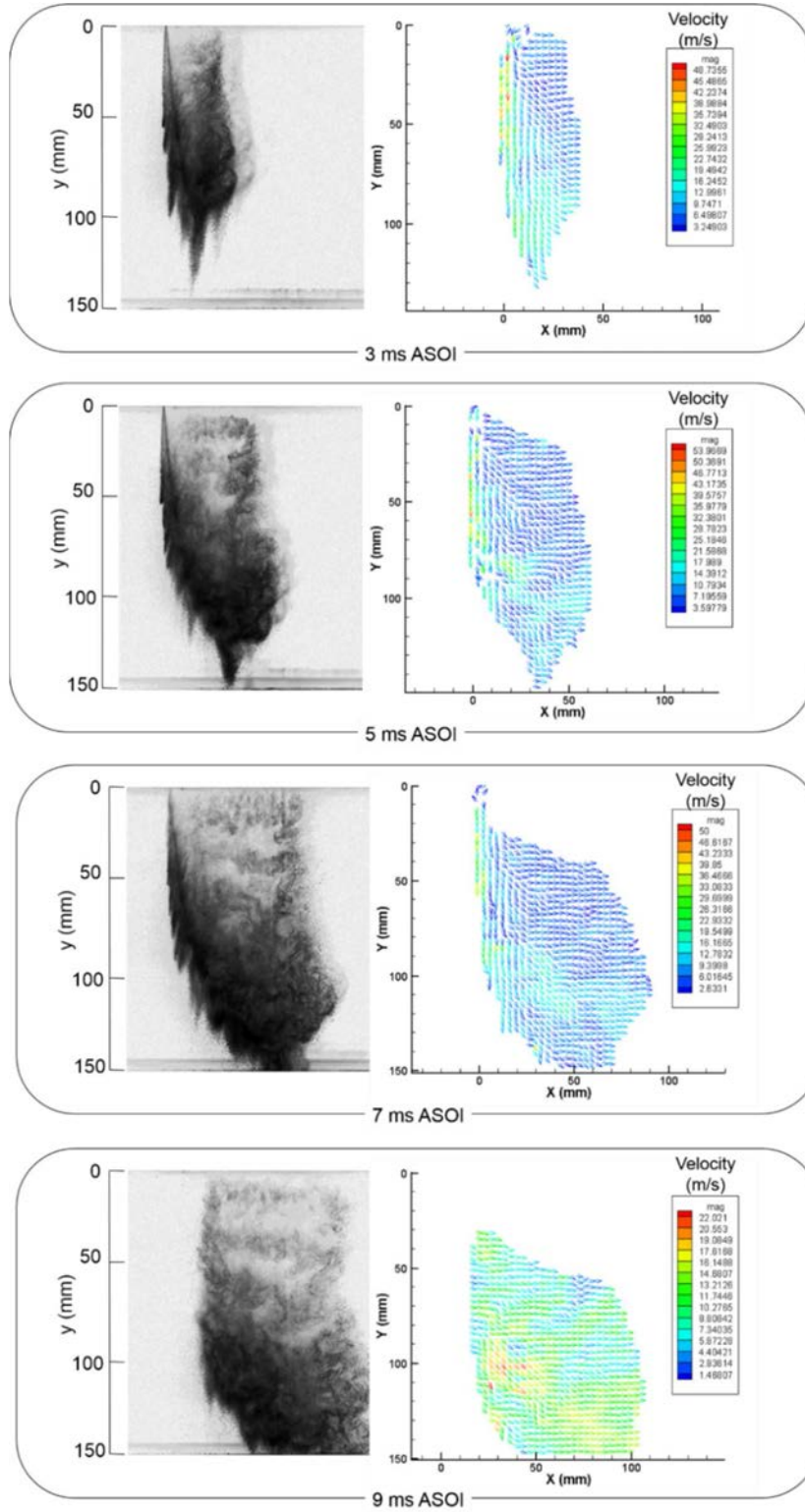


Figure 6.3 Velocity distribution of spray in cross-flow of 9.2 m/s in various time ($P_{inj} = 10\text{MPa}$, $T_{dF} = 7\text{ms}$).

The velocity distribution of the spray in cross-flow of 4.9 and 9.2 m/s in various time are listed in Fig. 6.2 and 6.3, respectively. The pictures show the velocity distributions during the injection and after injection. The experimental injection pressure is 10 MPa and the injection duration is 7 ms.

Before the impingement, in the cross-flow of 4.9 m/s the two tips structure can be observed and the phenomenon is similar to that in the quiescent ambient, however excepting the big tip there are several small tips appear when the cross-flow increases to 9.2 m/s. In the quiescent and low cross-flow velocity ambient the high velocity vectors concentrate in the two tips while this phenomenon disappears in the cross-flow of 9.2 m/s.

With the cross-flow, the high velocity vectors distribute in the windward of the spray (the upstream of the cross-flow) or in the edge of the spray in the upstream of the cross-flow. In the upper part of the spray, the non-uniform tiny droplets are observed, but this phenomenon is very hard to be found in the velocity vector picture.

In the leeward part of the spray the velocities are smaller than the velocities in the windward part of the spray, and the directions of the vectors in the upper part in the windward part of the spray are more horizontal than that in the leeward part of the spray. It illustrates that the droplets in the upper part in the leeward part of the spray are entrained into the cross-flow.

In the quiescent surroundings, the droplets of the spray are broken by the relative movement with ambient gas, and the big droplets which own large vertical momentum are divided into many small droplets, hence the surface resistance which is produced by the ambient gas increases, resulting in the small droplets decelerate rapidly and some tiny droplets lose their vertical momentum or be entrained into the air flow, which is caused by the spray movement. Those tiny droplets can be blown away by the cross-flow, because the size of those droplets is small enough and the vertical momentum is very low. The droplets in the surface of the spray are broken and also making the ambient gas moving whose directions is same with the main droplets, so the inner droplets of spray get the lower resistance from ambient gas, moreover the extents of the droplets breaking and vertical momentum losing are less than that of the droplets in the surface of the spray. The inner droplets of the spray get the high resistance till the droplets in the surface of the spray are blown away by the cross-flow. The inner droplets which remain high vertical momentum can break into small droplets and lose the vertical momentum, thereafter the small droplets in the new surface of the spray can be blown away again by the cross-flow. In this case, some tips structure

appear in the cross-flow of 9.2 m/s. The entrained small droplet movements are not simply vertical ahead to the downstream of the cross-flow, the swirling or rolling movements probably happen in those droplets according to the non-uniform distribution of the intensity and the fluctuations in the velocity distributions. The flow field is influenced by the spray, the swirling like Karman vortex probably happen in the leeward of the spray.

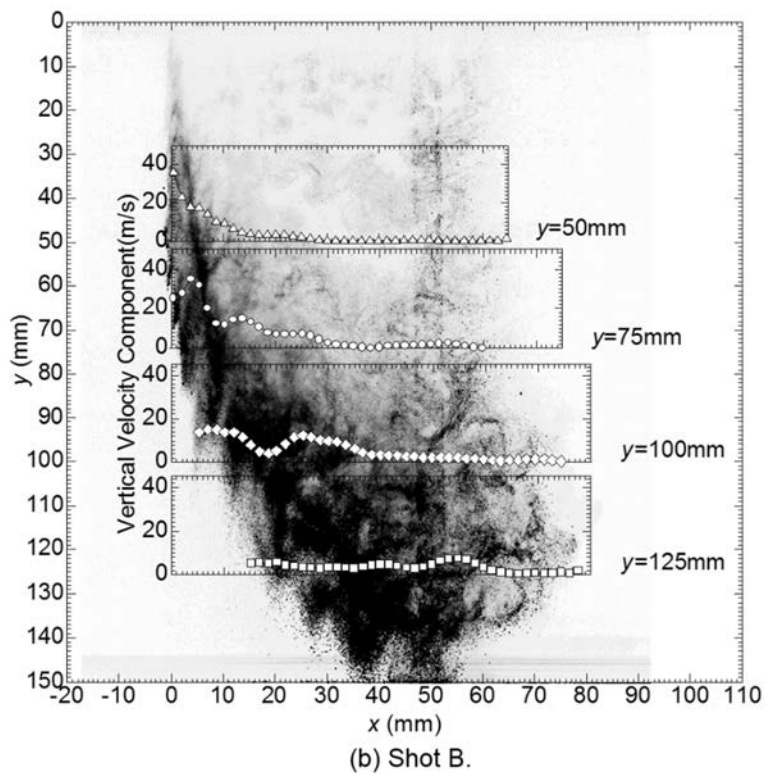
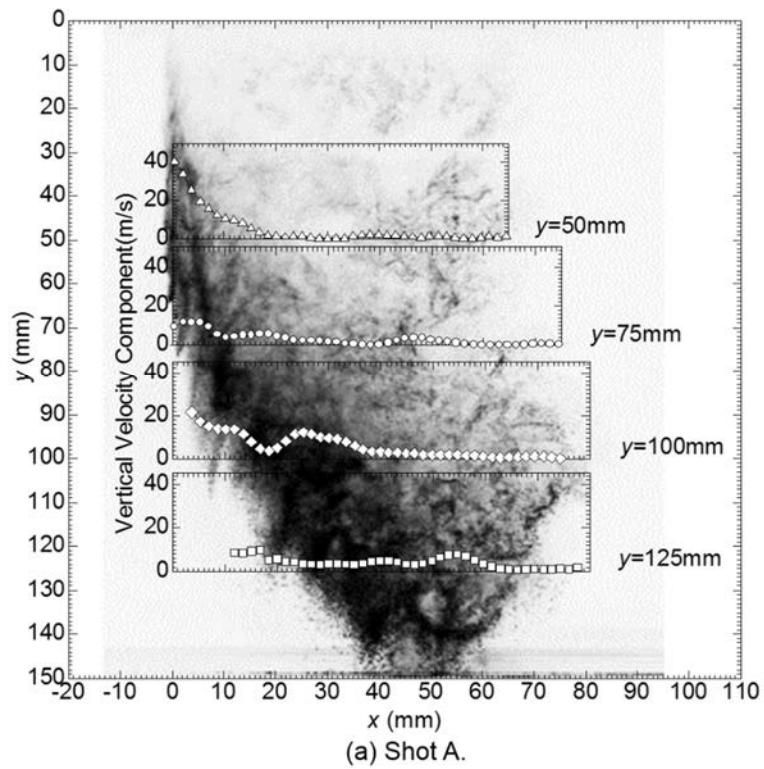
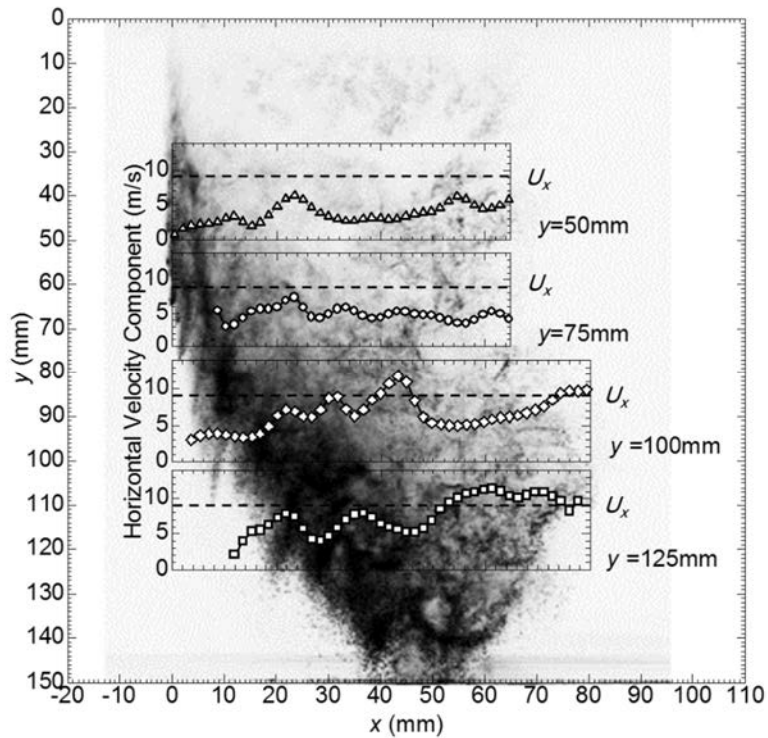
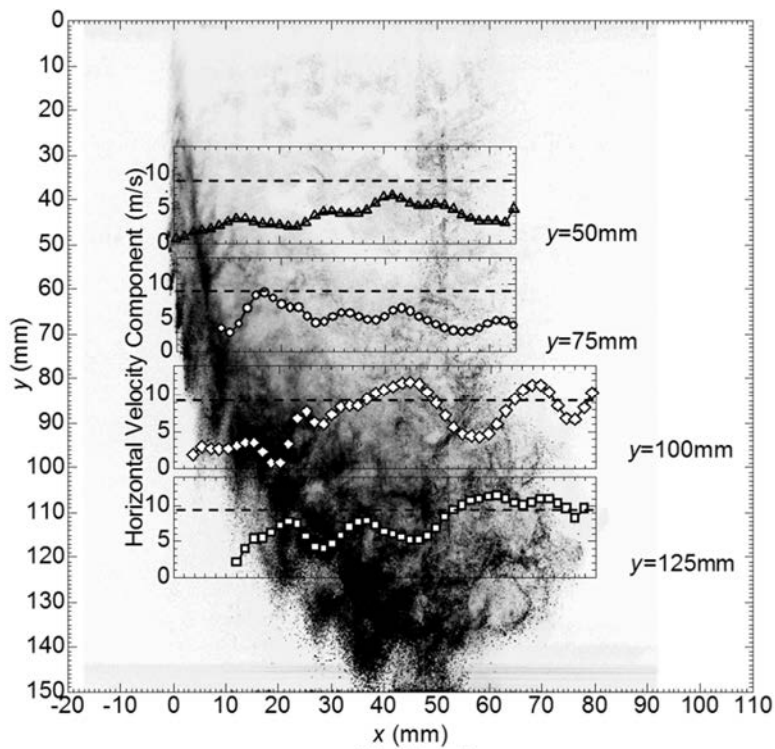


Figure 6.4 Vertical component of the droplet velocity along the direction of the cross-flow ($P_{inj} = 10$ MPa, $U_x = 9.2$ m/s and $t = 7$ ms ASOI).



(a) Shot A.



(b) Shot B.

Figure 6.5 Horizontal component of the droplet velocity along the direction of the cross-flow ($P_{inj} = 10$ MPa, $U_x = 9.2$ m/s and $t = 7$ ms ASOI).

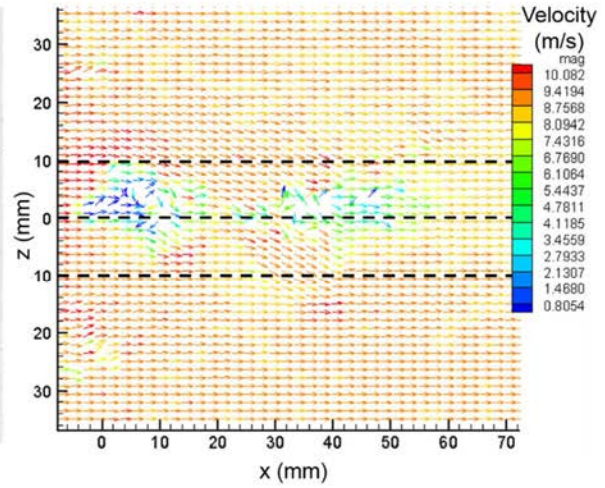
The vertical components of the velocities at different vertical positions are analyzed at $P_{inj}=10\text{MPa}$ and $t=7$ ms ASOI, as shown in Fig. 6.4. It is seen that in two different shoots, the droplets near nozzle own high velocities, and the values decrease with increasing the vertical distance. Along the direction of the cross-flow, the vertical components show some fluctuations. It is possible that the tiny droplet loses its vertical moment easily, meanwhile the cross-flow may entrain into the spray. The spray axis has been plotted out based on the maximum values of the vertical component, as the white dash line shown in Fig. 6.4. Downstream the spray-axis, the vertical component decreases much.

The horizontal velocities distribution at the positions of $y=50, 75, 100$ and 125 mm in xoy plane are analyzed, respectively. The results are shown in Fig. 6.5. At the position of $y=50$ mm, the velocity distributions are unordered along the x direction, however, it can be observed that the area with higher velocity almost distributed in vicinity of dense droplets while lower velocities area distributed near the region of thin droplets. Although there are lots of reasons which may cause droplets distribute unevenly in the section, one possible cause is that the vortex may be induced in this area. The vertical components of the velocity near the nozzle were very high, and hence the upper spray could be assumed as a solid cylinder. Then a vortex may be formed downstream the solid cylinder (spray). And the droplets mingled in vortex air which cause droplets distribute unevenly. Owing to the effect of vortex, the actual velocities of droplets change much. This phenomenon have been discussed in the chapter 5. The maximum points of vertical velocities concentrate near the profile of spray in upstream of cross-flow. It indicates that the droplets with high velocity remain around the edge of spray. The horizontal velocities in some areas even exceed the cross-flow velocity, as seen in $y=100$ and 125 mm. Comparing the positions of the peaks of the horizontal component, the curve (black double dash dot line in Fig. 6.5) acquired by linking the high horizontal velocities points seems like an offset curve of spray axis (white dash line in Fig. 6.5). The horizontal velocities in the curve of spray center are lower than that of the cross-flow while the velocities of droplets in some area of downstream are higher than that of the cross-flow. The variation of the horizontal velocity of a droplet can be affected by not only cross-flow but also the coalescences of droplets when the initial direction of velocity is guided along the direction of cross flow. The upstream droplets formed a curve wall with droplets, while the downstream droplets maybe guided to change the direction from vertical to horizontal. Consequently, it is possible that the horizontal velocity component may exceed the cross-flow

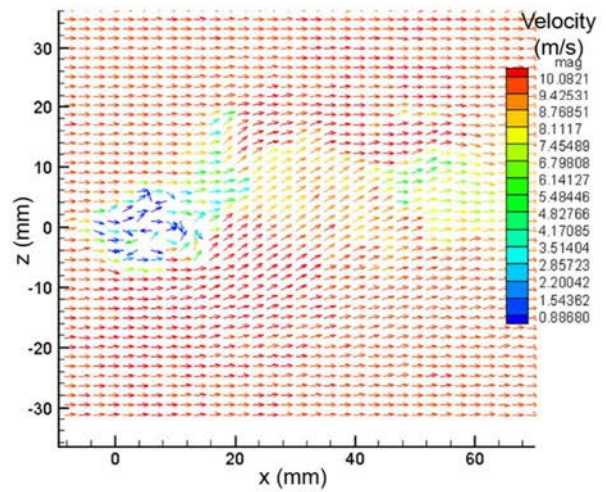
velocity. The swirling or rolling movements happening in those droplets also can cause the high velocity phenomenon.

6.2 Velocity Distribution in Horizontal Planes

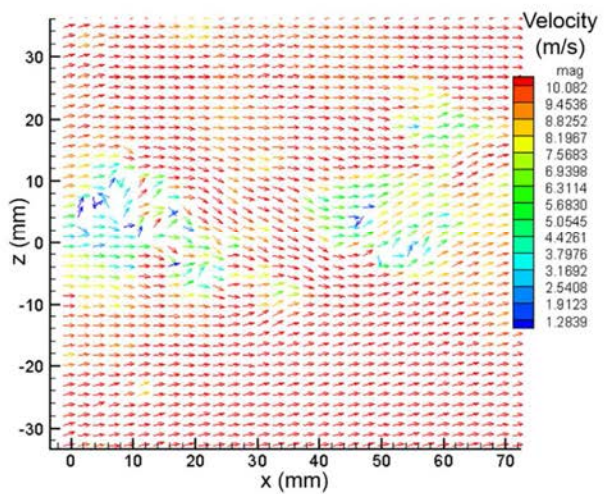
Plane of $y = 25$ mm



Plane of $y = 50$ mm



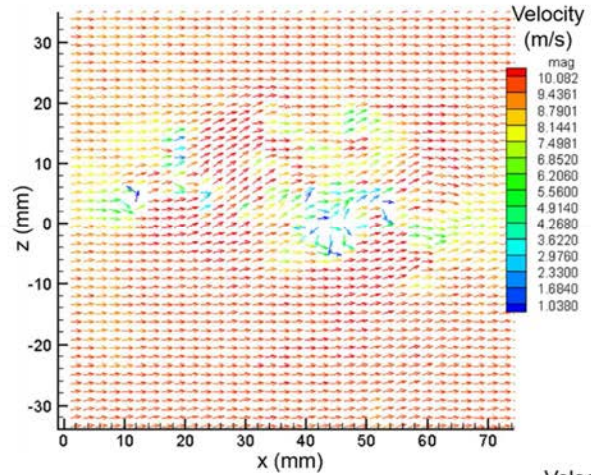
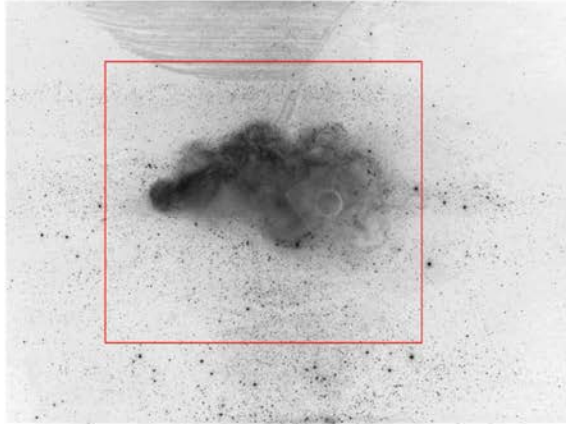
Plane of $y = 75$ mm



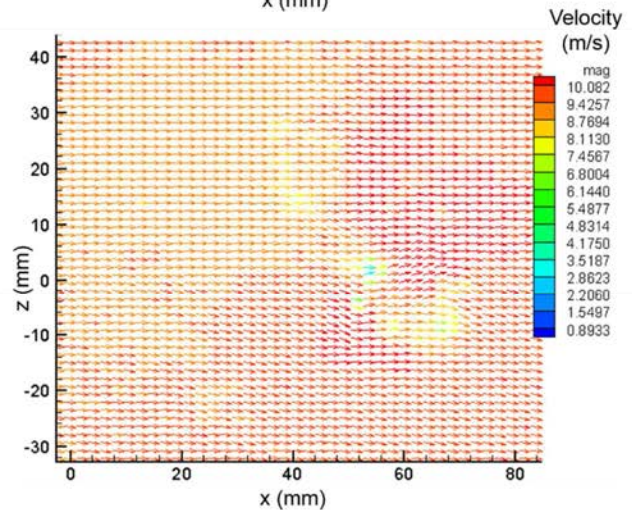
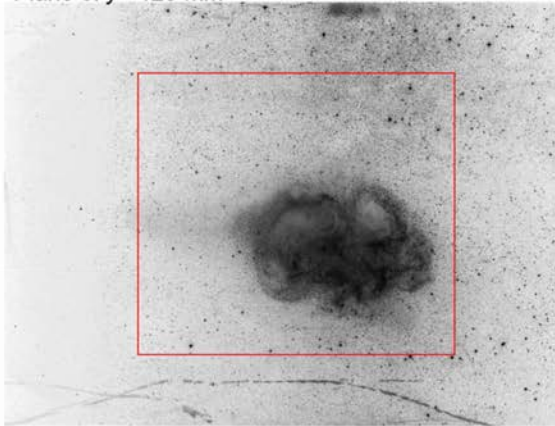
(a) Image of spray and tracer in cross-flow

(b) Velocity distribution

Plane of $y=100$ mm



Plane of $y=125$ mm



(a) Image of spray and tracer in cross-flow

(b) Velocity distribution

Figure 6.11 Velocity distribution in various horizontal planes under cross-flow of 9.2 m/s ($P_{inj}=10$ MPa, $t=7$ ms ASOI, red rectangle is the test area).

To further understand the structure of the spray and investigate the droplet movements in the cross-flow, the velocity distributions in various horizontal planes are measured by PIV technique in the atmospheric wind tunnel. The velocity distribution at atmosphere of the spray can be observed more clearly than that in the pressure ambient experiments. In this section, the discussion is based on the results of the horizontal planes of atmospheric experiments. The injection pressure is 10 MPa and the injection duration is 7 ms, and the cross-flow velocity is 9.2 m/s. The measuring position is the planes of $y=25, 50, 75, 100$ and 125 mm.

Figure 6.11(a) shows the raw images of the horizontal planes at the time of 7 ms ASOI. MgO (magnesium oxide) as the tracer particles is utilized in this measurement. In that case, the droplets and MgO can be used as tracer particles during the experiments, hence the spray and flow field

velocity distributions can be got at some time. The droplets of the spray in the horizontal plane does not present a simply movement but rolling or swirling.

The velocity distributions are shown in Fig. 6.11(b) coinciding the area of the red rectangle in the planes of $y=25, 50, 75, 100$ and 125 mm at the time of 7 ms ASOI. In the plane of $y=25$ mm, the vectors change very much such as the value and the directions of them. Some small value vectors appear near the original position, the directions of the vectors in the area from $z=-10$ mm to $y=10$ mm are disorder and some opposite directions appear in that area. In the plane of $y=50$ mm the disorder phenomenon also exists but is more regular than that in the plane of $y=25$ mm, and some rolling structures are presented in that area. In the planes of $y=75$ and 100 mm, the area of the velocity disorder enlarges, however, the small value of the vector and big value of the vector appear alternately along the direction of the cross-flow. In the plane of $y=125$ mm, the disorder area becomes very small, it is not matched with the image of the spray.

The vectors, which present the velocity distribution of the whole field, are obtained by tracing the droplets and the tracer particles (MgO). The low velocities appear near the original position, and the directions are disorder. The main spray is bended slightly and lean to the leeward of the original line of $x=0$ mm. It indicate that the disorder area in the upper part of the spray is in the high droplet concentration area, and the droplets in that area own high vertical velocities. The laser sheet is arranged horizontally, the droplets with high vertical velocities can traverse the plane illuminated by the laser sheet. So this particles cannot be shown in the two images which taken by the CCD camera, than the disorder phenomenon probably happen after processing. Additionally, the velocities of the droplets in that area in the horizontal plane are very small.

In the leeward, because of the influence of the spray the cross-flow field is no longer uniform, the MgO and the tiny droplets entrained by the flow are used to measure the velocity distribution by the PIV system. The swirling or rolling movements are observed in the raw images, however, the vectors cannot preset the velocity distribution. There are lot of reasons which can cause this phenomenon. The most probably reason is that the swirling or rolling structure is also moving with cross-flow and the rolling velocity is smaller than the moving velocity. The rolling structure is composed by the droplets, the movements of the droplets can be divided into two part: a high speed movement along the cross-flow and a low speed movements of following the rolling structure. In the time interval Δt , the displacement of one droplets or tracer is measured by the PIV system, the displacement in the direction of the cross-flow will much bigger than the displacement

of following the rolling, than the displacements of all the droplets in the rolling are represented in the direction of the cross-flow. The presentations of the vectors which include the rolling movements are that the directions of the vectors change and value of them become non-uniform. This phenomenon can be clearly observed in the plane of $y=125$ mm in Fig. 6.11.

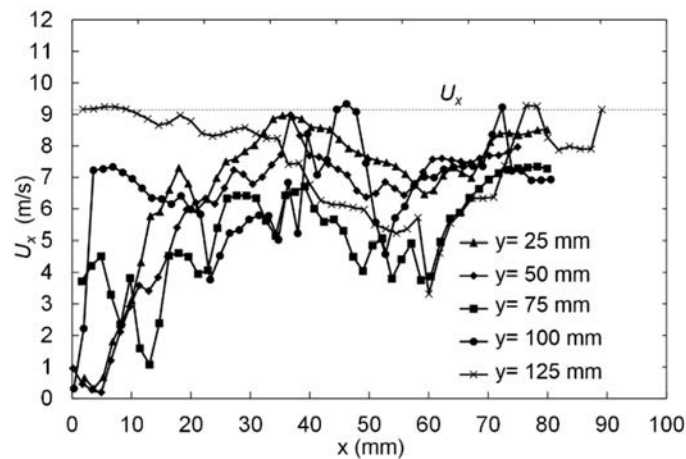


Figure 6.12 Horizontal velocity distribution in the line of $z=0$ mm in various horizontal planes ($P_{inj}=10$ MPa, $t=7$ ms ASOI).

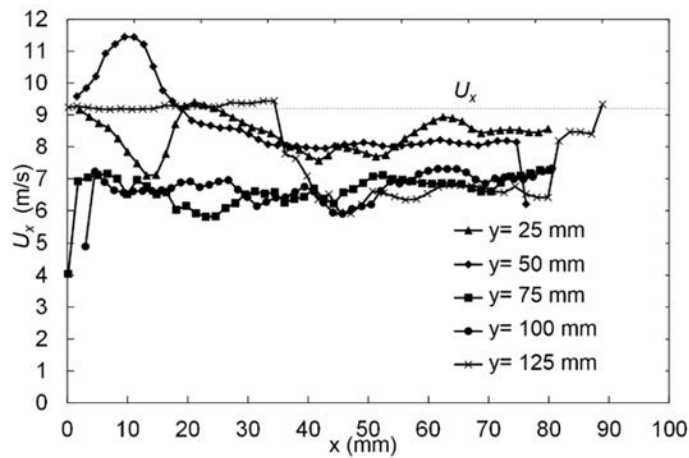


Figure 6.13 Horizontal velocity distribution in the line of $z=-10$ mm in various horizontal planes ($P_{inj}=10$ MPa, $t=7$ ms ASOI).

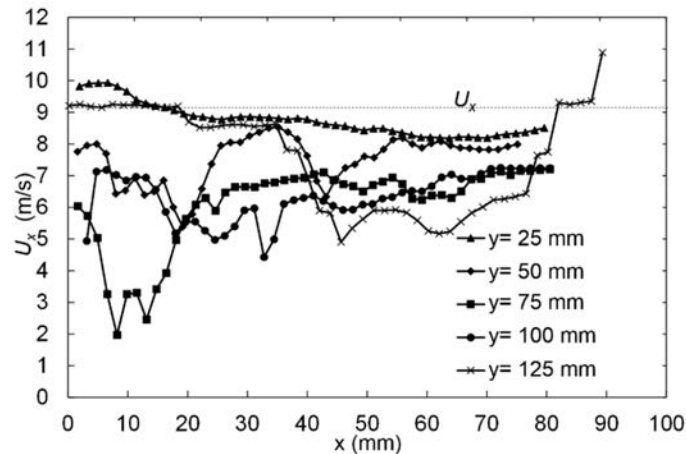


Figure 6.14 Horizontal velocity distribution in the line of $z = 10$ mm in various horizontal planes ($P_{inj} = 10$ MPa, $t = 7$ ms ASOI).

The horizontal velocities in the lines of $z = 0, -10$ and 10 mm in the plane of $y = 25, 50, 75, 100$ and 125 mm (as the dashed lines shows in Fig. 6.11, the plane of $y = 25$ mm) are extracted, as shown in Figs. 6.12, 6.13 and 6.14.

In the line of $z = 0$ mm, the value of the horizontal velocities own the tendency of first increasing then relative stabilizing. The fluctuation in the curves of the horizontal velocities is distinct, and the maximum value also exceed the velocity of the cross-flow. However, the exceeding points are different from that in extracted in the velocity plane results. Because the results come from different spray, even the injection pressure, injection duration and ambient conditions are same, the details of the structure and movements presents differently, but the basic characteristics are same.

The fluctuation of the velocities in the line of $z = 0$ mm is much higher than that in the lines of $z = -10$ and 10 mm. It is indicated that the droplet movements in the center are more complex than that in the edges of the spray in the same horizontal plane. The field can be influenced by the spray, the influenced field is in the leeward of the spray, and in that area the air flow movement become complex. The line of $z = 0$ mm is in the influenced air flow area, the droplets obtain the momentum from the air flow and move following the air flow. The lines of $z = -10$ and 10 mm are in the sides of the spray, the field of the air flow is more stable than that in the center. The droplets or MgO particles obtain the momentum from the air flow, which is less influenced by the spray, they get the horizontal velocity rapidly and can keep in a relative constant condition.

6.3 Vorticity Distribution

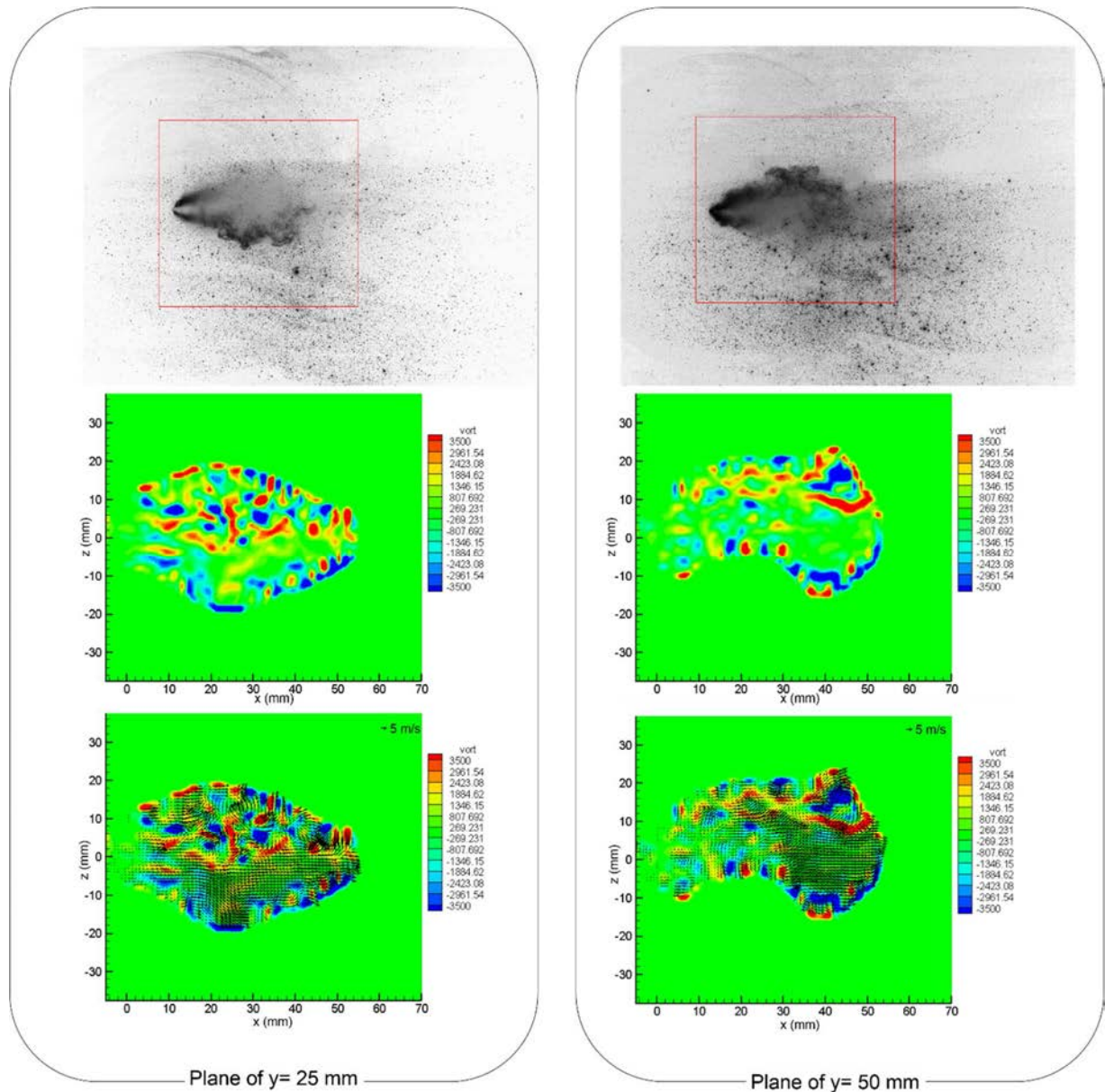


Figure 6.15 Vorticity distribution in planes of $y= 25$ and 50 mm

$$(P_{inj} = 10 \text{ MPa}, U_x = 9.2 \text{ m/s}, t = 5 \text{ ms ASOI})$$

The vorticity, which is a pseudo-vector field that describes the local spinning motion of a fluid near some point, can be utilized to analyze the movement of the air flow. It can be understood that the spray structure and movements in the cross-flow become irregular, and why the swirling happens in the cross-flow field. The vorticity distributions are measured in the planes of $y= 25$ and 50 mm, and the raw images and the vorticity with the vectors are listed in Fig. 6.15.

The vorticity distribution have a range, in this range the vorticity changes very much while the vorticity equals 0 in the other area out of this range. The directions of the vorticity present an interlaced distribution by the observation of the color changing (the red color and the blue color present the different direction of the vorticity). It can be observed in the vorticity images with vectors, in the high value of the vorticity the velocity directions change much.

The vorticity is formed in the field by the interaction between the cross-flow and the spray. When the cross-flow flow past the spray, in the leeward of the spray the movements like vortex happen. The vortex can make the interlaced vorticity and results in the fluctuations happen in the field. When the fluctuations become too large, it is considered that the turbulence happens in that area. As the discussing in the chapter 5, in the upper part of the spray the Karman vortices happen in the leeward. However, the Reynolds number of this situation is in the value of the state of Transition-in-shear-layers, in which the secondary transition takes place along the free shear layers while the boundary layers remain full laminar. It means the boundary of the vortices distribution can be observed clearly, however, the swirling phenomenon became weak in the vortex and movement in the vortex become complex due to the secondary vortices.

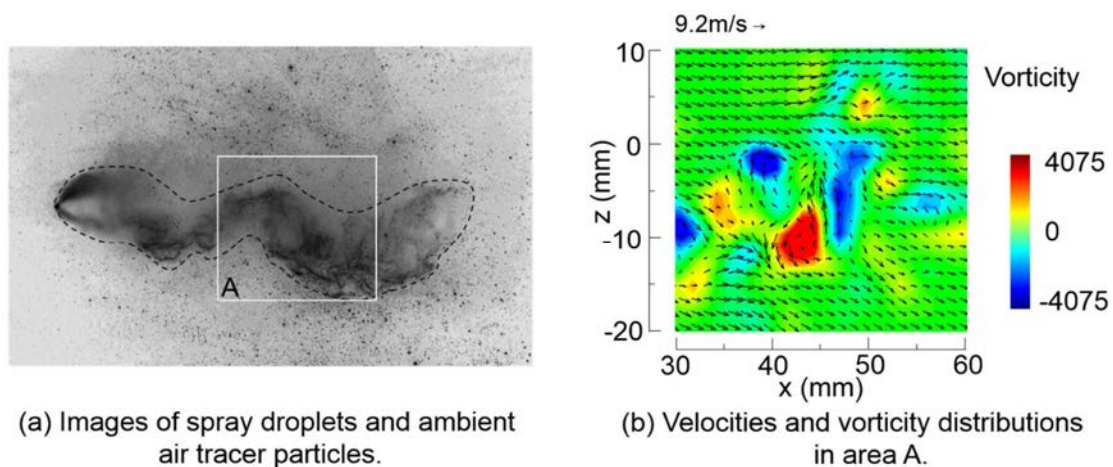


Figure 6.16 PIV analysis of flow fields of spray droplets and ambient air
 ($y=25\text{ mm}$, $P_{inj}=10\text{MPa}$, $U_x=9.2\text{m/s}$, 5ms ASOI).

Figure 6.16 shows the velocity and vorticity distributions of the flow field in the horizontal plane of $y=25\text{ mm}$, in which spray droplets and tracer particles are taken by CCD camera of PIV system. The dashed line in Fig. 6.16 (a) was drawn to distinguish the spray and tracer. The distribution of velocity outside of the dashed line area represents constantly, the value is around 9.2 m/s . However, the velocities in the area of the dashed line are no longer uniform. The velocity and vorticity

distributions in area A are shown in Fig. 6.16(b). In the distribution of velocity, the vectors shows the value and direction of the velocities, the swirling phenomenon can be observed but not apparently, because the complex movements happen in vortex, the secondary vortices are filled in the spray. The staggered vorticity distribution is represented, this phenomenon agrees with the discussion above.

6.4 Summary

In the vertical plane of $z=0$ mm without the cross-flow, the phenomenon of the two tips structure is very distinct and the main directions of the velocity vectors are ahead along the two tips before impinging the bottom wall, and the spray presents a swelling tendency and the droplets velocities become unsteady in the middle part. After impingement, the two tips structure and its velocity distribution phenomena present no longer distinctly and the velocity distributions of the droplets become normal, the high velocity parts concentrate in the center line of the spray, and the low velocity vectors distribute in the both sides of the main spray. The rolling-up phenomenon happens after impingement, otherwise the vector directions meet this movement.

Before the impingement, in the low velocity of the cross-flow the two tips structure can be observed and the phenomenon is similar to that in the quiescent ambient, however excepting the big tip there are several small tips appear when the cross-flow increases. The droplets in the upper part in the leeward part of the spray are entrained into the cross-flow.

In the pressure ambient condition, the velocity distributions in the high ambient pressure become more order than that in the low ambient pressure. The value of the velocity in the same position decreases with the ambient pressure increasing. When the ambient pressure increases, the extent of the bending edge of the spray increases distinctly.

From the velocity distributions in the horizontal plane, the disorder velocity distributions appear near the original area. The velocities in the center line ($z=0$ mm) present a tendency of first increasing than keeping, while the value of that in the edge lines ($z= -10$ and 10 mm) shows much stable. The velocity fluctuations in the center is much stronger than that in the both sides in the horizontal plane.

The vorticity presents an interlaced distribution with different directions. The happening of the vorticity owns regional, in the range of the leeward of the spray the vorticity can be observed.

Chapter 7 Spatial Distributions of Droplets and Their Sizes

The droplet distributions in the spray will be discussed in this section by analyzing the scattered light intensity of the spray images in various conditions. Mie scattering photography was utilized to obtain the spray images of various sections. The droplet sizes of the spray were measured in various location with and without the cross-flow.

7.1 Spatial Distributions

The concentration and droplet size can be measured by analyzing the planar Mie scattering images of the spray (Kalt et al., 2007). The concentrations of the spray droplets are discussed by the counter images in this part. The counters are obtained by distinguishing the different intensities of the images. In the Mie scattering images, the bright area means the high scattering intensity, namely the droplet density is high in this area at least. The range of the intensity is defined from the minimum 0 to the maximum 255.

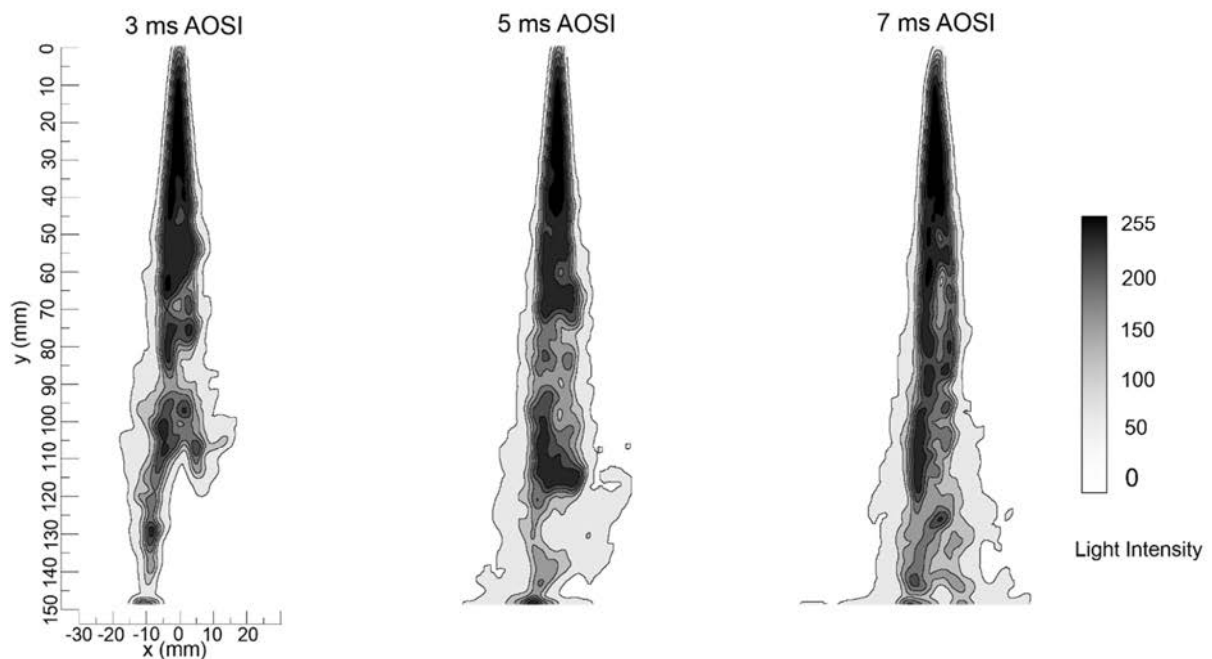


Figure 7.1 Distributions of scattered light intensity in horizontal plane
($P_{inj} = 10\text{MPa}$, $U_x = 0\text{ m/s}$).

In the upper part of the spray ($y= 0$ to 30 mm), the droplets are concentrated in the center of the spray according to the images in Fig. 7.1 in the no cross-flow condition. In the middle part of the spray ($y= 30$ to 80 mm), the droplets begin to diffuse due to the decreasing of the intensity, moreover the low intensity areas appear in the both sides. In the lower part of the spray ($y > 80$ mm), the asymmetrical distributions of light intensity are observed in various time. Before the impingement, the spray concentrate along the two tips while the rarefied droplets enrich the edge of the spray. The low intensity areas can be observed in the spray center line, which the tips are not along with.

The droplets in the upper part of the spray are in the breaking stage, in which the droplets own high vertical momentum and its density is very high. Only the little tiny droplets can be formed in the edge of the spray, and attach which the dense droplet without the influence of the ambient gas flow. In the middle part of the spray, with the breaking continuing the small droplets increase. Due to the resistance of ambient gas, the vertical momentum the small droplets decreases rapidly. The diffusion of them are generated by the ambient air movements, which are caused by the spray moving. The many small droplets are formed in the lower part of the spray, because the droplet breaking is adequate in that area. Otherwise, the concentrations become more uniform than that in the upper part of the spray.

In the cross-flow of 9.2 m/s, in the upper part of spray the high light intensity areas concentrate in the upstream of cross-flow (the windward), moreover the tiny droplet is hardly observed in the windward while lower intensity areas disperse in the leeward of spray (see Fig. 7.2). The high intensity area (high droplets concentration) presents a bended curve structure due to the guide of cross-flow as well as the rarefied droplets distribution is non-uniform. In the lower part of the spray, the high intensity areas reduce gradually and the branches phenomenon disappears from approximate $y= 90$ mm. The area of spray increases obviously due to the dispersing of the cross-flow.

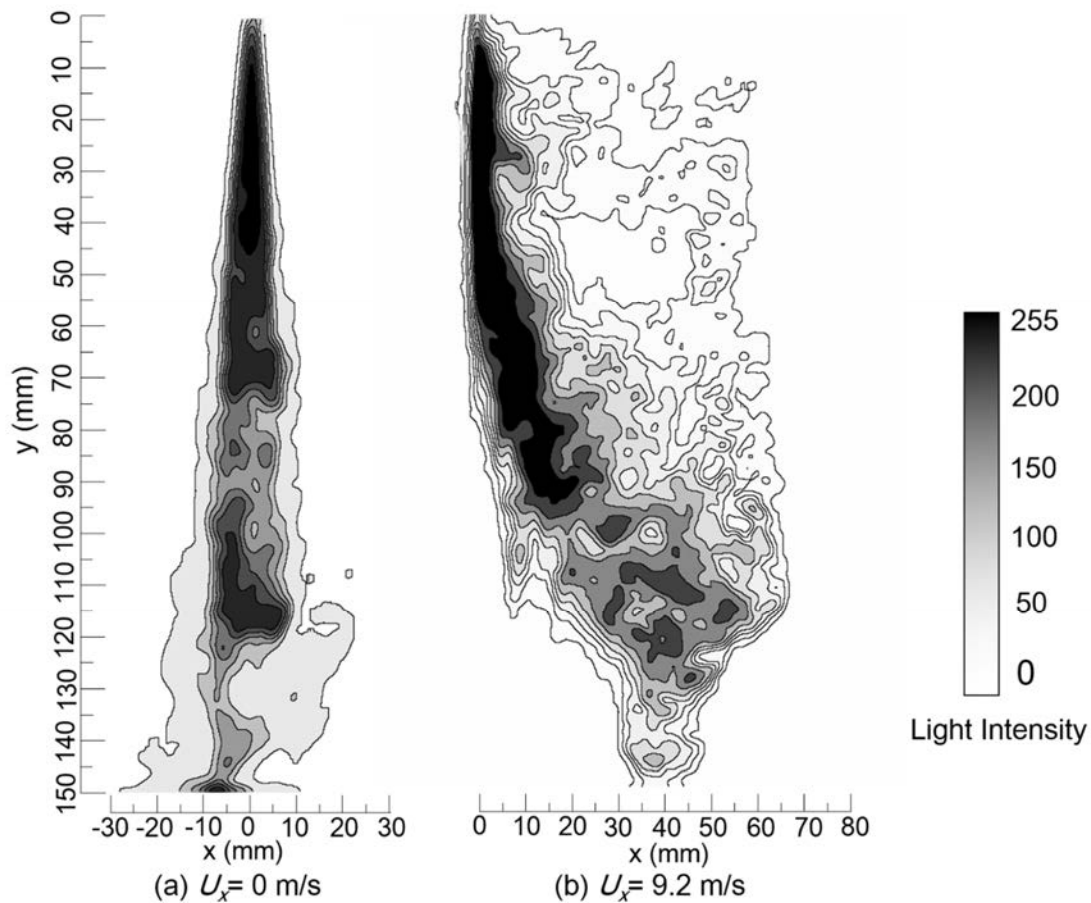


Figure 7.2 Distributions of scattered light intensity in horizontal plane

($P_{inj} = 10\text{MPa}$, $U_x = 9.2\text{m/s}$, 5m ASOI).

The tiny droplets are entrained into the cross-flow, because the influence of the cross-flow on them are more serious than that of the vertical momentum. However, those droplets in the upper part of spray distribute in the edge of the spray, and they are easy to be blown by the cross-flow. The dense droplets, which own high vertical momentum, remain in the center of the spray. In the lower part of the spray, the most of droplets are blown by the cross-flow more or less. The high concentration area is bended and the two tip structure disappeared. The distribution of the droplet concentration represents non-uniform due to complex movement of the droplets.

Those phenomena can be observed more clearly in the horizontal tomographic images in Fig. 7.3. In the upper area of the spray the asymmetrical structure can also lead to the rarefied distribution of droplets in the vertical plane, the vortex phenomenon is observed according to the stagger droplet concentration. The lower part planes of the spray show that the droplets

concentrate in the upstream of the cross-flow, furthermore the spray area increases from $y=25$ to 100 mm and the lower part the droplets concentrate more uniformly than that in upper part. It can be observed that the main spray is blown to the downstream of cross-flow.

In the plane of $y=25$ mm, the intensity of the droplets presents weak, however, the spray column in the plane is composed of the dense droplets, the intensity in that area should be very high. The possibility for this phenomenon is that the light cannot be captured by the camera due to the shading of the dense droplet in the lower part of the spray. Although this effect maybe exist, the droplet distributions can be described by the intensity contour map. It is reasonable that the intensity in the area of downstream is low, because the break-up of the fuel is insufficient and only a small number of the tiny droplets can be flow away from the spray column. There are some circles arrayed in the contour map in the downstream area, because the entrained droplets follow the air flow movement, which is moving in vortices. This effect works not significant from the plane of $y=50$ mm. The high light intensity area appears in the spray column. The main column of the spray is no longer circular, and the droplets are peeled off from both sides of the column. It is clear that the break-up enhanced comparing with the plane of $y=25$ mm, the whole area of the spray increases.

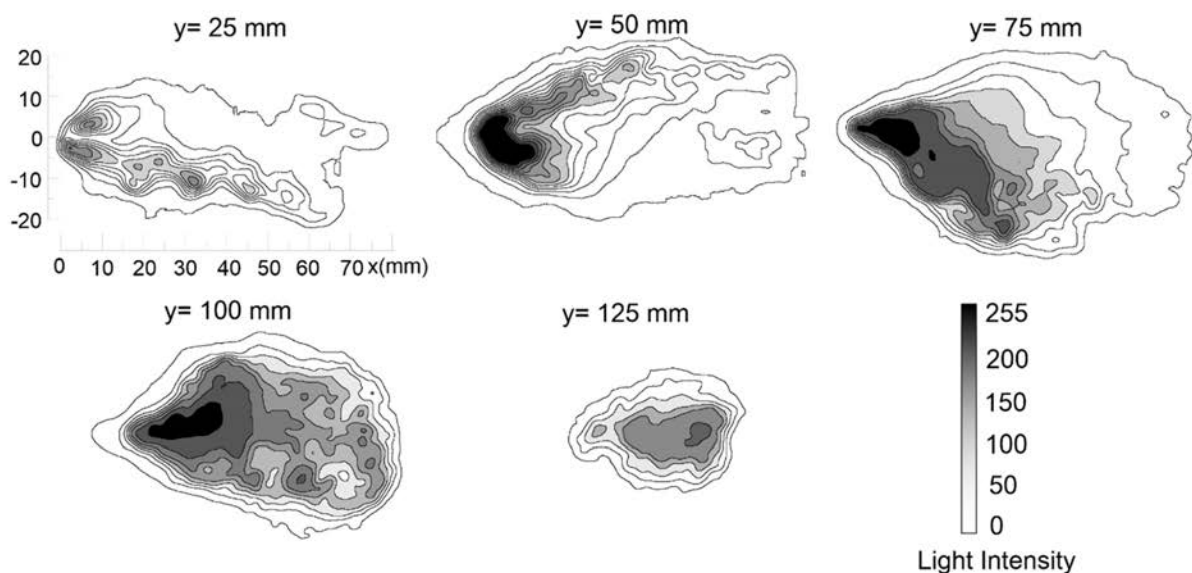


Figure 7.3 Distribution of scattered light intensity in various horizontal planes

($P_{inj} = 10$ MPa, $U_x = 9.2$ m/s, 5 ms ASOI).

In the lower part of the spray, the distributions become more uniform to some extent. The high intensity areas expand due to the break-up and diffusion of the spray. The droplet dense decreases gradually from the main spray column to the outside of downstream in the plane of $y=75$ mm. In this plane, the fuel is under break-up and the spray column is disappearing. In that case, the droplets are continuously blown to the downstream, and the vortex phenomenon becomes weak due to the disappearing of the spray column. The droplet distributions in the plane of $y=100$ mm become more uniform than that in any other planes, and some dense droplet groups appear in the downstream area. The fuel break-up becomes adequately except some droplets, which originally exist inside of the spray and be exposed after that the surrounding droplets are blown away by the cross-flow. The rolling up and swirling phenomenon, which is caused by the interaction of the ambient gas and spray and even exist without cross-flow, is enhanced by the cross-flow. The performance is the turbulence like phenomenon, which make the droplets uniform. The area of the spray in the plane of $y=125$ mm becomes small, because the bended structure of the spray. However, a little high intensity area exists in the upstream of the spray while main high intensity areas exist in the downstream. The downstream area is the main spray part, it is not doubt that this area is dense. The little high intensity area in the upstream of the spray is the droplets, which originally exist inside of the spray and be exposed after that the surrounding droplets are blown away by the cross-flow. This droplets owns larger sizes and high vertical momentum.

7.2 Droplet Size Distribution

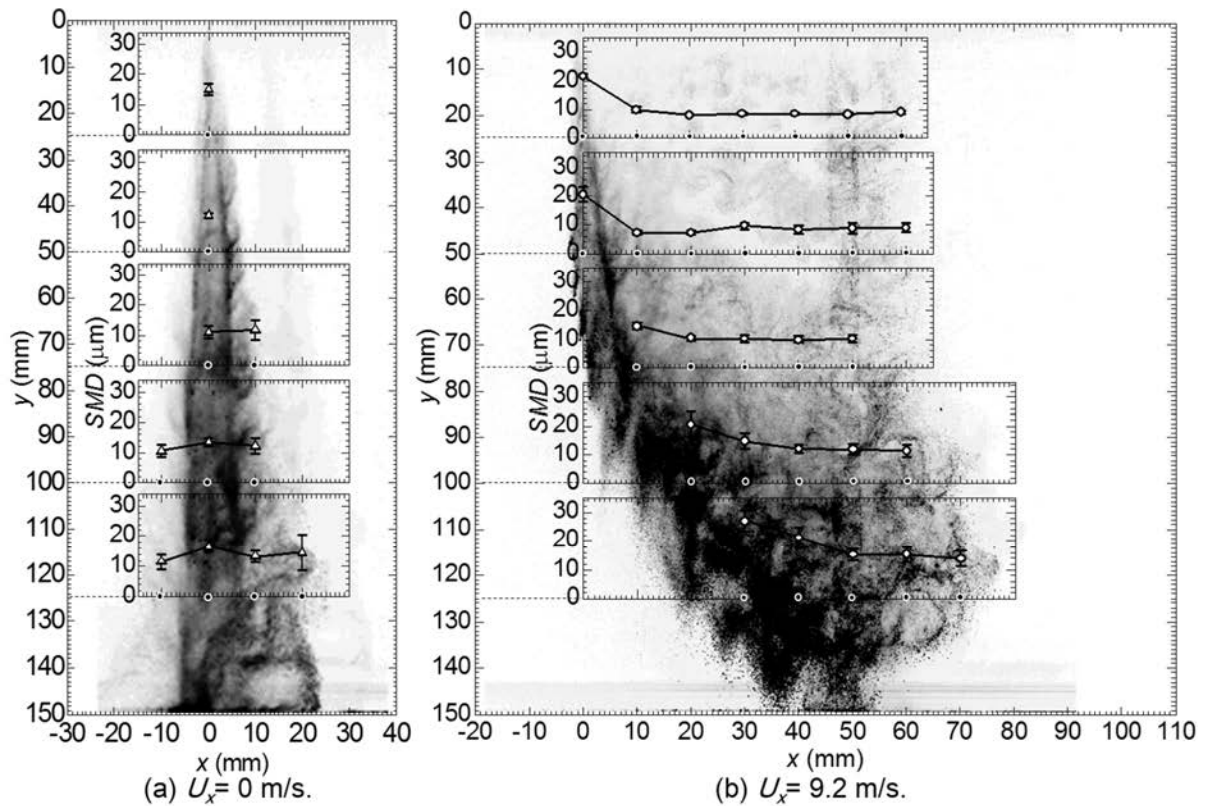


Figure 7.4 Droplet size distributions ($P_{inj} = 10\text{MPa}$, $U_x = 0, 9.2\text{ m/s}$, $P_a = 0.1\text{Mpa}$, around 7 ms ASOI).

The droplet size distributions were measured using LDSA equipment at various points, and the results are shown in Fig. 7.4. Under the condition of no-cross-flow, along the centre line of the spray, the droplet diameters (SMD) presented a slightly decreasing tendency, with the droplets at both sides slightly smaller than those at the centre line. The droplet size was slightly smaller in the area of $x < 0\text{ mm}$ compared to that in the area of $x > 0\text{ mm}$. Because of the two-tip structure of the spray injected by the VCO nozzle, the main branch is close to the centre line, and the other branch is in the area of $x > 0\text{ mm}$. Under the condition of a cross-flow of 9.2 m/s, the droplet sizes decreased along the direction of the cross-flow. Additionally, the droplet sizes in the upper part of the spray remained at around 10 μm , except for the first points, while the sizes in the lower part of the spray gradually decreased. Large droplets were concentrated in the upstream area of the cross-flow, and the values were larger than those under the no-cross-flow condition. This illustrated that

the large droplets were distributed in the high droplet concentration areas according to the preceding droplet concentration discussion. The droplets in the upper area of the spray were at the breaking stage and had a large vertical momentum. Hence, only a small quantity of tiny droplets could be entrained by the cross-flow. The proportion of large droplets at the position of $x = 0$ mm in the cross-flow was higher than that under the no-cross-flow condition, which caused the SMD to be slightly larger in the cross-flow compared to the no-cross-flow condition.

7.3 Cross-flow Effects on Atomization

The aerodynamic force plays an important role in the fuel break-up. The droplets own high vertical velocities in the upper of the spray. At that time, the spray droplets in the surface and inner spray are in the same level of velocity. The interaction of the spray and ambient gas arouses the high aerodynamic force, which acts on the surface of the spray column. The small droplets are peeled from the column and their velocities decrease rapidly. The velocity decreased droplets are entrained in the air flow, while aroused by the relative movements of the spray and ambient gas. The process is one of the factors of the diffusion of the spray. The droplets which have lost their vertical momentum are pushed aside and replaced by the high momentum droplets. Those droplets will repeat the break-up process. However, the central core spray droplets cannot be affected so strong, because the inner air flow have already owned the vertical velocities due to the previous droplet movements, than aerodynamic force affected on the latter droplets of inner spray becomes small. It results in that the inner droplet break-up is worse than the surface droplet and they own high vertical momentum, as shown in Fig. 7.5.

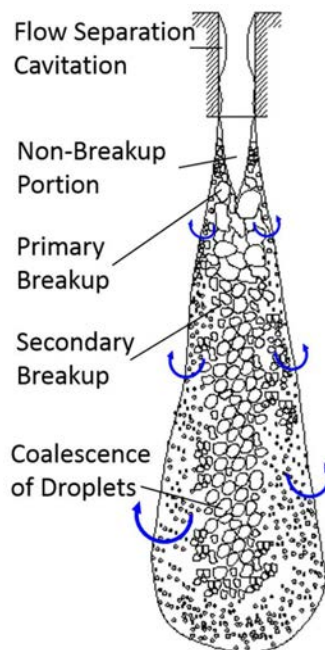


Figure 7.5 Schematic of spray breakup under quiescent ambient.

This situations can be improved under the cross-flow condition. Firstly, the aerodynamic force could be enhanced by the increasing relative velocities between fuel and ambient gas. It leads to

the improvement of the periphery droplet break-up. Next, the interaction of the cross-flow and spray could arouse some instable movement like vortex in the upper part of spray and turbulence. However, the contributions of the low velocity cross-flow is not very serious in the spray break-up, sometimes the coalescences of droplets occur in this condition.

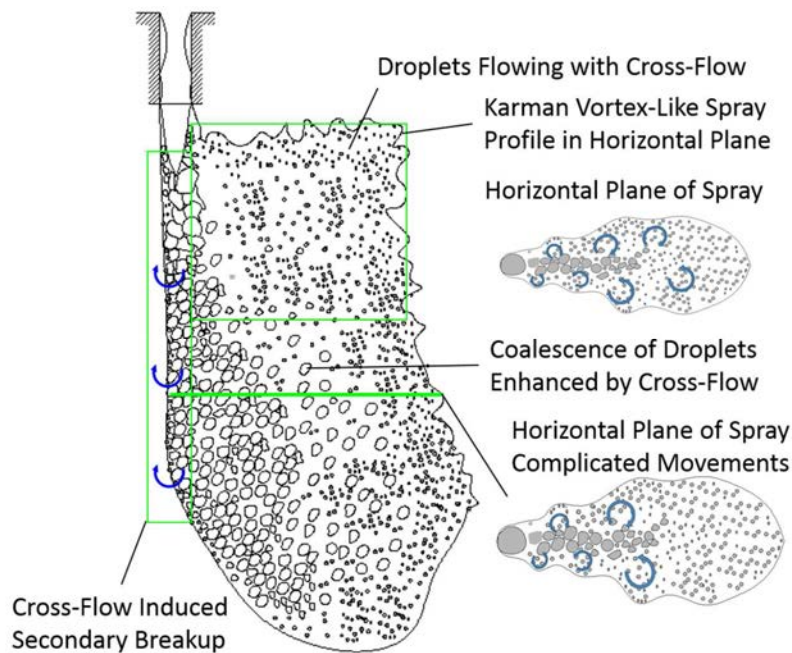


Figure 7.6 Processes of break-up in cross-flow.

The most significant effect is the entrainment of the cross-flow. The cross-flow owns the ability of blowing the periphery broken droplets into downstream, therefore the central core droplets require the opportunity to be exposed in the ambient gas, as Fig. 7.6(a) shows. The exposed droplets with high vertical momentum could break due to the increasing of the aerodynamic force, as Fig. 7.6(b) shows. The broken droplets can easily lose their vertical momentum and be entrained by the cross-flow, the now inner droplets will replace them and repeat the process. The improvement of the central core droplet break-up results in the smaller SMDs in the cross-flow condition. The central core droplet break up increases the proportion of the droplet disintegration.

7.4 Summary

The droplet distributions and sizes are discussed in this chapter. The diffusion of the spray is more obvious in the lower part of the spray than that in the upper part of the spray, droplets disperse along the spray center in the no-cross-flow condition. The minority droplets are blown away by the cross-flow in the upper part of the spray which the droplet distribution becomes non-uniform in the lower part of the spray under the cross-flow of 9.2 m/s at atmosphere. The droplets are squeezed into the center line, and the phenomena of the droplet concentrating along two tips disappear with ambient pressure increasing. The droplet diffusing becomes hard when the ambient pressure increased. In the pressure ambient, the non-uniform distribution, which is similar to that at atmosphere, appears when the cross-flow velocity increases to some extent.

Droplets concentrated in the spray center under the no-cross-flow condition, while a large number of droplets remained in the upstream area of the spray with the cross-flow. Otherwise, larger droplets were distributed in the high-concentration area. Additionally, the diameter of the droplets decreased along the direction of the cross-flow.

The cross-flow can improve the atomization by the entrainment. The cross-flow owns the ability of blowing the broken droplets with low number density in periphery into downstream, therefore the droplets with high number density in central core require the opportunity to be exposed in the ambient gas. The exposed droplets with high vertical momentum could break due to the increasing of the aerodynamic force. The broken droplets can easily lose their vertical momentum and be entrained by the cross-flow, the new inner droplets will replace them and repeat the process.

Chapter 8 Effects of Ambient Pressure on Spray Characteristics

The characteristics of the spray on the cross-flow under various ambient pressure will be discussed in this chapter.

8.1 Temporal Profiles in Various Pressure Ambient

The characteristics of the sprays injected into various pressure ambient are different. The differences of profile and structure of the spray can be observed directly. The spray profiles in atmospheric condition was presented in the previous part (see Figs. 4.3). An arrangement which can compare the spray file at same time is shown in Fig. 8.1, the ambient pressure of 0.2, 0.4 and 0.6 MPa are selected in this part. The test fuel is ethanol and the injection duration is 7 ms.

The spray profiles in atmospheric condition were presented in the previous part (see Fig.4.3), the temporal variations of the spray in various ambient pressure are shown in Fig. 8.1, the ambient pressure of 0.2, 0.4 and 0.6 MPa are selected in this part. The test fuel is ethanol and the injection duration is 7 ms.

From the three picture in Fig. 8.1, with increasing the ambient pressure the penetrations of spray in vertical direction become shorter significantly. At the beginning of the spray (0.4 ms ASOI), the penetration is larger than 20 mm in 0.2 MPa ambient pressure, and the value decreases approximate 5 mm when the ambient pressure increased 0.2 MPa. This content of decreasing become different from 1.2 ms ASOI, the distance which the droplets can reach become shorter and shorter. The spray impinges the bottom wall around 2.4 ms ASOI in 0.2 MPa ambient pressure, however, in that time the spray tip reaches the position of $y= 85$ mm in 0.4 MPa ambient pressure which that only reaches the position of approximate $y= 70$ mm.

The profiles of the spray have changed obviously with increasing the ambient pressure, as shown in Fig. 8.1. In the low ambient pressure (as 0.2 MPa), the spray profiles, which are very similar to that in atmosphere, own tips and these penetrations of the two tips are different, namely the velocity of the right side spray is higher than the lift side, because of the reaching distances. However, this kind of phenomenon become weak when the ambient pressure increase to 0.4 MPa, thereafter the two tip structure disappears when the ambient pressure increase to 0.6 MPa. In the high ambient pressure (0.6 MPa), the acute tip structure of the spray is hardly observed, especially after 0.8 ms

ASOI, the spray tip becomes blunt.

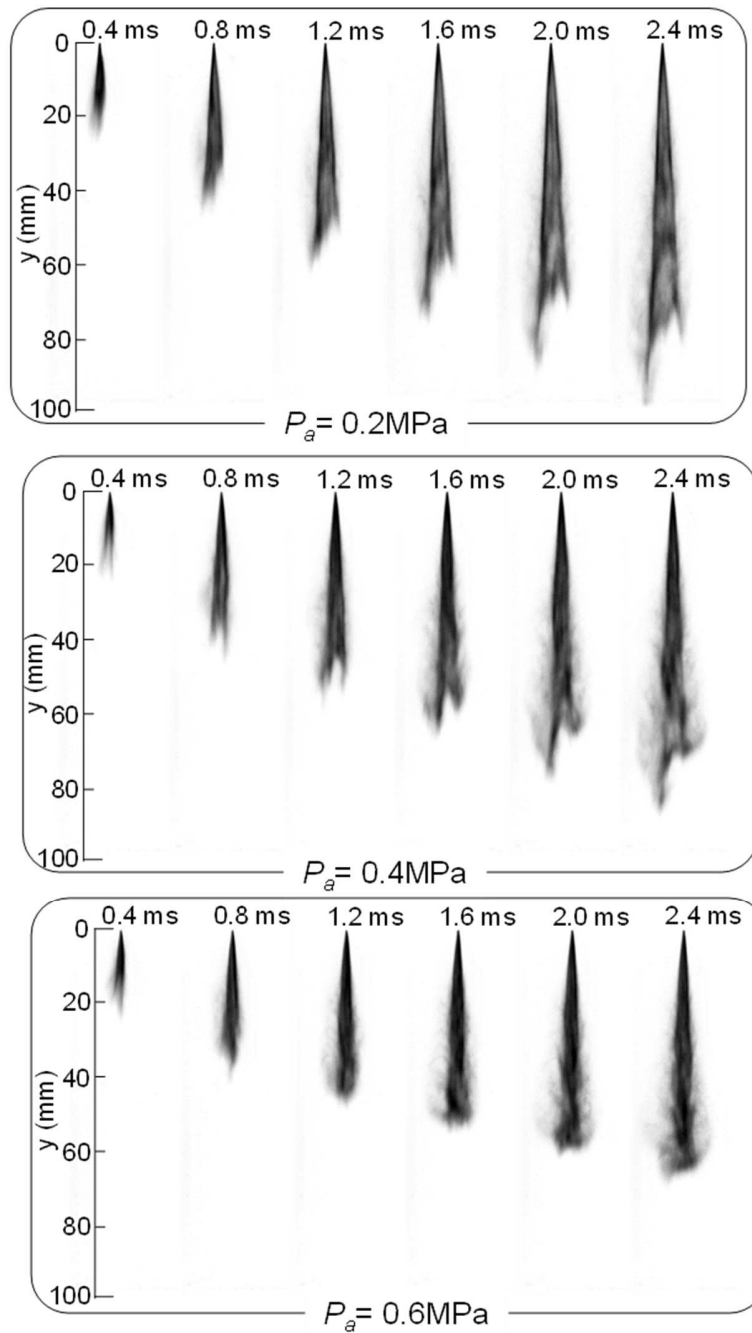


Figure 8.1 Temporal variations of spray in pressure ambient ($P_{inj}= 10\text{MPa}$, $U_x=0\text{ m/s}$, time is ASOI).

The concentration of the droplets in the spray also changed by observing the intensity and volume of the spray images. In the low ambient pressure condition (as 0.2 MPa), the high intensity

areas concentrate along the two tips, and in the both side the tiny droplets can be observed, as well as the droplets in the spray are loose. When the pressure increase to 0.4 MPa, the intensity in the upper part of the spray become high, in spite of that in the lower part keep the structure as that in 0.2 MPa. However, with the disappearing of the two tips, the intensity of the spray represents high in the center of the spray and tiny droplets in the edge of the spray decrease significantly in the ambient pressure of 0.6 MPa.

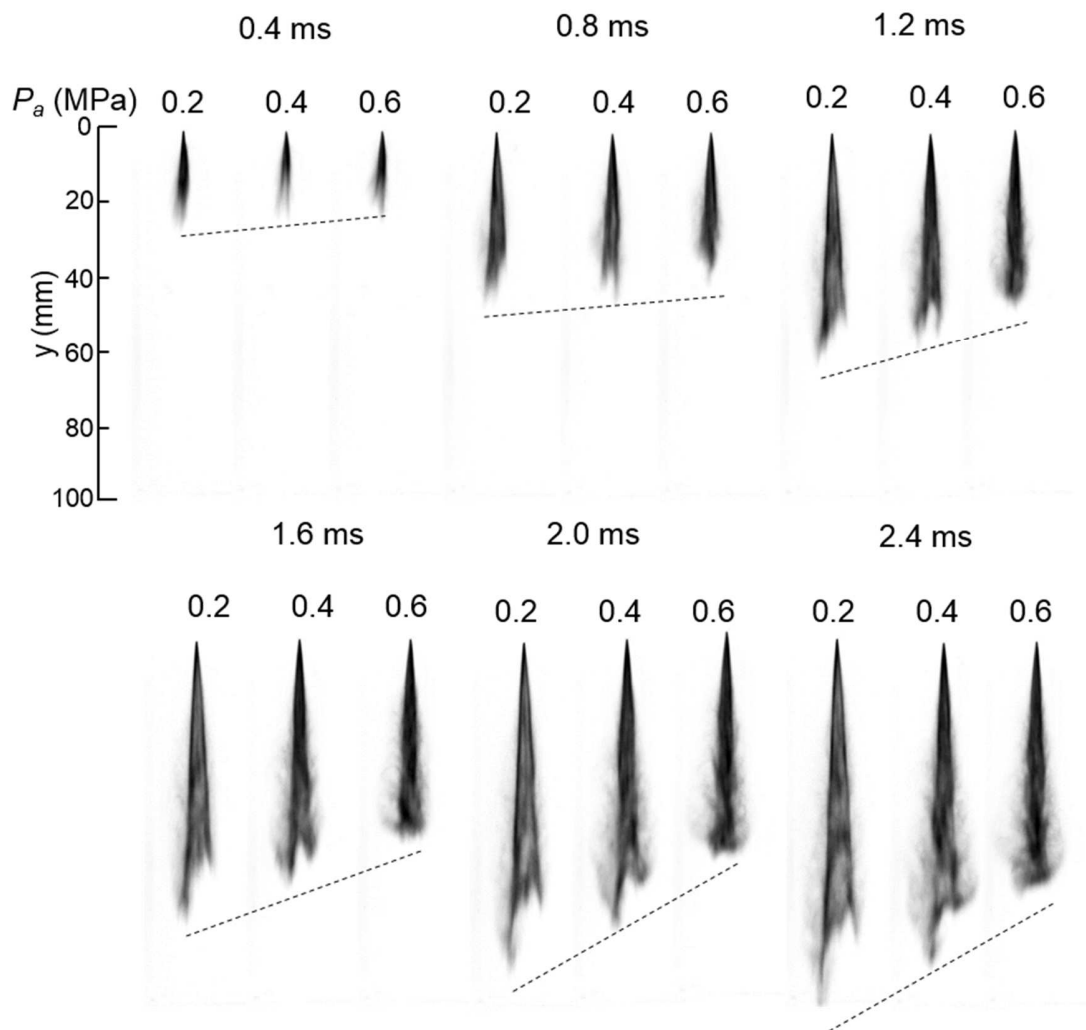


Figure 8.2 Spray variations under different pressure ambient ($P_{inj}=10\text{MPa}$).

With increasing of the ambient pressure, the difference of pressure between the injection pressure and ambient pressure decreases, which can lead to the initial velocity of the droplet of spray injected from nozzle become smaller. The penetration will decrease if the initial velocity of the droplets of spray decreases, because of the momentum decreasing.

The density of the ambient gas increases when the ambient pressure increases, which results in the droplets of the spray will bear larger resistance of the ambient gas. The droplets can lose their momentum more quickly than that in the low density ambient. The droplets of the spray are squeezed by the high density gas, therefore the tip structure disappears and the volume become smaller.

Figure 8.3 shows the temporal profiles of the spray in the cross-flow of 16.8 m/s and the 0.4 MPa ambient. Before 1.2 ms ASOI, the two tips structure can be observed and the lengths of the two tips are almost same, and the spray represent a slight bend, otherwise the spray is swelled by the tiny droplets flowing away. From 2.4 ms ASOI to 4.8 ms ASOI, that phenomenon continues, moreover the spray profile is bended obviously especially in the lower part of the spray; some new tips appear in the lower part of spray in the upstream of the cross-flow (windward side), and in the downstream of the cross-flow (leeward side) the droplets movement become strong according to the non-uniform intensity distribution; the tiny droplets are entrained into the cross-flow in the upper part of the spray. From 5.4 ms ASOI, the tips of the spray disappear gradually, and the rolling movement can be observed in the lower part of the spray. The high intensity of the spray concentrates in the windward side especially in the upper part of the spray. The spray impinges bottom wall around 4.8 ms ASOI, which are later than that in cross-flow of 0 m/s. The horizontal moving distance of droplets cannot match the velocity of the cross-flow 16.8m/s, for example, in 5.4 ms ASOI, the furthest distance (horizontal penetration) is approximate 40 mm while the distance should be around 90 mm if the droplets velocity equals the cross-flow velocity.

To understand the effects of the various velocities of the cross-flow on the spray in the pressure ambient. The temporal variation of the spray in the pressure ambient of 0.4 MPa with the cross-flow velocity varying from 8.1 m/s to 16.7 m/s are listed in Fig. 8.4.

In the low velocity of the cross-flow, the significant bend is hardly observed. The profiles of the spray in the cross-flow of 8.1 m/s are enlarged in the leeward side, however that swelling can be observed in the lower part of the spray in the windward side, as the image of 3.6 ms ASOI shows. The high intensity area also concentrate in the windward side of the spray. With the increasing of the cross-flow velocity, the vertical penetration decreases and the bended area appears. The Bended area appears from bottom with increasing the cross-flow velocity and the bended content increases. The movements in the lower part of the spray becomes obvious in the high cross-flow velocity.

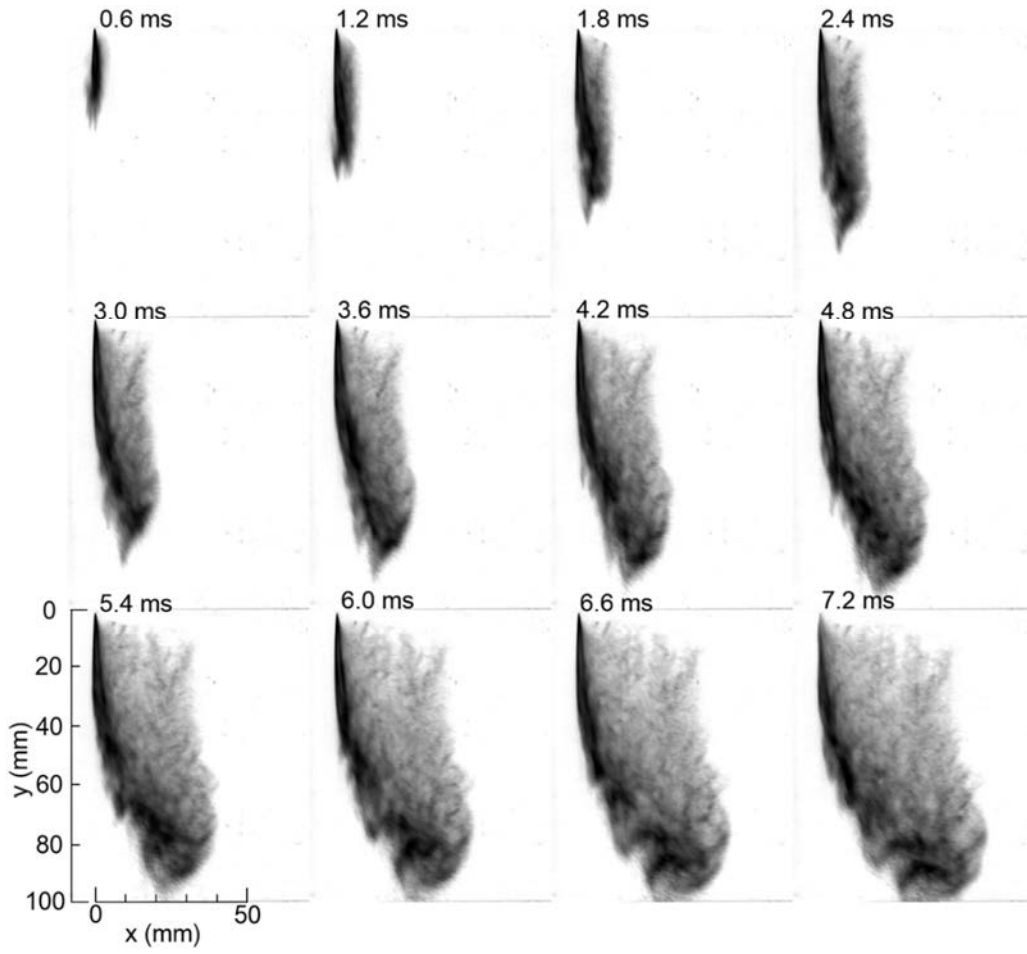


Figure 8.3 Temporal variations of spray in pressure ambient with cross-flow ($P_{inj}= 10\text{MPa}$, $U_x=16.8\text{ m/s}$, $P_a= 0.4\text{ MPa}$, time is ASOI)

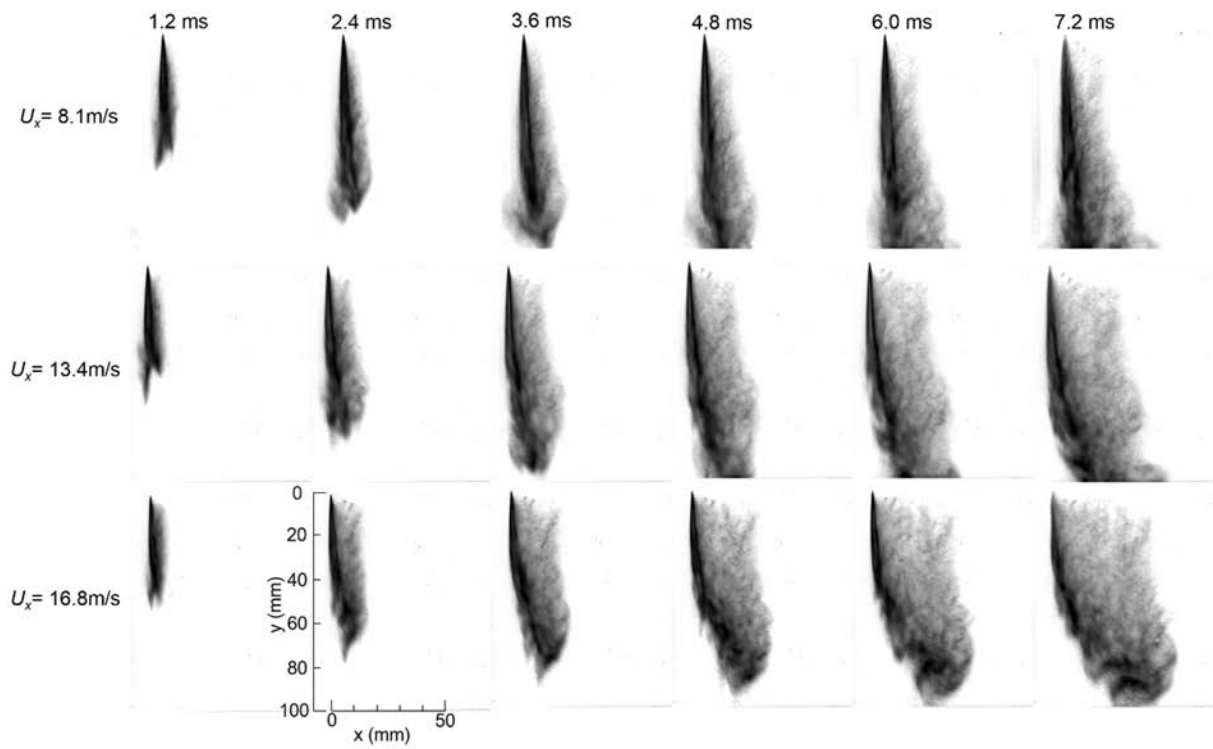


Figure 8.4 Temporal variations of spray in pressure ambient with various cross-flow velocity flow ($P_{inj} = 10 \text{ MPa}$, $P_a = 0.4 \text{ MPa}$, time is ASOI).

8.2 Penetrations of Spray in Various Pressure Ambient

The penetrations are divided into the vertical penetration and horizontal penetration in this study, the definition have been introduced in the previous discussion. Figure 8.5 shows the vertical penetrations of the spray in ambient of 0.1, 0.2, 0.4, 0.6 MPa, and the injection duration is 7 ms. Because the observation section height is 100 mm, the maximum vertical penetration is less than 100 mm. The spray impinges the bottom wall quickly in the ambient of 0.1 MPa, around 1.2 ms ASOI which the impingement happens in 4.5 ms ASOI when the ambient pressure is 0.6 MPa. This phenomenon can be observed in Fig. 8.1. The tendencies of those curves meet that in atmospheric condition, which have been discussed in 4.2.2.

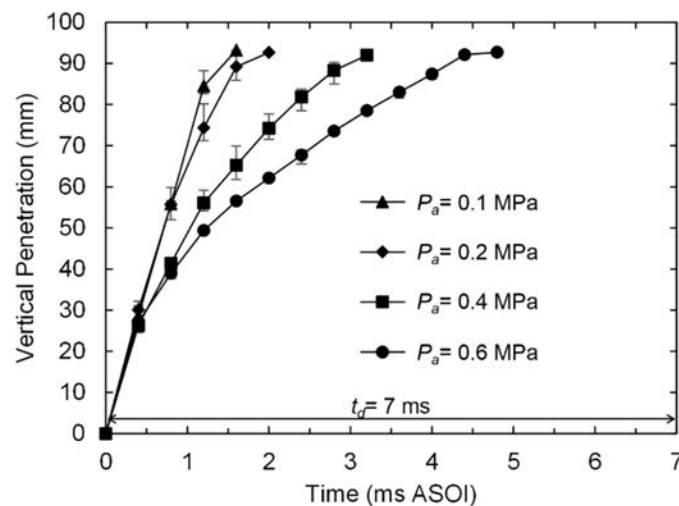


Figure 8.5 Vertical penetrations of spray in various pressure ambient ($P_{inj}=10$ MPa, $U_x=0$ m/s, time is ASOI)

The vertical penetrations of the spray in the cross-flow of 0, 8.1, 13.4, 16.8 m/s are listed in Fig. 8.6. Before 1.5 ms ASOI, the penetrations of the spray hardly change. It indicated that the cross-flow effect on the spray in this period is very weak, due to the insufficient droplets breaking up. After 1.5 ms ASOI, the curve of 0 m/s keeps the original tendency. In the same time, the vertical penetration of the high cross-flow velocity is longer than that of the low cross-flow velocity.

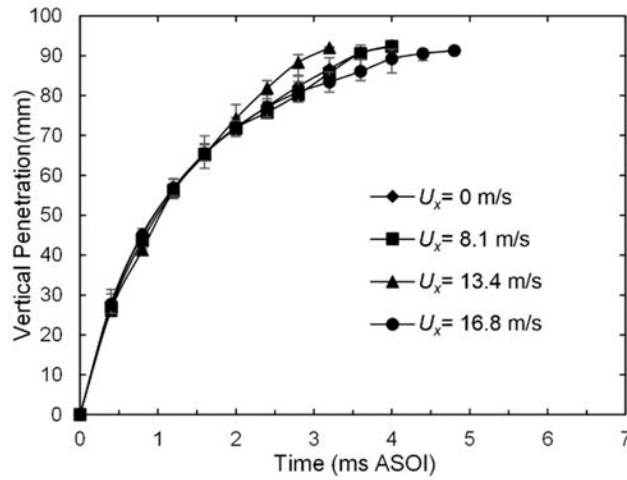


Figure 8.6 Vertical penetrations of spray in various cross-flow velocities ($P_{inj}= 10\text{MPa}$, $P_a=0.4$ MPa, time is ASOI).

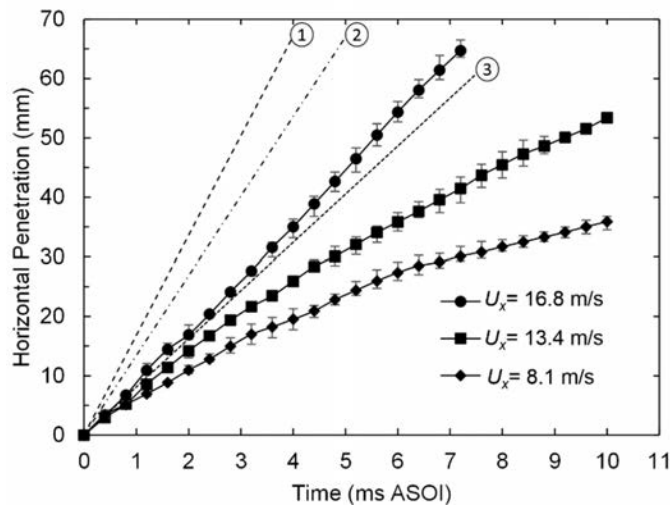


Figure 8.7 Horizontal penetrations of spray in various cross-flow velocities, Cross-flow movement: ① 16.8 m/s, ②: 13.4 m/s, ③: 8.1 m/s ($P_{inj}= 10\text{MPa}$, $P_a=0.4$ MPa, time is ASOI).

The horizontal penetration of the spray in the cross-flow of 8.1, 13.4 and 16.8 m/s are plotted in Fig. 8.7. The penetrations of the spray in the cross-flow of 16.8 m/s and 13.4 m/s represent a linear increasing while that in the cross-flow of 8.1 m/s owns some fluctuations, but the main tendency is closed to a linear line. In the high cross-flow condition, the cross-flow flow is strong enough to delay the impingement time. However, in the low cross-flow condition, the spray impinges the bottom quickly and the roll up the droplets, which can result in the large horizontal penetration in the early period. The dashed lines shows the cross-flow movements in the velocities of 16.8, 13.4 and 8.1 m/s. In this case, the droplets moving velocity is not reach or smaller than the cross-flow

velocity in the pressure ambient, which is different from the conclusion that the droplet velocity is bigger than the cross-flow velocity to some extent in atmospheric conditions. In the pressure ambient, the penetration of spray or the droplet movement distance is approximate a half of the movement of the cross-flow. There are many possible reasons which lead to this phenomenon. The pressure ambient effects on the spray is stronger than that of the cross-flow or the large horizontal penetration cannot be detected. In the atmospheric experiments, the observation chamber height is 150 mm, and the horizontal penetrations which are measured are behind $y=100$ mm. In this case, the horizontal penetrations become short.

Figure 8.8 lists the tomographic images of the spray in the cross-flow of 10 m/s under ambient pressure of 0.1, 0.3, 0.4, 0.5 MPa, the cross-flow velocity is 10 m/s and the time is 7 ms ASOI (the end of injection). The small droplets are blown away by the cross-flow in the leeward of spray, the displacements of the droplets are larger in 0.1 MPa than that in the higher ambient pressure. The droplet distribution does not presents uniformly especially in the low ambient pressure, and with the increasing of the ambient pressure the distribution of droplets in the upper part of the spray in the leeward become more concentrated. The rolling or swirling movements of the droplets can be observed in that area, however, with the ambient pressure increasing this phenomenon becomes weak.

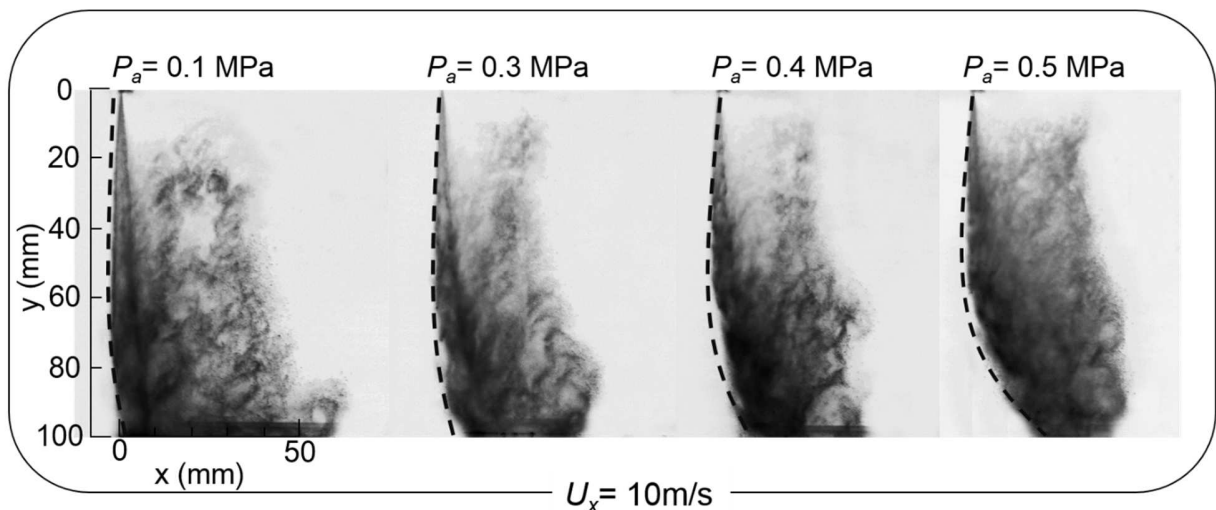


Figure 8.8 Tomographic images of spray in various pressure ambient ($P_{inj}=10$ MPa, $U_x=10$ m/s, 7 ms ASOI)

The profiles of the spray in the upstream change distinctly in the various pressure ambient. The profile of the spray in the upstream is almost straight in the ambient pressure of 0.1 MPa. Because

the impingement distance become shorter comparing that in the atmospheric wind tunnel experiments. However, the bended profiles can be found in the higher ambient pressure conditions, such as 0.3, 0.4 0.6 MPa. Additionally, those profiles are bended more seriously with the ambient pressure increasing.

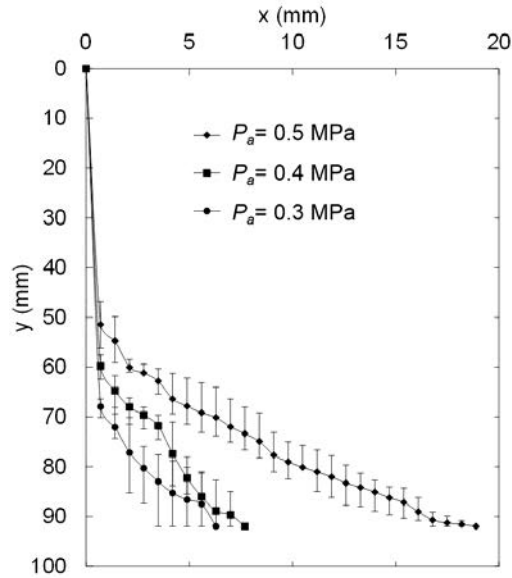


Figure 8.9 Profile of spray in upstream side ($P_{inj}= 10$ MPa, $U_x= 10$ m/s and $t= 7$ ms ASOI).

To further understand the changes of the profiles of the spray in the upstream, the points in the profiles are plotted in Fig. 8.9. That profile formation depends on the cross-flow velocity, fuel initial velocity, fuel density, ambient gas density etc. The phenomenon can be explained by using q (liquid to air momentum flux ratio= $\rho_l U_l^2 / \rho_g U_x^2$). In this condition, the constant parameters are fuel density ρ_l and the cross-flow U_x ; when the ambient pressure increases, the pressure difference between the injection pressure P_{inj} and P_a becomes decreases, which results in the initial velocity U_l of the spray decreases; the density of the ambient air ρ_g increases significantly when the ambient pressure increases. Hence, the liquid to air momentum flux ratio q decreases when the ambient pressure increases, which results in the profiles of the spray in the upstream are bended more serious in the high ambient pressure than that in the low ambient pressure.

8.3 Velocity Distribution in Vertical Planes

In this section, the vertical velocity distribution in the plane of $z=0$ mm will be discussed. The injection pressure 10 MPa and the injection duration 7 ms are same as the atmospheric experiments. The cross-flow velocity was set in 0 and 10 m/s while the ambient pressures were adjusted to 0.3, 0.4 and 0.5 MPa.

The velocity of the droplets in the spray decreases according to the velocity distributions in various ambient pressure in Fig. 8.10. The velocity distribution in the low ambient pressure presents more uniform than that in the high ambient pressure, otherwise the droplets become more concentrated in the center line of the spray when the ambient pressure increases. The non-uniform velocities also appear in the both sides of the spray, however the extent of that become weak when the ambient pressure increases.

The spray is bended by the cross-flow, because the heights of the observation section of atmospheric experiments and the pressure ambient experiments are different, the extents of the bending comparison between the two kinds of experiments is difficult. In the atmospheric experiments, the main bending area is in the lower part of the spray under $y=100$ mm, however the pressure observation section height is 100 mm, hence the bending in the spray is not so distinct. But in the ambient pressure of 0.5 MPa, the bending of the spray in windward side presents obviously, as shown in Fig. 8.11. It is not difficult to find that in ambient pressure of 0.4 MPa the bending extent is larger than that in the 0.3 MPa. It means that the bending extent in the windward side increase with the increasing of the ambient pressure. In the high ambient pressure surrounding, the main velocities of the droplets of the spray decrease and the swirling or rolling phenomenon becomes weak.

The initial velocity of the spray is depended on the pressure difference between injection pressure and ambient pressure. The pressure difference become small when the ambient pressure increase, which leads to the initial velocity of the spray decreases. The ambient gas no longer be influenced like that at atmosphere, because the droplets of the spray own less vertical momentum. The breaking of the droplets is also be affected due to the increased vertical velocity. Additionally, the ambient gas density become large when the ambient pressure increases, hence the resistance upon the droplets become big. The spray diffuses less than that in the low ambient pressure.

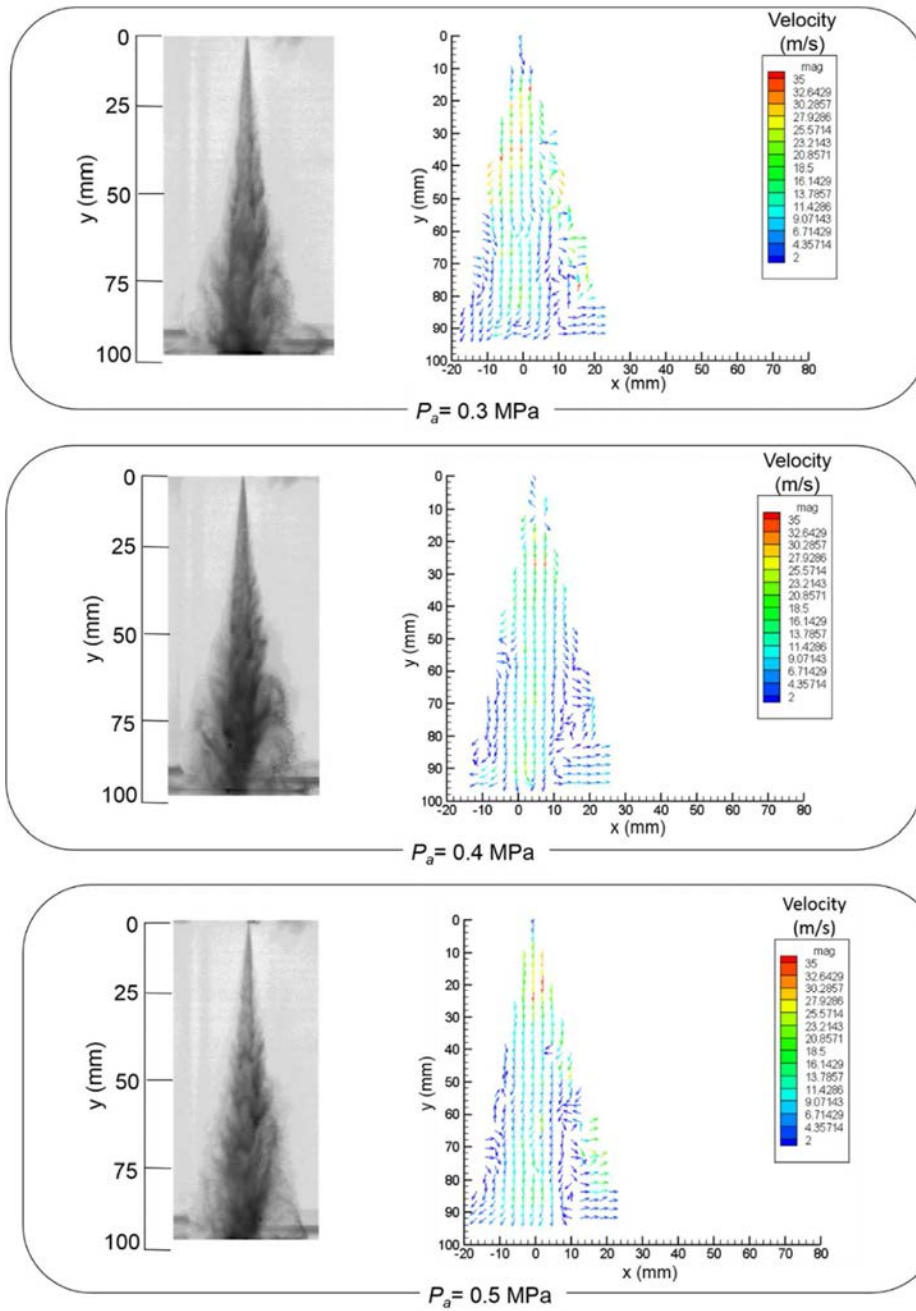


Figure 8.10 Velocity distribution of spray without cross-flow in various ambient pressure ($P_{inj} = 10\text{MPa}$, $T_d = 7\text{ms}$).

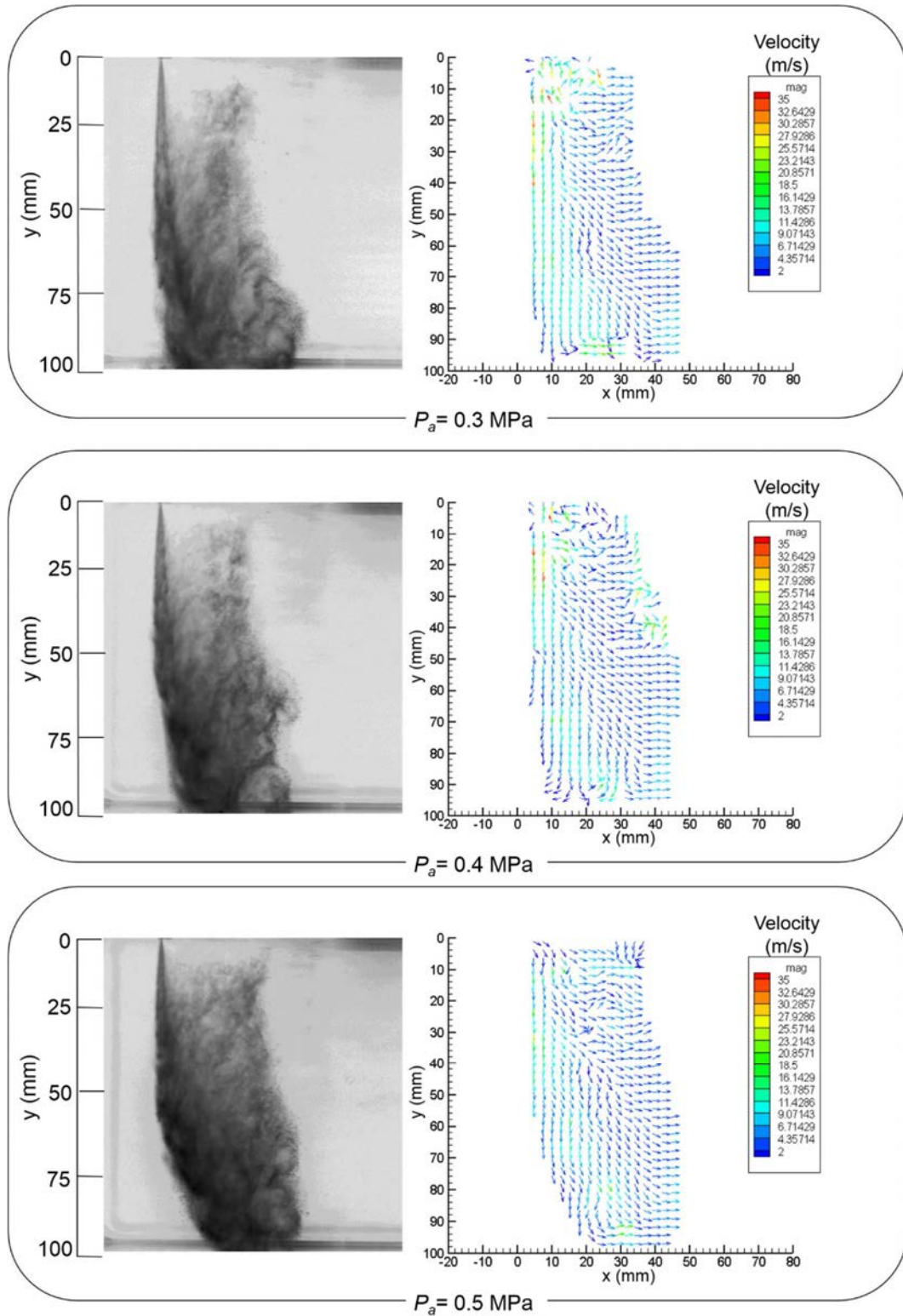


Figure 8.11 Velocity distribution of spray in cross-flow of 10 m/s in various ambient pressure ($P_{inj} = 10$ MPa, $T_d = 7$ ms).

The bending extent increases with the ambient pressure increasing. Firstly, the ambient gas density increases when the ambient pressure increase. In the same cross-flow, in the high ambient pressure the momentum of the ambient gas become larger than that in low ambient pressure. The movement of the droplets in the cross-flow field should be obey the conservation law of momentum. The increased ambient gas momentum can influence spray more in the horizontal direction. Secondly, the initial velocity of the spray decreases with the increasing of the ambient pressure. The vertical momentum loses easily when the cross-flow exists. Finally, the q (liquid to air momentum flux ratio= $\rho_l U_l^2 / \rho_g U_x^2$) can used in explain this phenomenon. The constant parameters are fuel density ρ_l and the cross-flow U_x ; when the ambient pressure increases, the pressure difference between the injection pressure P_{inj} and P_a becomes decreases, which results in the initial velocity U_l of the spray decreases; the density of the ambient air ρ_g increases significantly when the ambient pressure increases. Hence, the liquid to air momentum flux ratio q decreases when the ambient pressure increases, which results in the profiles of the spray in the upstream are bended more serious in the high ambient pressure than that in the low ambient pressure.

The components of the droplet velocities in horizontal and vertical in the lines of $y= 25, 50$ and 75 mm in plane of $z= 0$ mm are plotted in Figs. 8.12, 8.13 and 8.14, respectively.

The horizontal components of the droplet velocity own a tendency of increasing from $x= 5$ mm to $x= 30$ mm in the three lines. Thereafter, the fluctuations appear and the decreasing happens in the end of the curves. The mean horizontal components of the velocity in high ambient pressure present more stable and larger than that in low ambient pressure in the three lines. The value of the horizontal components of the velocity in three lines assume no obvious different distribution.

The values of the vertical components of the droplet velocity in thee lines leap to a peak, then decrease. The approximate tendencies are same, however the peak points and the fluctuations are different in three lines. The vertical components of the velocity in the low ambient pressure are larger than that in the high ambient pressure. The curve is smoother in the high ambient pressure.

In the high ambient pressure surrounding, the diffusion of the spray becomes hard and the ambient gas movement which is caused by the spray become weak. The effects of the cross-flow on the spray become strong with the ambient pressure increasing.

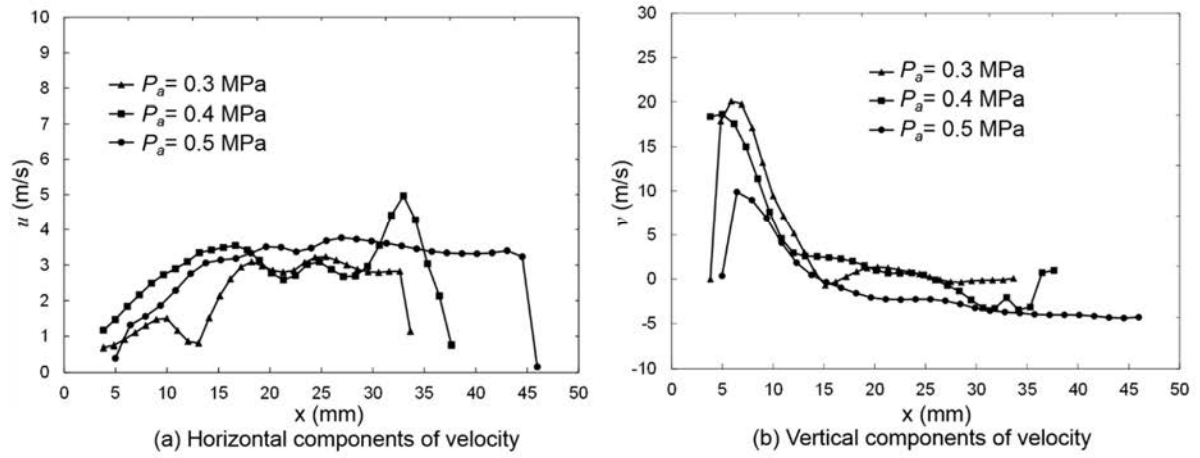


Figure 8.12 Velocity distribution in the line $y = 25$ mm (plane of $z = 0$ mm).

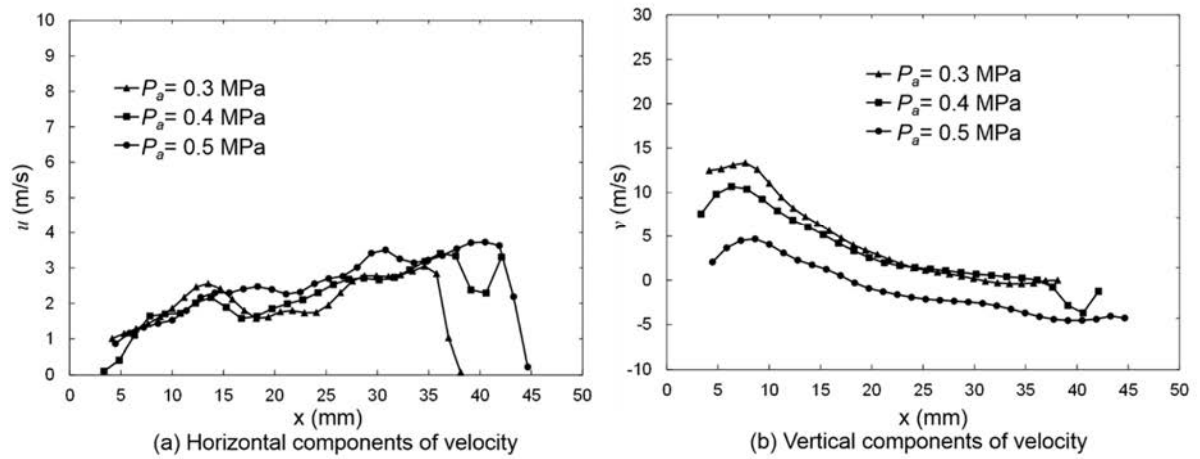


Figure 8.13 Velocity distribution in the line $y = 50$ mm (plane of $z = 0$ mm).

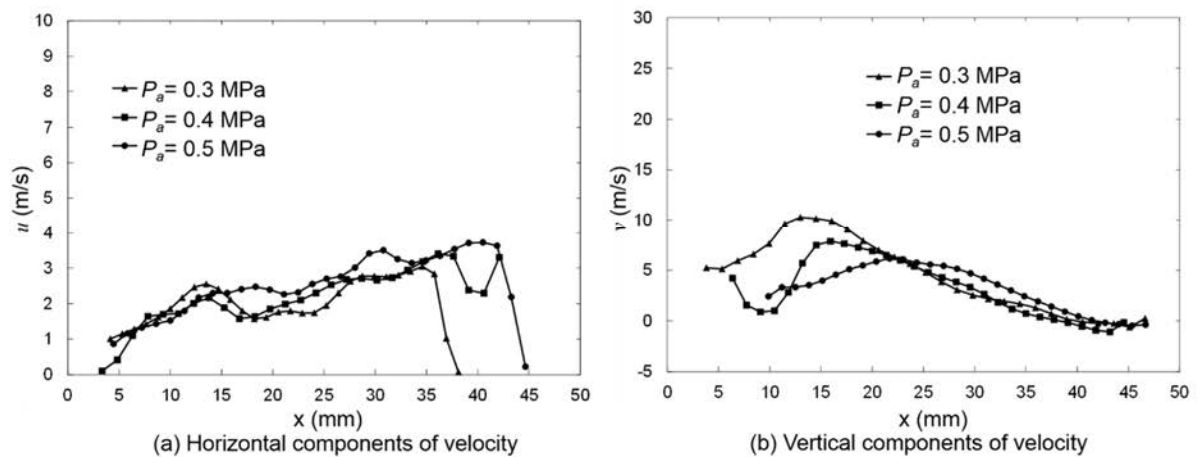


Figure 8.14 Velocity distribution in the line $y = 75$ mm (plane of $z = 0$ mm).

8.4 Droplet Distribution

The scattered light intensity of the spray images can describe the droplet distributions in the spray. Mie scattering photography was employed to obtain the spray images in the vertical plane.

The differences between the images of the spray in various pressure ambient are the profiles, with the increasing of the ambient pressure the two tips structure disappear and the spray becomes symmetrical. The droplet concentrations coincide to the structures, the droplets mainly concentrate along the two tips in the low pressure ambient, thereafter they distribute symmetrically with the ambient pressure increasing, as shown in Fig. 8.15. The content of the concentration of the spray in the low pressure ambient is weaker than that in the high pressure ambient, because the light intensity in spray in the low pressure ambient is more uniform than that in the high pressure ambient, moreover the main droplets concentrate more close to the center of the spray in the high pressure ambient. However, the diffusing of the spray in the high pressure ambient in horizontal is more obvious than that in the low pressure ambient.

With the increasing of the ambient pressure, the difference between the injection pressure and ambient pressure decreases while the density of the ambient gas increases. The less initial velocity can be obtained due to the decreased pressure difference. The increasing of the initial velocity of spray is an important reason of phenomenon described above. The ambient gas resistance on the droplets becomes strong, because of the increasing of the gas density. In this case, the two tips of the spray are squeezed to the center of the spray. The droplets in the edge side are decelerated rapidly and flow with the gas movements, which are cause by the perturbation of the spray. Although this kind of diffusion appears, the droplets are concentrate in the center line. This kind of concentration makes the droplet much denser. It means that the ambient pressure increasing, which restrains the droplet diffusion, is no benefit for the mixture of air and fuel.

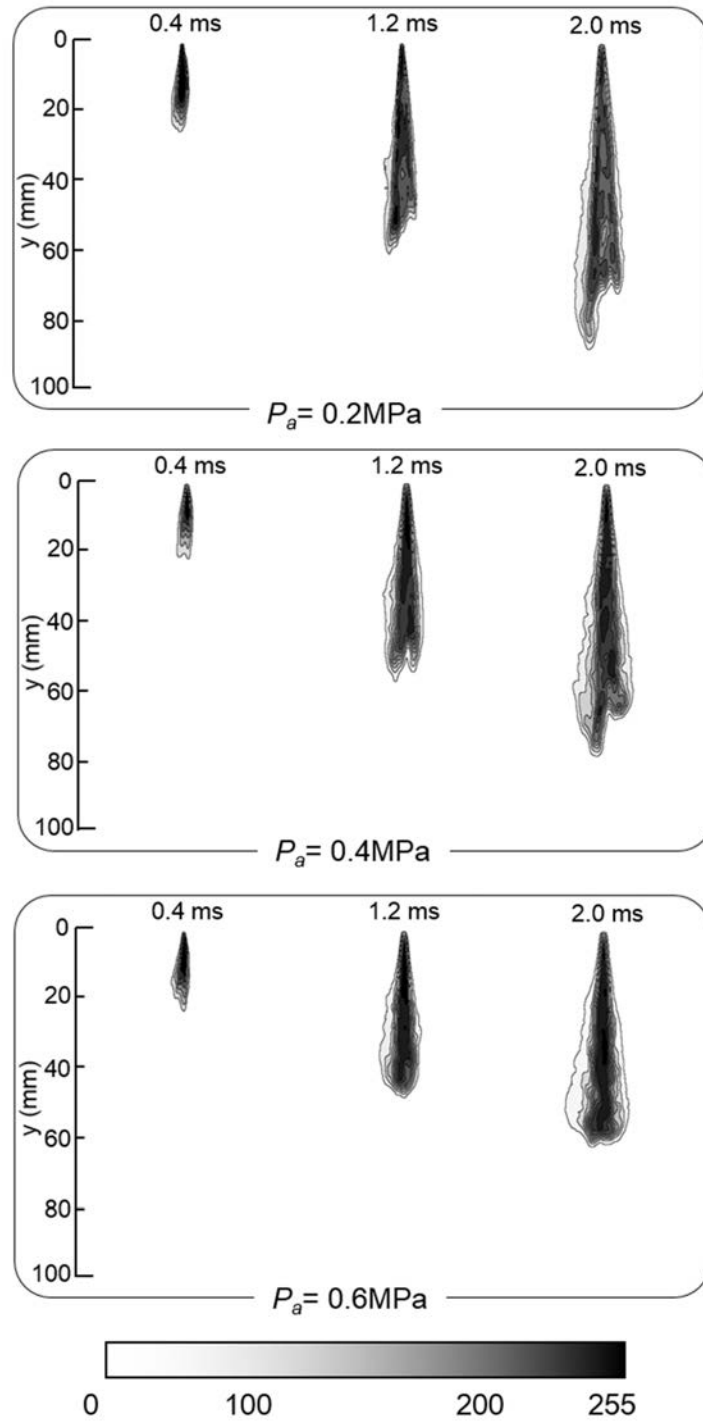


Figure 8.15 Distribution of scattered light intensity in various ambient pressure

($P_{inj} = 10 \text{ MPa}$, $U_x = 0 \text{ m/s}$, $P_a = 0.2, 0.4$ and 0.6 MPa).

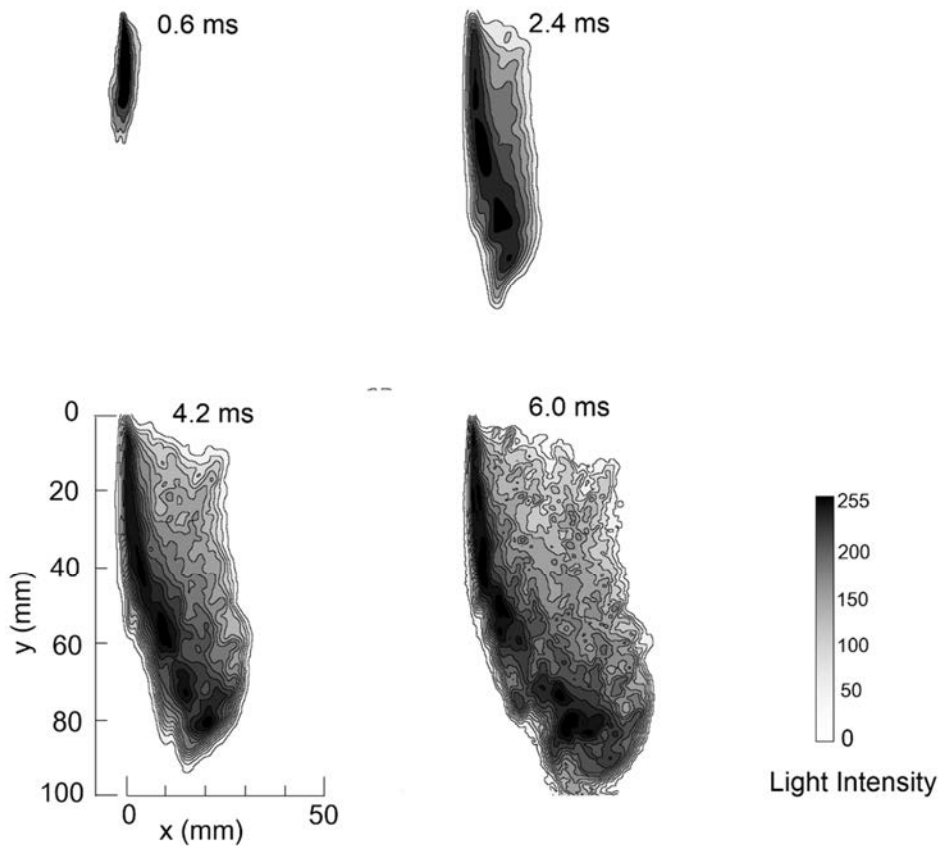


Figure 8.16 Distribution of scattered light intensity in ambient pressure of 0.4 MPa

$$(P_{inj} = 10\text{MPa}, U_x = 16.8 \text{ m/s}).$$

To understand the droplet concentration changes under same ambient pressure in the same cross-flow in various time, the distribution of the scattered light intensity in ambient pressure of 0.4 MPa are listed in Fig. 8.16. It is similar to the atmospheric condition that the main droplets in the spray concentrate in the windward part in the spray, but the diffusing content is different from that in the low ambient pressure. The droplets concentrate compactly, the more small droplets which are entrained are observed in the leeward in the upper part of the spray.

It indicates that the spray diffusing in the pressure ambient have a decline, the influence of the ambient pressure on the droplets is more serious than that of the cross-flow. With the ambient pressure increasing, the initial velocity of the spray decrease, the atomization becomes bad. The big droplets are uneasy to be entrained into the cross-flow or move slightly. In this case, the spray droplet movements no longer represent complex like that in the low ambient pressure ambient. For

example, the vortex phenomenon, which have been observed in the upper part of the spray in leeward under atmosphere, is hardly to see in this condition. The vortex phenomenon probably exists in the high pressure ambient condition, however, the representation cannot be observed by the big droplets.

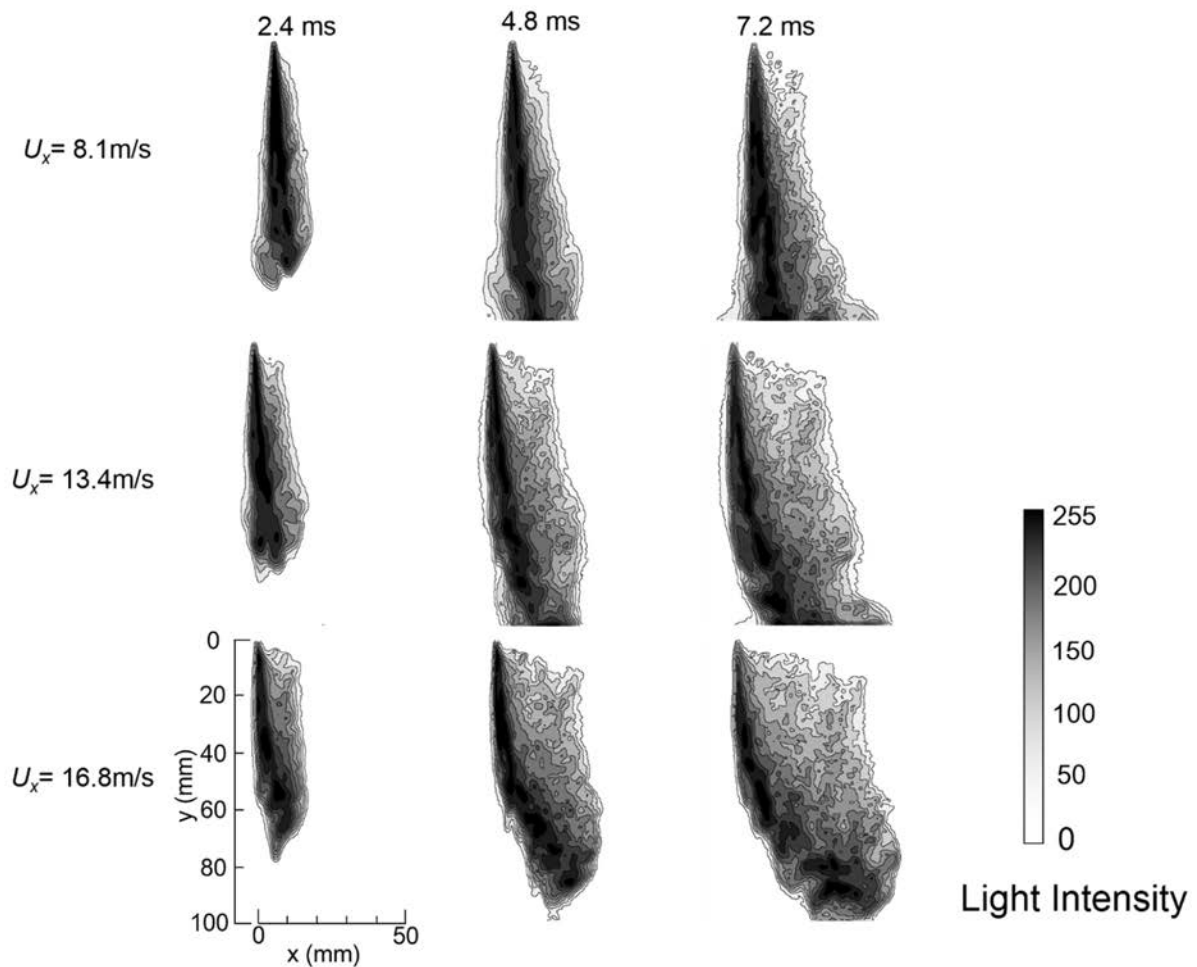


Figure 8.17 Distribution of scattered light intensity in ambient pressure of 0.4 MPa

($P_{inj} = 10 \text{ MPa}$, $U_x = 8.1, 13.4, \text{ and } 16.8 \text{ m/s}$).

The spray droplets distributions are not influenced very much in the low cross-flow condition. The droplets in the edge of the spray at the upstream are squeezed into the spray, and the minority droplets are blown out of the spray by the cross-flow, the most droplets remain in the center of the spray at the 8.1 m/s cross-flow, as shown in Fig. 8.17. The changes happen in the lower part of the spray with the increasing the cross-flow velocity. The distributions in lower part of the spray

no longer concentrate in the skewed center line, but the non-uniform distributions appear in this part. In the high cross-flow condition ($U_x = 16.8$ m/s), the phenomenon is more similar to that in the atmosphere. It is indicated that the effects of the cross-flow velocity and the ambient pressure have a balance. The increased ambient pressure restrains the diffusion of the spray while the increased cross-flow velocity enhance the droplet dispersing along the cross-flow at atmosphere.

The droplet concentrations can be presented by the distribution of scattered light intensity in various ambient pressure images, as shown in Fig. 8.18. The droplets concentrate in the main spray, however, many high dense droplet groups appear in the downstream of the cross-flow in the ambient pressure of 0.1MPa. It means the spray diffuses well in the low ambient pressure cross-flow field. With the ambient pressure increasing, the dense droplet groups disappear in the upper part of the spray. The droplets mainly distribute in the bended structure.

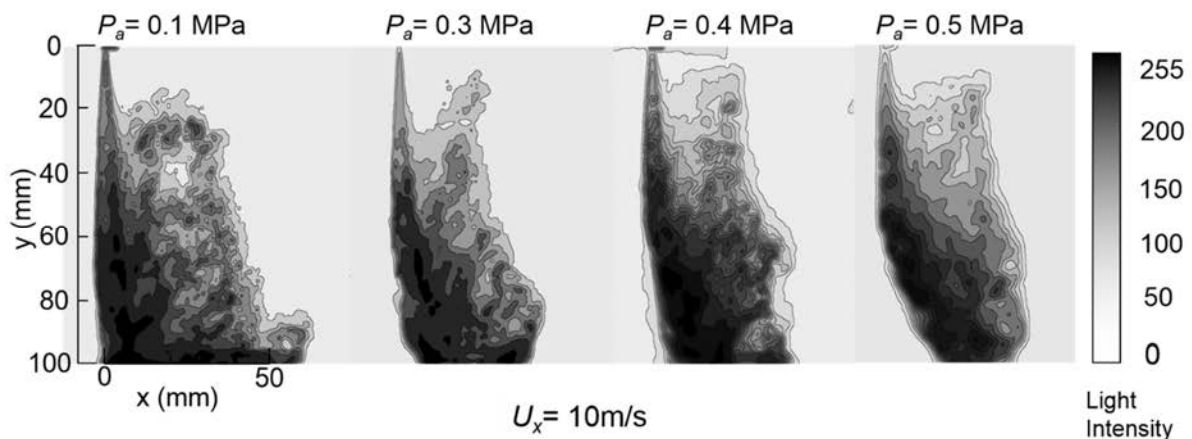


Figure 8.18 Distribution of scattered light intensity in various ambient pressure ($P_{inj} = 10$ MPa, $t = 7$ ms ASOI, $U_x = 0$ m/s, $P_a = 0.1, 0.3, 0.4$ and 0.5 MPa).

8.5 Summary

The effects of the ambient pressures on the spray have been discussed in this part. The profiles of the spray under quiescent ambient and the cross-flow ambient with various ambient pressure have been listed. The penetrations of the spray under various ambient pressures have been measured for the discussions. The velocity distributions and the droplet concentrations on the various ambient pressures were discussed.

The penetration decreases and the tips of the spray disappear gradually with increasing the ambient pressure in the quiescent condition. With the cross-flow, the vertical penetrations of the spray in the high ambient pressure become shorter than that in the low ambient pressure. The displacements of the droplets in horizontal decrease obviously with the ambient pressure increases. The profile of the spray in the upstream side of the cross-flow become more bending in the same cross-flow velocity with increasing the ambient pressure.

The increased ambient pressure can restrain the spray diffusion to some extent. The bended structure of the spray are enhanced in the high pressure ambient in the cross-flow field. The velocity distributions become ordered when the ambient pressure increases. The droplets concentrate to the main spray with the high ambient pressure.

Chapter 9 Numerical Simulation

9.1 Basic Equations and Modeling

9.1.1 Basic Equations

The fuel break up are composed of two processes, the primary break up and the secondary break up. The primary break up occurs in the area near the nozzle with large Weber number. The secondary break up mainly occurs in the spray outside area, in which the effects of air motion increase. The spray modeling involves multiphase flow issues, which needs to resolve the conservation equations of the gaseous phase and the liquid phase simultaneously. There are many models for the various atomization processes, such as momentum interaction between droplets and gas, turbulent dispersion, evaporation, secondary break up, and impingement. The typical models include TAB model (O'Rourke and Amsden, 1987), GM model, WAVE model (Liu and Reitz, 1993), KH-RT model (Su et al, 1996), Huh-Gosman model (Huh et al, 1998), and LISA model (Schmidt et al, 1999).

In TAB model, the vibration and deformation of droplets are analyzed by the analogy of spring mass system, the correlations of droplet deformations are built based on this theory, and the break up types are adjusted by the deformations. This model is suit for the situation of low Weber number. GM model was proposed by Reitz and Diwakar (1987), it divides the spray droplet break up into two types, bag break up and stripping break up. This model is built based on the single droplet break up, which owns the advantage of simplifying the application. However, it cannot represent the effects of the flow inside nozzle on the droplet break up. Recently, the instable surface wave theory is considered as an important method in investigating the droplet break up and widely utilized in building the internal combustion engine models. It indicates that the increasing of the Kelvin-Helmholtz (KH) instable waves result in the droplets stripping from liquid column, this model is suited for conditions of high relative velocity and high ambient gas density. KH-RT model is an improvement of the WAVE model, the disturbance is included in this model. The LISA model represents that the KH instable waves occur in the surface of liquid film. The cavitation effects are involved in this model.

The fuel spray was analyzed based on Lagrangian spray module, which resolves the conservation equations of the liquid phase and the vapor phase simultaneously. A group of droplets

with the identical properties are represented by a parcel in the liquid phase simulation with a statistical discrete droplet method (Hoethorst et al., 1991; Liu et al., 1993). A source term of an additional transport equation for the vapor void fraction in Eulerian formulation was employed to describe the vapor of spray.

The conservation equations of mass, momentum and energy for the multiphase flows are shown as Eqs. 9.1 to 9.3.

$$\frac{D\rho}{Dt} + \rho \frac{\partial u_i}{\partial x_i} = 0 \quad , \quad (9.1)$$

$$\rho \frac{Du_j}{Dt} = \rho \left(\frac{\partial u_j}{\partial t} + u_i \frac{\partial u_j}{\partial x_i} \right) = - \frac{\partial P}{\partial x_j} + u_i \frac{\partial \tau_{ij}}{\partial x_i} + f_j \quad , \quad (9.2)$$

$$\rho \frac{De}{Dt} = \nabla \cdot (\lambda_h \nabla T) - P(\nabla \cdot \vec{u}) + \mu \varphi + \frac{\dot{Q}_s}{dx_1 dx_2 dx_3} \quad , \quad (9.3)$$

where, x_i and x_j are the coordinates in the different directions (m); u_i and u_j are the velocity components in the different axis (m/s); τ_{ij} is stress tensor (N); f_j is the body force (N); e is internal energy (J); λ_h is heat transfer coefficient (w/(m·K)); T is temperature (K); μ is dynamic viscosity (Pa·s); φ is dissipation function; and \dot{Q}_s is heat flux (J). Equation 9.1 is the continuity equation, Equation 9.2 shows the conservation of momentum, and Equation 9.3 describes the conservation of energy.

The basic Reynolds averaged Navier-Stokes (RANS) governing equations were used in this study for shortening the calculation time and simplifying the processing. The standard $k - \varepsilon$ model was chosen to provide the description of the turbulent kinetic energy and its dissipation rate (Launder and Spalding, 1974).

The numerical simulation of the spray in the cross-flow was implemented using CFD code AVL FIRE®. In this part, the sub-models will be presented, such as the sub models of the spray break-up, droplets interaction, evaporation, and wall interaction.

The parameters of this simulation are listed in table 9.1. The core injection model was selected as the primary break-up model. There are two primary break-up models in AVL FIRE, Blob injection and core injection. The Blob injection model usually be used in the high pressure

Table 9.1 Parameters selection for simulation.

Process	Model	Index of Coefficients	Description	Selected Value
Primary Break-up	Core Injection	C_1	Specify turbulent time scale (Critical to spray tip penetration)	10
		C_2	Specify break-up length scale (critical to spray spreading angle)	5
		C_3	Specify aerodynamic time scale (critical to spray shape)	0
Secondary Break-up	Huh/Gosman	C_1	Specify break-up length (Critical to spray tip penetration)	2
		C_2	Specify aerodynamic wavelength	0.5
Evaporation	Dukowicz	E_1	Heat transfer parameter	1
		E_2	Mass transfer parameter	1
Wall interaction	Walljet0		No break-up	

injection like diesel injection. It indicates that a competition of the effects on break-up between turbulence and aerodynamic force exists. While the core injection model describes that the break-up is mainly caused by the aerodynamic force. In this study, the injection pressure is not very high comparing with diesel injection, the core injection model was selected as the simulation model. In the practical calculations, the results presented un-conspicuous difference between this two models. It illuminate that the primary break-up works weakly in the spray break-up.

The secondary break-up model employed the Huh/Gosman model. Wave model is widely used in the diesel spray simulations, it suits the conditions of high injection pressure and multi-hole injector. KH-RT model is an improvement of the WAVE model, the disturbance is included in this model. The cross-flow is a significant parameter in this study, the effects of the cross-flow on the spray should be represented in the simulations.

This experiments were taken under room temperature, however, the test fuel was ethanol and evaporation should be considered. The Dukowicz model was selected as the evaporation model, in which the heat transfer and mass transfer are considered to same. This simulation focused on observing the effects of the cross-flow on the spray, the impingement problem is next step work. In that case, the impingement model was set as walljet0, which is the simplest impingement model without break-up.

9.1.2 Simulation mesh and injection

A calculation domain, which coincided the real size of the observation section, was used in the simulation, as shown in Fig. 9.1. The mesh size is $2\text{mm}\times 2\text{mm}$ and distribute uniformly. The inlet and outlet were set as the velocity inlet and outlet with pressure of atmosphere. The nozzle was arranged in the origin of the coordinate system and that was some to the real position. The calculation time was set to 20ms, and the injection started at 5ms and ended at 12ms. Because the pressure changed gradually to constant before 5ms, if the injection started before 5ms, the uniform ambient cannot be achieved. The injection duration was 7 ms, and the injection total mass was 8.862mg, which was measured from the practical nozzle. Hole-type nozzle was selected as the test injector. It was no way to simulate the VCO structure in the simulation, it indicated that the spray profile and penetration were difficult to meet the experimental results.

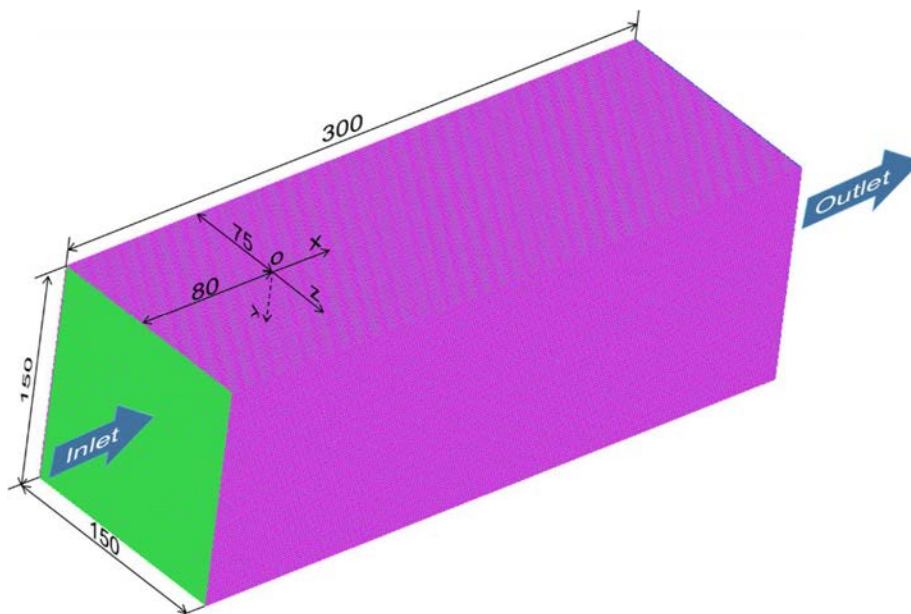


Figure 9.1 Computational mesh for spray simulation (Unit: mm).

9.2 Spray Profile Variations

The observation of the spray profiles is the most direct way to understand the spray and the cross-flow effects. The profile variations of simulation will be discussed in this part.

Figure 9.2 shows the profiles of the spray under quiescent ambient. Comparing with the experimental results (see Fig. 4.3), the two tip structures cannot be observed in this simulation. The sprays are almost symmetrical to the spray center line. Droplets concentrate along the center line. The diffusing of spray in horizontal is smaller than the experimental results. The spray tendency and the distribution are almost same to the experimental results. The wall impinging times are slight different, around 3.8ms ASOI the spray tip reach the bottom wall in experiments, while the spray impingement occurs after 4 ms ASOI.

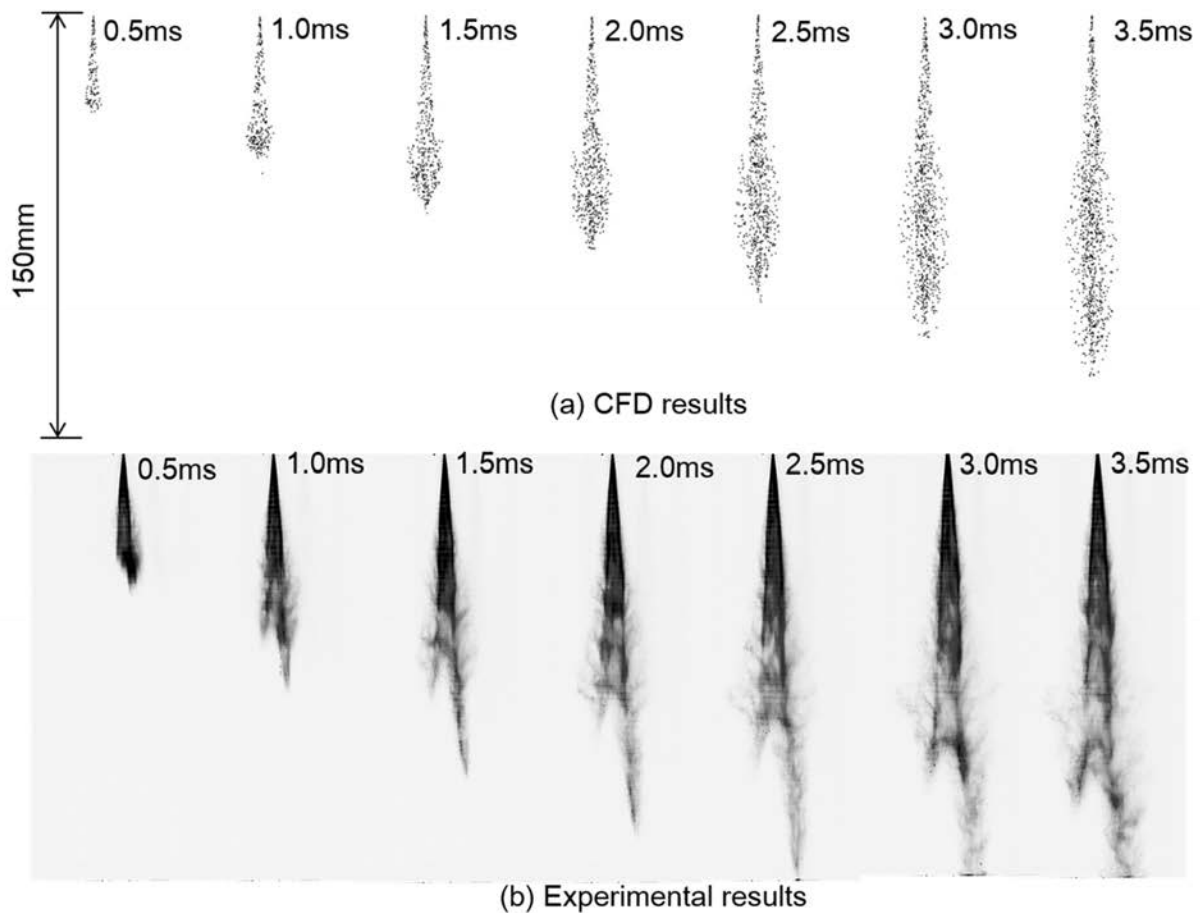
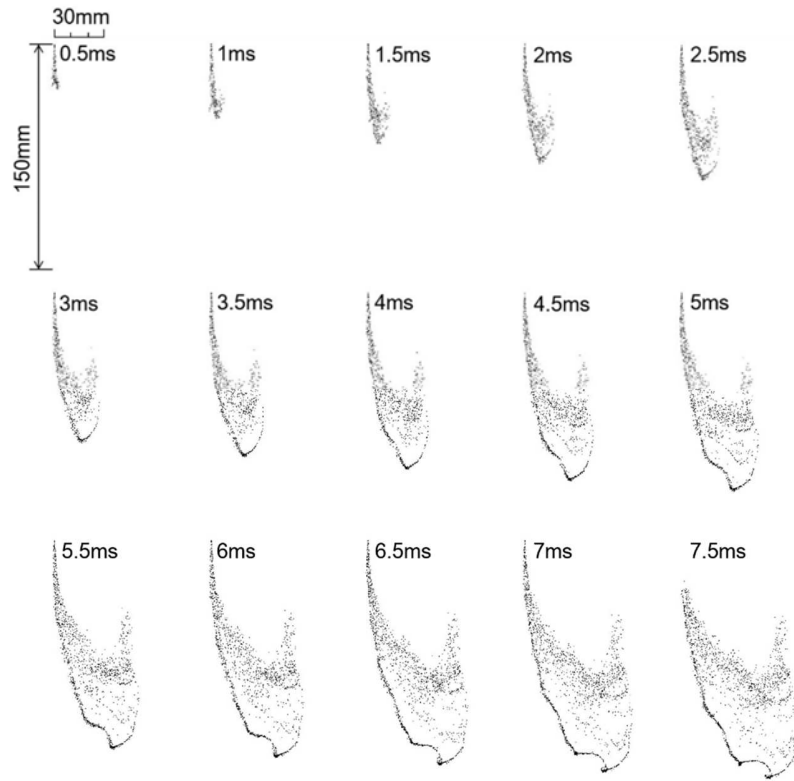


Figure 9.2 Profile variations of spray without cross-flow ($P_{inj}= 10\text{MPa}$, $t_d= 7\text{ms}$, and time is ASOI).

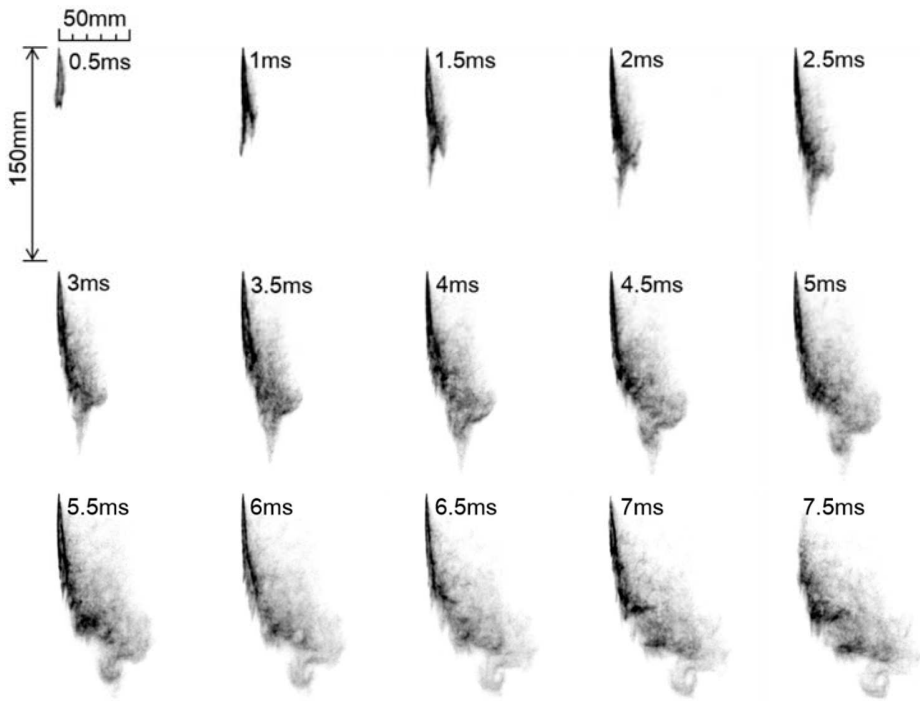
The profiles of spray simulated by CFD are shown in Fig. 9.3(a). The sprays are bended by the cross-flow, which is similar to the experimental results shown in Fig. 9.3(b). Before 1ms ASOI, the spray profile changes are hardly to observe, the tiny droplets move to the downstream of the cross-flow. However, in the upper part of the spray downstream the cross-flow there is no droplet, the profiles in that area like an opposite 'check mark'. The lower part of this an opposite 'check mark' increases over time. The profile edges of the spray in the upstream are smooth before 4.5 ms ASOI, while the curves become no longer smooth in the lower part begin at 4.5 ms ASOI. This phenomenon is very similar to the experimental results, because the droplet movements in the lower part become swirling or rolling. The droplets in the edges line of spray in upstream is denser than other parts, which coincides to the experimental results. However, the main distributions are different from the experimental results. The tip structures, which appear in the edges line of the spray in upstream, cannot be observed in the CFD results. The simulation is based on the hole-type nozzle, but the VCO feature cannot be described by the calculation models.

The top view profiles are shown in Fig. 9.4. This view images cannot be obtained by the practical experiments. From Fig. 9.4, the displacements of the droplets are observed clearly, because only horizontal projections are shown. The sprays are not very symmetrical to the x axis, especially the last 4 images. The wave structure appears in the profiles of the spray. The densest area is close to the nozzle position, namely the main spray column. Additionally, the droplets concentrate in the middle line and both sides, which are different from the experimental analysis. The diffusions in horizontal are enlarged comparing to the spray without cross-flow. This phenomenon is similar to that of the experiments. It is indicated that the cross-flow enhances the horizontal diffusions.

There are many reason which can cause the difference between the experimental results and CFD results. Firstly, the nozzle model difference may result in the spray structure difference. As described, the VCO nozzle spray owns two tips under the low pressure ambient. This structure cannot be detailed in the models. Secondly, the break-up model parameters should be advanced to suit the profile of the spray. The spray can be more close to the experimental results with the right parameters in the break-up models. There are many parameters, which present different physical meanings. It is difficult to adjust the parameters in the best values at one time. Finally, the mesh drawing may be another reason. The fine mesh can improve the calculation results and shorten the



(a) CFD results



(b) Experimental results

Figure 9.3 Profile variations of spray under cross-flow of 9.2 m/s ($P_a = 10\text{MPa}$, $t_d = 7\text{ms}$).

calculation time. The mesh in the spray area can be drawn denser, the more detailed results can be obtained.

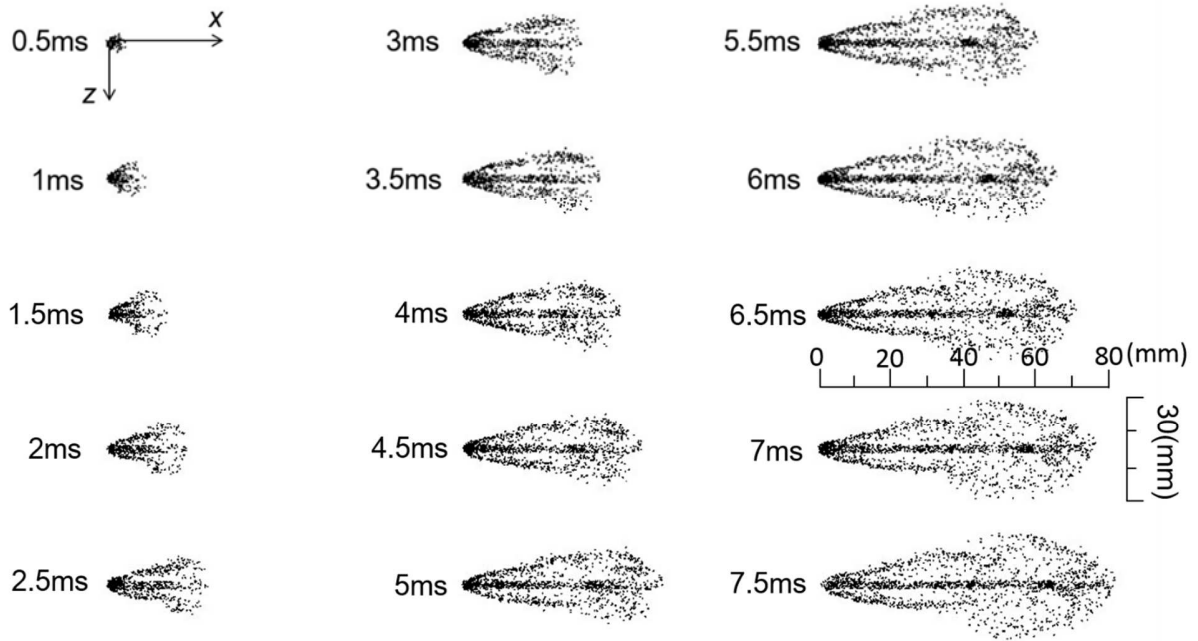


Figure 9.4 Profile variations of spray (Top view, $P_a= 10\text{MPa}$, $t_d= 7\text{ms}$).

9.3 Spray Penetrations

Penetration is an important parameter in the investigation of the spray characteristics. Usually, the spray length between the nozzle hole and the spray tip is defined as the penetration. In this study, the penetrations include two parts, vertical penetration and horizontal penetration. The definitions have been shown in Fig.4.4. In this part, the penetrations of simulation will be discussed comparing with the experimental data.

Without the cross-flow, the vertical penetrations are the normal penetrations, which have been defined by other researchers. According to Hiroyasu and Arai (1990), the penetration of spray owns two stages, the penetration grows linearly in the first stage while the penetration becomes a function of $t^{\frac{1}{2}}$. The experimental and CFD results are shown in Fig. 9.5. There are some difference between those two data. The experimental penetration is higher than CFD penetration at the same time.

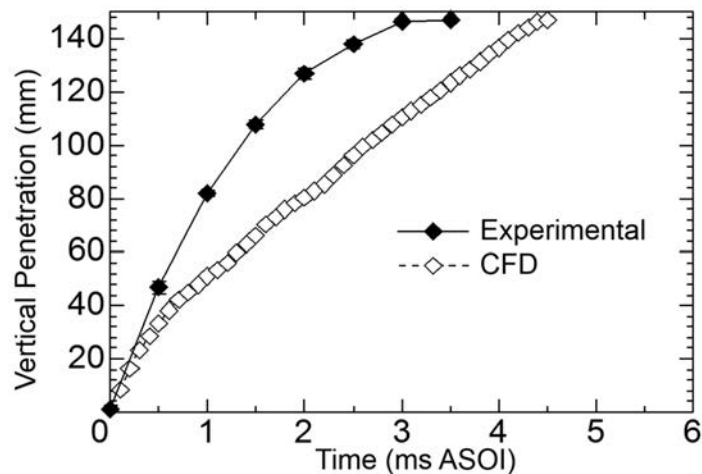


Figure 9.5 Vertical penetration of spray without cross-flow ($P_a= 10\text{MPa}$, $t_d= 7\text{ms}$).

The parameters of the simulations were set using the experimental conditions, such as ambient pressure, injection duration, and test fuel. Those difference may be caused by the two reasons. The insufficient calculation model of nozzle and break-up models. The two penetration stages in the CFD data cannot be observed clearly. The injection pressure setting in the simulation was controlled by the mass of the injection, in that case the injection feature cannot be presented by the simulation.

With the cross-flow, the vertical penetrations are the lengths of the spray in vertical over time. The experimental results and CFD results are shown in Fig. 9.6. As the penetration without cross-flow, the CFD penetrations are shorter than that of the experiments at the same time point. The tendencies of them are almost same. The effects of the cross-flow on the spray are weak in the early stage of the spray, thereafter the vertical penetrations are shortened by the cross-flow comparing with that in the no-cross-flow condition.

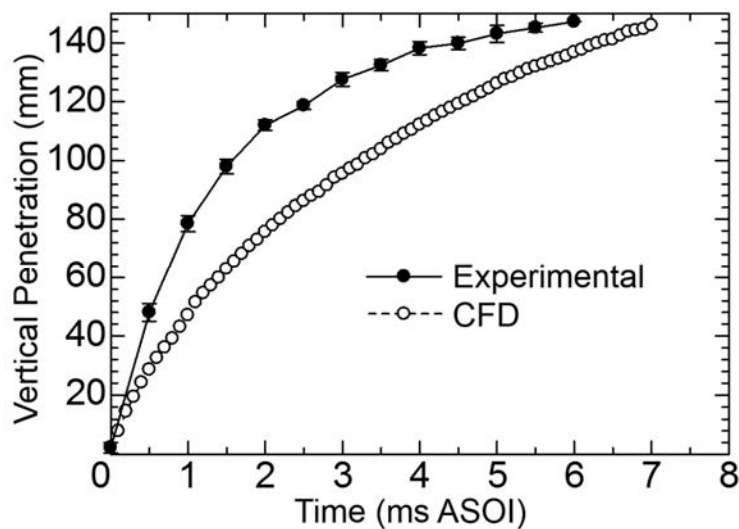


Figure 9.6 Vertical penetrations of spray with cross-flow of 9.2 m/s ($P_a= 10\text{MPa}$, $t_d= 7\text{ms}$).

Horizontal penetrations are the horizontal lengths of the spray, it is mainly dependent on the cross-flow velocity. Figure 9.7 shows the experimental and CFD results of the horizontal penetrations. The penetrations distribute linearly with different slopes. The slope of the experimental data is slightly larger than that of CFD data. From the slope of the CFD data, the droplet velocity is close to the cross-flow velocity.

In the practical experiments, the droplet movement is complex, which can be observed from the profile variations of the spray under cross-flow. The swirling or rolling phenomenon appears in the spray. However, in the spray simulation, this kind of phenomenon is hardly to be seen (see Fig. 9.4). The droplets, which own horizontal velocity, move like a parabola. The interaction of air flow and spray could not be represented by the CFD models.

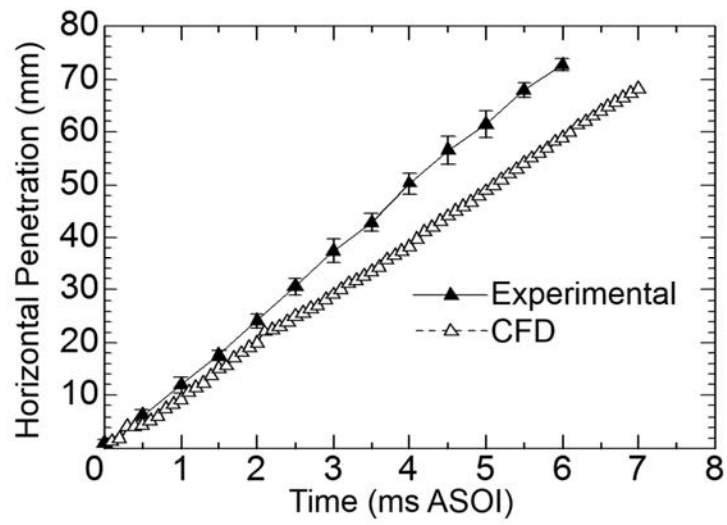


Figure 9.7 Horizontal penetration of spray cross-flow of 9.2 m/s ($P_a= 10\text{MPa}$, $t_d= 7\text{ms}$).

9.4 Velocity Distributions

Velocity distributions of the flow field is significant for analyzing the spray characteristics. The experimental investigation based on PIV technique has been discussed in Chapter 6. In the vertical plane of $z=0$ mm without the cross-flow, the phenomenon of the two tips structure is very distinct and the main directions of the velocity vectors are ahead along the two tips before impinging the bottom wall, and the spray presents a swelling tendency and the droplets velocities become unsteady in the middle part. After impingement, the two tips structure and its velocity distribution phenomena present no longer distinctly and the velocity distributions of the droplets become normal, the high velocity parts concentrate in the center line of the spray, and the low velocity vectors distribute in the both sides of the main spray. The rolling-up phenomenon happens after impingement, otherwise the vector directions meet this movement.

Figure 9.8 shows the velocity distributions of $z=0$ mm plane. The high velocities are distribution along the center line of the spray in the condition of the no-cross-flow, as shown in Fig. 9.8(a). The velocity decreases gradually in radial directions. Some roll-up structures are observed around spray and the bottom wall.

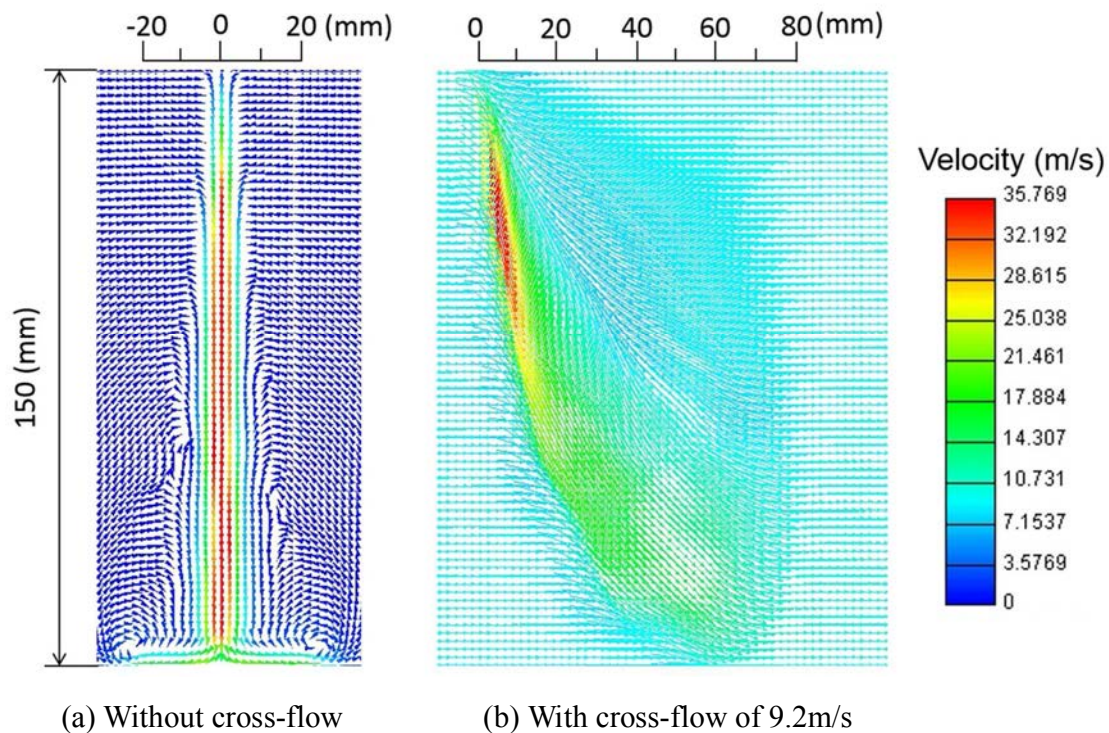


Figure 9.8 Velocity distributions of spray ($P_a=10$ MPa, $t=7$ ms ASOI).

The velocity distribution in the plane of $z=0$ mm with the cross-flow of 9.2 m/s is shown in Fig. 9.8(b). The high velocities concentrate in the upstream of the cross-flow in the upper part of spray. In the leeward of the spray, the velocity decreases and the directions changes. This distribution is similar to the PIV results (see Fig. 6.3). The CFD velocities present much smoother than that of the experimental results, and the velocity distribution more uniform. In the leeward of upper part of spray, the velocity distribution presents the ambient gas movements, hence the difference exists between them.

In the condition of the no-cross-flow, the droplets of the spray are broken by the relative movement with ambient gas, and the big droplets which own large vertical momentum are divided into many small droplets. Hence, the surface resistance which is produced by the ambient gas increases. It results in the small droplets decelerate rapidly and some tiny droplets lose their vertical momentum or be entrained into the air flow, which is caused by the spray movement. Those tiny droplets can be blown away by the cross-flow, because the size of those droplets is small enough and the vertical momentum is very low. The droplets in the surface of the spray are broken and also making the ambient gas moving whose directions is same with the main droplets, so the inner droplets of spray get the lower resistance from ambient gas, moreover the extents of the droplets breaking and vertical momentum losing are less than that of the droplets in the surface of the spray.

To understand the details of the velocity distribution of the cross-flow field, the horizontal velocity distributions in the planes of $y=25, 50, 75, 100,$ and 125 mm of CFD results are shown in Fig. 9.9. The measuring time is 7 ms ASOI (end of the injection). The experimental velocity distributions have been shown in section 9.2 (see Fig. 6.11). In the simulation results, the high velocity areas appear in the both sides of the spray, and with the spray column increasing the areas enlarge. In the upper part ($y < 50$ mm), the velocity distributions are symmetrical, however, in the lower part the symmetrical velocity distribution no long exists. In some areas, the velocities exceed the cross-flow velocity of 9.2 m/s, this phenomenon appeared in the experimental results.

In the upper part of the field, when the air flow passing the spray column the pressure around the column changes. The pressure in the windward side of the spray will increase rapidly and the leeward side pressure will decrease simultaneously, and the spray column approximates a circle. In that case, the air can be accelerated by the pressure difference around the spray column, which causes the velocities exceed the cross-flow velocity. In the lower part, this kind of spray column

disappeared due to the break-up of the spray, however, the droplet movements are no longer uniform as the upper part. The interaction between the cross-flow and the spray makes the field instable, which is like the turbulences. This phenomenon can be observed from the experimental results, some swirling and rolling exist in the spray, which can make the velocity distribution asymmetrical and some velocities exceed the cross-flow velocity.

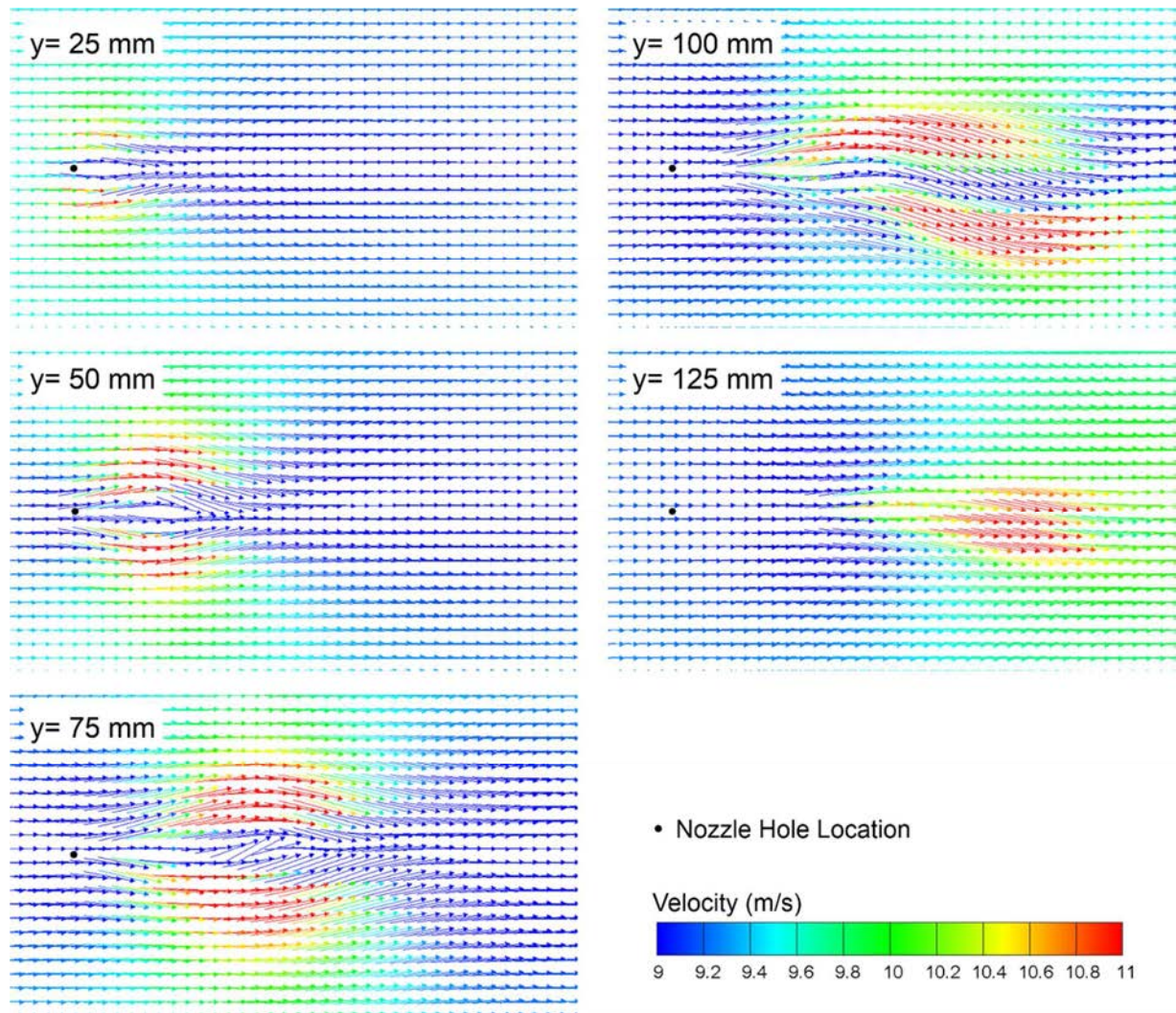


Figure 9.9 Velocity distributions of cross-flow field in various horizontal planes ($P_a= 10\text{MPa}$, $t= 7\text{ms ASOI}$).

9.5 Droplet Size Distributions

The droplet size is a critical parameter in the fuel atomization, and it affects the air-fuel mixture significantly. The droplet size distributions have been discussed by the experimental method in the previous discussion. The SMDs are around $15\mu\text{m}$. In this section, the droplet size distributions of the simulation will be represented.

The droplet size distributions under the conditions of with/without the cross-flow are shown in Fig. 9.10. The droplet sizes are larger in the upper of the spray than that in the low part in the condition of the no-cross-flow (see Fig. 9.10(a)). Additionally, the atomization in the surface of the spray is better than that of the inner spray, some large droplets always exist along the spray center line in the condition of the no-cross-flow condition. Those phenomena change in the condition of the cross-flow, the large droplets only exist in the upper part of the spray, and they hardly appear in the lower upper of the spray. The most of droplet sizes distribute in the range of

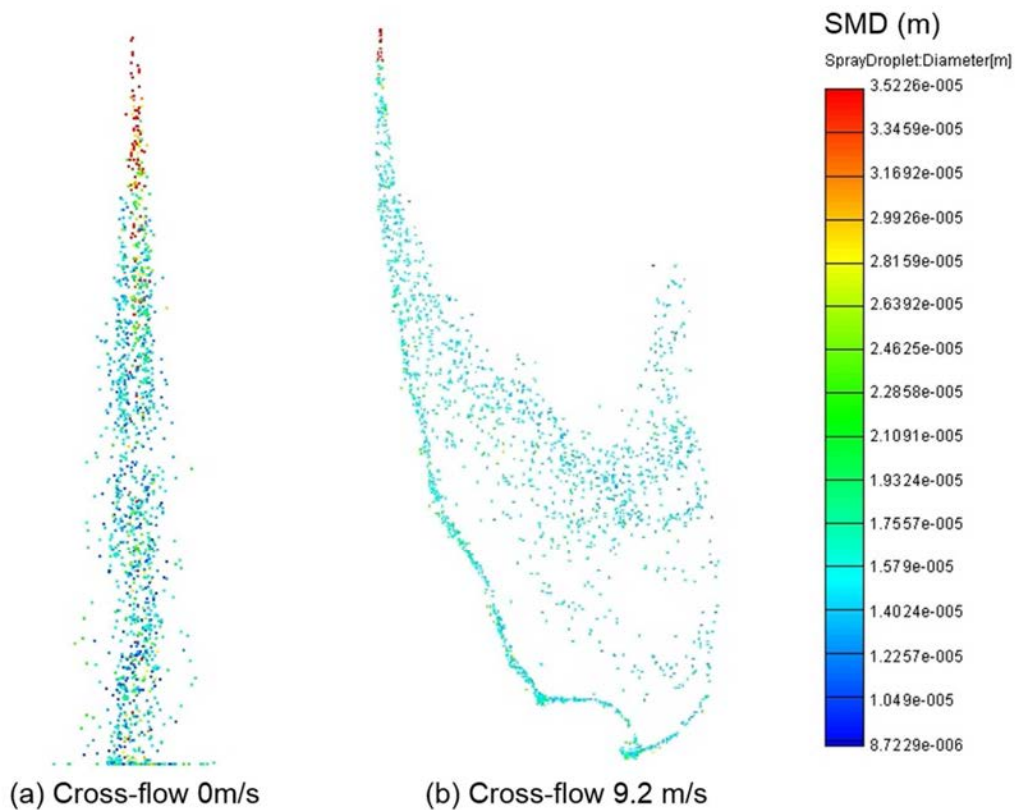


Figure 9.10 Droplet size distributions of spray ($P_a= 10\text{MPa}$, $t= 7\text{ms ASOI}$).

15~20 μm . In the spray edge in the windward, the droplet sizes are slightly larger than that in the leeside, which is similar to the experimental results.

The averages of the SMDs in various time are shown in the Figure 9.11. The SMDs become constant of about 17 μm after 1.5 ms ASOI. The droplet sizes decrease quicker in the cross-flow condition than that in the no-cross-flow condition. It is indicated that the cross-flow benefit the spray atomization.

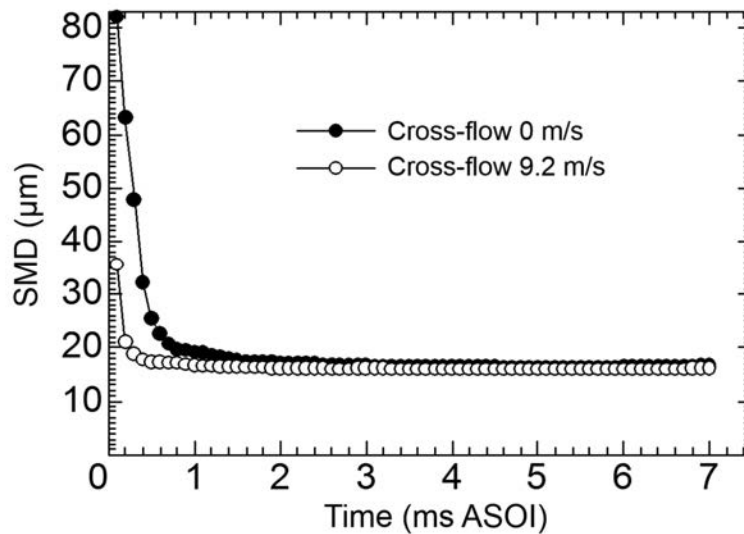


Figure 9.11 Droplet sizes of spray ($P_a=10\text{MPa}$, $t_d=7\text{ms}$).

The spray break-up includes two processes, the primary break-up and secondary break-up. The aerodynamic force affects the break-up very much, especially in the secondary break-up. The cross-flow enhance the aerodynamic force, which improves the atomization. The larger droplets with high velocity exist long the spray center line when the cross-flow is 0m/s. The possible reason is that the inner spray droplets are surrounded by the surface droplets and the air flow have already formed by the previous droplets, aerodynamic force on the inner droplets is very weak. The inner droplet break-up is retained without cross-flow. In the cross-flow condition, the situations change, the aerodynamic force can be enhanced by the cross-flow, moreover, the broken droplets can be blown to the downstream and the inner droplets can be exposed in the ambient gas, with the high velocity the droplets can disintegrate. And the tiny droplets can be blown to downstream and the inner droplets are exposed again, and the process repeats.

9.6 Summary and Future Simulation Work

The numerical simulation was taken for analyzing the cross-flow effects on spray. Some results have been presented, such as the spray profiles, penetrations, velocity distributions, and the droplet size distributions. Although there are some difference between the simulation results and experimental results, the most parts of them agree well.

The profile variations of the simulation can illuminate the cross-flow effects on the spray, it performances the bended profiles in the cross-flow condition. The penetrations, which include vertical penetrations and horizontal penetrations, own the same tendencies with the experimental results. In the vertical plane, the velocity distributions are similar to the PIV results, while the velocities exceeding the cross-flow velocity can be observed in the horizontal planes as the experimental velocity distribution. Some large droplets exist in the center line of spray without the cross-flow, while the droplet size distribution becomes more uniform with cross-flow.

The numerical simulation is a useful method to investigate the characteristics of the spray. However, the ideal simulations, which is the most close to the practical experiments, are based on the right selecting of models and parameters. Those models and parameters are selected according to the experimental conditions. The simplification of models and incorrect parameters will result in the inaccuracy in the simulation.

In the near future, the simulations will be improved by optimizing the models and parameters. And more condition simulations will be taken, such as changing the parameters of the ambient pressure, fuel, and injection duration.

Chapter 10 Conclusions

10.1 Experimental Methods and Implementation

The experimental methods, which were used in this study, were illuminated with the backgrounds and principles. There are two main kinds of experiments in this study, the experiments based on the atmospheric wind tunnel and the experimental based on the pressure wind tunnel. The former is used to simulate the condition of the surrounding of the homogenous charge combustion model, while the latter is used to simulate the condition of the surrounding of the stratified charge combustion model.

The high speed video photography was employed using Mie scattering method, the profiles, penetration, and droplet concentration could be analysis from those images, which were taken in various planes in horizontal and vertical. The continuous illuminators, which include the Xenon lamp and the continuous wave laser (sheet), were used in experiments. The PIV system was used to measure the velocity distributions of the spray and air field. The principle of the PIV was briefly introduced. Laser diffraction size analyzer was employed to measure the droplet sizes in various points, hence the droplet size distribution could be obtain by assembling those points.

The experimental setup of the atmospheric ambient (based on atmospheric wind tunnel) was presented, the details of the components were listed, such as the functions, types, and arrangements. The wind tunnel is composed of a diffusion chamber, a rectification chamber and a contraction chamber. There are five pieces of meshes with different size in the rectification chamber, and the observation section was made of transparent acryl. The cross-flow performance was checking by measuring the velocity distributions and turbulence in various points.

The high pressure wind tunnel was designed for the high pressure ambient cross-flow experiments. This wind tunnel was different from the circuit wind tunnel. The pressure wind tunnel was implemented using the velocity and back pressure, which were provided by the pressure gas and throttling of pressure wind tunnel. Before the design, the confirmatory calculations were made. The parts of the pressure wind tunnel were presented, such as sizes, material, and assembly. The pressure wind tunnel was a pressure vessel in some sense. The design and strength checking were followed the standards of the pressure vessel design manual. Before the experiments, the safety checking was implemented by filling liquid into pressure wind tunnel and pressurizing the liquid. The control system was designed for triggering the experiments. A pressure sensor and a hot-wire

anemometer with high sensitivity were used for acquiring the pressure and velocity signals, a PLC was employed as the control unit, and a touch screen was used as a man-machine interface.

10.2 Global Structure of Spray in Cross-Flow

The spray injected by the VCO nozzle is asymmetrical in the low ambient pressure due to the special structure of the nozzle.

At constant injection pressure, the vertical penetration decreases with an increase of the cross-flow velocity, however, such tendency becomes weak when the injection pressure is increased. With increasing the velocity of the cross-flow and the injection pressure, the horizontal penetration increases. The droplets distribution presents inhomogeneous in the upper region of spray; the horizontal component of spray velocity shows large fluctuations, especially in the downstream region of the spray where the value even exceeds the cross-flow velocity.

10.3 Cross-Sectional Structure of Spray

The structures in horizontal plane in the upper part of the spray present asymmetrical, and the droplet distributions are different in various horizontal planes. In the lower part of the spray the structure becomes symmetrical, however the strong movements can be observed.

The projected spray half angles present two flat lines in both sides, and the values of them in positive and negative are almost symmetrical about $\alpha = 0$ without the cross-flow. The projected spray half angles distribute unsteadily with increasing of the cross-flow velocity, otherwise the absolute value of the projected spray angles with cross-flow are much bigger than that without cross-flow.

The Karman vortices happen in the upper part of the spray in leeward when the cross-flow flow past the spray. The frequencies of the vortices are measured in two ways, the results are in the frequency range of the theoretical calculation. Additionally, the secondary vortices could happen in the upper part of the spray in the leeward, which leads to the distinct interlaced Strouhal vortices cannot be observed clearly.

10.4 Spray Droplets Flow Field

In the vertical plane of $z=0$ mm without the cross-flow, the phenomenon of the two tips structure is very distinct and the main directions of the velocity vectors are ahead along the two tips before impinging the bottom wall, and the spray presents a swelling tendency and the droplets velocities become unsteady in the middle part. After impingement, the two tips structure and its velocity distribution phenomena present no longer distinctly and the velocity distributions of the droplets become normal, the high velocity parts concentrate in the center line of the spray, and the low velocity vectors distribute in the both sides of the main spray. The rolling-up phenomenon happens after impingement, otherwise the vector directions meet this movement.

Before the impingement, in the low velocity of the cross-flow the two tips structure can be observed and the phenomenon is similar to that in the quiescent ambient, however excepting the big tip there are several small tips appear when the cross-flow increases. The droplets in the upper part in the leeward part of the spray are entrained into the cross-flow.

From the velocity distributions in the horizontal plane, the disorder velocity distributions appear near the original area. The velocities in the center line ($z=0$ mm) present a tendency of first increasing then keeping, while the value of that in the edge lines ($z=-10$ and 10 mm) shows much stable. The velocity fluctuations in the center is much stronger than that in the both sides in the horizontal plane.

The vorticity presents an interlaced distribution with different directions. The happening of the vorticity owns regional, in the range of the leeward of the spray the vorticity can be observed.

10.5 Spatial Distribution of Droplets and Their Sizes

The droplet distributions and sizes are discussed in this chapter. The diffusion of the spray is more obvious in the lower part of the spray than that in the upper part of the spray, droplets disperse along the spray center in the no-cross-flow condition. The minority droplets are blown away by the cross-flow in the upper part of the spray which the droplet distribution becomes non-uniform in the lower part of the spray under the cross-flow of 9.2 m/s at atmosphere. The droplets are squeezed into the center line, and the phenomena of the droplet concentrating along two tips disappear with ambient pressure increasing. The droplet diffusing becomes hard when the ambient pressure increased. In the pressure ambient, the non-uniform distribution, which is similar to that

at atmosphere, appears when the cross-flow velocity increases to some extent.

Droplets concentrated in the spray centre under the no-cross-flow condition, while a large number of droplets remained in the upstream area of the spray with the cross-flow. Otherwise, larger droplets were distributed in the high-concentration area. Additionally, the diameter of the droplets decreased along the direction of the cross-flow.

10.6 Effect of Ambient Pressure on Spray Characteristics

The discussions of effects of ambient pressure on spray characteristics are focused on the profiles of the spray under quiescent ambient and the cross-flow ambient with various ambient pressure, the penetrations, the velocity distributions and the droplet concentrations of the spray under various ambient pressures.

The penetration decreases and the tips of the spray disappear gradually with increasing the ambient pressure in the quiescent condition. With the cross-flow, the vertical penetrations of the spray in the high ambient pressure become shorter than that in the low ambient pressure. The displacements of the droplets in horizontal decrease obviously with the ambient pressure increases. The profile of the spray in the upstream side of the cross-flow become more bending in the same cross-flow velocity with increasing the ambient pressure.

In the pressure ambient condition, the velocity distributions in the high ambient pressure become more order than that in the low ambient pressure. The value of the velocity in the same position decreases with the ambient pressure increasing. When the ambient pressure increases, the extent of the bending edge of the spray increases distinctly.

Summarily, the increased ambient pressure can restrain the spray diffusion to some extent; the bended structure of the spray are enhanced in the high pressure ambient in the cross-flow field; the velocity distributions become ordered when the ambient pressure increases; and the droplets concentrate to the mainly spray with the high ambient pressure.

10.7 Numerical Simulation

The numerical simulation was taken for analyzing the cross-flow effects on spray. Some results have been presented, such as the spray profiles, penetrations, velocity distributions, and the droplet

size distributions. Although there are some difference between the simulation results and experimental results, the most parts of them agree well.

The profile variations of the simulation can illuminate the cross-flow effects on the spray, it performances the bended profiles in the cross-flow condition. The penetrations, which include vertical penetrations and horizontal penetrations, own the same tendencies with the experimental results. In the vertical plane, the velocity distributions are similar to the PIV results, while the velocities exceeding the cross-flow velocity can be observed in the horizontal planes as the experimental velocity distribution. Some large droplets exist in the center line of spray without the cross-flow, while the droplet size distribution becomes more uniform with cross-flow.

The numerical simulation is a useful method to investigate the characteristics of the spray. However, the ideal simulations, which is the most close to the practical experiments, are based on the right selecting of models and parameters. Those models and parameters are selected according to the experimental conditions. The simplification of models and incorrect parameters will result in the inaccuracy in the simulation.

10.8 Recommendations for Future Works

The previous works are the fundamental investigation for further understanding mechanism of the spray and air flow in the combustion cylinder. There are differences between the fundamental experiments and practical conditions in real engine. The future work should take the investigations which are more close to the practical conditions. Firstly, the experiments of impingement with the cross-flow can be taken in the existing experimental device, it is important to combine the two conditions, which affect the spray and air-fuel much in the combustion chamber. Thereafter, the more experiments, such as using the fuel, nozzle type, injection duration, spray direction, need to take under the cross-flow conditions. Additionally, the simulations will be improved by optimizing the models and parameters. And more condition simulations will be taken, such as changing the parameters of the ambient pressure, fuel, and injection duration.

Reference

- Alkidas, A.C.**, Combustion advancements in gasoline engines, *Energy Conversion and Management*, vol. 48, pp. 751-2761, 2007.
- Andrews, G.E., Bradley, D., and Hundy, G.F.**, Hot wire anemometer calibration for measurements of small gas velocities, *Int. J. Heat Mass Transfer*, vol. 15, pp. 1765-1786, 1972.
- Arai, M., Shimizu, M., and Hiroyasu, H.**, Similarity between the breakup lengths of a high speed liquid jet in atmospheric and pressurized conditions, *Los Alamos National Laboratory*, 1991.
- Auriemma, M., Corcione, F.E., Macchioni, R., Seccia, G., and Valentino, G.**, LDV measurements of integral length scales in an IC engine, *SAE Technical Paper*, 961161, 1996.
- Bai, B.F., Zhang, H.B., Liu, L., and Sun, H.J.**, Experimental study on turbulent mixing of spray droplets in crossflow, *Experimental Thermal and Fluid Science*, vol. 33, pp. 1012-1020, 2009.
- Balat, M. and Balat, H.**, Recent trends in global production and utilization of bio-ethanol fuel, *Applied Energy*, vol. 86, pp. 2273-2282, 2009.
- Baumgarten, C.**, *Mixture Formation in Internal Combustion Engines*, Springer-Verlag Berlin Heidelberg New York, 2006.
- Befrui, B., Corbinelli, G., Robart, D., and Reckers, W.**, LES simulation of the internal flow and near-field spray structure of an outward-opening GDI injector and comparison with imaging data, *SAE Technical Paper*, 2008-01-0137, 2008.
- Bhatia, J.C., Durst, F., and Jovanovic, J.**, Corrections of hot-wire anemometer measurements near walls, *J. Fluid Mech.*, vol. 122, pp. 411-431, 1982.
- Bloor, M.S.**, The transition to turbulence in the wake of a circular cylinder, *Journal of Fluid Mechanics*, vol.19, pp.290-340, 1964.
- Bradshaw, P.**, The effect of wind-tunnel screens on nominally two-dimensional boundary layers, *J. Fluid Mech.*, vol. 22, part 4, pp. 679-687, 1965.
- Chehroudi, B., Chen, S.H., Bracco, F.V., and Onuma, Y.**, On the intact core of full-cone spray, *SAE Technical Paper*, 850126, 1985.
- Chigier, N.**, Optical imaging of sprays, *Progress in Energy and Combustion Science*, vol.17, pp.

- 211-262, 1991.
- Chigier, N.**, Group combustion models and laser diagnostic methods in sprays: A review, *Combustion and Flame*, vol. 51, pp. 127-139, 1983.
- Church, W. and Farrell, P.V.**, Effects of intake port geometry on large scale in-cylinder flows, *SAE Technical Paper*, 980484, 1998.
- Clerk, D.**, Cylinder actions in gas and gasoline engines, *SAE Journal*, vol. 8, pp. 523, 1921.
- Colton, B.**, The outlook for energy: A view to 2040, ExxonMobil, 2014, <http://corporate.exxonmobil.com/en/energy/energy-outlook>.
- Cossali, G.E., Brunello, G., and Coghe, A.**, LDV characterization of air entrainment in transient diesel sprays, *SAE Technical Paper*, 910178, 1991.
- Dan, T., Takagishi, S., Senda, J., and Fujimoto, H.**, Organized structure and motion on diesel spray, *SAE Technical Paper*, 970641, 1997.
- DeCorso, S.M., and Kemeny, G.A.**, Effect of ambient and fuel pressure on nozzle spray angle, *Trans. Of ASME*, vol. 79, no. 3, pp. 607-615, 1957.
- Dent, J.C.**, A basis for the comparison of various experimental methods for studying spray penetration, *SAE Technical Paper*, 710571, 1971.
- Dillon, M.E., Wang, G., and Huey, R.B.**, Global metabolic impacts of recent climate warming, *Nature*, vol. 467, pp. 704-706, 2010.
- Drake, M.C., Fansler, T.D., Lippert, A.M.**, Stratified-charge combustion: modeling and imaging of a spray-guided direct-injection spark-ignition engine, *Proceedings of the Combustion Institute*, vol. 30, pp. 2684-2691, 2005.
- Drake, M.C., Fansler, T.D., Solomon, A.S., and Szekely, G.A.**, Piston fuel films as a source of smoke and hydrocarbon emissions from a wall-controlled spark-ignited direct-injection engine, *SAE Technical Paper*, 2003-01-0547, 2003.
- Eichseder, H., Baumann, E., Muller, P., and Neugebauer, S.**, Potential and risks of gasoline direct injection engine for passenger car drivelines, *MTZ worldwide*, vol. 61, pp. 2-5, 2000.
- Energy conservation vs. energy efficiency**, Natural Resources Canada, 2014, <http://www.nrcan.gc.ca/energy/efficiency/buildings/eeb/key/3969>.
- Fansler, T.D. and Drake, M.C.**, “Designer diagnostics” for developing direct-injection gasoline engines, *Journal of Physic: Conference Series*, vol. 45, pp. 1-17, 2005.
- Fujimoto, H., Sugihara, H., Tanabe, H., and Sato, G.T.**, Investigation on combustion in medium

- speed marine diesel engines using model chambers, *CIMAC-Congress*, Helsinki, 1981.
- Gavaises, M., Abo-serie, E., and Arcoumanis, C.,** Nozzle hole film formation and its link to spray characteristics in swirl-pressure atomizers for direct injection gasoline engines, *SAE Technical Paper*, 2002-01-1136, 2002.
- Getsinger, D.R., Gevorkyan, L., Smith, O.I., and Karagozian, A.R.,** Structural and stability characteristics of jets in crossflow, *Journal of Fluid Mechanics*, vol.760, pp.342-367, 2014.
- Ghosh, S. and Hunt, J.C.R.,** Spray jets in a cross-flow, *Journal of Fluid Mechanics*, vol.365, pp.109-136, 1998.
- Gold, M., Stokes, J., Morgan, R., Heikal, M., Sercey, G.D., and Begg, S.,** Air-fuel mixing in a homogeneous charge DI gasoline engine, *SAE Technical Paper*, 2001-01-0968, 2001.
- Groth, J., and Johansson, A.V.,** Turbulence reduction by screens, *J. Fluid Mech.*, vol. 197, pp. 139-155, 1988.
- Guo, M., Kishi, R., Shi, B., Ogata, Y., and Nishida, K.,** Cross-flow Effect on Behavior of Fuel Spray Injected by Hole-Type Nozzle for D.I. Gasoline Engine, *SAE Technical Paper*, 2013-01-2553, 2013.
- Guo, M., Kishi, R., Shi, B., Ogata, Y., and Nishida, K. (2015).** Effects of Cross-Flow on Fuel Spray Injected by Hole-Type Injector for Direct Injection Gasoline Engine, *Atomization and Sprays*, vol. 25. 11/5/2014, from <http://www.dl.begellhouse.com/journals/6a7c7e10642258cc,forthcoming,11375.html>
- Gülder, Ö.L., Smallwood, G.J., and Snelling, D.R.,** Diesel spray structure of transient full cone dense diesel sprays, *Commodia 94*, pp. 355-360, 1994.
- Harada, J., Tomita, T., Mizuno, H., Mashiki, Z, and Ito, Y.,** Development of direct injection gasoline engine, *SAE Technical Paper*, 970540, 1997.
- Hayakawa, M., Takada, S., Yonesige, K., Nagaoka, M., and Takeda, K.,** Fuel spray simulation of slit nozzle injector for direct-injection gasoline engine, *SAE Technical Paper*, 2002-01-1135, 2002.
- He, L. and Ruiz, F.,** effect of cavitation on flow and turbulence in plain orifices for high speed atomization, *Atomization and sprays*, vol. 5, pp. 569-584, 1995.
- Heil, B., Weining, H.K., Karl, G., Panten, D., and Wunderlich, K.,** *Concepts for reducing fuel consumption and emissions in spark-ignited engines, part 2*, *MTZ worldwide*, vol. 63, pp. 17-23, 2001.

- Heywood, J.B.**, Internal combustion engine fundamentals, *Singapore: McGraw-Hill Book Company*, 1988.
- Hiroyasu, H. and Arai, M.**, Structures of fuel spray in diesel engines, *SAE Technical Paper*, 900475, 1990.
- Hiroyasu, H. and Arai, M., and Tabata, M.**, Empirical equations for the Sauter mean diameter of a diesel spray, *SAE Technical Paper*, 890464, 1989.
- Hiroyasu, H. and Nishida, K.**, Fuel spray trajectory and dispersion in a D.I. diesel combustion chamber, *SAE Technical Paper*, 890462, 1989.
- Hiroyasu, H., Shimizu, M., and Arai, M.**, Breakup length of a liquid jet and internal flow in a nozzle, *ICLASS-91*, 1991.
- Huethorst, J.A.M. and Marra, J.**, Motion of marangeoni-contracted water drops across inclined hydrophilic surface, *Langmuir*, vol. 7, pp. 2756-2763, 1991.
- Hun, K.Y., Lee, E., and Koo, J.Y.**, Diesel spray atomization model considering nozzle exit turbulence conditions, *Atomization and Sprays*, vol. 8, pp. 453-469, 1998.
- IEA (International Energy Agency)**, Energy Technology Perspectives 2014, www.iea.org/etp, 2014.
- Im, K.S., Lin, K.C., Lai, M.C, and Chon, M.S.**, Breakup modeling of a liquid jet in cross flow, *International Journal of Automotive Technology*, vol. 12, no. 4, pp. 489-496, 2011.
- Imberdis, O., Hartmann, M., Bensler, H., Kapitza. L., and Thevenin, D.**, A numerical and experimental investigation of a DISI-engine intake port generated turbulent flow, *SAE Technical Paper*, 2007-01-4047, 2007.
- Kang, K.K., Cho, H.S., Baik, S.K., and Bae, J.I.**, The fuel spray structure of high pressure direct swirl injector for gasoline injection system, *SAE Technical Paper*, 2004-01-0541, 2004.
- Kawamura, K., Saito, A., Kanda, M., Kashiwagura, T., and Yamamoto, Y.**, Spray characteristics of slit nozzle for DI gasoline engines, *JSME*, vol. 46, pp.10-16, 2003.
- Katashiba, H., Honda, T., Kawamoto, M., Sumida, M., Fukutomi, N., and Kawajiri, K.**, Improvement of center injection spray guided DISI performance, *SAE Technical Paper*, 2006-01-1001, 2006.
- Khalighi, B. and Huebler, M.S.**, A transient water analogue of a dual-intake-valve engine for intake flow visualization and full-field velocity measurements, *SAE Technical Paper*, 880519, 1988.
- Khalighi, B and Huebler, M.S.**, A transient water analogue of a dual-intake-valve engine for

- intake flow visualization and full-field velocity measurements, *SAE Technical Paper* 900059, 1990.
- Kim, Y.J., Lee, S.H., and Cho, N.H.**, Effect of air motion on fuel spray characteristics in a gasoline direct injection engine, *SAE Technical Paper*, 1999-01-0177, 1999.
- Klopfenstein, R.**, Air velocity and flow measurement using a Pitot tube, *ISA Transactions*, vol. 37, pp. 257-263, 1998.
- Kobayashi, Y., Ishima, Y. and Obakata, T.**, Spray characteristics of a high-pressure swirl injector for DISI engines under high ambient temperature and pressure conditions, *SAE Technical Paper*, 2008-01-0130, 2003.
- Koch, T., Schanzlin, K., Boulouchos, K.**, Characterization and phenomenological modeling of mixture formation and combustion in a direct injection spark ignition engine, *SAE Technical Paper*, 2002-01-1138, 2002.
- Kong, J. and Bae, C.**, Effect of nozzle hole geometry on non-evaporating diesel spray characteristics at high-pressure injection, *Atomization and Sprays*, vol. 22, pp. 1-22, 2012.
- Lacis, A.A., Hansen, J.E. Russell, G.L., Oinas, V., and Jonas, J.**, The role of long-lived greenhouse gases as principal LW control knob that governs the global surface temperature for past and future climate change, *Tellus B*, vol. 65, 2013.
- Lauder, B.E. and Spalding, D.B.**, The numerical computation of turbulent flows, *Comp. Meth. Appl. Mech. Eng.*, vol. 3, pp. 269-289, 1974.
- Lee, C.S., Lee, K.H., Chon, M.S., and Kim, D.S.**, Spray structure and characteristics of high pressure gasoline injectors for direct-injection engine applications, *Atomization and Spray*, vol. 11, pp. 35-48, 2001.
- Lee, D.C.**, A study of air flow in an engine cylinder, *NACA report 653*, 1939.
- Lee, S., Kim, W., and Yoon, W.**, Spray formation by a swirl spray jet in low speed cross-flow, *Journal of Mechanical Science and Technology*, vol. 24, pp. 559-568, 2010.
- Liu, A.B. and Reitz, R.D.**, Modeling the effects of drop drag and break-up on fuel spray, *SAE Technical Paper*, 930072, 1993.
- Liu, L., Liu, W.Q., Wu, L.Q., Zhao, C.L.**, LDV measurements of velocities and turbulence intensities in a production SI engine under motored and firing condition. *SAE Technical Paper*, 1999-01-0955, 1999.
- Marchi, A., Nouri, J., Yan, Y., and Arcoumanis, C.**, Spray stability of outwards opening pintle

- injector for stratified direct injection spark ignition engine operation, *International Journal of engine research*, vol. 11, no. 6, pp. 413-437, 2010.
- Marko, K.A., Li, P., Rima, L., and Ma, T.,** Flow field imaging for quantitative cycle resolved velocity measurements in a model engine, *SAE Technical Paper*, 860022, 1986.
- Mitroglou, N., Nouri, J.M., Yan, Y., Gavaises, M., and Arcoumanis, C.,** Spray structure generated by multi-hole injectors for gasoline direct-injection engines, *Int. J. Engine Res.*, vol. 7, pp. 255-270, 2006.
- Moriyoshi, Y., Uchida, R., Takagi, M., and Kubota, M.,** Numerical and experimental analyses of mixture formation process using a fan-shaped DI gasoline spray: examinations on effects of crosswind and wall impingement, *SAE Technical Paper*, 2009-01-1502, 2009.
- Mitroglou, N., Nouri, J.M., Yan, Y., Gavaises, M., and Arcoumanis, C.,** Spray structure generated by multi-hole injectors for gasoline direct-injection engines, *SAE Technical Paper*, 2007-01-1417, 2007.
- Moon, S., Bae, C., Choi, J., and Abo-Serie, E.,** The influence of airflow on fuel spray characteristics from a slit injector, *Fuel*, vol. 86, pp. 400-409, 2007.
- Moon, S., Choi, J., Abo-Serie, E., and Bae, C.,** The effects of injector temperature on spray and combustion characteristics in a single cylinder DISI engine, *SAE Technical Paper*, 2005-01-0101, 2005.
- Moon, S., Matsumoto, Y., Nishida, K., and Gao, J.,** Gas entrainment characteristics of diesel spray injected by a group-hole nozzle, *Fuel*, vol. 89, pp. 3287-3299, 2010.
- Motallebi, F.,** A review of the hot-wire technique in 2-D compressible flows, *Prog. Aerospace Sci.*, vol. 30, pp. 267-294, 1994.
- Myung, C.L. and Park, S.,** Exhaust nanoparticle emissions from internal combustion engines: A review, *International Journal of Automotive Technology*, vol. 13, no. 1, pp. 9-22, 2012.
- Naber, J.H., and Siebers, D.L.,** Effects of gas density and vaporization on penetration and dispersion of diesel sprays, *SAE Technical Paper*, 960034, 1996.
- No, S.Y.,** Empirical correlations for penetration height of liquid jet in cross flow-a review, *ILASS-Europe 2011, 24th Annual Conf. on Liquid Atomization and Spray Systems, Estoril, Portugal*, 5-7 Sept. 2011.
- Nouri, J.M., Whithelaw, J.H.,** Gasoline spray in uniform crossflow, *Atomization and Sprays*, vol. 17, pp.621-640, 2007.

- Nouri, J.M. and Whitelaw, H.**, Spray characteristics of a gasoline direct injector with short durations of injection, *Experiments in Fluids*, vol. 31, pp. 377-383, 2001.
- Oken Corp**, http://www.oken.co.jp/web_oken/Keisan_jp.htm, 2013.
- Ortmann, R., Arndt, R., Raimann, J., Grzeszik, R., and Wurfel, G.**, Methods and analysis of fuel injection, mixture preparation and charge stratification in different direct injected SI engines, *SAE Technical Paper*, 2001-01-0970, 2001.
- O'Rourke, P.J. and Amsden, A.A.**, The TAB method for numerical calculation of spray droplet breakup, *SAE Technical Paper*, 872089, 1987.
- Padala, S., Le, M.K., Kook, S., and Hawkes, E.R.**, Imaging diagnostics of ethanol port fuel injection sprays for automobile engine applications, *Applied Thermal Engineering*, vol. 52, pp. 24-37, 2013.
- Padala, S., Kook, S., and Hawkes, E.R.**, Effect of ethanol port-fuel-injector position on dual-fuel combustion in an automotive-size diesel engine, *Energy Fuels*, vol. 28, no. 1, pp. 340-348, 2014.
- Panão, M.R.O., Moreira, A.L.N., and Durão, D.F.G.**, Effect of a cross-flow on spray impingement with port fuel injection systems for HCCI engines, *Fuel*, vol. 106, pp. 249-257, 2013.
- Park, S.H., Kim, H.J., Suh, H.K., and Lee, C.S.**, Atomization and spray characteristics of bioethanol and bioethanol blended gasoline fuel injected through a direct injection gasoline injector, *International Journal of Heat and Fluid Flow*, vol. 30, pp. 1183-1192, 2009.
- Persoons, T., Van den Bulck, E., and Hoefnagels, A.**, Experimental Study of Pulsating Flow in a Close-Coupled Catalyst Manifold on a Charged Motored Engine using Oscillating Hot-Wire Anemometry, *SAE Technical Paper*, 2006-01-0623, 2006.
- Peterson, B., Reuss, D.L., and Sick, V.**, High-speed imaging analysis of misfires in a spray-guided direct injection engine, *Proceedings of the combustion institute*, vol. 33, pp. 3089-3096, 2011.
- Peterson, B. and Sick, V.**, Simultaneous flow field and fuel concentration imaging at 4.8 kHz in an operating engine, *Applied Physics B*, vol. 97, pp. 887-895, 2009.
- Raffel, M., Willert, C., and Kompenhans, J.**, *Particle image velocimetry*, Germany: Springer, 2000.
- Reeves, M.**, *Particle image velocimetry applied to internal combustion engine in-cylinder flows*,

- PhD, Loughborough University of Technology, 1995.
- Reitz, R.D., and Bracco, F.V.**, Mechanisms of breakup of round liquid jets, *Encyclopedia of Fluid Mechanics*, Gulf Pub, NJ, vol. 3, pp. 233-249, 1986.
- Reitz, R.D., and Diwakar, J.**, Structure of high-pressure spray, *SAE Technical Paper*, 870598, 1987.
- Roisman, I.V., Araneo, L., and Tropea, C.**, Effect of ambient pressure on penetration of a diesel spray, *International Journal of Multiphase Flow*, vol. 33, pp. 904-920, 2007.
- Rottenkolber, G., Gindele, J., Raposo, J., and Dullenkopf, K.**, Spray analysis of a gasoline direct injector by means of two-phase PIV, *Experiments in Fluids*, vol. 32, pp. 710–721, 2002.
- Ryan III, T.W. and Callahan, T.J.**, Homogeneous charge compression ignition of diesel fuel, *SAE Technical Paper*, 961160, 1996.
- Saito, A., Ohsawa, K., Kawamura, K., Shirakawa, S., and Tanasawa, Y.**, Spray characteristics of swirl nozzle used for diesel engines, *International Conference on Liquid Atomization and Spray System*, London, pp. 1-11, 1985.
- Schneider, S.H.**, Global warming: are we entering the greenhouse century, *San Francisco: Sierra Club Books*, 1989.
- Schanzlin, K., Koch, T., Tzannis, A.P., and Boulouchos, K.**, Characterization of mixture formation in direct injected spark ignition engine, *SAE Technical Paper*, 2001-01-1909, 2001.
- Schmidt, D., Nouar, I., Senecal, P., Rutland, C., Martin, J.K., Reitz, R.D., and Hoffman, J.A.**, Pressure-Swirl Atomization in the Near Field, *SAE Technical Paper*, 1999-01-0496, 1999.
- Schwarz, C., Schunemann, E., Durst, B., Fischer, J., and Witt, A.**, Potentials of the spray-guided DI combustion system, *SAE Technical Paper*, 2006-01-1265, 2006.
- Sedarsky, D., Paciaroni, M., Berrocal, E., Petterson, P., Zelina, J., Gord, J., and Linne, M.**, Model validation image data for breakup of a liquid jet in crossflow: part I, *Exp Fluids*, vol. 49, pp. 391-408, 2010.
- Settles, G.S.**, Schlieren and shadowgraph techniques: visualizing phenomena in transparent media, Springer, Berlin, 2006.
- Shack, D.H. and Reynolds, W.C.**, Application of particle tracking velocimetry to the cyclic variability of the pre-combustion flow field in a motored axisymmetric engine, *SAE Technical Paper*, 910475, 1991.

- Shi, B., Shimokuri, D., and Ishizuka, S.,** Methane/oxygen combustion in a rapidly mixed type tubular flame burner, *Proceedings of the Combustion Institute*, vol. 34, no. 2, pp. 3369-3377, 2013.
- Skogsherg, M., Dahlander, P., and Denbratt, I.,** Spray shape and atomization quality of an outward-opening piezo gasoline DI injector, *SAE Technical Paper*, 2007-01-1409, 2007.
- Soteriou, C., Andrews, R., Smith, M., and Kunkulagunta, T.,** Through the diesel nozzle-a journey of discovery II, *ILASS-Europe*, Zürich, 2001.
- Soteriou, C., Andrews, R., and Smith, M.,** Direct injection diesel sprays and the effect of cavitation and hydraulic flip on atomization, *SAE Technical Paper*, 950080, 1995.
- Spicher, U., Reissing, J., Kech, J.M., and Gindele, J.,** Gasoline direct injection (GDI) engines-development potentialities, *SAE Technical Paper*, 1999-01-2938, 1999.
- Stegemann, J., Seebode, J., Baltés, J., Baumgarten, C., and Merker, G.P.,** Influence of throttle effects at the needle seat on the spray characteristics of a multihole injection nozzle, *ILASS-Europe 2002, 18th Annual Conf. on Liquid Atomization and Spray Systems, Zaragoza, Spain*, 9-11 Sept. 2002.
- Stenzler, J.N., Lee, J.G., Santavicca, D.A., and Lee, W.,** Penetration of liquid in a cross-flow, *Atomization and Sprays*, vol. 16, pp.887-906, 2006.
- Su, T.F., Patterson, M.A., Reitz, R.D., and Farrell, P.V.,** Experimental and Numerical Studies of High Pressure Multiple Injection Sprays, *SAE Technical Paper*, 960861, 1996.
- Szekely, G.A., Alkida, A.,** Combustion characteristics of a spray-guided direction stratified-charge engine with a high-squish piston, *SAE Technical Paper*, 2005-01-1937, 2005.
- Tagaki, Y., Itoh, T., Muranaka, S., Iiyama, A., Iwakiri, Y., Urushihara, T., and Naitoh, K.,** Simultaneous Attainment of Low Fuel Consumption, High Output Power and Low Exhaust Emissions in Direct Injection SI Engines. *SAE Technical Paper*, 980149, 1998.
- Tajima, K., Tsuru, D., Kawauchi, S., and Kato, H.,** Spray model verification via observation of diesel spray propagation in parallel flow field to injection direction, *ILASS-Japan 2011*, pp. 194-198, 2011.
- Tamaki, N., Shimizu, M., and Hiroyasu, H.,** Enhanced Atomization of a liquid jet by cavitation in a nozzle hole, *8th Int. Conf. on Liquid Atomization and Spray Systems*, Pasadena, CA, USA, 2000.
- Tanaka, Y., Takano, Y., and Sami, H.,** Analysis on behaviors of swirl nozzle spray and slit nozzle

- spray in relation to DI gasoline combustion, *SAE Technical Paper*, 2003-01-0058, 2003.
- Taylor, A.M.K.P.**, Science review of internal combustion engines, *Energy Policy*, vol. 36, pp. 4657-4667, 2008.
- Timoshenko, S., and Woinowsky-Krieger, S.**, Theory of plates and shells, McGraw-hall, 1959.
- Tolinger, J.D.**, Particle and flow field holograph, *Combustion Measurements*, pp. 55-89, 1991.
- Wei, T., Smith, C.R.**, Secondary vortices in the wake of circular cylinder, *Journal of Fluid Mechanics*, vol.169, pp.513-533, 1986.
- Wu, P.K., Kirkendall, K.A, Fuller, R.P., and Nejad, A S.**, Breakup processes of liquid jets in subsonic crossflows, *Journal of Propulsion and Power*, vol. 13, no. 1, pp. 64-73, 1997.
- Wu, P.K. and Faeth, G.M.**, Onset and end of drop formation along the surface of turbulent liquid jet in still gases, *Phys. of Fluids*, vol. 7, no. 11, 1995.
- VanDerWege, B.A., Han, Z., and Lyer, C.O.**, Development and analysis of a spray-guided DISI combustion system concept, *SAE Technical Paper*, 2003-01-3105, 2003.
- Yoshizaki, T., Yuzaki, K., Nishida, K., Hiroyasu, H., Yamashita, H., and Kaneda, K.**, Experiments and modeling on spray distributions in the combustion chamber of a direct injection diesel engine, *SAE Technical Paper*, 961820,1996.
- Youle, A.J. and Salters, D.G.**, A conductivity probe technique for investigating the breakup of diesel sprays, *Atomization and sprays*, vol. 4, pp. 253-262, 1994.
- Zdravkovich, M.M.**, *Flow around circular cylinders: vol 1: fundamentals*, Oxford, pp. 79-85, 1997.
- Zhang, G., Xu, M., Zhang,Y., Zhang, M., and Cleary, D.J.**, Macroscopic characterization of flash-boiling multi-hole sprays using planer laser-induced exciplex fluorescence. Part II: Cross-sectional spray structure, *Atomization and Sprays*, vol. 23, no. 3, pp. 265-278, 2013.
- Zhao, F.Q., Lai, M.C., and Harrington, D.L.**, A review of mixture preparation and combustion control strategies for spark-ignited direct gasoline engines, *SAE Technical Paper*, 970627, 1997.
- Zhao, F.Q., Lai, M.C., and Harrington, D.L.**, Automotive spark-ignited direct-injection gasoline engines, *Progress in Energy and Combustion Science*, vol. 25, pp. 437-562, 1999.
- Zhao, H., and Ladommatos, N.**, Engine combustion instrumentation and diagnostics, *Society of Automotive Engineers, Inc.*, 2001.
- Zhu, J.Y., Nishida, K., and Kuti, O.A.**, PIV study on flow of spray and surrounding gas under

non-evaporating and evaporating conditions, *ICLASS 2012, 12th Triennial International Conf. on Liquid Atomization and Spray Systems, Heidelberg, Germany, 2-6 Sept. 2012.*

Appendix

The program of the control system

1. I/O distribution

Table I. Input ports setting

Input	Function
X000	Start Setting
X001	Stop
X002	Start

Table II. Output ports setting

Output	Function
Y000	DG Trigger

Table III. Analog-digital conversion setting

4AD	Function	Remark
U0\G0	First Module	
H0011	Channel Attribute	Pressure Signals
H0001	Channel Attribute	Velocity Signals

Table IV. Relay setting

Relay	Function
M0	Start
M1	Data Writing
M2	Compare
M100	D0<D203,ON
M101	D203<D0<D204,ON
M102	D0>204,ON
M200	D1<D208,ON
M201	D208<D1<D209,ON

M202	D1>D209,ON
------	------------

Table V. Register setting

Register	Function	Remark
D0	Channel 1 Pressure	
D1	Channel 2 Velocity	
D2	Channel 3	
D3	Channel 4	
D5	For Calculation	
D6	For Calculation	
D7	For Calculation	Advance
D8	For Calculation	
D9	For Calculation	
D10	For Calculation	
D200	Setting Data of Pressure	
D201	Plus Deviation of Pressure	
D202	Minus Deviation of Pressure	
D203	Lower Limit of Pressure	$D203=D200-D201$
D204	Upper Limit of Pressure	$D204=D200+D202$
D205	Setting Data of Velocity	
D206	Plus Deviation of Velocity	
D207	Minus Deviation of Velocity	
D208	Lower Limit of Velocity	$D208=D205-D206$
D209	Upper Limit of Velocity	$D209=D205+D207$
D211	Coefficient K of Hot Wire	$K*100$
D300	Channel 1 Pressure	After Translating
D301	Channel 2 Velocity	
D302	Channel 3	
D303	Channel 4	

2. Program of PLC

0	LD	X000			
1	OR	M0			
2	ANI	X001			
3	OUT	M0			
4	LD	M8002			
5	MOV	H11	U0\G0		
10	LD	M0			
11	EMOV	U0\G10	D0	K4	
18	LD	M0			
19	MUL	D0	K5	D5	
26	SUB	D5	K2000	D6	
33	DIV	D6	K4	D300	
40	LD	M0			
41	DIV	D1	K50	D7	
48	MUL	D7	D211	D8	
55	DIV	D8	K80	D301	
62	LD	X002			
63	OR	M1			
64	AND	M0			
65	OUT	M1			
66	LD	M0			
67	AND	M1			
68	SUB	D200	D201	D203	
75	ADD	D200	D202	D204	
82	SUB	D205	D206	D208	
89	ADD	D205	D207	D209	
96	LD	M0			
97	AND	M1			
98	ZCP	D203	D204	D300	M100
107	ZCP	D208	D209	D301	M200
116	LD	M0			
117	AND	M101			
118	AND	M201			
119	OR	M2			
120	ANI	X001			
121	OUT	M2			
122	LDP	M2			
124	OR	Y000			
125	ANI	T200			
126	OUT	Y000			

127	OUT	T200	K50
130	LD	X003	
131	ZRSTP	D0	D4
136	LD	X004	
137	ZRSTP	D200	D400
142	END		